SUPRAMOLECULAR POLYMETALLIC CLUSTERS AND GRIDS: SELF-ASSEMBLY, STRUCTURE, AND MAGNETIC PROPERTIES

VICTORIA A. MILWAY

Supramolecular polymetallic clusters and grids: Self-assembly, structure, and magnetic properties.

By

Victoria A. Milway, B. Sc. (Honours)

A thesis submitted to the

School of Graduate Studies

in partial fulfillment of the

requirements for the degree of

Doctor of Philosophy

Department of Chemistry

Memorial University of Newfoundland

St. John's Newfoundland Canada

Abstract:

A series of tritopic 2,6-picolinic dihydrazone ligands with electron rich (Cl, S) functional groups incorporated onto the 4-position of the central pyridine ring was synthesized. The ligands were reacted with transition metal salts, resulting in [3x3] square $M(II)_9$ grids with Mn(II), Cu(II), Ni(II) and Co(II) salts, $Cu(II)_8$ pinwheels and, in one case, a $Ni(II)_6$ partial grid fragment. The Cl and S-based functional groups take part in a series of intermolecular H-bonding, Cl···N, S···N and S···S interactions in the crystalline state, which completely disrupt the π-stacking usually observed in complexes with this type of ligand. In the $Cu(II)_8$ pinwheels these interactions cause stacking of the molecules, leading to an intermolecular ferromagnetic interaction in one case and an intermolecular antiferromagnetic interaction in another. The functionalized $Mn(II)_9$ [3x3] grids were reacted with other transition metal cations, resulting in partially oxidized [3x3] $[Mn(II)_xMn(III)_{9-x}]$ grids for reactions with Cu(II), Fe(III) and Au(III). With $KAg(CN)_2$, the product was a typical $Mn(II)_9$ grid with a polymeric $Ag(CN)_x$ chain serving as a counter anion. There were no direct bonding connections between the chain and the grid, but several short Ag···S intermolecular contacts were observed. With $AgNO_3$, the product was a three dimensional network of grid molecules bridged to each other via two or four Ag(I) bridges. X-ray structures for a wide selection of the complexes are discussed and the magnetic properties of the clusters and grids examined in detail. Exchange models have been developed and exchange integrals determined for many $M(II)_9$ grids and $Cu(II)_8$ pinwheel clusters. The $Cu(II)_8$ clusters are most unusual in that strict magnetic orbital orthogonality leads to rare intramolecular ferromagnetic exchange.

Acknowledgements:

I would like to thank my supervisor, Dr. Laurence Thompson, for all the guidance and support he has offered me over the course of both my undergraduate and graduate programs. I owe much of my interest in chemistry to him.

I would also like to thank my supervisory committee, Dr. Robert Davis, and Dr. David Thompson, for their help and suggestions. I especially appreciate the fine touch of irony they used in reviewing this document.

I would like to acknowledge the effort of Dr. Robert McDonald, David Miller, Dr. Judith Howard, Elinor Spencer, and Louise Dawe for the collection and refinement of crystal data. Julie Collins, Kai Zhang and Tim Kelly are gratefully acknowledged for NMR data, along with Tareque Abedin, Zhiqiang Xu, and Stewart Parsons for magnetic data.

I would like to thank all the former members of the Thompson research group, Liang Zhao, Zhiqiang Xu, Steve DeGrace, Stewart Parsons, Virginie Niel, and Hilde Grove for teaching me what they could about chemistry. I learned so much from all of them, especially Zhiqiang Xu, my big brother in chemistry. No less deserving of thanks are the later members of the group, Tim Kelly, Louise Dawe, Peter Blanchard, Tareque Abedin, Subrata Dey, and Randy Royle, who also had a lot to teach, and who made me think about what I know. I would like to thank them all for being my friends as well as my coworkers.

Thanks also to my friends and family for their love and support. Thanks to my parents, Steve and Chris, for being there and for their understanding and unwavering

support. Thanks to my sister, Ginny, for making me laugh, and for the occasional personalized sticker. Thanks to my fiancé, Steven Benjamins, for his love and support, his enthusiasm, and his occasional translation of German references. I couldn't have done it without any of them.

Finally, I would like to acknowledge Dr. Laurence Thompson, the Chemistry Department, the School of Graduate Studies, and NSERC for financial support during my program.

Table of Contents:

List of Figures:

List of Tables:

List of Schemes:

List of Symbols and Abbreviations:

DNA	deoxyribonucleaic acid
NMR	nuclear magnetic resonance
QCA	quantum dot cellular automata
Qubits	quantum bits
S	spin quantum number
H	external magnetic field
B	magnetic induction
I	intensity of magnetization
κ	volume susceptibility
P	magnetic permeability
χ_g	mass susceptibility
ρ	density
χ_m	molar susceptibility
M	molar mass
χ'_m	corrected molar susceptibility
μ_{eff}	effective magnetic moment
k	Boltzmann constant
N	Avogadro's number
T	temperature
β	Bohr magneton
e	electronic charge

h	Planck's constant
m	mass (electron mass)
c	speed of light
C	Curie constant
θ	Weiss (or Weiss-like) constant
J	exchange integral
g	Landé splitting factor
S'	total spin quantum numbers
E(S')	energy of total spin quantum numbers
H_{ex}	exchange Hamiltonian
α	fraction of paramagnetic impurity
TIP	temperature independent paramagnetism
VC	vector coupling
FMD	full matrix diagonalization
ITO	irreducible tensor operators
M_s	saturation magnetization
Ω(S')	degeneracy function
FT-IR	Fourier transform-infra red
UV	ultra-violet
Vis	visible
nir	near infra red
LCMS	liquid chromatography mass spectrometry

APCI	atmospheric pressure chemical ionization
SQUID	superconducting quantum interference device
CV	cyclic voltammogram (voltammetry)
DPV	differential pulse voltammogram (voltammetry)
Mp	melting point
DMF	dimethylformamide
DMSO	dimethylsulfoxide
STM	scanning tunnelling microscope
HOPG	highly ordered pyrolytic graphite
CITS	current image tunnelling spectroscopy
Py	pyridine
μ_{mol}	magnetic moment per mole
$E_{1/2}$	half-wave potential
E_p	peak potential
TEAP	tetraethylammonium perchlorate
E_{pulse}	pulse potential
dca	dicyanamide
LFSE	ligand field stabilization energy
ε	extinction coefficient
λ	wavelength
D	zero-field splitting
BVS	bond valence sum

NHE	normal hydrogen electrode
HSAB	hard soft acid base (theory)

Chapter 1: General introduction

1.1: Supramolecular chemistry, self-assembly, and ligand design:

Any discussion of supramolecular chemistry should begin with an attempt to define the term. This task has become more difficult recently as more researchers from diverse fields have become involved. The original definition of the term, coined by Jean-Marie Lehn was "chemistry of molecular assemblies and of the intermolecular bond". This definition limited supramolecular chemistry to systems of molecules held together by intermolecular forces such as hydrogen bonding, π- π interactions, and van der Waals interactions. This definition would encompass fields such as host-guest chemistry and hydrogen bonding networks in carboxylic acids, but exclude covalent bonds. Since its conception, supramolecular chemistry has undergone rapid growth to include the self-assembly of molecular arrays and even large molecules from molecular components, and some covalent interactions such as metal-ligand bonding now fall under the umbrella of supramolecular chemistry [1].

The key concept in supramolecular chemistry is self-assembly. Self-assembly is a process used in nature to efficiently create large biomolecules such as proteins and DNA. For the present discussion, a more specific definition is required. Self-assembly involves the non-covalent interaction of at least two well defined sub-units into an aggregate whose properties are different from those of the original subunits. Additionally, the subunits will assemble such that the most stable (thermodynamic) aggregate is formed, and the aggregates formed will be discrete clusters rather than infinite arrays or polymers. Self-assembly processes are generally very efficient because the products are usually

both enthalpically and entropically favoured. Additionally, the individual processes involved are reversible, which allows the system to repair errors in the structure [2]. The remainder of the discussion of self-assembly will be limited to polynuclear coordination complexes.

Self-assembly processes can be broken down into two main categories; serendipitous self-assembly and rational design. Serendipitous self-assembly makes use of ligands which have several different potential binding modes, and metals which can vary their coordination geometry. There is no attempt to control the final structure of the product, and it is difficult to predict the outcome of the reaction. Starting materials tend to be simple, often commercially available ligands, because it is impossible to judge whether the starting material will be useful until a reaction is performed. It is important to realize that while the final product of the reaction may not be controlled, certain techniques are used to encourage the formation of polynuclear products [3]. An excess of metal with respect to the ligand binding sites encourages bridging between metal centers. Bridging of metal cations can also be encouraged by arranging the geometry of the donor sites on a ligand such that they cannot all bind to the same metal cation. Coordinatively unsaturated metal complexes can undergo ligand rearrangements resulting in bridged polynuclear complexes. Many interesting and unexpected clusters have been synthesized using serendipitous self-assembly, including $Fe(III)_{17}$ and $Fe(III)_{19}$ aggregates [4], a $Cu(II)_{36}$ cluster [5], and a mixed oxidation state Mn_{84} torus [6].

Serendipitous self-assembly is initially less useful to those interested in producing structures with specific properties. However, the examination of trends in

serendipitously formed products can be very useful in the understanding of the bonding forces and other factors involved in self-assembly processes. In this manner, the study of these compounds can lead to the ability to alter the structure, composition and properties of the product, in a rational way. The use of templating molecules or ions, for example, can greatly influence the structure of a product. This has been observed in many systems, such as the crown ethers [7], and the hexa and octanuclear rings of Saalfrank [8], whose size can be selected based on the size of the alkali metal template used. An excellent example of this step between serendipitous self-assembly and rational design for polymetallic clusters occurs in a group of heterometallic wheel compounds prepared by Winpenny and coworkers [9]. Starting from studies of a well characterized compound, $[Cr_8F_8(O_2CCMe_3)_{16}]$ [10,11], a series of similar heterometallic wheels of varying ring sizes has been synthesized. The synthesis involves the addition of an excess of a second metal cation, such as Ni(II), Cd(II), Fe(II) or Mn(II), to a mixture of CrF_3, pivalic acid, and a secondary amine template. The ring size of the resultant heterometallic wheel can be controlled by changing the template [12,13], and the properties of the wheel can be tuned by changing the metal cations [13]. It is also possible to make isostructural wheels using different carboxylic acids [13]. This is particularly interesting because it allows functionalization of the complex for surface studies and possible device development [13,14]. An example of a heterometallic wheel, $[NMe_2H_2][Cr_7NiF_8(O_2C^tBu)_{16}]$, is pictured in Figure 1.1.

Rational design is used when the goal is to prepare a complex that has a specific structure and properties. It differs from serendipitous self-assembly in that the ligands

and metal cations are carefully chosen, so that the ligand binding sites match the coordination requirements of the metal. In this way, the possibility of unexpected products is reduced. Starting materials tend to be more elaborate, and lengthy synthetic procedures are frequently used to produce a ligand or precursor complex to fill a particular role.

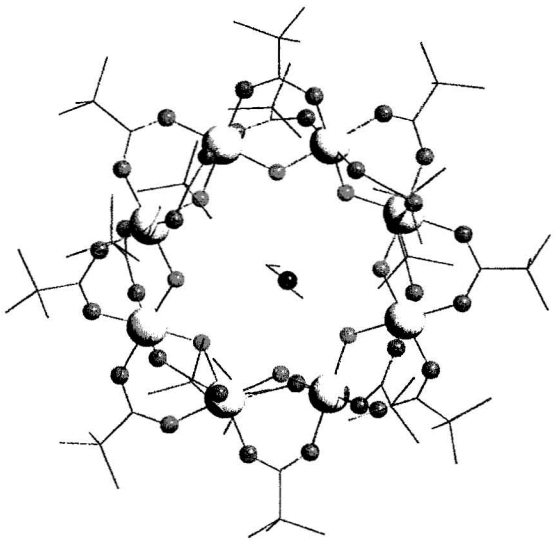

Figure 1.1: The heterometallic wheel compound $[NMe_2H_2][Cr_7NiF_8(O_2C^tBu)_{16}]$. M = brown, O = red, N = blue, F = green [15].

Ligand design is crucial in rational design, not only in terms of the topology of the product, but also in terms of the properties of the complex. Good ligands for rational design possess several important characteristics. They are rigid, which prevents bending of the ligand and the adoption of unexpected coordination modes. They are chelating, which increases the stability of the coordination complex. The best ligands further increase the stability by situating donor atoms in the ligand backbone in such a way as to

form five or six membered chelate rings in the complex. Ligands used in rational design are built to fulfill, or to partially fulfill the coordination requirements of a metal cation. Donor sites are situated at angles which match the preferred geometry of the cation to make binding more favourable. This matching of the ligand binding sites to the metal cation is known as the coordination algorithm [16].

The principles of rational design can be best explained by way of examples. The construction of supramolecular squares, grids and ladders has generated a great deal of interest due to the high efficiency of the synthetic processes, the flat and regular geometries of the molecules and the interesting magnetic and electrochemical properties that they possess.

A large family of [m x n] grid type complexes has been synthesized by Jean-Marie Lehn and coworkers. [2x2] [3x3] and [4x4] grids (m = n), and [2x3] ladders can all be prepared using the same family of ligand molecules and a variety of transition metal cations [17-23]. An example of a ditopic ligand is pictured in Figure 1.2. The ligands are entirely aromatic based, and as a result are rigid and planar. The coordination pockets of the ligands each contain three nitrogen atom donors, which are oriented at approximately 90° to each other. The result is that the geometry of the pocket is nearly ideal for the coordination of an octahedral metal cation. Because the donors are in the same plane, the pocket will fill *mer*-sites of the metal cation, which encourages the coordination of the cation by a second ligand molecule, oriented perpendicular to the first. Further examination of the ligand reveals that coordination to a transition metal cation will result in a series of five membered chelate rings. This property adds stability

to the compound, but it also assures linearity in the arrangement of the metal cations. The terpyridine-like environment of the coordination pockets was created by linking bipyridine units with pyrimidine bridges. The pyrimidine rings bridge adjacent metal cations, and because the π orbitals are accessible, they could support metal-metal interactions, resulting in magnetic, or perhaps electrochemical interactions.

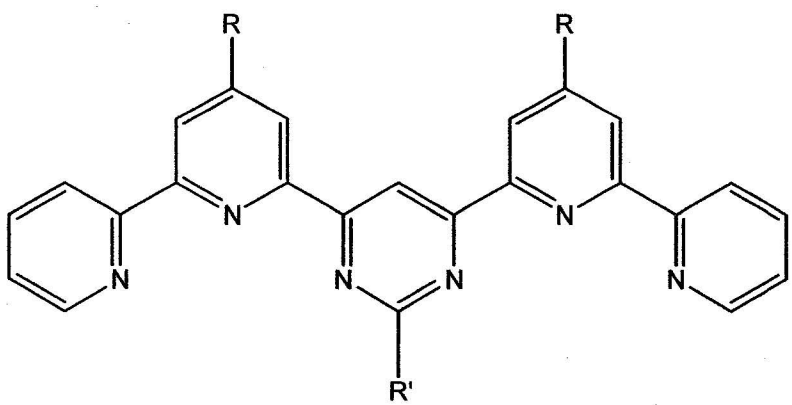

Figure 1.2: Model ditopic terpyridine-like ligand.

An example of a [2x2] Co(II) grid with a ditopic terpyridine-like ligand (4,6-bis(2'',2'-bipyrid-6'-yl)-2-phenylpyrimidine, Figure 1.2, R = H, R' = phenyl) [17] is pictured in Figure 1.3. The $Co(II)_4$ complexes with the terpyridine-like ligands are of particular interest as due to their electrochemical properties. The complexes undergo a total reduction of eleven electrons over ten reversible steps at a temperature of -20° C [18].

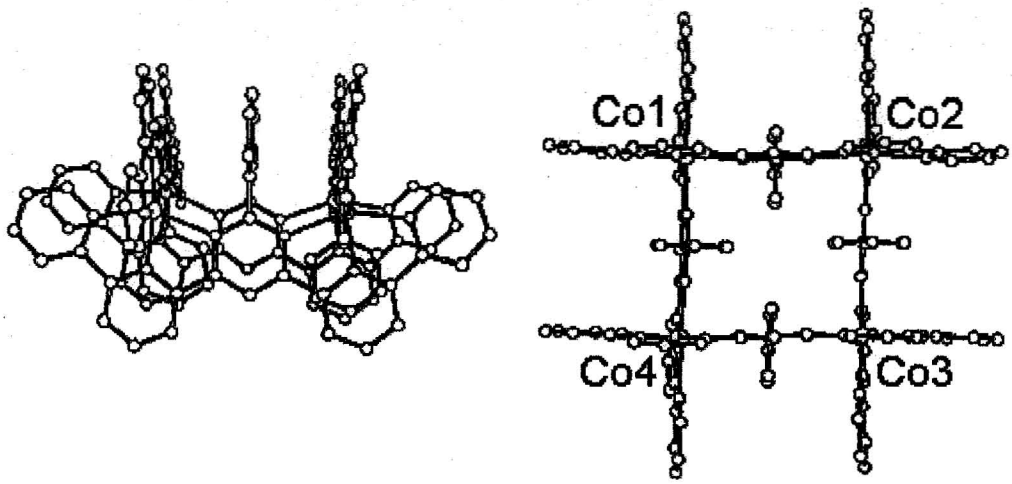

Figure 1.3: [2 x 2] Co(II) with 4,6-bis(2'',2'-bipyrid-6'-yl)-2-phenylpyrimidine.

The terpyridine-like ligands can be extended relatively easily to tritopic compounds (Figure 1.4a) [20-21]. While the ligand properties are much the same as those of the related ditopic ligands, [3x3] grids have only been reported for non-magnetically active metals, such as Pb(II) and Zn(II) with these ligands [20]. A [3x3] $Ag(I)_9$ grid with a distorted diamond-shaped core has been reported for a different type of aromatic-based ligand, 6,6'-bis[2-(6-methylpyridyl)]-3,3'-bipyridazine (Figure 1.4b). The design principles behind the bipyridazine-like ligand were the same as those used for the terpyridine-like ligands; the (bidentate) ligand coordination pockets fulfill half of the coordination pockets of the (tetrahedral) metal cation, requiring a second ligand to be oriented perpendicular to the first to completely fill the metal coordination requirements. In this case, the match between the Ag(I) cations and the ligands was not as efficient. The cations were forced to adopt a very distorted tetrahedral environment, and the overall

geometry of the complex was distorted. The product of the self-assembly process is obviously thermodynamically stable enough to offset the energetically unfavourable effects of the distortion in both the Ag(I) coordination environments and the ligand backbone.

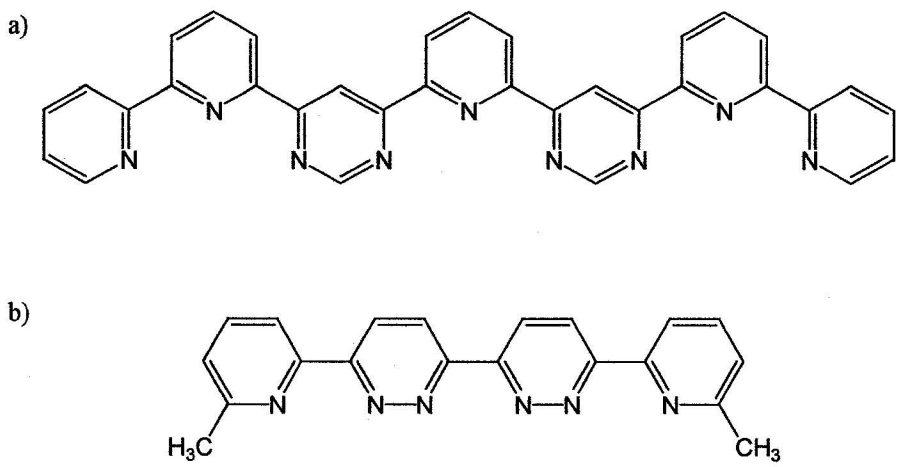

Figure 1.4: a) tritopic terpyridine-like ligand. b) tritopic bipyridazine-like ligand.

The tritopic terpyridine-like ligands can also be used to prepare [2x3] ladder compounds. The products resemble an incomplete [3x3] grid in which the central row of coordination sites is vacant. The formation of the incomplete grids has been attributed to the rotation of the arms of the ligand around the single bonds to the central pyrimidine ring. This arrangement is more energetically favourable than the linear conformation in the unbound ligand. This problem will be discussed in relation to amidrazone-based ligands in Chapters 4, 5, and 7.

The terpyridine-based ligand systems can also be extended to produce tetratopic ligands (Figure 1.5). A [4x4] $Pb(II)_{16}$ grid has been produced using this system, however no structures have been obtained, and the product was characterized mainly by ^{207}Pb NMR [21].

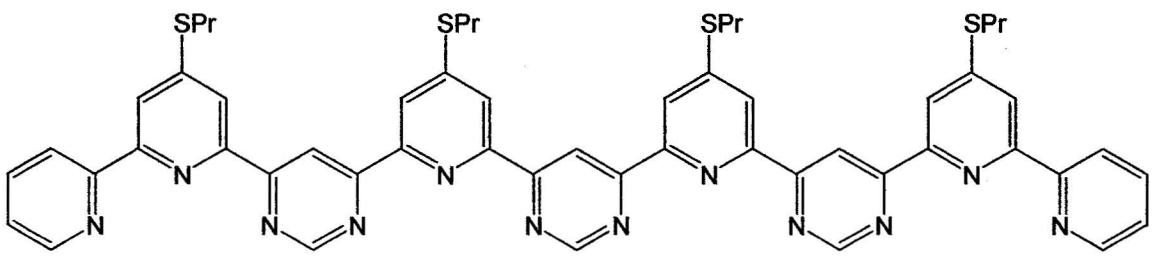

Figure 1.5: Tetratopic terpyridine-like ligand used to produce [4x4] Pb(II) grid.

Grid complexes have also been synthesized by Thompson and coworkers. Ligands based on the ditopic ligand POAP (Figure 1.6) have been used to synthesize [2x2] [22-26], [3x3] [26-29], [4x4] [30] and even [5x5] [31] grid complexes with a variety of transition metal cations. The POAP based ligands differ from the terpyridine-like ligands in that instead of the entirely aromatic backbone, a hydrazone groups is used to link terminal pyridine rings. The synthetic procedures are based on simple organic reactions, and the ligand synthesis is much less challenging than that of the terpyridine-like ligands. The design principles are similar to those used in the terpyridine ligands. The donors are arranged to form stable five-membered chelate rings when coordinated to the metal cation. The metal cations are bridged by a hydrazone oxygen atom in order to

allow spin communication between the paramagnetic centers. The hydrazone groups used to link the terminal pyridine rings are unsaturated resulting in the whole ligand being rigid and largely planar.

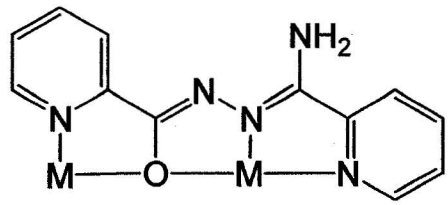

Figure 1.6: The ditopic amidrazone-based ligand POAP.

POAP and its ditopic derivatives have two coordination pockets, one of which is tridentate and contains a pyridine nitrogen donor, a diazine nitrogen donor and a hydrazone oxygen donor. The other pocket is bidentate, with a pyridine nitrogen donor and a hydrazone oxygen donor. Because the bidentate pockets do not completely fulfill half the coordination requirements of an octahedral metal cation, there is some coordinative unsaturation in POAP-based [2x2] grids. The vacant coordination sites are filled by anions or solvent molecules. [2x2] grids with POAP and derivatives have been prepared for a variety of transition metal cations, including Mn(II), Cu(II), Ni(II), Co(II) and Zn(II). All of these compounds are magnetically active, with the exception of the d^{10} Zn(II) compounds. The [2x2] $Cu(II)_4$ grids are ferromagnetic, due to orbitally orthogonal bridges between cations, and all other examples are antiferromagnetic. An example of a [2x2] grid with Cu(II) and POAP is shown in Figure 1.7 [23].

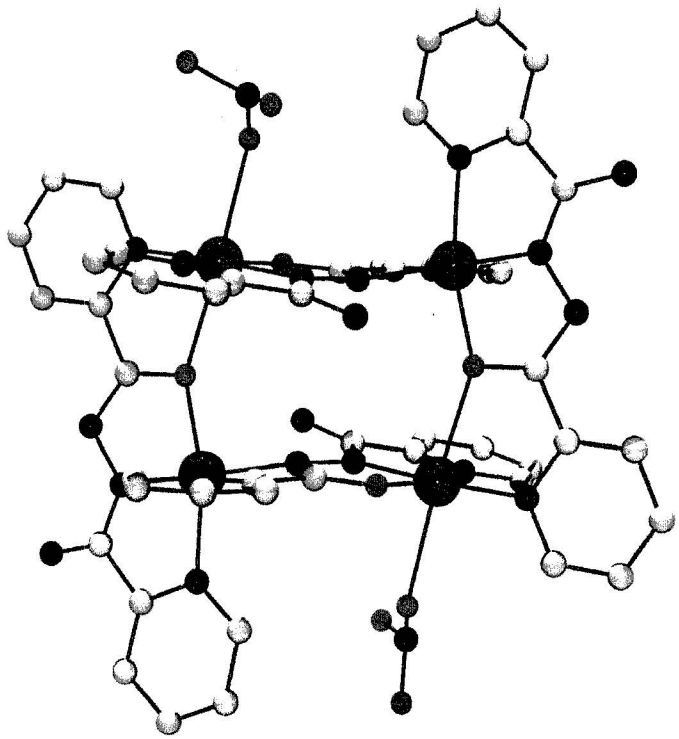

Figure 1.7: [2x2] grid compound $[(POAP\text{-}H)_4Cu_4(NO_3)_2](NO_3)_2(H_2O)_4$. Cu = magenta, N = blue, O = red, C = grey. Nitrate O atoms are disordered over two sites.

The extension of POAP into tritopic ligands will be discussed in Chapter 2. [3x3] $M(II)_9$ grids of tritopic, POAP-like ligands and Mn(II), Cu(II), Ni(II) and Co(II), and their properties will be discussed in detail in Chapters 3, 5, 6.

The focus of the upcoming chapters is on the coordination chemistry leading to the supramolecular structures discussed and their properties. However, the non-covalent interactions between molecules play an important role not only in the extended structures of the compounds in the crystalline state, but to an extent in the formation of the molecules themselves (Chapters 3, 7), and in their physical properties (Chapter 4). It is,

therefore, important to consider the types of intermolecular interactions present in the crystal structures. An understanding of the intermolecular forces present in the crystalline state can also lead to a better understanding of interactions between a molecule and a surface (*vide infra*) [32].

1.2: Supramolecular chemistry and technology:

The resurgence in interest in supramolecular chemistry has been driven by the impetus to develop new technologies. In 1965, Gordon Moore, one of the founders of Intel, predicted that the complexity of integrated circuits, or chips, would increase by a factor of two every year. He later revised his law, as it came to be known, to say that the complexity of chips would double every two years [33]. Moore's Law was proved correct over time, and the high tech industry is the only industry to ever record exponential growth. Lately it has become common knowledge that this growth is threatened by the economic factors such as the increasing costs of manufacturing the more complex chips, but also by fundamental physical limitations, such as thermal erasure of data in the increasingly smaller components, and short-circuiting of chips due to quantum mechanical tunnelling through logic gates. Data storage technologies face similar problems [34].

Many of the fundamental limitations in data storage and integrated circuits exist because the present technologies rely on the bulk properties of matter. Present magnetic storage technology, for example, uses small metal oxide particles as bits, the ones and zeros that make up binary code. As the size of these bits decreases, the energy required to flip the magnetic dipole of the particle approaches the thermal energy at room

temperature. The magnetic dipoles will then flip randomly, resulting in loss of data [34]. If a single molecule could be used as a bit, this problem could be eliminated, as the magnetic dipole of a single molecule is an intrinsic property.

Supramolecular systems have several advantages as potential new technological platforms. The molecules are large, generally with dimensions in the nanometer range, and are relatively easy to detect and address. Supramolecular systems form by self-assembly processes, which are highly efficient, and possess the ability for self-reparation through reversible processes. Supramolecular systems would order themselves on surfaces for instance, in a predictable, reproducible fashion due to the intermolecular forces between molecules and between molecules and the surface. The variety of supramolecular systems and their flexibility allows tuning of the physical properties.

The number of scientific publications concerning the application of molecular and supramolecular systems to technological problems has grown nearly as fast as the industry itself. Approaches vary as widely as the construction of individual electrical components from carbon nanotubes [35-36] to the use of organic molecules as bistable switches in a crossbar architecture [37-38].

Quantum dot cellular automata (QCA) are interesting because they are potentially useful either in conventional or quantum computing. They can be envisaged as structured charge containers, where the individual QCA would consist of a cell (or molecule) which contained differently charged redox centers. The redox centers should be able to communicate within the cell, but the charge should not be delocalized. The cell would have two degenerate ground states (one and zero), which could be interconverted by an

internal change in distribution of electron density (essentially the movement of at least two electrons). Electrostatic interactions between neighbouring cells make it favourable for them to have the same configuration, thus the degeneracy within the cell is lifted. Switching the charge distribution in one of the cells would cause the neighbouring cells to switch distributions as well, enabling the construction of logic gates [39]. Mixed oxidation state $[Mn(II)_5Mn(III)_4]$ grids, similar to compounds discussed in Chapters 3 and 6 are excellent candidates for QCA systems. The possibility of using grid type molecules as QCA has been reviewed by Lehn [40].

Supramolecular systems are also suitable for quantum computing applications. In quantum computing, the bits (qubits) are quantum mechanical two state systems. The main challenge remaining in the development of quantum computers is to achieve control of the switching process while maintaining long decoherence times. Electron or nuclear spins (or molecules which simulate them) are promising in this regard, because they are natural two state systems, with long decoherence times with respect to the spin degree of freedom. One or two qubit gates can be envisioned, where a one qubit gate would rely on either magnetic fields or on electronically tuning a single spin into resonance with an oscillating field [41]. A two-qubit gate would consist of two spins which have an exchange interaction that could be controlled electrically. A redox gate between two magnetically active particles is a good example. Antiferromagnetically coupled clusters with an $S = ½$ ground state are considered suitable for this purpose [42]. In this regard, the heterometallic wheel compounds prepared by Winpenny and coworkers are good

candidates [14], as are the $[Mn(II)_5Mn(III)_4]$ grid compounds similar to those discussed in Chapters 3 and 6 [43].

1.3: Magnetism in molecules:

1.3.1: Introduction to magnetism:

All matter contains electrons, therefore, all matter possesses magnetic properties. Practically, this means that matter will react in some way when a magnetic field is applied to it [44-45]. When an object is placed in a homogeneous magnetic field, H, the magnetic field within the object is different from that outside the object, and the object is said to be magnetized. The magnetic field inside the object is called the magnetic induction and is represented by the symbol B. The strength of the magnetic induction is related to the strength of the external field by the expression:

$$B = H + \Delta H \qquad [1]$$

ΔH represents the difference between the external magnetic field and the internal field of the object. ΔH is proportional to the intensity of the magnetization of an object (magnetic moment per unit volume), I, and the magnetic induction can be expressed by:

$$B = H + 4\pi I \qquad [2]$$

The magnetic susceptibility per unit volume, κ, is more commonly used than the intensity of magnetization. The two properties are related by:

$$\kappa = I/H \qquad [3]$$

Dividing [2] by H allows the magnetic induction to be related to the volume susceptibility:

$$B/H = 1 + 4\pi\kappa \qquad [4]$$

The quantity B/H is called the magnetic permeability and is given the symbol P. Any experimental determination of magnetic susceptibility depends on the accurate measurement of P. In practice, it is more convenient to work in units of mass rather than of volume. The volume susceptibility can be converted to mass susceptibility by:

$$\chi_g = \kappa/\rho \qquad [5]$$

ρ is the density, and χ_g is the susceptibily per gram of material. It can be converted to the molar susceptibility, χ_m, by:

$$\chi_m = \chi_g M \qquad [6]$$

where M represents the molecular weight of the material.

Magnetic properties can be divided into two general types, diamagnetism and paramagnetism, depending on whether a substance possesses unpaired electrons. If there are no unpaired electrons in a substance, the magnetic permeability, P, is less than one, and κ and χ are negative. The density of lines of magnetic force within the substance is less than the density of lines of force outside of the substance, and the substance is weakly repelled from the external magnetic field. The substance is said to be diamagnetic. Diamagnetic susceptibility values are small, generally ranging from -1 to -100×10^{-6} e.m.u. and are independent of field strength and temperature. It is important to recognize that because diamagnetism is a property associated with paired electrons, the magnetic properties of all matter have a diamagnetic component. When the magnetic properties of a paramagnetic substance are measured, it is therefore necessary to make a correction for the diamagnetic component. The diamagnetic susceptibilities of a substance are essentially additive, so the diamagnetic contribution to the overall magnetic

susceptibility can be estimated by summation of the individual susceptibilities of the atoms of a substance (the diamagnetic correction). The susceptibilities per gram atom of many atoms, complex cations and anions, and common ligand molecules have been tabulated, and are collectively know as Pascal's constants. The diamagnetic correction for a substance is added to its susceptibility to account for its diamagnetic properties.

If there are unpaired electrons in a substance, the magnetic permeability, P, is greater than one, and κ and χ are positive. The density of lines of magnetic force within the substance is greater than the density of lines of force outside of the substance, and the substance is attracted to the external magnetic field. The substance is said to be paramagnetic. The magnitude of paramagnetic effects is much greater than that of diamagnetic effects; typical values range from 100 to 100, 000 x 10^{-6} e.m.u. Paramagnetism is independent of field strength, but dependent on temperature. Paramagnetic effects result from the interaction of the orbital and the spin angular momenta of unpaired electrons with the external magnetic field. A useful quantity for the discussion of paramagnetism is μ_{eff}, the effective magnetic moment. It can be calculated from the molar susceptibility after it has been corrected for the diamagnetic component (χ'_m):

$$\mu_{eff} = \left(\frac{3k}{N\beta^2}\right)^{\frac{1}{2}} (\chi'_{mol} T)^{\frac{1}{2}} = 2.828(\chi'_{mol} T)^{\frac{1}{2}} \qquad [7]$$

In the above expression, k is the Boltzmann constant, N is Avogadro's number, T is the temperature in Kelvin, and β is the Bohr magneton, which is defined by:

$$\beta = \frac{eh}{4\pi mc} = 0.927x10^{-20} erg \cdot gauss^{-1} \qquad [8]$$

where e is the electronic charge, h is Planck's constant, m is the electron mass, and c is the speed of light.

Paramagnetic effects are dependent on temperature, and in many cases the relationship:

$$\chi'_m = C/T \qquad [9]$$

is followed, where C is the Curie constant. The relationship is known as the Curie law. The relationship was later modified to include the temperature correction term, θ, which is generally used to account for interactions between paramagnetic centers. The modified relationship is called the Curie-Weiss law:

$$\chi'_m = C/(T - \theta) \qquad [10]$$

To continue the discussion about paramagnetism, it is necessary to draw the distinction between magnetically dilute and magnetically concentrated substances. In the above discussion it was assumed that the paramagnetic centers in the substance do not interact with each other. This is generally true in cases where a metal ion is coordinated by large ligands, for example, or is heavily solvated. When the paramagnetic centers are directly bonded, as in a metal or alloy, or when metal cations are bridged by suitable anions or ligands, for instance, spin-spin interactions are possible, and the substance is said to be magnetically concentrated [44-46]. Interactions between paramagnetic centers lead to two further divisions in magnetic properties; ferromagnetism and antiferromagnetism.

In a ferromagnetic substance, the spin magnetic dipoles of neighbouring paramagnetic centers tend to align parallel to each other creating magnetic domains and therefore increasing the observed magnetic susceptibility for the substance. Ferromagnetic effects are dependent on both the strength of the applied field and the temperature. At low temperature the spins align parallel to each other as described, resulting in higher than expected susceptibility values. As the temperature is increased, the spins become randomized, and at a given temperature, the Curie temperature, the substance will begin to behave as a simple paramagnet, and will obey the Curie-Weiss law. For ferromagnetic substances, the Weiss θ correction in the Curie-Weiss law is generally positive.

In an antiferromagnetic substance, unpaired electrons on neighbouring paramagnetic centers tend to align antiparallel to each other, effectively acting like paired electrons, and decreasing the observed susceptibility of the compound. Antiferromagnetic effects are field independent, but temperature dependent. At low temperatures, the spin magnetic dipoles are aligned antiparallel to each other, and the magnetic susceptibility is lower than expected, but as the temperature is increased, thermal randomization occurs. At the Neél temperature, the substance will begin to behave as a simple paramagnet, and follow the Curie-Weiss law. The Weiss constant, θ, is generally negative for antiferromagnetic substances.

Two other types of magnetic behaviour are known to occur. In ferrimagnetic compounds, antiparallel alignment of spins occurs between ions with different numbers of unpaired electrons. As a result there is incomplete cancellation of spins, and a net

magnetic moment remains. In metamagnetism, the substance shows both ferromagnetic and antiferromagnetic ordering. Metamagnetic behaviour can be detected in nominally antiferromagnetic compounds by varying the applied field, resulting in an apparent change in intensity in the coupling. These last two types of magnetic behaviour are beyond the scope of this work and will not be discussed in detail.

1.3.2: Magnetism in polynuclear complexes:

Paramagnetism is caused by changes in energy levels in the atom or ion as it interacts with a magnetic field. It is therefore necessary to be able to define all of the spin states and corresponding energy levels and relate them to the susceptibility of the compound in order to understand the magnetic behaviour. Calculation of the spin states can be accomplished in several ways and will be discussed later. The energies are calculated using a Heisenberg spin Hamiltonian, which includes interactions among the paramagnetic centers, ligand field effects, and Zeeman splitting terms:

$$H = -\sum_{i<j} J_{ij} \cdot S_i \cdot S_j + \sum_i S_i \cdot D_i \cdot S_i + \mu_B \sum_i S_i \cdot g_i \cdot B \qquad [11]$$

The above Hamiltonian is generally simplified by ignoring the ligand field effects ($\Sigma_i S_i \cdot D_i \cdot S_i$) and assuming that the g factors (g represents the Landé splitting factor) are identical and isotropic. This leaves only the exchange integral, J, to be evaluated. The total spin quantum number combinations, S', and their energies, E(S'), generated using the exchange Hamiltonian can be substituted into the Van Vleck equation to calculate the susceptibility for the system. The generalized form of the Van Vleck equation is:

$$\chi_M = \frac{N\beta^2 g^2}{3kT} \frac{\sum S'(S'+1)(2S'+1)e^{-E(S')/kT}}{\sum (2S'+1)e^{-E(S')/kT}} \qquad [12]$$

The Van Vleck equation is generally modified to include the fraction of paramagnetic impurity (α), the temperature independent paramagnetism (TIP) and a Weiss-like temperature correction, θ, which represents intermolecular exchange effects:

$$\chi_M = \frac{N\beta^2 g^2}{3k(T-\theta)} \frac{\sum S'(S'+1)(2S'+1)e^{-E(S')/kT}}{\sum (2S'+1)e^{-E(S')/kT}} (1-\alpha) + \frac{N\beta^2 g^2 S(S+1)\alpha}{3kT} + TIP$$

[13]

Calculation of the spins states for a group of interacting paramagnetic centers is not a trivial task. There are three commonly used methods. The first is a vector coupling based approach developed by Kambe [47]. It is perhaps the easiest to understand and use, but is most useful for systems with few paramagnetic centers and a degree of symmetry. Examples of the use of a vector coupling scheme to calculate spin states and corresponding energies are located in Appendix 1.

The second method is full matrix diagonalization (FMD) [48]. This method is very powerful, as it allows quick calculation of the spin states and their energies for a large variety of systems. It is the method which is used in the software package MAGMUN4.1 [49] which will be discussed in the next section. The chief disadvantage of this method is that the Hamiltonian matrix dimensions increase dramatically with the number of paramagnetic centers, so exact diagonalization exceeds the capabilities of PCs for systems with a large number of unpaired electrons.

The use of irreducible tensor operators (ITO) is also used to generate the spin states for systems of paramagnetic centers. This method reduces the size of the matrices required to solve the exchange problem, and therefore reduces the computing time required, however the mathematics required to set up this method is more complex. This method was not used to model the magnetism in any of the systems discussed in later chapters, so a more detailed discussion is beyond the scope of this work.

1.3.3: MAGMUN4.1 and fitting magnetic data for polynuclear systems:

MAGMUN4.1 is a Windows© based software package that has been developed to model the magnetic properties for polynuclear structures with a large variety of topologies [50]. In order to use the program one must first define a model for the compound. First, one would draw a model of the system, with the paramagnetic centers numbered. For the purposes of this discussion, we will assume a trinuclear Cu(II) system resembling an equilateral triangle (Figure 1.8). It is important to note that systems of any geometry can be modelled, including three dimensional systems. An input file, OW01.ini (Figure 1.9), is set up, in which the spin quantum numbers for the paramagnetic centers are entered in line one (e.g. 1 1 1 for the trinuclear d^9 system). It is not necessary for all of the centers to have the same spin.

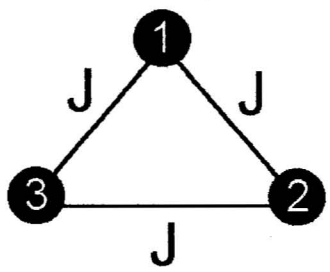

Figure 1.8: Magnetic model for a $Cu(II)_3$ triangle.

In line two, one would define the coupling between paramagnetic centers (e.g. 12, 23, 31, for the equilateral triangle). In line three, the relative strengths of the coupling (J, the exchange energies) are entered. For a system where all the J values are equal, for instance for the equilateral triangle, -1 cm^{-1} is a convenient value. The exchange energy, J, to be determined by a non linear regression of the data, will then be a multiple of unity, and will be positive for ferromagnetic systems and negative for antiferromagnetic systems, as one would expect. While -1 cm^{-1} is convenient for one J systems, any number will work, but the J calculated by the non-linear regression must be multiplied by the coupling strength defined in OW01.ini to determine the actual J value for the system. Finally, the name of the output file is defined in line four of OW01.ini, and the file is saved. Figure 1.9 shows an example OW01.ini input file, for the trinuclear Cu(II) triangle.

```
Spins: 1 1 1
Couplings: 12 23 31
Strengths: -1 -1 -1
Output: Cu(II)3triangle
```

Figure 1.9: MAGMUN4.1 input file for $Cu(II)_3$ triangle model.

The non-linear regression routine in MAGMUN4.1 does not allow the direct fitting of two different J values. For systems with different J values, the system can be modelled by choosing appropriate ratios of values for the coupling strengths in the OW01.ini file. For instance, if a system had both an antiferromagnetic and a

ferromagnetic component, one could model it by setting the coupling strengths at -1 for the antiferromagnetic exchange (J1) and 0.1 for the ferromagnetic exchange (J2). The non linear regression would then return one fitted J, which would be multiplied by each of the coupling strengths to yield the two different J values for the system. It is important to note that as one J is being defined as a fraction of the other (in the above example, J1 = 10 x J2) the fit is not rigorous. However the ability to set the different J values confers a great deal of flexibility on the system types which can be modelled using MAGMUN4.1.

After the exchange model has been defined in OW01.ini, the program OW01.exe is used to calculate the spin states and energies for the system. This process eliminates the need for the user to derive an exchange equation for the system. OW01.exe generates two output files, a *.eig and a *.spk. The *.spk file is used in conjunction with MAGMUN4.1 to model the magnetic data. An example of the *.spk file for the trinuclear Cu(II) system from the earlier discussion is included as Figure 1.10, and some examples of input files and *.spk files for systems discussed in subsequent chapters of this work are included in Appendix 2. The *.spk file containing the spin state and energy data is loaded into MAGMUN4.1, and data can be fitted to the modified van Vleck equation described, using menu based commands. Fitted data can be saved directly as a text file, or exported into a Microsoft Excel© spreadsheet.

MDA 01.00 SPK 00
#PROGRAM:
Program OW0L, (c) Oliver Waldmann, Version 11.5.01
#HAMILTONIAN:
Heisenberg Hamiltonian
#SYSTEM:
Spins = 1/2 1/2 1/2
Couplings = 1-2 2-3 3-1
#PARAMETER:
Strengths = -1 -1 -1
Emin = -0.75
#COMMENT:
sorted spektrum with classification
#DATA:

0	1	1
0	1	0
1.5	3	0

Figure 1.10: *.spk file for $Cu(II)_3$ triangle. Column one defines the relative energy and column two defines 2S' + 1.

MAGMUN4.1 is also capable of modelling magnetization vs. field data data using standard Brillouin functions. Magnetization data are useful in the understanding of the magnetic ground state of a system. The dependence of the molar magnetization on an external field is described using the Brillouin function Bs(y) [51]:

$$M_s = Ng\beta SBs(y) \qquad [14]$$

where

$$Bs(y) = \frac{2S+1}{2S}\coth\left(\frac{2S+1}{2S}y\right) - \frac{1}{2S}\coth\left(\frac{1}{2S}y\right) \qquad [15]$$

and

$$y = \frac{gS\beta H}{kT} \qquad [16]$$

At low temperatures and large magnetic field strengths, the magnetic energy of the system, gSβH, approaches the thermal energy, kT, and the magnetization approaches its maximum value, the saturation magnetization, M_s. Because BH/kT > 1 and the Brillouin function approaches 1, the saturation magnetization is described by:

$$M_s = Ng\beta S \qquad [17]$$

Graphical representations of the magnetization generally use Nβ units, so the magnetization is described by gS for a given temperature. MAGMUN4.1 uses the magnetization, in Nβ units, and the field data to generate a profile based on g, S, and T values entered by the user. Magnetization vs. field profiles for several spin states, generated for g = 2 and T = 2 K are shown in Figure 1.11.

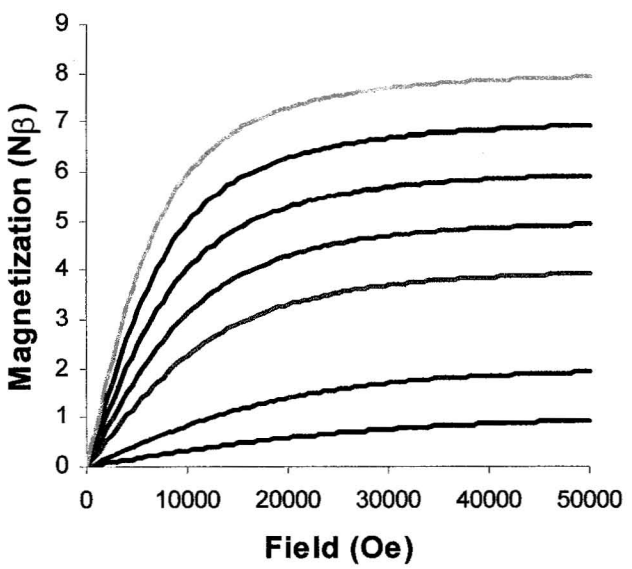

Figure 1.11: Magnetization vs. field plots for S = ½ (black), S = 1 (pink), S = 3/2 (yellow), S = 2 (red), S = 5/2 (purple), S = 6/2 (green) and S = 7/2 (blue) S = 4 (orange) generated with MAGMUN4.1.

Chapter 2: Physical measurements and ligand synthesis

2.1: General comments on ligand synthesis:

A ligand must possess several important characteristics in order to be useful in the predictable, reproducible preparation of grid-type compounds by self-assembly methods. In Chapter 1, the terpyridine-like ligands developed by Lehn and coworkers [17, 20-21, 52-53] were discussed as a starting material for the formation of grid and ladder compounds (Figure 2.1). With an entirely aromatic background, these ligands are rigid and planar, so twisting or bending of the ligand does not generally occur, and unexpected products are rare. Each of the contiguous terpyridine units forms a pocket which provides three nitrogen donors, oriented such that they satisfy half of the coordination requirements of a *mer*-octahedral metal cation. This arrangement has two important consequences; the first is that the ligand is chelating, and thus binds more strongly to the metal cation than would a monodentate ligand, and the second is that fulfilling half of the coordination requirements encourages coordination of the metal cation by another ligand. The *mer*- arrangement of the donors ensures that the second ligand must be oriented perpendicular to the first in order to coordinate the metal. The combination of these factors leads to a very successful family of grid producing ligands.

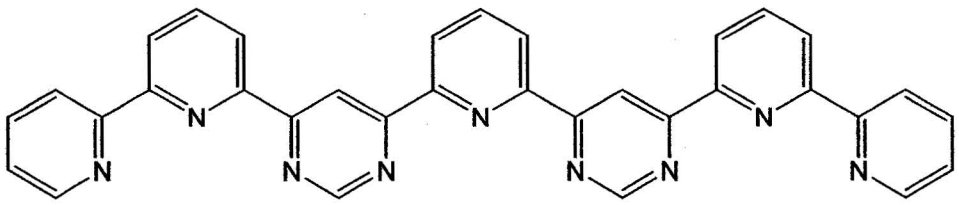

Figure 2.1: A tritopic terpyridine-like ligand.

The amidrazone based ligands 2POAP and derivatives (Figure 2.2) represent an alternative type of system for grid self-assembly [27, 32, 55-55]. Rigidity and planarity in the ligand backbone are achieved by connecting substituted pyridine rings with hydrazone linkages. This leads to a series of contiguous coordination pockets with different coordination environments. The center pocket contains one nitrogen donor from the central pyridine ring, and two hydrazone oxygen donors, while the side pockets contain one pyridine nitrogen donor, one diazine nitrogen donor, and one hydrazone oxygen donor. The donor atoms are again arranged to satisfy half of the coordination requirements of a *mer*-octahedral metal cation.

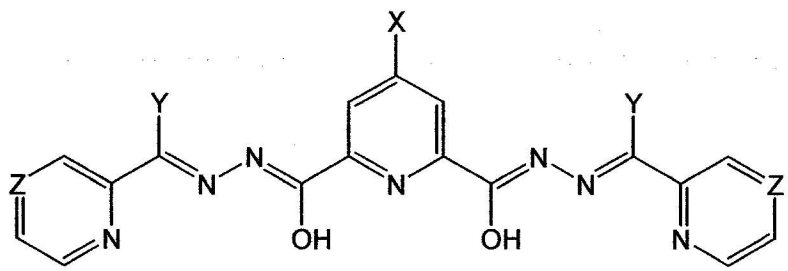

2POAP: X = H, Y = NH_2, Z = CH
Examples of other functional groups:
X = Cl, $S^-NH_4^+$, SMe, SEt, SCH_2COOH, 2-pyrimidine, OH, OMe
Y = CH_3, phenyl, pyridyl
Z = N

Figure 2.2: 2POAP and some derivatives.

The 2POAP-like ligands are conformationally flexible. When the ligand is doubly deprotonated, the ligand tends to adopt a flat linear conformation. This results in

three contiguous coordination pockets which can bind metal cations with hydrazone oxygen atom bridges (Figure 2.3a). [3x3] grid molecules and $Cu(II)_8$ pinwheels form with ligands in the linear conformation (Chapters 3 and 4). The ligands do, however, contain single bonds and rotation around these bonds can lead to other conformations. In some cases half of the ligand rotates around the single bond between the central pyridine ring and the hydrazone linker resulting in a bent conformation (Figure 2.3b). In this binding mode, grid formation is impossible, but $Cu(II)_8$ pinwheel molecules (Chapter 4) and grid fragments (Chapter 5) have been found to form. In one case, both halves of the ligand were observed to revolve around the bond between the central pyridine and the hydrazone linker. This resulted in a v-shaped ligand (Figure 2.3c) which formed a mononuclear, square planar Ni(II) compound (Chapter 7). The ligand conformation appears to be affected both by the metal cation, and by the charge on the ligand.

The use of the hydrazone functional groups as linkers has important consequences on the properties of the complex. The metal cations in adjacent pockets of a grid molecule will be bridged by short hydrazone oxygen linkages in the case of linear ligand coordination, or by a diazine group in cases where an arm of the ligand has rotated around a single bond. In the terpyridine-like ligands, bridging occurs through the π-system of the bridging pyrimidine ring. The shorter oxygen and diazine bridges ensure better overlap of the magnetic orbitals, and thus more efficient spin communication, leading to enhanced magnetic properties compared with the bridging via the pyrimidine π-system. The enhanced metal-metal communication may also affect electrochemical properties. The coordination environments provided by the side and center pockets in

2POAP-like ligands are different, and the preparation of mixed metal or mixed valent compounds is possible, based on the coordination preference of the metal cations for a harder or softer environment [62]. The 2POAP-like ligands are also relatively simple to prepare, and a large variety of compounds can be synthesized, since the hydrazone functional groups will react readily with imino-esters, aldehydes and ketones.

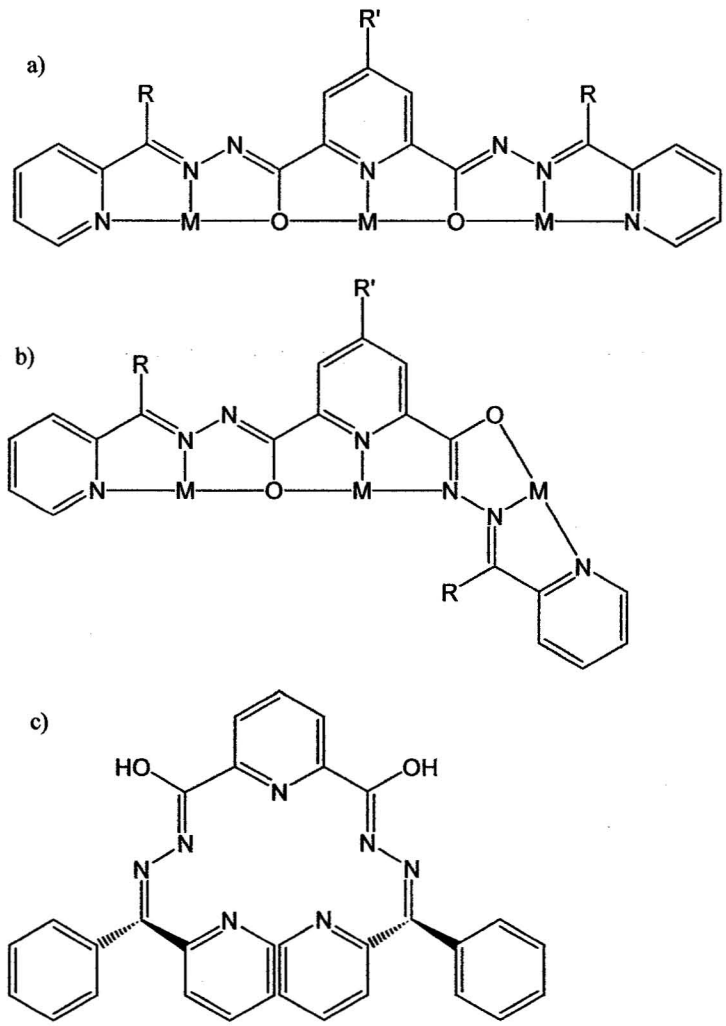

Figure 2.3: Some conformations of 2POAP-type derivatives.

The magnetic, electrochemical and spectroscopic properties of the [3x3] $Mn(II)_9$ grid compounds of 2POAP-like ligands make them attractive candidates for molecule based devices, such as bistable switches or qubits for quantum computing applications. In order for device development to be feasible, it is necessary to be able to immobilize the molecule on a surface. In the case of 2POAP-type grids, the most straight-forward way to do this is by functionalization of the ligand at the 4-position of the central pyridine ring (see Figure 2.2, X position) with groups suitable for surface adhesion. This leads to the incorporation of six such functional groups in each [3x3] grid molecule, three on each face of the grid, which project outward to make surface contact. Soft, electron rich atoms like chlorine and sulphur would serve to attach a grid molecule to a gold or graphite surface, while harder donor atoms, such as oxygen, could attach molecules to a TiO_2 surface.

The preparation of Cl and S-functionalized diester and dihydrazone precursors will be discussed, as well as the preparation of several new functionalized 2POAP-type ligands.

2.2: Methodology:

2.2.1: Synthesis of chlorinated precursors:

The functionalization of the 2POAP-like ligands is not trivial as it involves the construction of the central pyridine ring in order to assure substitution at only the para-position of the ring. This is accomplished via a multi-step synthesis, starting with the synthesis of acetone dioxalic ester. The ester can be condensed by reaction with HCl in water to yield chelidonic acid [56], which is in turn transformed to chelidamic acid by

reaction with NH_4OH [57]. Chlorination and aromatization are achieved by reaction of chelidamic acid with PCl_5 [58, 59]. The resulting acid chloride is hydrolysed and then esterified, to produce diethyl-4-chloro-2,6-pyridinedicarboxylate, which serves as a precursor for all of the functionalized 2POAP-like ligands. The synthesis of the chlorinated ligand precursors is summarized in Scheme 2.1. The precursors are known compounds, however the syntheses have been modified for optimization of yield, and thus full synthetic procedures are included. All procedures have been repeated several times, and average yields are reported.

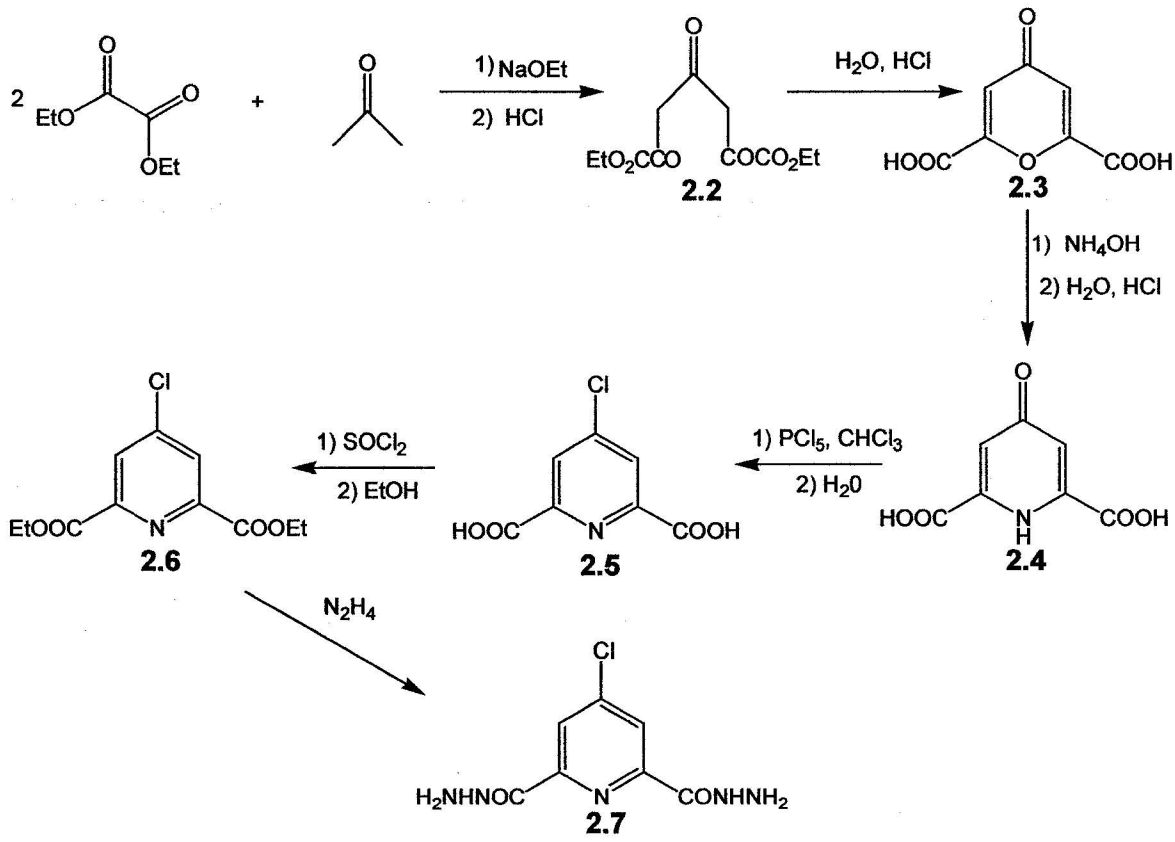

Scheme 2.1: Synthesis of chlorinated ligand precursors.

2.2.2: Synthesis of thioether precursors:

The thioether diesters can be synthesized from diethyl-4-chloro-2,6 pyridinedicarboxylate by reaction with the appropriate xanthogenate [60]. Potassium ethyl xanthogenate is commercially available, while potassium methyl xanthogenate was synthesized [61]. The thioether dihydrazones are synthesized from the thioether diesters in the same manner as **2.7**. Synthesis of the thioether precursors is shown in Scheme 2.2.

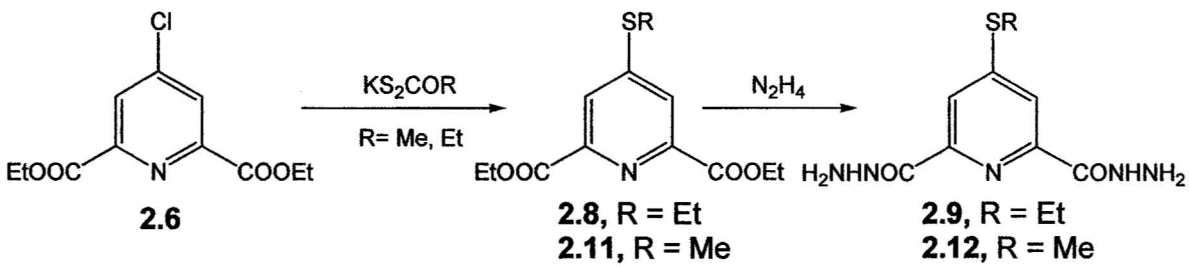

2.6

2.8, R = Et
2.11, R = Me

2.9, R = Et
2.12, R = Me

Scheme 2.2: Synthesis of thioether precursors.

2.2.3: Synthesis of ligands from functionalized precursors:

A variety of ligands can be prepared from the functionalized precursors. The syntheses of those discussed in this work are summarized in Scheme 2.3.

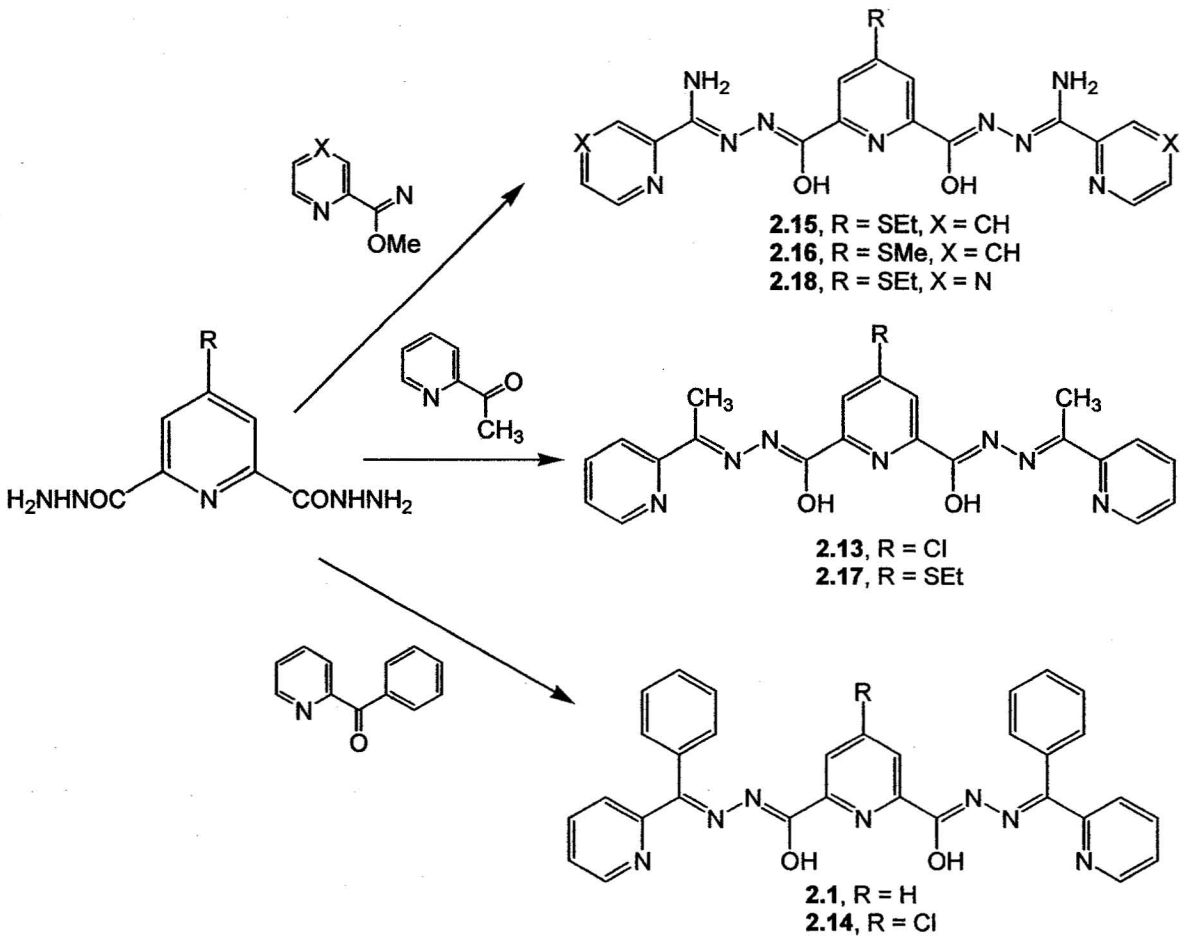

Scheme 2.3: Synthesis of 2POAP-like ligands.

2.3: Experimental:

2.3.1: Materials:

Commercially available solvents and chemicals were used without further purification.

Perchlorate salts and complexes are potentially explosive and were only prepared in small quantities, taking appropriate precautions.

2.3.2: Physical measurements:

2.3.2.1: Spectroscopy:

Infrared spectra were recorded as Nujol mulls between NaCl plates using a Matteson Polaris FT-IR instrument. NMR spectra were obtained with a Bruker AVANCE 500 MHz spectrometer. Solvents used are quoted in the appropriate experimental section. UV-vis-nir measurements were obtained using a Cary 5E dual beam spectrometer either as Nujol mulls on filter paper pressed between glass slides, or in solution in matched quartz cells. In the latter case, the solvent used is quoted in the appropriate experimental section.

2.3.2.2: Mass Spectrometry:

LCMS measurements were taken on an Agilent 1100 Series LC/MSD in APCI mode. See the relevant experimental section for solvent details.

2.3.2.3: Elemental Analyses:

Microanalyses were carried out by Canadian Microanalytical service, Delta, B.C., Canada.

2.3.2.4: Magnetic measurements:

Variable Temperature magnetic data were collected with a Quantum Design MPMS5S SQUID magnetometer using field strengths in the range 0.1-5 T. Background corrections for the sample holder assembly and diamagnetic components of the complexes were applied.

2.3.2.5: Electrochemical measurements:

Electrochemical data were obtained with a BAS Epsilon system in CV and DPV modes with an Ag/AgCl sat. reference electrode (0.199 V vs. NHE at 25 ◦C). The working electrode was platinum, unless otherwise stated in the text. The auxiliary electrode was a platinum wire. Experiments were performed in acetonitrile, with tetraethylammonium perchlorate ($[NEt_4ClO_4] \approx 0.1$ M) as a supporting electrolyte. Solutions were purged with N_2 for several minutes prior to measurements being taken.

2.3.2.6: Crystallography:

Details of the data collection and refinement are located in the experimental section of the appropriate chapters, and Appendix 3.

2.3.3: Synthesis of ligands and precursor molecules:

2.3.3.1: Synthesis of 2POPP (**2.1**)

2-benzoylpyridine (10.01 g, 55 mmol) was dissolved in methanol (250 mL). 2,6-pyridinedicarboxylic acid hydrazone (5.0 g, 26 mmol) was added and the mixture was refluxed for 18 hours. The product, a white powder (12.32 g, 90 %) was collected by suction filtration and washed with diethyl ether. Mp: 275-278 °C. Selected IR data (Nujol mull, cm^{-1}): 3284 (ν N-H), 1695 (ν C=O), 1558 (ν C=C), 997, (ν py). LCMS ($CHCl_3$): m/z = 526 (M+H). Elemental analysis: Found (%): C; 70.76, H; 4.46, N; 18.88. Calc (%), for $C_{31}H_{23}N_7O_2$: C; 70.84, H; 4.41, N; 18.66.

2.3.3.2: Acetone dioxalic ester (**2.2**):

Sodium (46 g, 2.0 mol) was dissolved in warm absolute ethanol (600 mL). The sodium ethoxide solution was divided in half, and half was kept warm. Dry, reagent

grade acetone (58 g, 1.0 mol) and diethyl oxalate (150 g, 1.0 mol) were added to half of the sodium ethoxide solution, and the resulting brown solution was stirred until a thick precipitate formed (~2 mins). The remaining (warm) sodium ethoxide and additional diethyl oxalate (160 g, 1.1 mol) were added simultaneously to the mixture. The resulting mixture was stirred and warmed for 30 mins. (In cases where the mixture was very thin, 150 mL ethanol was distilled off, in place of the warming). The resulting mixture was added to a mixture of HCl (conc, 300 mL) and ice (800 mL). The mixture was stirred until homogeneous. The resulting cream coloured product was collected by suction filtration. Average yield 180 g, 70%. This product was used without further purification or characterization.

2.3.3.3: Chelidonic acid (**2.3**):

Acetone dioxalic ester (150 g, 0.58 mol) was added to HCl (conc, 300 mL). The resulting mixture was refluxed for 24 hours, resulting in a dark red solution and pale brown precipitate. The precipitate was collected by suction filtration, and washed with cold water. Average yield 100 g, 93 %. Selected IR data (Nujol mull, cm^{-1}): 3575, 3475 (ν O-H), 1732, 1640 (ν C=O), 1585 (ν C=C). LCMS (methanol): m/z = 185 (M+H).

2.3.3.4: Chelidamic acid (**2.4**):

Chelidonic acid (100 g, 0.54 mol) was added to NH_4OH (conc., 1.1 L) and refluxed for 24 hours, resulting in a brown solution. The solution was acidified to approximately pH 3. The resulting pale brown precipitate was collected by suction filtration. Average yield 89 g, 90 %. Selected IR data (Nujol mull, cm^{-1}): 3601, 3448

(ν O-H), 1723, 1663 (ν C=O), 1613 (ν C=C). LCMS (methanol): m/z = 184 (M +H), 391 (2M+Na).

2.3.3.5: 4-chloro-2,6-pyridine dicarboxylic acid (**2.5**):

Chelidamic acid (75 g, 0.41 mol) was slowly added to a mixture of PCl_5 (343 g, 1.65 mol) in chloroform (1.2 L). The resulting dark brown mixture was refluxed for 72 hours, resulting in a dark brown solution. The chloroform was removed by rotary evaporation, and the resulting thick dark brown mixture was slowly added to cold water (1.0 L). The mixture was stirred until it had cooled to ambient temperature, and the product, a pale brown powder, was collected by suction filtration. Average yield 80 g, 88 %. Selected IR data (Nujol mull, cm^{-1}): 3607, 3444 (ν O-H), 1730 (ν C=O), 1616, 1577 (ν C=C).

2.3.3.6: Diethyl-4-chloro-2,6-pyridinedicarboxylate (**2.6**):

2.5 (79 g, 0.39 mol) was slowly added to $SOCl_2$ (300 mL). A few drops of DMF were added to the resulting brown mixture. The mixture was refluxed for 24 hours, and the $SOCl_2$ was removed by rotary evaporation. The flask containing the mixture was submerged in an ice bath, and absolute ethanol (150 mL) was added slowly. The resulting mixture was stirred for 12 hours, and the ethanol was removed by rotary evaporation. The resulting clear, brown solution was chilled in the freezer until a fluffy white solid formed. The solid was collected by suction filtration, and washed with two 5 mL portions of very cold ethanol. Average yield 75 g, 75 %. Mp (for sample recrystallized from ethanol): 89-92 °C (lit value 92-94°C). Selected IR data (Nujol mull, cm^{-1}): 3075 (ν C-H ar), 1719 (ν C=O), 1573 (ν C=N).

2.3.3.7: 4-chloro-2,6-pyridine dicarbohydrazide (**2.7**):

2.6 (5.04 g, 0.02 mol) was dissolved in absolute ethanol (100 mL). Anhydrous N_2H_4 (2.5 g, 0.08 mol) was added slowly via a dropping funnel. The mixture was stirred at ambient temperature for 18 hours, and the product, a white powder (4.45 g, 89 %), was collected by suction filtration, and washed with absolute ethanol and diethyl ether. Selected IR data (Nujol mull, cm^{-1}): 3327, 3208 (ν N-H), 3086 (ν C-H ar), 1692 (ν C=O), 1657 (ν C=C).

2.3.3.8: Diethyl-4-ethylthio-2,6-pyridinedicarboxylate (**2.8**):

2.6 (2.01 g, 7.80 mmol) and $KS_2COCH_2CH_3$ (potassium ethyl xanthogenate, 2.51 g, 0.16 mol) were ground together and the mixture was heated in a boiling water bath until gas evolution ceased (20 mins). Water (50 mL) was added to the resulting sticky orange tar and the resulting mixture was stirred for 10 mins, and extracted with three 50 mL portions of diethyl ether. The ether portion was washed with two 20 mL portions of water and dried over anhydrous $MgSO_4$. The ether was removed by rotary evaporation, and the resulting yellow oil was chilled. White crystals (2.00g, 90 %) formed over 2 hours. Mp: 48-50 °C (lit. value 49-50°C). LCMS (methanol): m/z = 284 (M+H). ^1H NMR (MeOH-d_4): (ppm) 8.0 (s, 2H, ar), 4.4 (q, J = 7.0 Hz, 4H, OCH_2), 3.2 (q, J = 7.5 Hz, 2H, SCH_2), 1.4 (m, 9H, CH_3).

2.3.3.9: 4-ethylthio-2,6-pyridinecarbohydrazide (**2.9**):

2.8 (0.63 g, 2.2 mmol) was dissolved in methanol (50 mL). Anhydrous hydrazine (0.17 g, 5.3 mmol) was dissolved in methanol (15 mL) and slowly added to the solution of **2.8** via a dropping funnel. A white precipitate began to form after 4 hours. The

mixture was stirred at ambient temperature for 18 hours, and the product, a white powder (0.54 g, 96 %), was collected by suction filtration. Mp: 213-216 °C. LCMS (MeOH + DMF): m/z = 255 (M), 256 (M+H). ^{1}H NMR (DMSO-d_6): (ppm) 10.6 (t, J = 5.0 Hz, 2H, C=ONH), 7.9 (s, 2H, ar), 4.6 (d, J = 6.5 Hz, 4H, NH_2), 3.2 (q, J = 8.5 Hz, 2H, SCH_2), 1.3 (t, J = 7.0 Hz, 3H, CH_3).

2.3.3.10: Potassium methyl xanthogenate (**2.10**):

KOH (57.2 g, 1.02 mol) was finely ground. Methanol (300 mL) was gradually added (Note, use a minimum of solvent to dissolve the KOH). The solution was cooled to ambient temperature, and CS_2 (76.5 g, 1.00 mol) was added slowly via a dropping funnel. The resulting clear yellow solution was stirred overnight. The volume of the solution was reduced until a thick yellow mixture formed and the product, a pale yellow powder (129 g, 88 %), was collected by suction filtration and recrystallized from absolute ethanol. Mp: > 250 °C (some thermal decomposition, darkening of colour, gas evolved). Selected IR data (Nujol mull, cm^{-1}): 1697, 1650 (ν C=O), 1141 (ν C=S).

2.3.3.11: Diethyl-4-methylthio-2,6-pyridinedicarboxylate (**2.11**):

2.6 (2.01 g, 7.80 mmol) and **2.10** (4.03 g, 0.28 mol) were ground together and heated over a boiling water bath until gas evolution ceased (10 mins). Water (30 mL) was added to the resulting orange tar, and the mixture was stirred for 10 mins and extracted with three 50 mL portions of diethyl ether. The ether portion was washed with two 20 mL portions of water and dried over $MgSO_4$. The ether was removed by rotary evaporation and the resulting yellow oil was chilled. White crystals (1.8 g, 85 %) formed overnight. Selected IR data (Nujol mull, cm^{-1}): 1739, 1708 (ν C=O), 1573 (ν C=C).

2.3.3.12: 4-methylthio-2,6-pyridinedicarbohydrazide (**2.12**):

2.11 (1.53 g, 5.68 mmol) was dissolved in methanol (50 mL). Hydrazine hydrate (85 %) (0.84 g, 0.02 mol) was dissolved in methanol (10 mL) and added to the solution of **2.11** via a dropping funnel. A white solid formed after 1 hour. The product, a white powder (1.5 g, 80 %), was collected by suction filtration. Mp: 214-216 °C. Selected IR data (Nujol mull, cm^{-1}): 3378, 3344 (ν O-H), 3309, 3181 (ν N-H), 1662 (ν C=O), 1631, 1577 (ν C=C).

2.3.3.13: Cl2POMP (**2.13**):

2-acetylpyridine (5.11 g, 42.1 mmol) was dissolved in methanol (100 mL). **2.7** (4.47 g, 19.5 mmol) was added, and the mixture was refluxed for 18 hours. The product, a white powder (7.87 g, 93 %), was collected by suction filtration. Mp: > 300 °C. Selected IR data (Nujol mull, cm^{-1}): 3293 (ν O-H), 1675 (ν C=O), 1578, 1558 (ν C=C), 1524 (ν C=N), 990 (ν py). LCMS (methanol + 10 % DMF): m/z = 436 (M+H). ^{1}H NMR (DMSO-d_6): (ppm) 11.5 (s, 2H, OH), 8.6 (d, J = 4.5 Hz, 2H, ar), 8.4 (s, 2H, ar), 8.2 (d, J = 8.0 Hz, 2H, ar), 7.9 (t, J = 7.8 Hz, 2H, ar), 7.5 (m, 2H, ar), 1.2 (s, 6H, CH_3). Elemental analysis: Found (%): C; 57.53, H; 4.07, N; 22.27. Calc. (%), for $C_{21}H_{18}N_7O_2Cl(CH_3OH)_{0.15}$: C; 57.65, H; 4.25, N; 22.25.

2.3.3.14: Cl2POPP (**2.14**):

2-benzoyl pyridine (7.44 g, 40.6 mmol) was dissolved in a solution of chloroform (220 mL) and methanol (30 mL). **2.7** (2.30 g, 19.0 mmol) was added, and the mixture was refluxed for 72 hours. The volume of the resulting pale yellow solution was reduced to 30 mL and 20 mL of methanol was added. The solution was heated for 10 minutes,

and a white precipitate formed. The product, a white powder (9.05 g, 85 %) was collected by suction filtration. Mp: 288-294 °C (some thermal decomposition, colour darkens). Selected IR data (Nujol mull, cm^{-1}): 3298 (ν O-H), 1698 (ν C=O), 1574 (ν C=C), 997 (ν py). LCMS ($CHCl_3$, -APCI mode): m/z = 560 (M). Elemental analysis: Found (%): C; 65.25, H; 3.95, N; 17.33. Calc. (%), for $C_{31}H_{22}N_7O_2Cl(CH_3Cl)_{0.25}$: C; 65.55, H; 4.00, N; 17.12.

2.3.3.15: SEt2POAP (**2.15**):

Sodium methoxide was prepared in situ by addition of Na (~0.11 g, 4.8 mmol) to methanol (100 ml). 2-cyanopyridine was added and the resulting solution was stirred at ambient temperature for 8 hours. The solution was neutralized with glacial CH_3COOH, and **2.9** (1.2 g, 5.0 mmol) was added. The mixture was stirred at ambient temperature for 56 hours and the product, a pale yellow powder (2.07 g, 90 %), was collected by suction filtration. Mp: 240-244 °C. Selected IR data (Nujol mull, cm^{-1}): 3413, 3386 (ν O-H), 3313, 3262, 3220 (ν N-H), 1627 (ν C=O), 1581, 1565 (ν C=C), 1529 (ν C=N), 995 (ν py). LCMS (methanol): m/z = 464 (M+H). ^1H NMR (DMSO-d_6): (ppm) 11.1 (s, 2H, OH), 8.6 (d, J = 4.5 Hz, 2H, ar), 8.2 (d, J = 8.5 Hz, 2H, ar), 8.0 (s, 2H, ar), 7.9 (t, 8.0 Hz, 2H, ar), 7.5 (t, J = 6.5 Hz, 2H, ar), 7.1 (s, 4H, NH_2), 3.2 (q, J = 7.2 Hz, 2H, CH_2), 1.4 (t, J = 7.5 Hz, 3H, CH_3). Elemental analysis: Found (%): C; 53.67, H; 4.29, N; 26.61. Calc. (%), for $(C_{21}H_{21}N_9O_2S)(CH_3OH)_{0.5}$: C; 53.85, H; 4.83, N; 26.29.

2.3.3.16: SMe2POAP (**2.16**):

Sodium methoxide was prepared in situ by addition of Na (0.30 g, 13 mmol) to methanol (100 mL). 2-cyanopyridine (0.84 g, 8.1 mmol) was added, and the resulting

solution was stirred for 5 hours and neutralized with glacial CH_3COOH. **2.12** (1.02 g, 4.2 mmol) was added and stirred at ambient temperature for 72 hours. The product, a white powder (1.53 g, 81 %), was collected by suction filtration. Selected IR data (Nujol mull, cm^{-1}): 3413, 3386 (ν O-H), 3317, 3255, 3193 (ν N-H), 1627(ν C=O), 1565 (ν C=C), 1535 (ν C=N), 995 (ν py). ^1H NMR (DMSO-d_6): (ppm) 11.1 (s, 2H, OH), 8.6 (d, J = 4.5 Hz, 2H, ar), 8.2 (d, J = 9.0 Hz, 2H, ar), 8.0 (s, 2H, ar), 7.9 (t, J = 7.8 Hz, 2H, ar), 7.5 (t, J = 6.3 Hz, 2H, ar), 7.1ppm (s, 4H, NH_2), 2.7ppm (s, 3H, CH_3), Elemental analysis: Found (%): C; 53.32, H; 4.22, N; 28.04. Calc. (%), for $C_{20}H_{19}N_9O_2S$: C; 53.44, H; 4.26, N; 28.04.

2.3.3.17: SEt2POMP (**2.17**):

2-acetylpyridine (2.24 g, 18.5 mmol) was dissolved in methanol (100 mL). **2.9** (1.51 g, 5.6 mmol) was added and the mixture was refluxed for 18 hours. The product, a white powder, was collected by suction filtration (2.24 g, 85 %). Mp: 288-291 °C. Selected IR data (cm^{-1}, Nujol): 3309 (ν O-H), 1693,1681 (ν C=O),1577, 1558 (ν C=C), 1523 (ν C=N), 991 (ν py). LCMS (methanol + 10 % DMF): (m/z): 462 (M+H). Elemental analysis: Found (%): C, 58.49; H, 4.80; N, 20.32. Calc. (%), for $C_{23}H_{23}N_7O_2S(CH_3OH)_{0.75}$: C, 59.74; H, 5.40; N, 20.20.

2.3.3.18: SEt2POAPz (**2.18**):

Sodium methoxide was prepared by dissolving Na (~0.4 g, 17 mmol) in methanol (150 mL). 2-cyanopyrazine (2.39 g, 23 mmol) was added and the resulting solution was stirred for 6 hours. **2.9** (1.4 g, 5.8 mmol) was added and the mixture was stirred for 18 hours, and refluxed for 2.5 hours. The product, a pale yellow powder (2.6 g, 94 %), was

collected by suction filtration. Mp: 270-274°C. Selected IR data (cm^{-1}, Nujol): 3405, 3320 (ν O-H), 3297, 3224 (ν N-H), 1681, 1643 (ν C=O), 1577 (ν C=C), 1519 (ν C=N), 991 (ν py). LCMS (methanol + 10 % DMF): m/z = 466 (M+H). Poor elemental analysis indicated contamination with a small amount of the solvolysis product $C_5H_6N_5$. See Chapter 7 for details on common solvolysis processes.

2.4: Summary:

The ligands **2.1, 2.13-2.18** were successfully synthesized. [3x3] $Mn(II)_9$ grid complexes of ligands **2.1**, **2.13**, **2.15**, and **2.18** will be discussed in Chapter 3. [3x3] $Mn(II)_9$ grid complexes of **2.15** have been further reacted with transition metal salts. The results of these reactions will be discussed in Chapter 6. Grid complexes of **2.14**, **2.15** and **2.18**, with metal cations other than Mn(II) will be discussed in Chapter 5. $Cu(II)_8$ pinwheel compounds with ligands **2.1**, **2.13** and **2.17** will be discussed in Chapter 4. Finally, unusual complexes of **2.14** and its solvolysis products, with Ni, Cu and Co will be discussed in Chapter 7.

Chapter 3: [3x3] $Mn(II)_9$ grids based on picolinic dihydrazone ligands

3.1: Preamble:

When rigid linear tritopic ligands such as 2POAP and its derivatives are reacted with Mn(II) salts, the outcome is almost invariably a [3x3] $Mn(II)_9$ grid complex (Figure 3.1). The core of the grid molecule consists of nine Mn(II) cations, arranged in a square [3x3] grid. All Mn(II) cations are bridged by ligand hydrazone oxygen atoms. The ligand molecules are arranged in parallel rows, with three ligands above, and three ligands below the nonanuclear core [27,55].

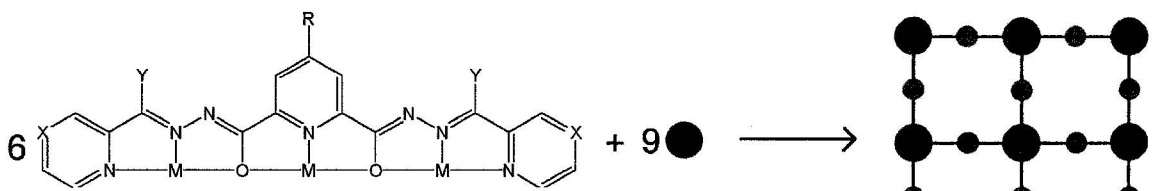

R = SEt, Y = NH_2, X = CH: SEt2POAP
R = SEt, Y = NH_2, X = N: SEt2POAPz
R = Cl, Y = CH_3, X = CH: Cl2POMP
R = H, Y = Ph, X = CH: 2POPP
R = $S^-NH_4^+$, Y = NH_2, X = CH: S2POAP
R = Cl, Y = NH_2, X = CH: Cl2POAP

Figure 3.1: 2POAP-like ligands self-assemble with Mn(II) cations for form $Mn(II)_9$ grids.

$Mn(II)_9$ grids form reliably, in high yield, and Mn(II) has not been observed to form complexes other than [3x3] grids with tritopic picolinic dihydrazone ligands, which is in contrast to other transition metal cations. Cu(II) has been observed to form octanuclear pinwheel compounds [28, 54, 63], Fe(III) to form pentanuclear, incomplete

grids with empty pockets in the side sites [64], and Ni(II) and Co(II) to form hexa- and heptanuclear partial grids where some of the central pockets of the grid are vacant [65].

The nine metal cations are held in close proximity in the grid molecule, which leads to interesting magnetic, electrochemical and spectroscopic properties [55, 66]. $Mn(II)_9$ [3x3] grids have been studied extensively. They are antiferromagnets and extensive coupling throughout the structure leads to a ground state where the central Mn(II) is essentially isolated, resulting in a ground state of S = 5/2 [27]. Additional measurements, including torque magnetometry and inelastic neutron scattering, have shown additional interesting properties of the $Mn(II)_9$ grid system, such as a field induced level crossing and accompanying change of the magnetic anisotropy from easy-axis to hard-axis type [67,68]. Theoretical studies indicate that coherent tunnelling of the Néel vector should also be possible in $Mn(II)_9$ grids [69].

The close proximity of the Mn(II) centers also leads to an unprecedented suite of metal based oxidations. It is possible to reversibly oxidize eight of the nine Mn(II) centers to Mn(III) within the range 0.6 -1.8 V vs. Ag/AgCl [27, 55, 66]. Stable, mixed oxidation state grids of the type $[Mn(II)_5Mn(III)_4]$ can be synthesized by both chemical and electrochemical means. This change in oxidation state is accompanied by the appearance of charge transfer bands in the visible-nir spectrum of the compounds [55,66]. The existence of these two stable metal oxidation state forms, which can be detected and differentiated either magnetically or spectroscopically, make the mixed oxidation state grids potential candidates for molecular devices. The mixed oxidation state $[Mn(II)_5Mn(III)_4]$ grids have a ground state of S = ½ as a result of the non-

compensation of spins in an antiferromagnetically coupled grid, and are a rare example of a mesoscopic spin-1/2 cluster, which could potentially be used in quantum computing [43].

In order to take advantage of the properties of the complexes in the device context it is necessary to be able to immobilize them on a surface. To this end, functionalized ligands were developed, which contained electron rich chlorine or sulphur donor sites, capable of interaction with surfaces. STM studies of S2POAP grids on gold (Au(111)) [55, 70, 71] and Cl2POAP grids on graphite (HOPG) [32] have been performed. In the gold studies, organized monolayers of grids were observed to form on the surface (Figure 3.2), while in the graphite studies current image tunnelling spectroscopy (CITS) was used to image the individual Mn(II) cations in the grid (Figure 3.3).

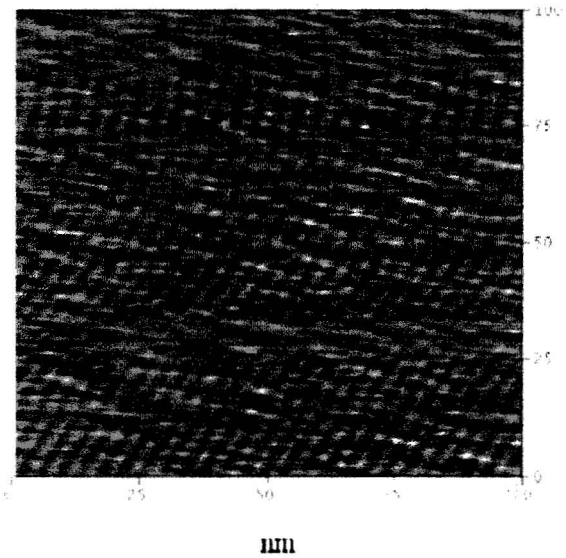

Figure 3.2: STM image of a monolayer assembly of S2POAP grids on Au(111) surface. Bright spots (dimensions ~ 2.6 x 2.6 nm) correspond to individual grid molecules.

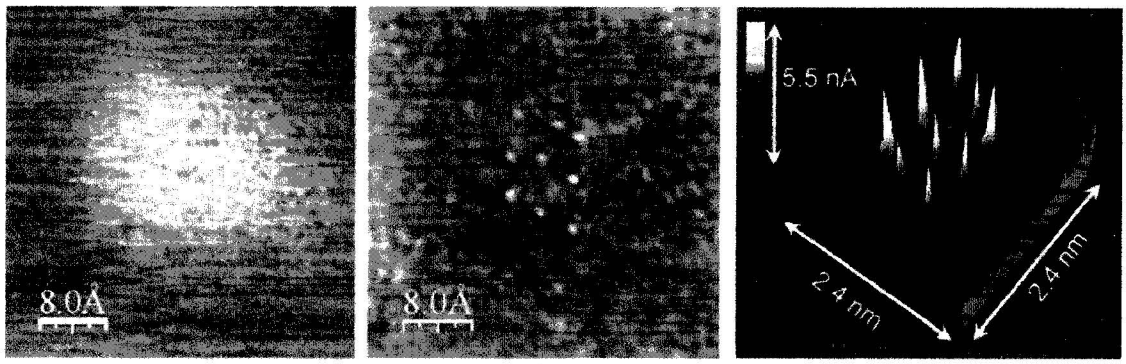

Figure 3.3: Simultaneous STM topography and CITS studies of Cl2POAP grids on graphite. Colours have been enhanced for maximum contrast. a) topographical image. b) 2D CITS image. Bright spots correspond to Mn(II) centers. c) 3D view of b) on an enlarged scale.

In this chapter, [3x3] $Mn(II)_9$ grid complexes of new 2POAP-like ligands will be presented. Structures and magnetic and electrochemical properties will be discussed with emphasis on the effect of the functional groups on these properties.

3.2: Experimental

3.2.1: Complex synthesis:

3.2.1.1: $[(SEt2POAP)_6Mn_9](CF_3SO_3)_9(H_2O)_{15}(CH_3CN)_4$ (3.1)

$Mn(CF_3SO_3)_2$ (2.5 mL, 0.059 g/mL, 1:1 MeOH/H_2O) was diluted with 1:1 methanol/acetonitrile solution (20 mL). SEt2POAP (0.1 g, 0.2 mmol) was added. A clear orange solution formed which was heated for one hour, filtered and allowed to cool. Red crystals (90 mg, 54 %), not suitable for X-ray diffraction, formed over several days.

Elemental Analysis: Found (%): C, 34.08; H, 2.65; N, 16.18. Calc. (%), for $[(C_{21}H_{19}N_9O_2S)_3(C_{21}H_{20}N_9O_2S)_3Mn_9](H_2O)_{15}(CH_3CN)_4$: C, 34.05; H, 3.18; N, 16.12.

3.2.1.2: $[(SEt2POAP)_6Mn_9](SCN)_6(H_2O)_{13}(CH_3OH)_2$ **(3.2)**

3.1 (0.05g, 0.01 mmol) was dissolved in methanol (10 mL). NH_4SCN (0.02g, 3 mmol) was dissolved in methanol (5 mL) and added to the previous solution. A deep red solution formed, which was heated for 15 minutes, filtered and allowed to cool. Red prismatic crystals (30 mg, 64 %), suitable for X-ray diffraction, formed over five days. Elemental analysis: Found (%): C; 41.15, H; 2.96, N; 21.32. Calc. (%) for $[(C_{21}H_{19}N_9O_2S)_6Mn_9](SCN)_6(H_2O)_{13}(CH_3OH)_2$: C; 41.16, H; 3.81, N; 21.49.

3.2.1.3: $[(Cl2POMP)_6Mn_9](ClO_4)_6(H_2O)_{15}$ **(3.3)**

Cl2POMP (0.1 g, 0.22 mmol) was added to a solution of $Mn(ClO_4)_2(H_2O)_x$ (0.18 g, 0.71 mmol) in methanol/water (15mL/10 mL). There was no visible reaction, so acetonitrile (10 mL) and enough triethylamine to adjust the mixture to pH = 8 were added. A brown precipitate formed and the mixture was heated for half an hour. Additional acetonitrile (40 mL) was added, which reduced the amount of precipitate by half. The precipitate was filtered off and the filtrate, a bright orange solution, was allowed to cool. After several days red rectangular crystals, suitable for X-ray diffraction, formed (60 mg, 67 %). Elemental analysis: Found (%): C; 38.06, H; 2.64, N; 14.65. Calc (%) for $[(C_{21}H_{16}N_7O_2Cl)_6Mn_9](ClO_4)_6(H_2O)_{15}$: C; 38.12, H; 3.35, N; 14.82.

3.2.1.4: $[(2POPP)_6Mn_9](NO_3)_6(H_2O)_{12}$ **(3.4)**

$Mn(NO_3)_2(H_2O)_x$ (0.17 g, 0.59 mmol) was dissolved in methanol (20 mL). 2POPP (0.10g, 0.2mmol) was added along with chloroform (5 mL). The ligand

dissolved, forming a clear yellow solution, which was heated for two hours during which it gradually turned orange. The solution was filtered and left to stand at room temperature. Deep red crystals (50 mg, 63 %) formed over a period of two weeks. Elemental Analysis: Found (%): C; 52.89, H; 3.37, N; 15.71. Calc. (%), for $[(C_{31}H_{21}N_7O_2)_6Mn_9](NO_3)_6(H_2O)_{12}$: C; 52.89, H; 3.58, N; 15.92.

3.2.1.5: $[(SEt2POAPz)_6Mn_9](CF_3SO_3)_6(H_2O)_{13.5}$ **(3.5)**

SEt2POAPz (0.10 g, 0.22 mmol) was added to a solution of $Mn(CF_3SO_3)_2$ (10 mL, 0.03 gmL^{-1}, 4:1 methanol: water). A pale orange mixture resulted. Acetonitrile (10 mL) was added and the mixture was heated for 10 mins. Water (10 mL) was added and the mixture was boiled, which resulted in a reduction in amount of precipitate and darkening of the colour. A small amount of yellow solid (<10 mg) was filtered off and the red filtrate was allowed to cool. Red needle-like crystals (80 mg, 48 %) formed overnight. Elemental analysis: Found (%): C; 32.66, H; 2.52, N; 20.96. Calc. (%) for $[(C_{19}H_{17}N_{11}O_2S)_6Mn_9](CF_3SO_3)_6(H_2O)_{13.5}$: C; 32.66, H; 2.95, N; 20.95.

3.2.2: Crystallography:

The diffraction intensities of a red-orange block shaped crystal of **3.2** (0.48 x 0.22 x 0.19 mm) were collected using graphite monochromatized MoKα radiation on a Bruker P4/CCD diffractometer at -80°C to a maximum 2θ value of 52.9°. The data were corrected for Lorentz and polarization effects. The structure was solved by direct methods [72, 73]. Some non-H atoms were refined anisotropically while the rest were refined isotropically. Hydrogen atoms were included in calculated positions with isotropic thermal parameters set twenty percent greater than those of their bonding

partners at the time of their inclusion, but were not refined. The methyl group of one thioethyl group was disordered and modeled with a 65:35 ratio of C21:C142 with isotropic refinement. Neutral atom scattering factors [74], and anomalous dispersion terms [75, 76] were taken from the usual sources. All calculations were performed using the teXsan crystallographic software package [77] of Molecular Structure Corporation except for refinement, which was performed using SHELXL-97 [72a].

The diffraction intensities of an amber block shaped crystal (0.35 x 0.12 x 0.20 mm) of **3.3** were measured using graphite monochromatized MoKα radiation on a Bruker Proteum M diffractometer with an Apex/Bede microsource radiation source. The main structure was treated similarly to **3.2**, but a good point atom model for the anions and solvent molecules could not be achieved. The Platon Squeeze procedure [78] was applied to recover ca. 3370 electrons per unit cell in a single void (6068 $Å^3$). This equates to 843 electrons per asymmetric unit.

A red-brown prismatic crystal of **3.4**, (0.76 x 0.30 x 0.29 mm) was treated similarly to **3.2**. Due to high thermal motion or disorder the nitrates and lattice water molecules were very "loose" and were refined isotropically. There is one nitrate missing in the model of the asymmetric unit, which equals two nitrates in total. This is probably represented by some of the electron density assigned to water molecules, but could not be discerned from the difference map due to limited data quality. Crystal data for **3.2**, **3.3** and **3.4** are abbreviated in Table 3.1.

Table 3.1: Summary of crystallographic data for **3.2**, **3.3**, **3.4**.

Compound	**3.2**	**3.3**	**3.4**
Empirical Formula	$C_{140.50}H_{156}O_{24}N_{60}S_{12}Mn_9$	$C_{126}H_{96}C_{16}Mn_9N_{42}O_{12}$	$C_{186}H_{138}N_{46}O_{30}Mn_9$
M/gmol^{-1}	3948.33	3097.61	3991.87
Crystal System	monoclinic	monoclinic	tetragonal
Space Group	$P2_1/c$ (#14)	$P2_1/c$	$P4_12_12$ (#92)
a/Å	28.447(3)	18.086(2)	20.279(1)
b/Å	21.338(2)	28.177(3)	
c/Å	33.290(4)	34.491(4)	54.873(6)
β/°	111.525(2)	94.693(2)	
V/ Å^3	18798(3)	17518(4)	22566(2)
ρ_{calcd}/gcm^{-3}	1.395	1.175	1.175
T/°C	-80(1)	-153(2)	-80(1)
R1	0.104	0.0718	0.111
wR2	0.369	0.2072	0.323

3.3: Results and Discussion:

3.3.1: Description of crystal structures:

3.3.1.1: $[(SEt2POAP)_6Mn_9](SCN)_6(H_2O)_{13}(CH_3OH)_2$ (3.2).

The structure of **3.2** is shown in Figure 3.4a, and significant bond lengths and angles are listed in Table 3.2. The homoleptic grid structure consists of a $[Mn_9(\mu\text{-}O_{12})]$ core with six of the heptadentate ligands in a roughly parallel arrangement, three above and three below the core. There are three different coordination environments for the Mn(II) cations; the corners have *cis*-MnN_4O_2 coordination spheres, the edges have *mer*-MnN_3O_3 coordination spheres, and the center has a *trans*-MnN_2O_4 coordination environment. Mn-N bond distances range from 2.129-2.355 Å, while Mn-O bond distances fall within the range of 2.126-2.341 Å. Mn-Mn distances lie in the range of

3.885-4.070 Å. The Mn-O-Mn bridging angles fall between 126.46° and 130.03°, which is comparable to other grid systems. The core of the grid is nearly square, with edge distances ranging from 7.772-7.922 Å between corner Mn(II) cations along the sides and of 10.866 and 10.605 Å diagonally across the core. A simplified view of the core, showing only coordinating atoms is shown in Figure 3.4b.

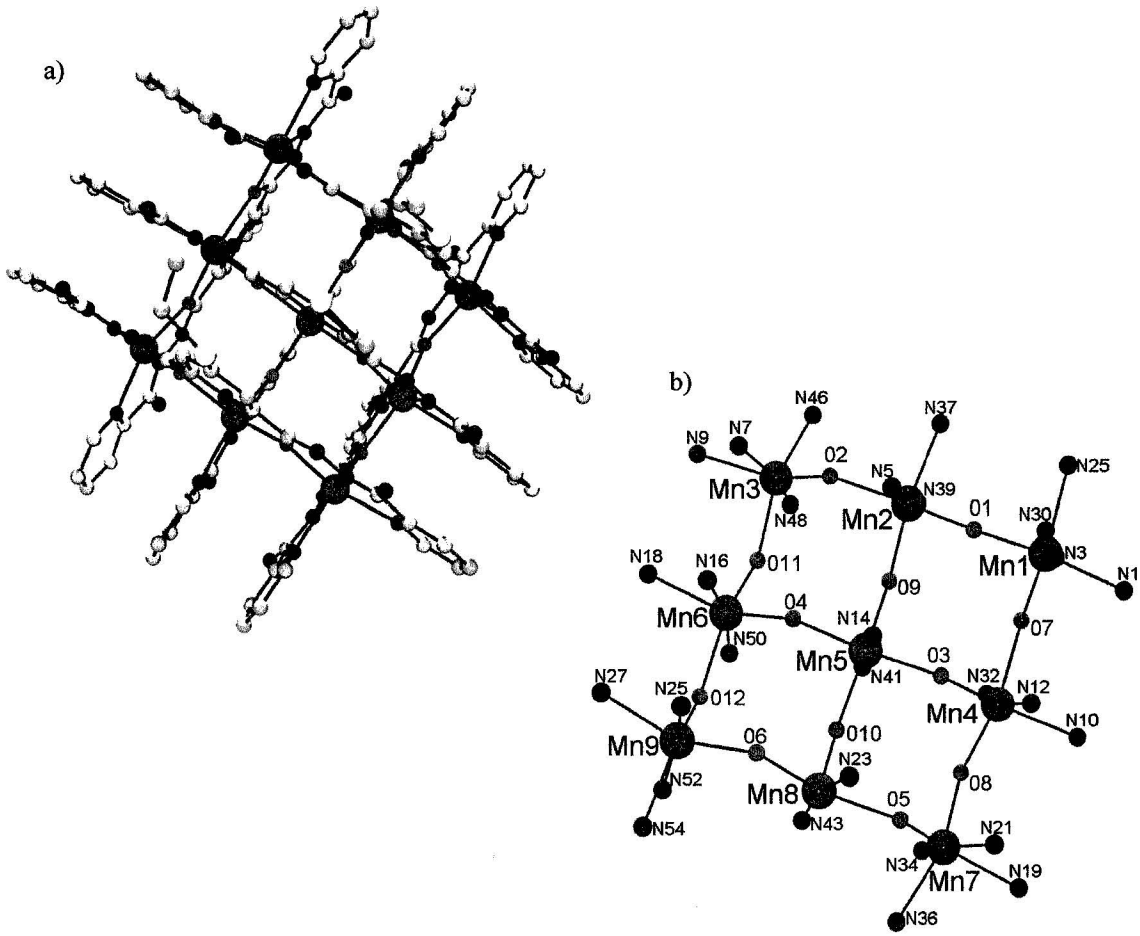

Figure 3.4: a) POV-RAY depiction of **3.2**; magenta = Mn, grey = C, blue = N, red = O, yellow = S. b) Simplified structure showing Mn (II) and coordinated atoms.

Table 3.2: Selected bond distances (Å) and angles (°) for **3.2**.

Mn1-N30	2.138(7)	Mn6-O4	2.126(5)
Mn1-N3	2.139(7)	Mn6-N16	2.140(7)
Mn1-O1	2.171(5)	Mn6-O11	2.175(6)
Mn1-O7	2.193(6)	Mn6-N50	2.188(7)
Mn1-N1	2.310(8)	Mn6-N18	2.313(8)
Mn1-N28	2.355(8)	Mn6-O12	2.341(6)
Mn2-N39	2.160(7)	Mn7-N34	2.150(7)
Mn2-O9	2.165(6)	Mn7-N21	2.166(7)
Mn2-O1	2.173(6)	Mn7-O5	2.177(5)
Mn2-N5	2.188(7)	Mn7-O8	2.186(6)
Mn2-O2	2.242(5)	Mn7-N36	2.305(8)
Mn2-N37	2.339(7)	Mn7-N19	2.344(8)
Mn3-N7	2.133(8)	Mn8-N43	2.148(6)
Mn3-N48	2.143(8)	Mn8-N23	2.153(6)
Mn3-O2	2.164(6)	Mn8-O10	2.157(6)
Mn3-O11	2.205(6)	Mn8-O6	2.177(5)
Mn3-N46	2.297(8)	Mn8-O5	2.211(5)
Mn3-N9	2.354(8)	Mn8-N45	2.330(7)
Mn4--N12	2.151(7)	Mn9-N25	2.130(7)
Mn4-O3	2.151(5)	Mn9-O6	2.159(5)
Mn4-N32	2.175(7)	Mn9-N52	2.181(7)
Mn4-O8	2.185(6)	Mn9-O12	2.217(6)
Mn4-O7	2.251(6)	Mn9-N54	2.310(7)
Mn4-N10	2.319(7)	Mn9-N27	2.310(7)
Mn5-N14	2.166(6)	S-S(intragrid):	3.767-4.061
Mn5-O10	2.175(6)	S-S(intergrid):	7.983 (shortest)
Mn5-N41	2.186(6)		
Mn5-O9	2.189(6)	S-N(inter):	3.751, 3.764
Mn5-O3	2.192(5)		
Mn5-O4	2.207(5)	Mn-Mn:	3.885-4.070
Mn1-O1-Mn2	128.3(3)	Mn1-O7-Mn4	130.0(3)
Mn3-O2-Mn2	128.7(3)	Mn4-O8-Mn7	128.9(3)
Mn4-O3-Mn5	127.0(3)	Mn2-O9-Mn5	126.9(3)
Mn6-O4-Mn5	128.4(2)	Mn8-O10-Mn5	127.5(3)
Mn7-O5-Mn8	128.4(3)	Mn6-O11-Mn3	127.7(3)
Mn9-O6-Mn8	128.8(3)	Mn9-O12-Mn6	126.5(3)

The Mn-N distances for the connections to terminal pyridine rings range from 2.297-2.355 Å, while for the central pyridine rings the distances range from 2.153-2.188 Å. The difference in Mn-N bond distances to central and terminal pyridine rings is large,

with very long Mn-N bonds to the terminal rings. This is typical of grids in this class and has been attributed to the stretching of the ligands over the nonanuclear core [55]. The pyridine rings have the same nearly parallel arrangement as in other grid systems, with the central pyridine rings laying 3.381-3.447 Å apart, while the terminal rings are 3.521-3.879 Å apart. These distances are quite close, and indicate that π-stacking plays an important role in the self-assembly and stability of the structure. Furthermore, the distances between central pyridine rings in **3.2** are shorter than average for Mn(II) grids [55]. This can be attributed to relatively short S-S distances of 3.767-3.966 Å between thioether groups. These distances are reasonable for weak S···S interactions [79-83].

The crystal packing in this structure is significantly different from other grids in this class [55], as there is no evidence of π-stacking in the unit cell. There are, however, several S···N contacts between an S atom of one grid and amine N atoms of neighbouring molecules. S···N interactions are of greater strength than π-stacking interactions and would be expected to dominate the packing arrangement. A portion of the extended structure is shown in Figure 3.5. Each grid is connected to its neighbours by two S···N contacts (3.751 and 3.764 Å) forming a chain. Similar intermolecular S···N contacts are quoted widely in the literature [79-83], and 3.7 Å is not unreasonable for a weak interaction. Each chain is separated from neighbouring chains by approximately 8 Å (S···S).

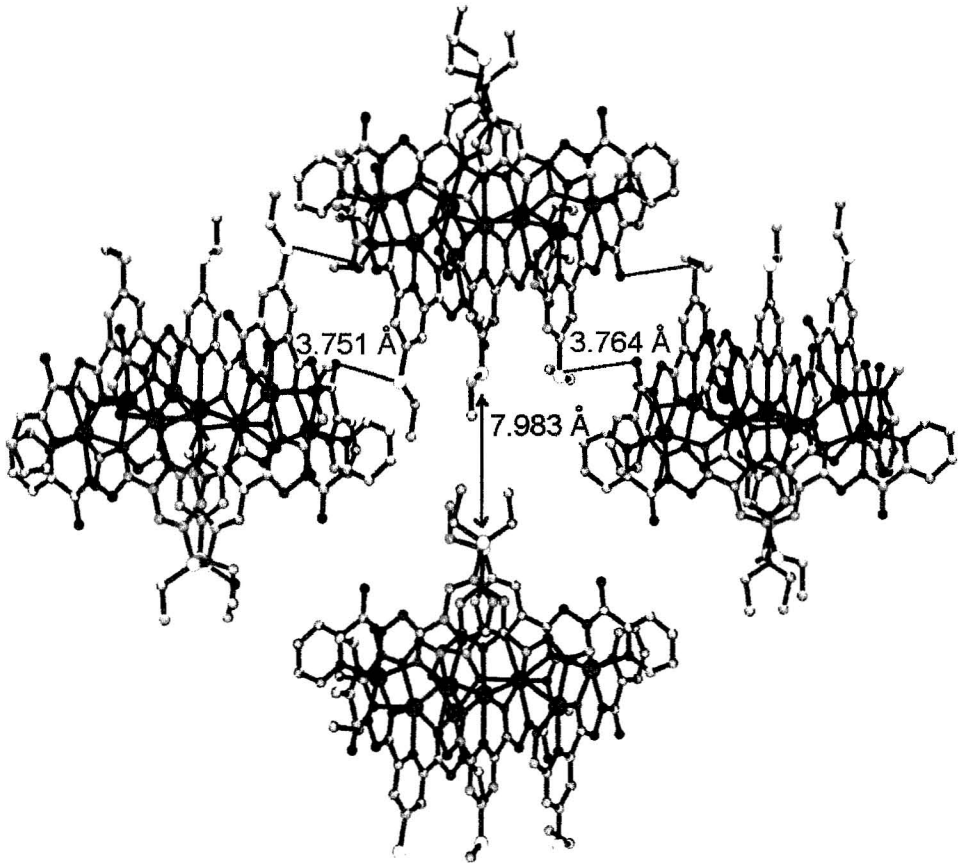

Figure 3.5: Extended structure of **3.2**. Intermolecular S···N contacts highlighted in green.

3.3.1.2: $[(Cl2POMP)_6Mn_9](ClO_4)_6(H_2O)_{15}$ (**3.3**).

The structure of **3.3** is depicted in Figure 3.6, and significant bond lengths and angles are included in Table 3.3. Due to the method of refinement, no counter anions or solvent molecules are present in the structure. It is, therefore, being included as a preliminary structural report. However, the level of refinement is sufficient that the main cation is clearly defined. The overall structure is typical of grid compounds with Mn-N bond lengths in the range of 2.159-2.302 Å, Mn-O distances ranging from 2.144-2.235 Å,

and Mn-O-Mn angles between 127.58° and 129.19°. Mn-Mn distances for adjacent centers fall between 3.913 Å and 4.010 Å. The Mn-Mn distances across the diagonal of the grid are 10.634 Å and 10.692 Å demonstrating once again the square nature of the core.

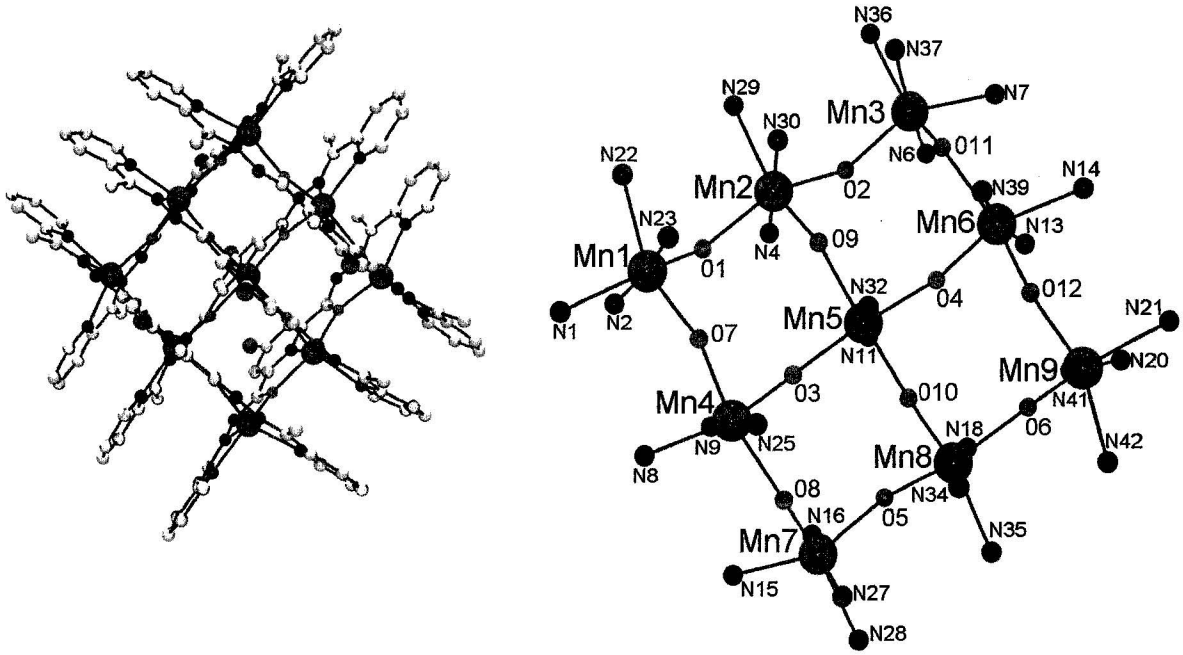

Figure 3.6: POV-RAY depiction of **3.3**. Magenta = Mn, grey = C, blue = N, red = O, green = Cl.

The ligand pyridine rings adopt a nearly parallel, slightly offset arrangement much like in the structure of **3.2**. In this case, the inter-ring distances for the terminal pyridine moieties range from 3.337 Å to 3.624 Å, while the distances between the central rings lie between 3.298-3.392 Å. These distances are much shorter than average for Mn(II) grids, which was also the case for **3.2**. The Cl atoms on the central rings lie

3.792-3.918 Å apart, and it is not unreasonable that a weak Cl-Cl interaction pulls the central rings into closer proximity than would otherwise be expected.

Table 3.3: Selected bond distances (Å) and angles (°) for **3.3**.

Mn1-O1	2.171(4)	Mn7-O8	2.177(4)
Mn1-O7	2.183(4)	Mn7-O5	2.187(4)
Mn1-N2	2.193(5)	Mn7-N16	2.189(5)
Mn1-N23	2.212(6)	Mn7-N27	2.200(5)
Mn1-N22	2.252(6)	Mn7-N15	2.259(5)
Mn1-N1	2.281(5)	Mn7-N28	2.290(6)
Mn2-N30	2.166(5)	Mn8-O10	2.144(4)
Mn2-N4	2.179(5)	Mn8-N18	2.167(5)
Mn2-O9	2.185(4)	Mn8-N34	2.202(5)
Mn2-O1	2.201(4)	Mn8-O5	2.230(4)
Mn2-O2	2.220(4)	Mn8-N35	2.250(6)
Mn2-N29	2.255(5)	Mn8-O6	2.256(4)
Mn3-O 2	2.174(4)	Mn9-O12	2.155(4)
Mn3-O11	2.181(4)	Mn9-N41	2.159(5)
Mn3-N6	2.194(5)	Mn9-O6	2.187(4)
Mn3-N37	2.194(5)	Mn9-N20	2.192(5)
Mn3-N7	2.265(5)	Mn9-N42	2.269(5)
Mn3-N36	2.270(6)	Mn9-N21	2.301(5)
Mn4-N25	2.174(5)	Mn1-O1-Mn2	128.57(19)
Mn4-O3	2.177(4)	Mn3-O2 -Mn2	128.02(19)
Mn4-N9	2.191(5)	Mn4-O3 -Mn5	128.12(17)
Mn4-O7	2.202(4)	Mn6-O4 -Mn5	129.19(17)
Mn4-O8	2.206(4)	Mn7-O5 -Mn8	128.84(17)
Mn4-N8	2.238(5)	Mn9-O6 -Mn8	129.05(18)
		Mn1-O7 -Mn4	128.35(19)
Mn5-O9	2.175(4)	Mn7-O8 -Mn4	128.43(18)
Mn5-N11	2.177(4)	Mn5-O9 -Mn2	128.17(18)
Mn5-N32	2.185(5)	Mn8-O10-Mn5	127.58(17)
Mn5-O3	2.193(4)	Mn3-O11-Mn6	128.0(2)
Mn5-O4	2.210(4)	Mn9-O12-Mn6	128.39(19)
Mn5-O10	2.217(4)		
Mn6-N39	2.171(5)	Cl-Cl(intra):	3.792-3.918
Mn6-N13	2.179(5)	Cl-Cl(inter):	3.357, 3.672
Mn6-O4	2.184(4)		
Mn6-O11	2.209(4)	Cl1-C126:	3.633
Mn6-O12	2.235(4)	Cl1-C59:	3.490
Mn6-N14	2.302(5)	Cl2-C122:	3.574
		Cl2-C63:	3.454
Cl3-C12:	3.766	Cl···H-C:	3.174, 91.03
Cl···H-C:	3.169 , 132.30		
Cl3-C70:	3.730		
Cl···H-C:	2.980 , 134.07		

A complete discussion of the extended interactions in **3.3** is not appropriate, as the solvent molecules and counter anions are absent from the structure, and there is thus no way to gauge their contribution to the packing. However, for the purposes of comparison to the other grids, the main interactions will be discussed. Efforts are ongoing to obtain a better data set which would allow a more complete analysis of the extended structure. The unit cell of **3.3** contains a complex series of interactions involving the Cl groups, but no significant π-π interactions. The unit cell is pictured in Figure 3.7. Pairs of grids are held together by Cl-Cl interactions, with contact distances of 3.357 Å (Cl5-Cl6', Cl6-Cl5') and 3.672 Å (Cl4-Cl6', Cl6-Cl4'). The former distance is short relative to the sum of the van der Waals radii for two chlorine atoms (3.5 Å) [84], indicating a moderate to strong interaction. A third grid molecule (half of a second dimer) interacts with the first pair with one Cl group to form Cl-C (or Cl···H-C) interactions with a methyl group of each member of the pair. The Cl-C distances are 3.730 Å, with Cl3···H70$_a$-C 2.980 Å, 134.07° and 3.766 Å, with Cl···H12$_a$-C 3.169 Å, 132.30°. H-bonds are generally considered to be shorter than the sum of the van der Waals radii of the atoms in question (2.90 Å for Cl and H), however, weak H-bond interactions involving poor donors like C-H can be significant even up to C-X separation lengths of *ca.* 4 Å [1]. The two Cl groups adjacent to the one involved in the H-bonding interactions appear to be in close contact (3.454-3.633 Å) with a pair of pyridine rings at the corner of one of the grid molecules in the initial pair. Each of the two chlorine atoms has a contact with each of the two pyridine rings found at the corner of the grid. The distances are Cl1-C59' = 3.490 Å, Cl1-C126' = 3.633 Å, Cl3-C122' = 3.574 Å, Cl3-C63' = 3.454 Å. Each grid has

two of these sets of contacts; one through its Cl groups and one through a pair of the corner pyridine rings.

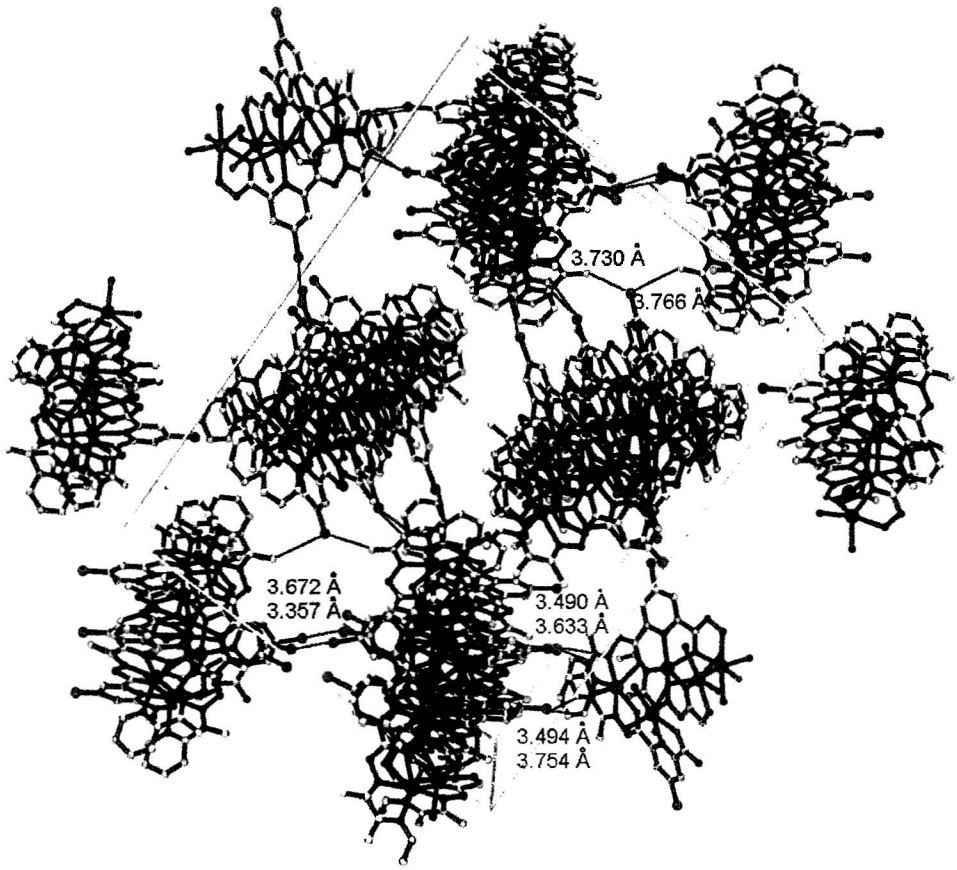

Figure 3.7: Unit cell of **3.3.** Cl···Cl and H-bonding contacts highlighted in black, Cl-py contacts in purple.

3.3.1.3: $[(2POPP)_6Mn_9](NO_3)_6(H_2O)_{12}$ (**3.4**)

The cation of **3.4** is shown in Figure 3.8a, and important bond distances and angles are listed in Table 3.4. Mn-N distances fall between 2.159 and 2.300 Å, with the longest of these (2.270-2.300 Å) occurring between Mn(II) centers and external pyridine rings. Mn-O bond distances range from 2.150 to 2.253 Å. Mn-Mn distances lie between

3.902 and 3.957 Å and Mn-O-Mn bridging angles range from 125.6 to 128.0°. These values are typical of the Mn(II) grids as a whole. The grid, however, has a pronounced distortion, forming a rhombus shaped rather than square shaped grid. This pronounced distortion of the core (Figure 3.8b) is not typical of Mn(II) grids and is thought to be partially due to the steric crowding caused by the phenyl groups of the ligand 2POPP. While the corner Mn to Mn distances along the edges of the core are normal (7.729, 7.851 Å), the diagonal distances, at 9.800 and 12.110 Å vary significantly from those in the average grid, resulting in a flattened, rhombus shaped grid.

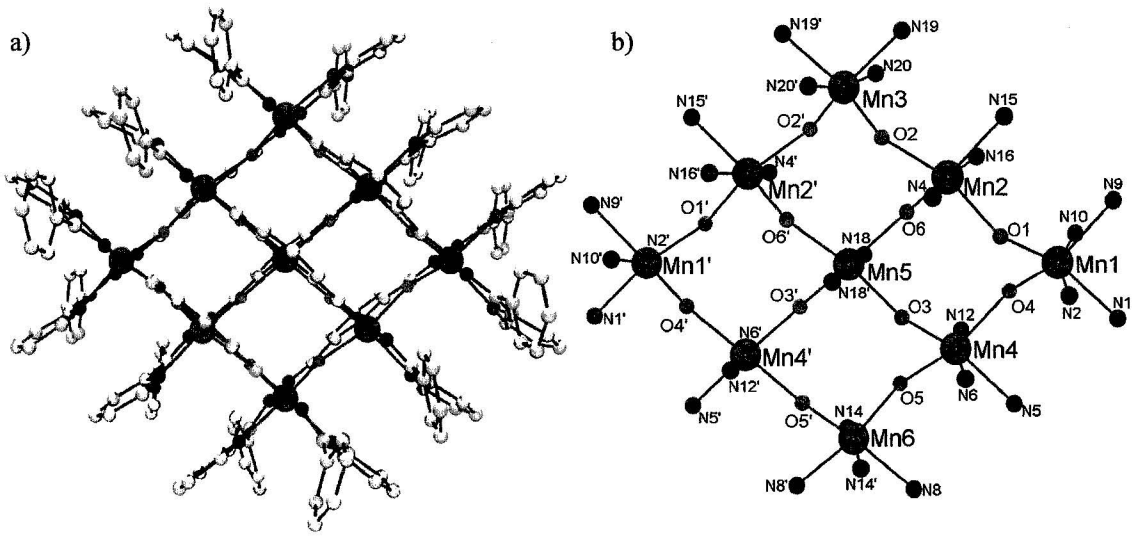

Figure 3.8: a) POV-RAY depiction of **3.4**. Magenta = Mn, blue = N, red = O, grey = C. b) core of **3.4**, showing Mn(II) and coordinating atoms.

There is extensive π-stacking within the grid. The terminal pyridine and phenyl groups of the ligands line up on opposite sides of each edge of the molecule. The phenyl groups have displaced π-stacking interactions with close contact distances ranging from

3.4-3.6 Å. The terminal pyridine rings have face-to-face interactions, and are much more parallel than the phenyl groups. Distances between terminal pyridine rings range from 3.5 - 4.1 Å. The central pyridine rings also display face-to-face stacking interactions. They are much more rigidly aligned, with distances ranging from 3.7-3.8 Å between corresponding C atoms in adjacent rings. The π-π interactions are clearly significant, and probably contribute to the distortion of the core and stability of the distorted molecule.

Table 3.4: Selected bond distances (Å) and angles (°) for **3.4**.

Mn1-O1	2.155(6)	Mn2-N4	2.180(7)
Mn1-O4	2.169(6)	Mn2-O6	2.175(6)
Mn1-N2	2.174(8)	Mn2-N16	2.233(7)
Mn1-N10	2.177(8)	Mn2-O1	2.246(6)
Mn1-N9	2.292(8)	Mn2-O2	2.253(6)
Mn1-N1	2.300(8)	Mn2-N15	2.278(7)
Mn3-O2	2.163(6)	Mn4-O3	2.150(6)
Mn3-O2	2.163(6)	Mn4-N12	2.160(7)
Mn3-N20	2.182(7)	Mn4-O5	2.210(6)
Mn3-N20	2.182(7)	Mn4-N6	2.220(7)
Mn3-N19	2.272(8)	Mn4-O4	2.229(6)
Mn3-N19	2.272(8)	Mn4-N5	2.273(8)
Mn5-N18	2.159(6)	Mn6-O5	2.174(6)
Mn5-N18	2.159(6)	Mn6-O5	2.174(6)
Mn5-O3	2.231(6)	Mn6-N14	2.184(8)
Mn5-O3	2.231(6)	Mn6-N14	2.184(8)
Mn5-O6	2.233(6)	Mn6-N8	2.270(8)
Mn5-O6	2.233(6)	Mn6-N8	2.270(8)
Mn1-O1-Mn2	128.0(3)	π-stacking:	
Mn3-O2-Mn2	127.3(3)	ph-py$_c$ docking:	3.583
Mn4-O3-Mn5	128.0(3)		3.878
Mn1-O4-Mn4	125.6(3)		3.471
Mn6-O5-Mn4	125.7(3)	ph-ph docking:	3.481
Mn2-O6-Mn5	127.4(3)		3.878
			3.763
H-bonding:			
O7···H36-C53	2.496, 126.47	ph-py$_t$ neighbouring:	3.728
O7···H47-C71	2.354, 134.42		3.868
O8···H57-C84	2.415, 154.83		4.065
O12···H43-C64	2.583, 129.65		

As this complex has no electron rich substituents on the central pyridine rings, the extended structure is dominated by slipped π- π interactions extending in three dimensions. A portion of the extended structure is depicted in Figure 3.9.

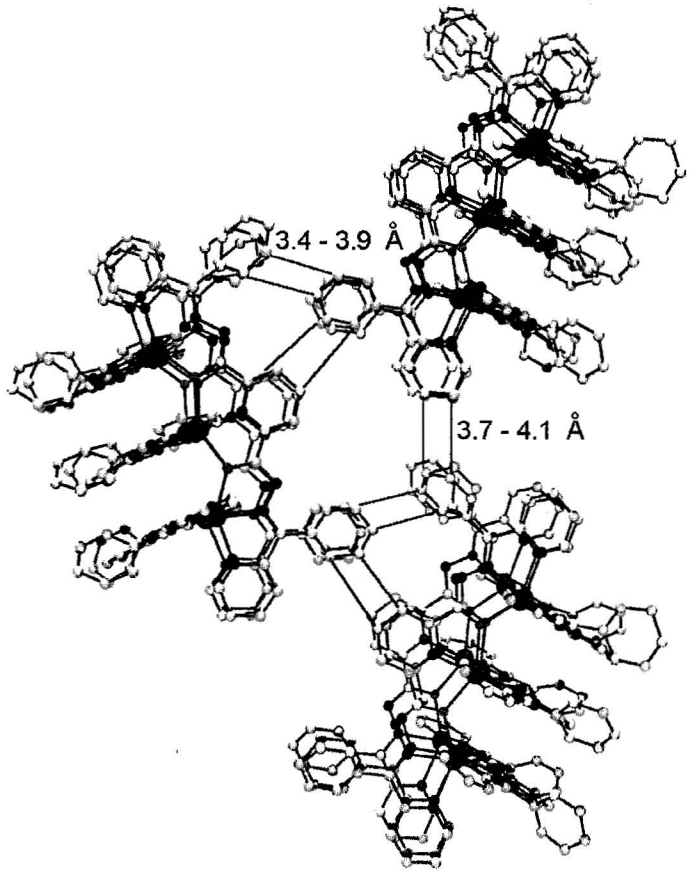

Figure 3.9: Extended structure of **3.4**, with π-π contacts highlighted in green.

The stacked terminal phenyl groups of one molecule are docked between the central pyridine rings and terminal phenyl groups of another. The distances between the terminal phenyl group of the first molecule and the rings of the second range from 3.4-3.9 Å. A third molecule lies next to the second, with distances of 3.7-4.1 Å between its terminal pyridine rings and the terminal phenyl rings of the second molecule. The third

molecule is docked with the first, in the fashion described, resulting in a chain. The same pattern is repeated with the rings oriented perpendicular to the original plane such that chains extend in three dimensions. In addition to the π-stacking there are several relatively short hydrogen bonding contacts between nitrate anions and aromatic protons, with O···H distances on the order of 2.3-2.5 Å, and O···H-C angles between 126-156°. These do not appear to affect the packing of the grids, but merely occupy the void spaces between them.

3.3.2: Magnetic Properties

The $Mn(II)_9$ grids have a $Mn_9(\mu\text{-}O_{12})$ core, where Mn(II) centers are bridged by hydrazone O atoms. The magnetic properties are dominated by intramolecular antiferromagnetic exchange. In general, the magnetic moment at room temperature lies between 16 and 17 μ_B and decreases to approximately 6 μ_B at 2 K. An illustration of the core of a typical grid is included as Figure 3.10. J1 represents the magnetic exchange between the eight outer Mn(II) centers, while J2 represents the coupling between the central Mn(II) and its nearest neighbours. Assuming an idealized [3x3] grid system the isotropic nearest neighbour exchange terms are represented by the following exchange Hamiltonian (Equation1). Dipole-dipole, second order ligand field and Zeeman terms are ignored.

$$H_{ex} = -J1(\Sigma_{i=1\text{-}7}\, S_1 \cdot S_{i+1} + S_8 \cdot S_1) - J2(S_2 + S_4 + S_6 + S_8) \cdot S_9 \qquad [1]$$

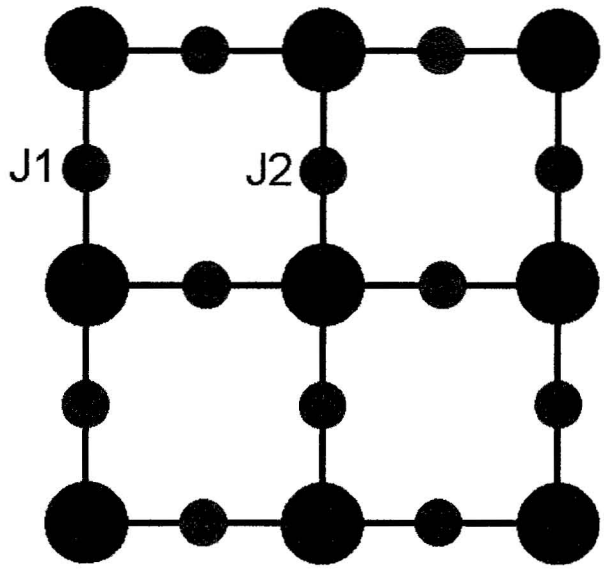

Figure 3.10: Magnetic model for [3x3] $Mn(II)_9$ grids.

Solving the isotropic exchange problem for a 45 spin, two J system like that of the Mn(II) grids is beyond the ability of PCs and of many mainframe computers. In some cases it is possible to impose spin rotational and D4 spin permutational symmetry on the system to simplify the problem, but even then the matrix diagonalization problem is too large to calculate the total spin states and their energies on most PCs (largest matrix dimension 22210). The alternative is to approximate the eight-membered ring as an isolated chain (reasonable for a ring size of eight centers), plus one additional isolated Mn(II) center. Assuming that the coupling between the central Mn(II) and the ring is negligible, which is consistent with the nominal 5/2 ground state typical of $Mn(II)_9$ grid systems [27, 55], you can then fit the data using the Fisher model (Equations 2 and 3) for a 5/2 chain where the large local spin is treated as a classical vector [85-87]. This model has been previously employed with some success [55].

$$\chi_{Mn} = \frac{Ng^2\beta^2 S(S+1)}{3KT}\frac{(1+u)}{(1-u)} \qquad [2]$$

$$u = \coth\left[\frac{JS(S+1)}{kT}\right] - \left[\frac{kT}{JS(S+1)}\right] \qquad [3]$$

$$\chi_{mol} = \left[\frac{(8\chi_{Mn} + 1.094g^2)}{T-\theta}\right](1-\alpha) + \left(\frac{1.094g^2}{T}\right)\alpha + TIP \qquad [4]$$

The variable temperature magnetic moment profile of **3.1** is shown in Figure 3.11. It is typical of a $Mn(II)_9$ grid, with a room temperature value of 17.2 μ_B, dropping to 6.0 μ_B at 2K, consistent with the 5/2 ground state. The data were fitted to equations 1-4 with the susceptibility scaled for eight spin coupled Mn(II) centers, and then corrected for the isolated Mn(II) center, the temperature independent paramagnetism (TIP), the fraction of paramagnetic impurity (α), and intermolecular exchange effects (θ, a Weiss-like temperature correction) (Equation 4). A good fit of the data gave the parameters g = 2.035, J = -4.0 cm^{-1}, α = 0.001, θ = -3K, TIP = 0 cm^3mol^{-1} (set at zero, since TIP is not usually significant for Mn(II)), $10^2R = 2.3$ ($R = [\Sigma(\chi_{obs}-\chi_{calc})^2/\Sigma\chi_{obs}^{\ 2}]^{1/2}$). The solid line in Figure 3.11 was produced using these parameters. The fact that the data were reproduced accurately over the entire temperature range suggests that the model is reasonable for [3x3] $Mn(II)_9$ grid compounds, which is consistent with earlier studies [55]. It should be noted that a full magnetic analysis has been performed on a 2POAP based $[Mn(II)_5Mn(III)_4]$ grid [66, 43], and J2 was found to be comparable to J1. Since J2

is between Mn(II) centers in the mixed oxidation state system, the same principle should hold true for the $Mn(II)_9$ system. When using the chain model the contribution of J2 generally manifests itself as a non-zero, negative θ value.

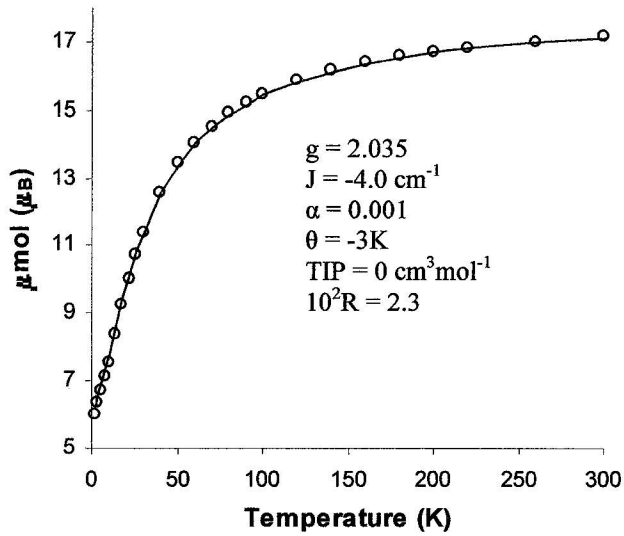

Figure 3.11: Magnetic moment vs. Temperature profile for **3.1**.

The magnetic profiles of **3.2**, **3.3**, **3.4** and **3.5** are similar to that of **3.1**. The data were fitted to equations 1-4, giving the parameters g = 2.03, J = -4.4 cm^{-1}, α = 0.001, θ = -3.5 K, TIP = 0 cm^3mol^{-1}, 10^2R = 2.9 for **3.2**, g = 2.01, J = -4.5 cm^{-1}, α = 0.001, θ = -1.5K, TIP = 0 cm^3mol^{-1}, 10^2R = 2.4 for **3.3**, g = 2.00, J = -4.8 cm^{-1}, α = 0.001, θ = -2 K, TIP = 0 cm^3mol^{-1}, 10^2R = 1.8 for **3.4** and g = 2.02, J = -4.7 cm^{-1}, α = 0.001, θ = -4.5 K, TIP = 0 cm^3mol^{-1}, 10^2R = 1.2 for **3.5.**

It is interesting to note that the magnetic profile of **3.4** does not differ substantially from that of the other $Mn(II)_9$ [3x3] grids, despite a pronounced structural distortion. Despite this distortion in the core of the molecule, Mn-N and Mn-O bond

lengths, and Mn-O-Mn angles fall within the normal range for compounds in this class. Since the magnetic properties depend on the effective overlap of the magnetic orbitals, the coordination environments of the metal cations, and the bridging angles between the metal sites are more important than the overall shape of the compound to the overall magnetic profile.

3.3.3: Electrochemical properties:

The cyclic voltammogram for an acetonitrile solution of **3.1** is depicted in Figure 3.12. It is typical of [3x3] $Mn(II)_9$ grids. There is a prominent, quasi-reversible peak, at approximately $E_{1/2} = 705$ mV ($\Delta E_p \sim 200$ mV), followed by four additional quasi-reversible waves at $E_{1/2} = 985$ mV ($\Delta E_p \sim 100$ mV), $E_{1/2} = 1133$ mV ($\Delta E_p \sim 90$ mV), $E_{1/2} = 1321$ mV ($\Delta E_p \sim 110$ mV) and $E_{1/2} = 1485$ mV ($\Delta E_p \sim 130$ mV).

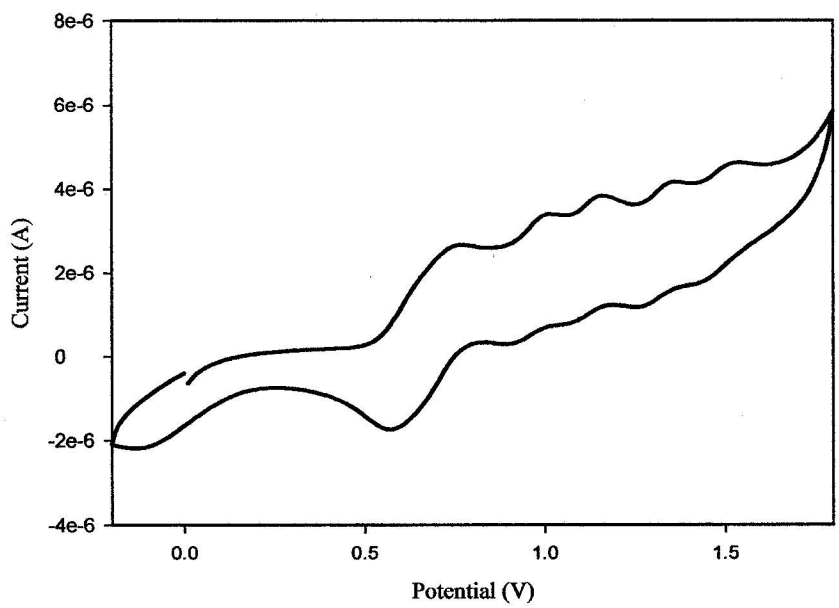

Figure 3.12: Cyclic voltammogram for **3.1** (Pt, CH_3CN, TEAP, vs. Ag/AgCl, using a 100 mV/s scan rate).

The half wave potentials are calculated from the differential pulse voltammogram, pictured in Figure 3.13. The potential at which the maximum current is achieved is related to the half-wave potential by the relationship:

$$E_{max} = E_{1/2} - \frac{E_{pulse}}{2} \qquad [5]$$

Equation 5 applies when the peak separations are large enough for the peak currents to be well resolved.

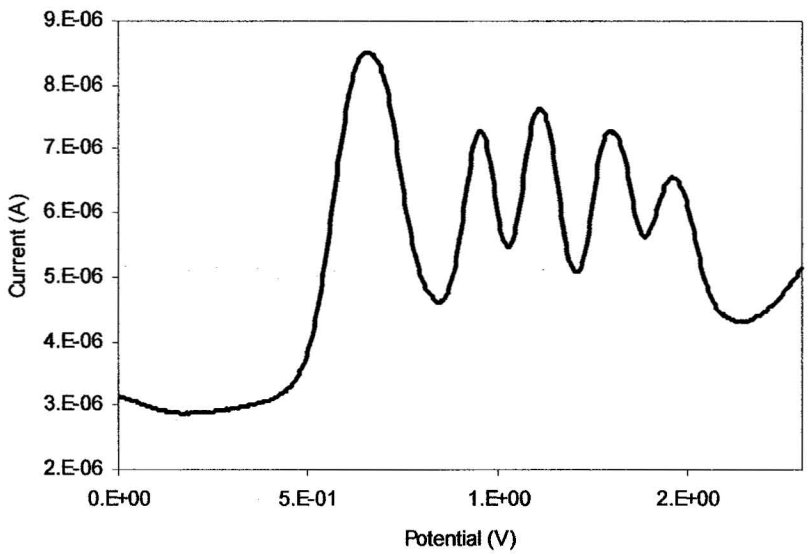

Figure 3.13: Differential pulse voltammogram for **3.1** (Pt, CH_3CN, TEAP, vs. Ag/AgCl, using an 8 mV/s scan rate, 50 mV pulse amplitude, 3 ms pulse width).

Previous controlled potential electrolysis studies on 2POAP [3x3] $Mn(II)_9$ grids have shown that the first wave corresponds to a four electron redox process, which is assigned to the oxidation of four Mn(II) centers to Mn(III). The other four waves are one electron oxidations corresponding to the oxidation of four other Mn(II) sites to Mn(III).

The first, four-electron, process has been assigned to the oxidation of the four corner sites, while the one electron oxidations are associated with the side sites [88]. No oxidation of the central Mn(II) site to Mn(III) has been observed, perhaps because it lies beyond the potential cutoff (~1.8 V vs. Ag/AgCl) associated with the platinum working electrode. The increasing oxidation potentials for the essentially equivalent side Mn(II) cations suggest communication between these metal centers, perhaps via the central Mn(II) site. It is possible that the increase in potential for the successive oxidations is associated with the difficulty of removing additional electrons from a system which already possesses a 10^+ charge.

The cyclic voltammogram for **3.3** is pictured in Figure 3.14. It is significantly different from that of **3.1** in that only one broad, poorly reversible oxidation wave is observed, and that it occurs at $E_{1/2} = 1225$ mV ($\Delta E_p \sim 280$ mV), which is significantly higher than the first oxidation wave of **3.1**. The differential pulse voltammogram (Figure 3.15) reveals a poorly defined shoulder at $E_{1/2} = 1730$ mV. It is possible that the first wave is the four electron oxidation observed for the corner Mn(II) sites to Mn(III) in amidrazone-based $Mn(II)_9$ [3x3] grids, and the shoulder is the first of the one electron oxidations of the side sites.

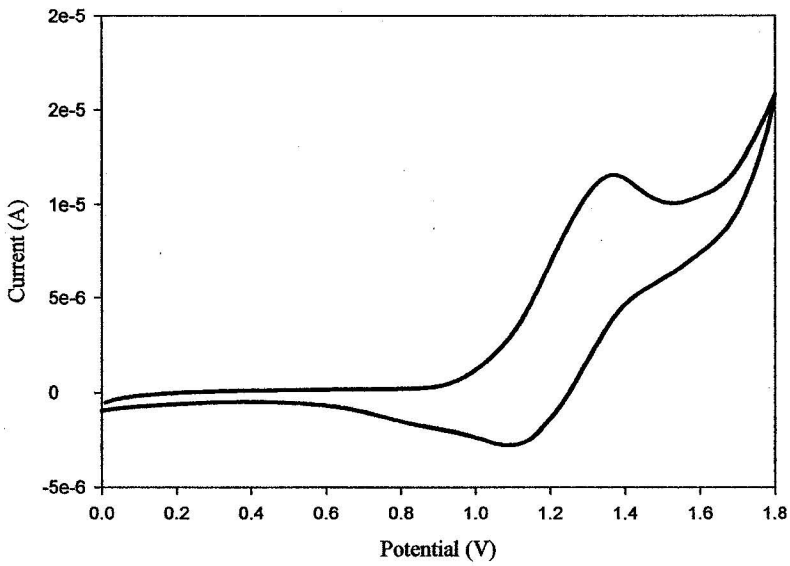

Figure 3.14: Cyclic voltammogram for **3.3** (Pt, CH_3CN, TEAP, vs. Ag/AgCl, using a 50 mV/s scan rate).

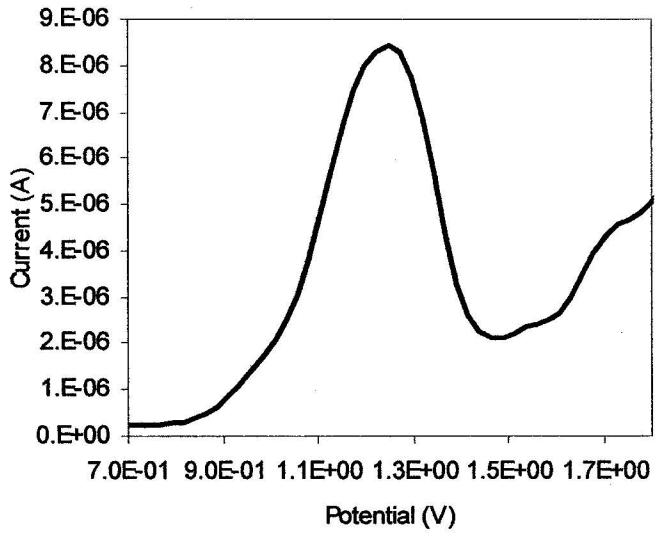

Figure 3.15: Differential pulse voltammogram for **3.3** (Pt, CH_3CN, TEAP, vs. Ag/AgCl, using a 20 mV/s scan rate, 50 mV pulse amplitude, 50 ms pulse width).

The electrochemistry of **3.4** is less well defined than that of **3.3**. There is one very broad, poorly defined wave discernable at a potential of approximately 1200 mV. The differential pulse voltammogram for **3.4** shows that the half wave potential for the process is 1175 mV. No other oxidations can be discerned. Compounds **3.3** and **3.4** are both prepared from Schiff-base ligands, as opposed to amidrazone-based ligands like 2POAP or SEt2POAP. In all cases reported so far, replacement of the amidrazone NH_2 group by aliphatic or aromatic groups appears to completely disrupt the suite of oxidations that has been observed in all amidrazone based [3x3] $Mn(II)_9$ grids [32]. This suggests an outer sphere mechanism involving the NH_2 groups. If this were the case, the order of oxidation of the Mn(II) sites to Mn(III) becomes clear; the corner sites, which are in proximity to two of the amidrazone NH_2 groups oxidize first, followed by the side sites, which are close to only one NH_2. The central site, near no amidrazone NH_2 groups, does not oxidize in the potential window of the platinum electrode. This explanation is compelling, as hard-soft acid-base theory [89] would predict the opposite order. The central site, with four oxygen atom donors is the hardest environment, and should therefore stabilize Mn(III) the most, followed by the side sites, with three oxygen atom donors, and finally the corner sites with only two oxygen donors. It is also possible that the oxidations are occurring in the order of accessibility of the Mn(II) cations. The corners are the most accessible, followed by the side sites, while the center is tightly bound at the center of the molecule. The Schiff-base ligands, with Y = CH_3 or phenyl (Figure 3.1), are bulkier than the NH_2 groups of the amidrazone ligands. The additional bulk of these groups could make access to the Mn(II) cations more difficult, and the

oxidations more difficult to achieve. This possibility could be tested by preparation of a ligand with Y = H, a small, non-amine group.

The cyclic voltammogram for **3.5** is depicted in Figure 3.16. It is more typical of the $Mn(II)_9$ [3x3] grids, clearly showing the first four electron oxidation at $E_{1/2} = 905$ mV ($\Delta E_p \sim 194$ mV), and the first three one electron oxidations, at potentials of $E_{1/2} = 1235$ mV ($\Delta E_p \sim 72$ mV), $E_{1/2} = 1397$ mV ($\Delta E_p \sim 84$ mV) and $E_{1/2} = 1597$ mV($\Delta E_p \sim 90$ mV). The differential pulse voltammogram for the compound (Figure 3.17) clearly shows all of the expected oxidations for a $Mn(II)_9$ grid, with the last one electron oxidation occurring $E_{1/2} = 1773$ mV.

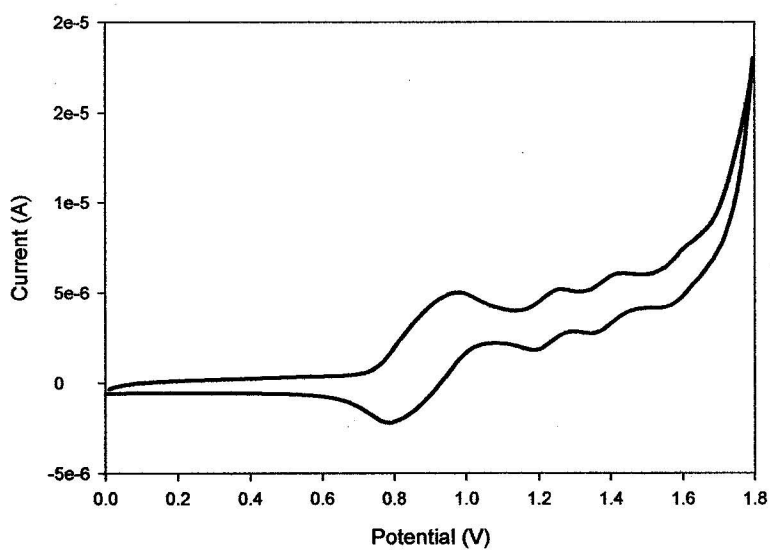

Figure 3.16: Cyclic voltammogram for **3.5** (graphite, CH_3CN, TEAP, vs. Ag/AgCl, using a 20 mV/s scan rate).

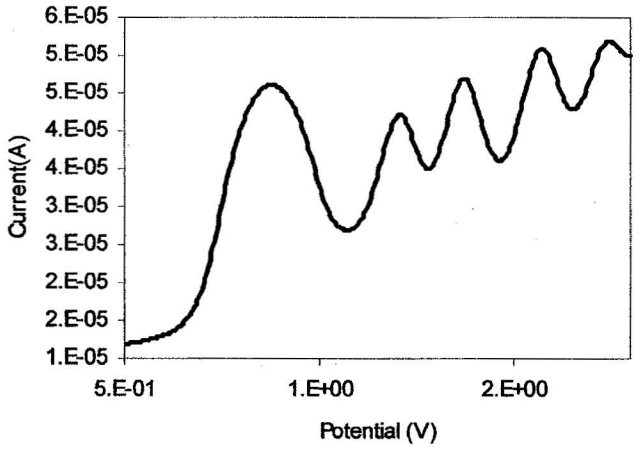

Figure 3.17: Differential pulse voltammogram for **3.5** (graphite, CH_3CN, TEAP, vs. Ag/AgCl, using a 20 mV/s scan rate, 50 mV pulse amplitude, 3 ms pulse width).

All of the oxidations in **3.5** occur at higher potentials than in **3.1**. The only significant difference between the two compounds is that **3.5** possesses terminal pyrazine rings instead of the pyridine rings in **3.1,** so it is reasonable to assume that the increase in oxidation potentials is associated with the change in substituents. Substituent effects have been noticed in other $Mn(II)_9$ grids, generally associated with the functional group on the 4-position of the central pyridine ring [66]. It was observed that the half-wave potentials of all five peaks increased as the functional group was changed, in the order OMe < Cl < H. Compound **3.1**, with an SEt functional group, falls in between Cl and H. Additionally, studies of [3x3] $Mn(II)_9$ grids with SMe2POAP show the characteristic electrochemical profile of a $Mn(II)_9$ grid, with half wave potentials very similar to those of **3.1** [90]. The electronics of these systems are obviously extremely sensitive to

substituent effects on the ligand backbone, which provides an opportunity to fine-tune the electrochemical properties of the grid.

3.4: Summary:

Several new [3x3] $Mn(II)_9$ grids with different ligand functional groups have been presented. The grid molecules all possess a $[Mn_9(\mu\text{-}O_{12})]$ core, where adjacent Mn(II) cations are bridged by ligand hydrazone oxygen atoms. In all cases, the Mn-N bond distances range from 2.129-2.300 Å, the Mn-O distances range from 2.126-2.341 Å, the Mn-Mn distances range from 3.885-4.070 Å, and the Mn-O-Mn angles range from 125.6-130.0°. While the ligand functional groups do not appear to have a large effect on the core of the molecule with respect to the Mn(II) coordination environments, there are structural differences between these compounds. The most important of these is the distortion of **3.4** from an approximately square grid, to a diamond or rhombus with diagonal distances of 9.800 and 12.110 Å. This effect appears to be due to steric crowding, or to additional π- π interaction associated with the ligand phenyl groups.

The functional groups also affect the packing in the crystal. In most [3x3] $Mn(II)_9$ grids, the intermolecular interactions are dominated by π-stacking of the grids at the corners of the molecule via the terminal pyridine rings of the ligand. The introduction of a Lewis basic functional group, e. g. Cl, creates a new series of intermolecular interactions including H-bonding and Cl···Cl interactions in the case of the Cl2POMP grid, and S···N interactions in the case of the SEt2POAP grid. These new interactions completely supersede π-stacking in the unit cells of the compounds.

Because the coordination environments of the Mn(II) centers and the Mn-Mn distances and Mn-O-Mn angles are relatively constant for [3x3] $Mn(II)_9$ grids, the overlap of the magnetic orbitals is equivalent, and the magnetic properties do not vary significantly between compounds with different functional groups.

The electrochemical properties of the $Mn(II)_9$ grids are remarkably sensitive to substituent effects. The Schiff-base ligand complexes **3.3** and **3.4**, which do not possess hydrazone NH_2 groups, have completely lost the characteristic electrochemical profile of the $Mn(II)_9$ grids. Instead of the usual quasi-reversible four electron oxidation at approximately 700 mV, a poorly reversible oxidation is observed at approximately 1.2 V. In the case of **3.3**, one other wave is discernable at higher potential, while in the case of **3.4**, no other oxidations are observed. This contrasts sharply with the four one electron oxidations generally observed within the range of 900-1500 mV in typical $Mn(II)_9$ grids. The amidrazone-based ligands, unlike the Schiff based ligands, have enhanced tautomeric delocalization due to the presence of the NH_2 groups. The additional delocalization may enhance communication between the Mn(II) sites, leading to the appearance of these four distinct waves.

Replacing the terminal pyridine rings with pyrazine also has a dramatic effect on the electrochemistry. The difference in half wave potentials for all five oxidations in compounds **3.1** and **3.5** is greater than 200 mV. As both compounds have ethyl thioether functional groups on the 4-position of the central pyridine ring, the effect can only be due to the pyrazine groups. Substituent effects due to the functional group on the central pyridine ring had been observed previously. Half wave potentials for all oxidations

increase as a function of substituent in the order OMe<Cl<SEt ≈ SMe<H. These substituent differences provide an opportunity to tune the oxidation potentials of the $Mn(II)_9$ grids, without significantly affecting their structural or magnetic properties, and could be very valuable in a device development context.

Chapter 4: Octanuclear Cu(II) pinwheel clusters: Structural and magnetic properties

4.1: Preamble:

When linear tritopic 2POAP type ligands are reacted with transition metal cations, the outcome is generally a nonanuclear [3x3] M_9 grid, comprised of six ligands, which are arranged in two groups of three parallel ligands. When Cu(II) is used, the situation becomes more complicated, as a variety of structural isomers are obtainable, which are a function of the Cu(II) salt and the reaction conditions. For instance, if a strongly binding counter anion, i.e. acetate, or a coordinating solvent i.e. DMSO is used, the product of the reaction is generally a heteroleptic trinuclear complex or trinuclear based chain molecular assembly. In the chain compounds, the coordination sphere of the metal cation is partially filled by solvent molecules or anions [91-93]. When the reaction is carried out using a less strongly coordinating anion in heated polar solvents, the usual outcome is a homoleptic [3x3] Cu_9 grid compound [54, 94]. Finally, when the reaction is carried out under mild conditions, for example with aprotic polar solvents like acetonitrile and only gentle warming, the product is a heteroleptic octanuclear pinwheel complex [28, 54, 63]. In several cases it is possible to convert amidrazone-based pinwheel complexes to grids by heating them in more polar solvents. This suggests that the pinwheel is the kinetic product of the reaction of Cu(II) with 2POAP type ligands, while the grid is the thermodynamic product. The complexes discussed in this chapter are all prepared using Schiff base ligands (Figure 1a, R = CH_3, Ph), which seem to form pinwheels preferentially even under forcing conditions, in contrast to those prepared from

amidrazone-based ligands. This is likely due to steric restrictions resulting from a bulkier group replacing the amine groups present in 2POAP.

The ligand coordination pocket arrangement provides a contiguous connection between metal ion centers in one of two binding modes as depicted in Figure 4.1.

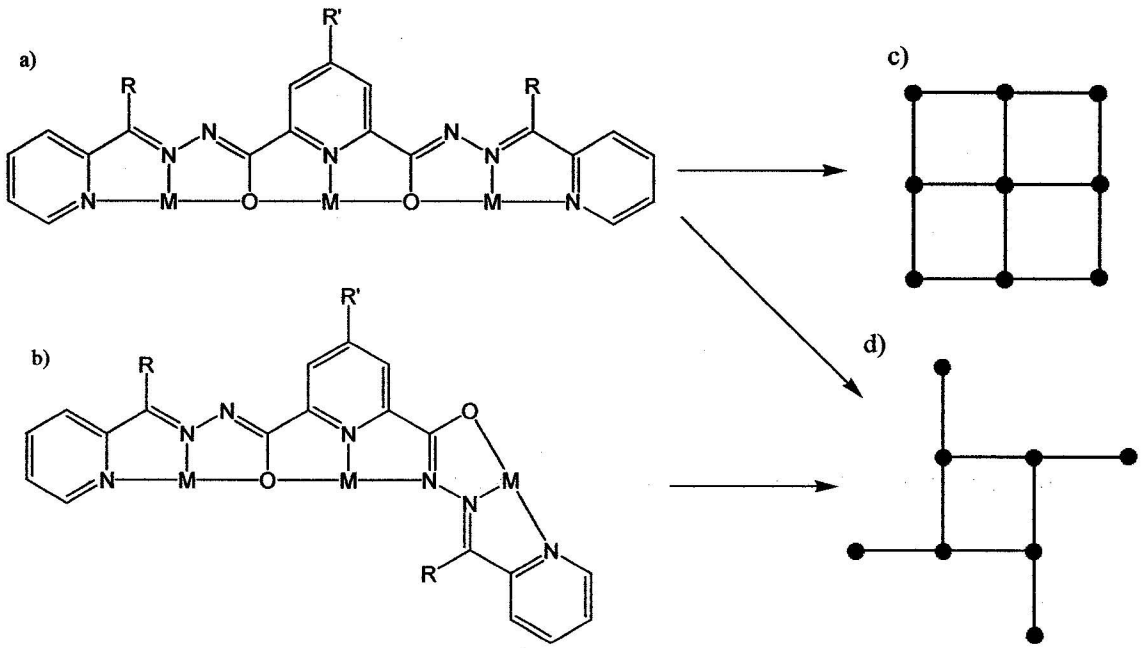

Figure 4.1: Binding modes of 2POAP derivatives.

The [3x3] grid complexes (c) adopt mode (a) only, while the pinwheel complexes (d) can adopt mode (a) or (b). The pinwheel complexes are comprised of four tritopic ligands, intersecting at the square Cu_4 central core, with the remaining four Cu(II) cations located on the arms of the pinwheel bound to the other ends of the ligands [28, 54]. The bridging to these peripheral Cu(II) centers depends on the binding mode of the ligand. With mode (a), the adjacent metal cations are bridged by hydrazone oxygen atoms. In mode (b) one end of the ligand is rotated around the single C-C bond to the central

pyridine ring, which leads to the diazine moieties forming bridges from the central metal cations to the outer cations. All examples studied so far have exhibited intramolecular ferromagnetic exchange, with nominally S = 8/2 ground states [28, 54, 63]. Examples of complexes with each ligand binding mode will be discussed.

Pinwheels are of important additional interest because they are heteroleptic clusters, which possess labile co-ligands. Replacement of these labile co-ligands with potential bridging groups provides a possible pathway to join the ferromagnetic subunits into larger networks. Large networks consisting of ferromagnetic molecular based subunits, may function as nano-meter scale magnets for possible use in high density data storage media. Attempts to make nano-scale magnets have been largely limited to the so-called single molecule magnets [95-100], or relatively simple extended inorganic structures, which make use of ligands like CN^- or $N(CN)_2^-$ to act as magnetic bridges between metal cations [101-103]. The former approach with mixed oxidation state manganese clusters has so far been limited by extremely low blocking temperatures, while in the latter cases with extended 2D and 3D systems T_c temperatures have been reported as high as room temperature and above. The specific linking of ferromagnetic subunits has been largely ignored, perhaps because of the paucity of suitable magnetic subunits, but also because the creation of suitable intermolecular interactions is not a trivial task. Several of the compounds discussed in this chapter display long range ordering in the crystal lattice, generally resulting from intermolecular interactions between ligand functional groups, or between these functional groups and anions. In some cases these interactions lead to long range magnetic cooperativity.

4.2: Experimental:

4.2.1: Complex synthesis:

4.2.1.1: $[(Cl2POMP)_4Cu_8(NO_3)_8](H_2O)_{15}$ (4.1)

$Cu(NO_3)_2 \cdot 3H_2O$ (0.21 g, 0.87 mmol) was dissolved in methanol (~15 mL). Cl2POMP (0.1 g, 0.21 mmol) was added, forming a clear green solution, which was heated for approximately 5 minutes. A green precipitate formed and water (~10 mL) was added to the mixture. The precipitate redissolved, leaving a clear green solution, which was filtered and left to stand at room temperature. Green rectangular prism shaped crystals (140 mg, 83 %) formed over several days, which were suitable for structural analysis. Elemental Analysis: Found (%): C, 33.55; H, 2.87; N, 16.72. Calc. (%) for $[(C_{21}H_{16}N_7O_2Cl)_4Cu_8(NO_3)_8](H_2O)_{15}$: C, 33.52; H, 3.15; N, 16.75;

4.2.1.2: $[(Cl2POMP)_4Cu_8(H_2O)_8](ClO_4)_8(H_2O)_7$ (4.2)

$Cu(ClO_4)_2 \cdot 6H_2O$ (0.17 g, 0.46 mmol) was dissolved in methanol (~10 mL). Cl2POMP (0.10 g, 0.21mmol) and water (~10 mL) were added yielding a clear green solution which was heated for approximately 15 minutes, then filtered and left to stand at room temperature. Green rectangular prism crystals (not suitable for structural analysis) formed after several days (90 mg, 81 %). Selected IR data (cm^{-1}, Nujol): 1097(v ClO_4). Elemental analysis: Found (%): C, 30.40; H, 2.63; N, 12.09. Calc. (%) for $[(C_{21}H_{16}N_7O_2)_4Cu_8(H_2O)_8](ClO_4)_8(H_2O)_7$: C, 30.48; H, 2.86; N, 11.85.

4.2.1.3: $[(Cl2POMP)_4Cu_8(N(CN)_2)_8](H_2O)_9(CH_3CN)_2$ (4.3)

$[(Cl2POMP)_4Cu_8(NO_3)_8](H_2O)_{15}$ (4.1) (0.20g, 0.07 mmol) was dissolved in hot water (~25 mL), and $Na(N(CN)_2)$ (0.06g, 0.7 mmol) was added to the resulting solution.

A green precipitate formed immediately, which was isolated and redissolved in 2:1 acetonitrile/water (~ 60 mL), and filtered. A green microcrystalline precipitate (80 mg, 43 %) formed after several days. The reaction was repeated in an H-tube. Crystals suitable for structural determination formed over two weeks. The products were identical, based on infrared spectra and magnetic properties. Selected IR data (Nujol, cm^{-1}): 2297, 2262, 2232, 2170, 2153 (ν $N(CN)_2$). Elemental analysis: Found (%): C, 41.54; H, 2.35; N, 24.75. Calc. (%) for $[(C_{21}H_{16}N_7O_2Cl)_4Cu_8(N(CN)_2)_8](H_2O)_9(CH_3CN)_2$: C, 41.41; H, 2.94; N, 25.08.

4.2.1.4: $[(2POPP)_4Cu_8(H_2O)_8](ClO_4)_8(H_2O)_{10}$ **(4.4)**

2POPP (0.10g, 0.2mmol) was added to a solution of $Cu(ClO_4)_2 \cdot 6H_2O$ (0.26g, 3.7 mmol) in acetonitrile (~10 mL). The resulting brown solution gradually turned green over 30 mins, and absolute ethanol (~ 10 mL) was added to the reaction flask. The solution was filtered and allowed to stand. Dark green crystals (140mg, 75 %), not suitable for X-ray diffraction, formed over several weeks. Selected IR data (Nujol, cm^{-1}): 1083 (υ ClO_4). Elemental Analysis: Found (%): C, 40.05; H, 2.84; N, 10.56. Calc. (%) for $[(C_{31}H_{21}N_7O_2)_4Cu_8(H_2O)_8](ClO_4)_8(H_2O)_{10}$: C, 40.01; H, 3.25; N, 10.54.

4.2.1.5: $[(SEt2POMP)_4Cu_8(H_2O)_8](PF_6)_8(CH_3OH)_6(CH_3CN)_{1.5}$ **(4.5)**

SEt2POMP (0.10g, 0.21mmol) was dissolved in a solution of $Cu(CF_3SO_3)_2$ (0.21g, 0.58mmol) in 2:1 methanol/acetonitrile (~15 mL) and heated for 15 minutes, whereupon NH_4PF_6 (0.19g, 1.2 mmol) was added. Heating was continued for a further 15 minutes and the solution was filtered and cooled. Green crystals and powder (90 mg, 47 %) formed over one week. The filtrate was conserved and more green crystals,

suitable for structural determination, formed over several weeks (combined yield 140 mg, 74 %). Elemental analysis: Found (%): C, 31.01; H, 2.50; N, 10.53. Calc. (%) for $[(C_{23}H_{19}N_7O_2S)_4Cu_8(H_2O)_8](PF_6)_8\,(CH_3OH)_6(CH_3CN)_{1.5}$: C, 31.15; H, 3.11; N, 10.61.

4.2.1.6: $[(SEt2POMP)_4Cu_8(H_2O)_8](ClO_4)_8(H_2O)_{11}$ (**4.6**)

SEt2POMP (0.10g, 0.21mmol) was added to a solution of $Cu(ClO_4)_2{\cdot}6H_2O$ (0.24g, 0.65mmol) in 1:1 methanol/acetonitrile (~15 mL). The mixture was heated for 30 minutes, over which time the ligand dissolved to yield a clear green solution, which was filtered and allowed to cool. Green crystals (90mg, 50 %) formed over several days. Selected IR data (cm^{-1}, Nujol): 1076 (υ ClO_4). Elemental analysis: Found (%): C, 31.71; H, 3.30; N, 11.39. Calc. (%) for $[(C_{23}H_{19}N_7O_2S)_4Cu_8](ClO_4)_8(H_2O)_{19}$: C, 31.71; H, 3.53; N, 11.26.

4.2.2: Crystallography:

The diffraction intensities of a green prismatic crystal of **4.1** (0.29 x 0.09 x 0.08 mm) were collected using graphite monochromatized Mo-Kα radiation on a Bruker P4/CCD diffractometer at -80 °C to a maximum 2θ value of 52.8°. The data were corrected for Lorentz and polarization effects. The structure was solved by direct methods [72, 73]. The non-H atoms were refined anisotropically. Hydrogen atoms on aromatic carbons and methyl groups were placed in calculated positions with thermal parameters set twenty percent greater than those of their bonding partners at time of their inclusion, while hydrogen atoms on water molecules were found and fixed to groups. Hydrogen atoms were not refined. Neutral atom scattering factors [74], and anomalous dispersion terms [75, 76] were taken from the usual sources. All calculations were

performed using the teXsan [77] crystallographic software package of the Molecular Structure Corporation except for refinement, which was performed using SHELXL-97 [72a].

A green prismatic crystal of **4.3** with dimensions of 0.8 x 0.2 x 0.15 mm was treated similarly. The model contains a partial occupancy disordered acetonitrile as lattice solvent which was refined isotropically. The corresponding nitrogen and carbon atoms were modeled as a partial occupancy nitrogen atom with the occupancy adjusted to reflect contributions from nitrogen and carbon. The hydrogen atoms of the acetonitrile were not included in the model, thus there are a total of six hydrogen atoms missing from the expanded structure.

A green prismatic crystal of **4.5** with dimensions 0.52 x 0.34x 0.18 mm was treated similarly to **4.1** and **4.3**, except the structure was solved using a Patterson orientation/translation search [104]. There are 4.5 hydrogen atoms missing from the lattice water and methanol molecules. Crystal data for **4.1**, **4.3**, and **4.5** are collected in Table 4.1.

4.3: Results and Discussion:

4.3.1: Description of crystal structures:

.4.3.1.1: $[(Cl2POMP)_4Cu_8(NO_3)_8](H_2O)_{15}$ (4.1)

The main cation is illustrated in Figure 4.2a, while an abbreviated structure showing only the coordinating atoms is included as Figure 4.2b. The individual pinwheels have a $[Cu_4\text{-}(\mu\text{-}O)_4]$ central core, where each pseudo-octahedral (N_4O_2) Cu(II) ion is bound to one end pocket and one central pocket of Cl2POMP. This central core is

very similar to the tetranuclear compounds produced using POAP and similar ditopic ligands [91]. The peripheral Cu(II) centers have square pyramidal geometries and are bonded to the other ends of the ligands by three donor atoms (N_2O). The other coordination sites are filled by nitrate anions. Within the tetranuclear core, adjacent Cu(II) centers are bridged by hydrazone oxygen atoms with Cu-O bond distances ranging from 1.993-2.340 Å and Cu-O-Cu angles of 139.1°. The Cu(II) centers lie 4.014 Å apart. Selected bond lengths and angles for the complex are listed in Table 4.2.

Table 4.1: Summary of Crystallographic data for **4.1**, **4.3**, **4.5**.

Compound	**4.1**	**4.3**	**4.5**
Empirical Formula	$C_{84}H_{88}N_{36}O_{44}Cl_4Cu_8$	$C_{104}H_{70}N_{54}O_8Cl_4Cu_8$	$C_{92.50}H_{106}O_{18.50}F_{48}S_4N_{28}Cu_8P_8$
M/gmol^{-1}	2956.01	2854.23	3702.35
Crystal System	tetragonal	Tetragonal	monoclinic
Space Group	I-4 (#82)	I-4 (#82)	C2/c (#15)
a/Å	21.2562(8)	20.8401(5)	36.251(5)
b/Å			13.134(2)
c/Å	12.7583(9)	13.1228(6)	35.387(5)
β/°			95.168(3)
V/ Å^3	5764.5(4)	5699.4(3)	16779(4)
ρ_{calcd}/gcm^{-3}	1.703	1.663	1.465
T/K	-80(1)	-80(1)	-80(1)
R1	0.055	0.029	0.096
wR2	0.1374	0.0772	0.3060

Both the square pyramidal and axially elongated octahedral Cu(II) centers have a $d_{x^2-y^2}$ ground state, with the unpaired electron residing in the short equatorial orbitals. The bridging connections within the core are long-short, and orbitally orthogonal, thus one would not expect to observe antiferromagnetic exchange within the core, despite the large Cu-O-Cu bridging angles. The ligand adopts binding mode (a) (Figure 4.1), so the

peripheral Cu(II) centers are bridged to the tetranuclear core by hydrazone oxygen atoms. The Cu-O bond lengths range from 2.003-2.213 Å, with Cu-O-Cu angles of 139.4°. The Cu-Cu distance between the core and peripheral Cu(II) centers is 4.074 Å. These bridging connections are also short-long and strictly orbitally orthogonal, so once again antiferrromagnetic exchange would not be expected to occur.

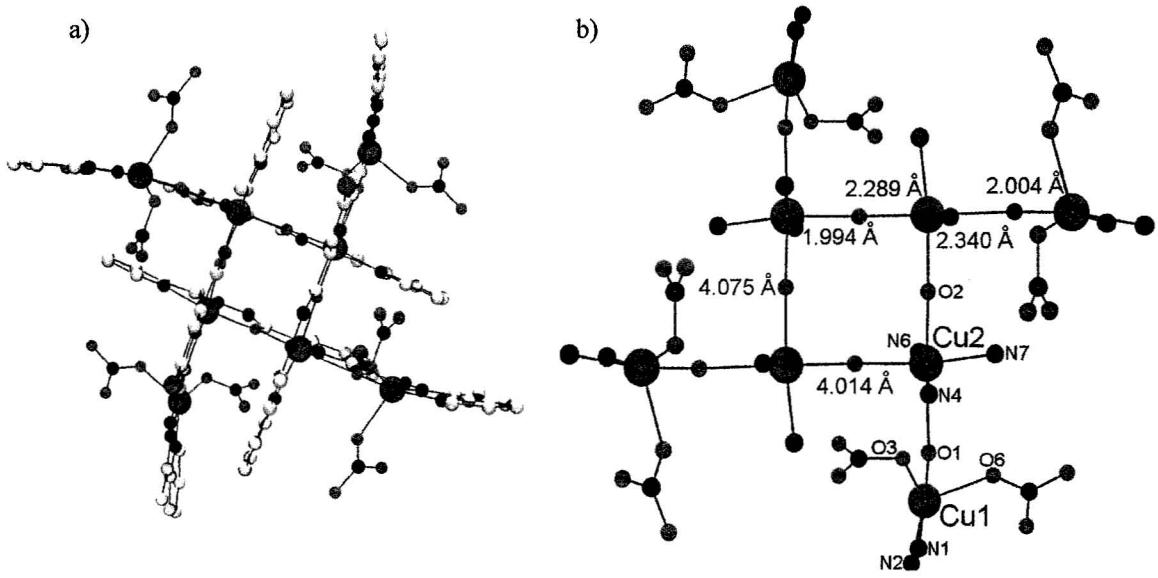

Figure 4.2: a) POV-RAY representation of the main cation in **4.1**. Magenta spheres represent Cu(II). Grey = carbon, blue = nitrogen, red = oxygen, green = chlorine. H atoms are omitted. b) Simplified structure showing bridging connections. Cu-Cu distances are highlighted in green.

There is a curvature of the ligand molecules in the structure which appears to be due to a hydrogen bonding interaction between a nitrate oxygen atom and an aromatic hydrogen atom on the terminal pyridine ring of the ligand. The O···H distance is 2.446 Å,

with an O···H-C angle of 150.33°. These values are reasonable for a hydrogen bond of moderate strength [1, 105]. The distortion of the ligand leads to a Cl-Cl separation of 9.019 Å, compared with 5.541 Å in **4.3** (*vide infra*) as the central pyridine rings bend away from each other. This type of ligand distortion has not been observed in other pinwheel compounds [28, 54, 63].

Table 4.2: Selected bond distances (Å) and angles (°) for **4.1**.

Cu2-N6	1.933(5)	Cu2-Cu2	4.015
Cu2-O2	1.993(4)	Cu1-Cu2	4.074
Cu2-N7	2.015(5)		
Cu2-N4	2.036(5)	O4-H16$_{ar}$	2.446, 150.33
Cu2-O2	2.289(4)		
Cu2-O1	2.340(4)	Cl3-Cl3	9.019
Cu1-N2	1.941(6)		
Cu1-O6	2.213(5)	Cl3-O3	3.417
Cu1-O1	2.003(5)	Cl3-O5	3.262
Cu1-N1	2.008(6)		
Cu1-O3	2.021(5)	Cl3-O8	3.265
		π-π	3.413-3.596
Cu2-O2-Cu2	139.1(2)	O6-H5$_{me}$	2.496, 143.00
Cu1-O1-Cu2	139.4(2)		

The unit cell of **4.1** is pictured in Figure 4.3. Long range ordering is apparent through vertical (z-axis) stacking of the molecules, as well as a diagonal interaction from the corners of the molecule. The vertical stacking (Figure 4.4) is dominated by electrostatic interactions between the Cl functional groups of the ligand and the oxygen atoms of the coordinated nitrate anions. There are two such contacts between each pair of molecules, with distances of 3.262 and 3.417 Å respectively, leading to a vertical chain. The van der Waals radii of Cl and O are 1.75 Å and 1.52 Å, respectively [84], so these distances are not unreasonable for a moderate or weak interaction.

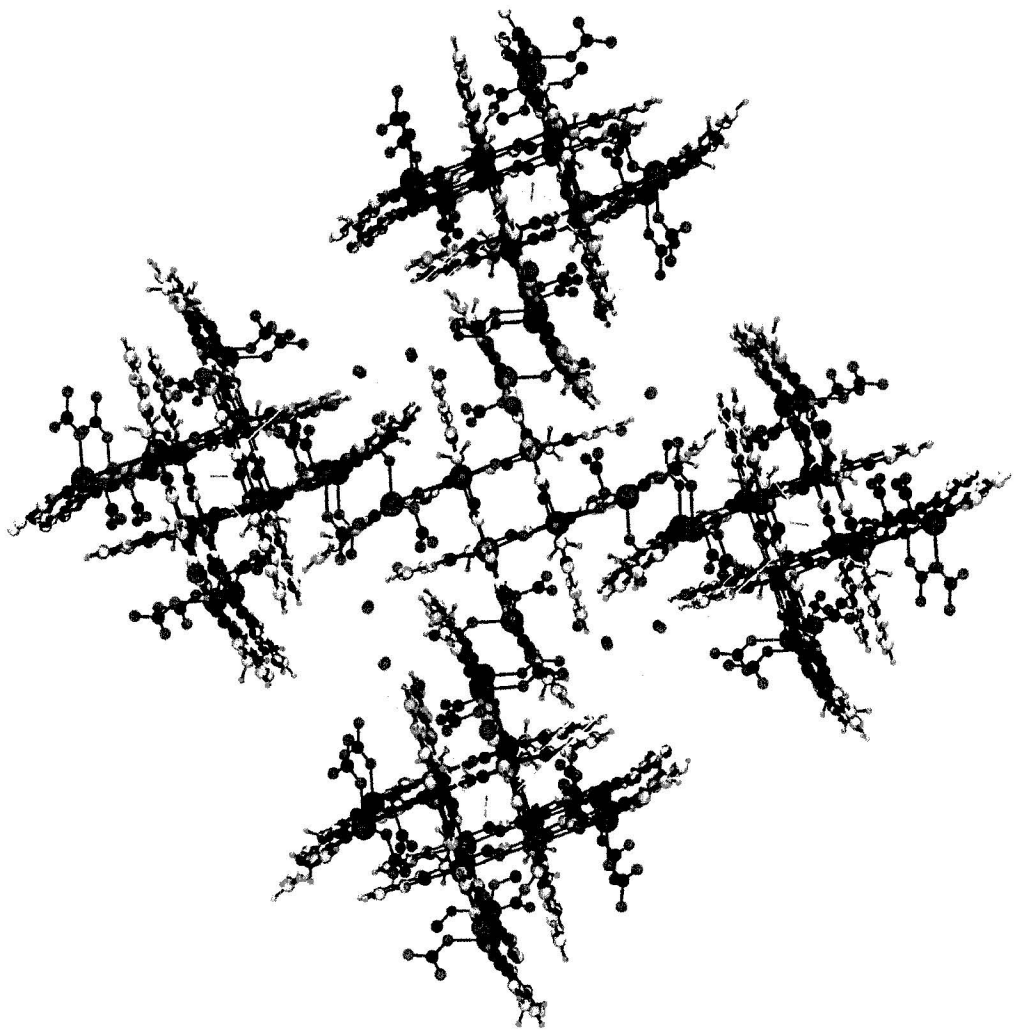

Figure 4.3: POV-RAY depiction of the unit cell of **4.1**.

The diagonal ordering (Figure 4.5 a, b) is more complicated, as several intermolecular interactions contribute. First, there is a relatively short $Cl^{\cdots}O_{nitrate}$ contact with a distance of 3.265 Å. This is comparable to the vertical stacking contacts and likely represents a medium strength interaction. There are also π-π contacts between a terminal pyridine ring of one pinwheel and a central pyridine ring of the pinwheel diagonally

above it. The shortest distance is 3.413 Å, between the N1 of the terminal pyridine ring, and C10 of the central pyridine ring. Other close contact distances range from 3.467-3.596 Å. These are relatively short π-π contacts, and are comparable to those observed in complexes of many 2POAP type ligands [55, 63, 109]. Finally, there is a hydrogen bonding interaction between a nitrate oxygen atom and a methyl hydrogen atom of the pinwheel diagonally above it. The distance is 2.496 Å, and the O···H-C angle is 143.00° which is reasonable for moderate to weak interactions.

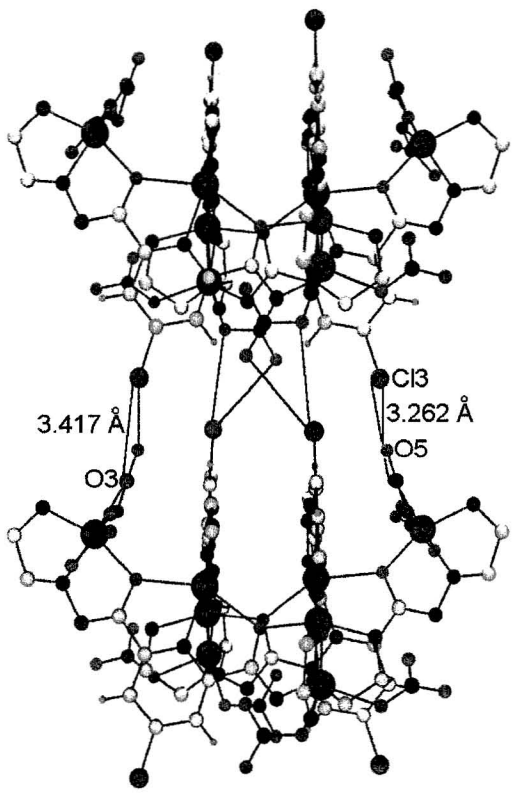

Figure 4.4: POV-RAY depiction of the vertical stacking in **4.1.** Terminal rings removed for clarity.

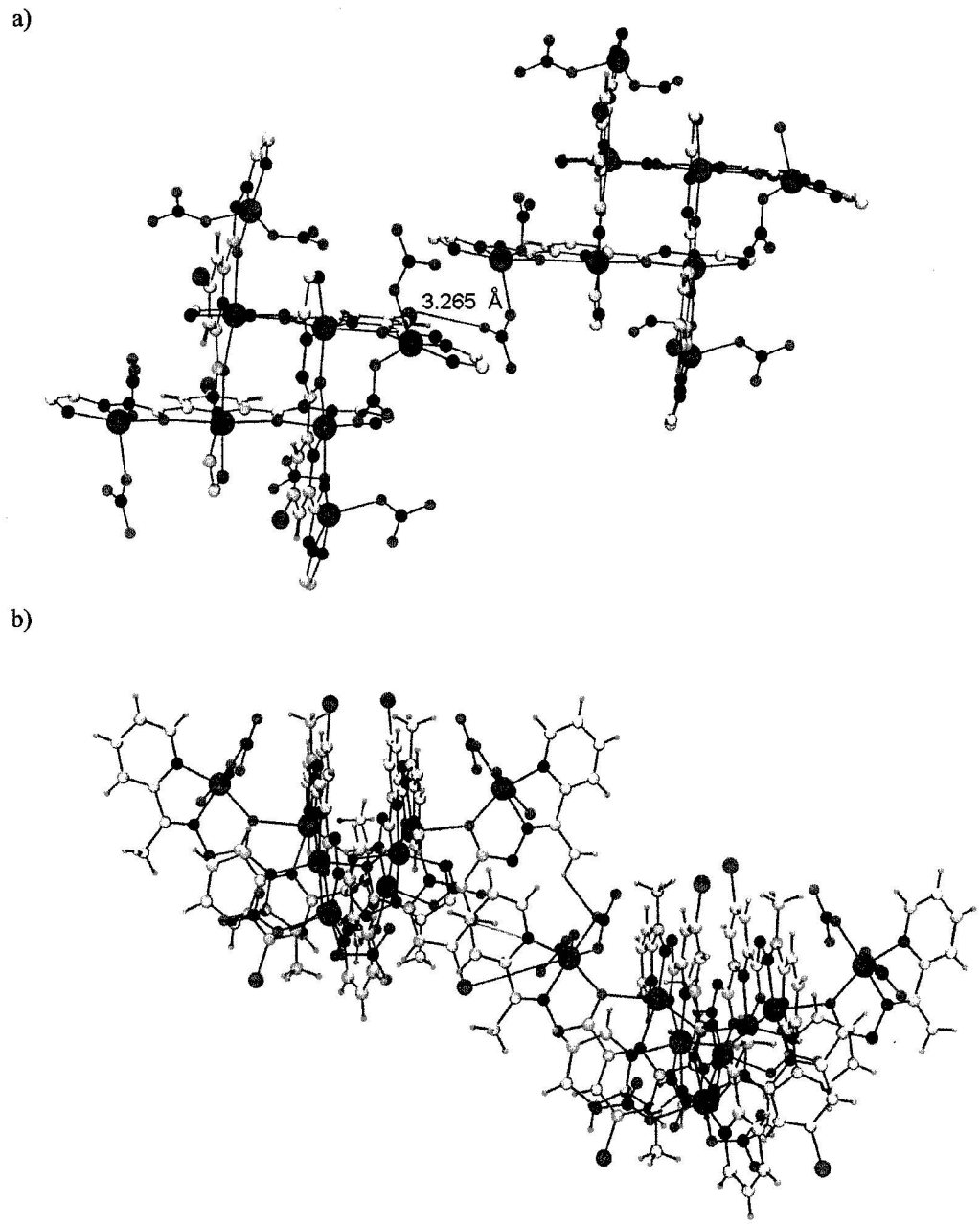

Figure 4.5: a) POV-RAY depiction of the diagonal stacking interactions of **4.1**. Cl-O contact, top view. b) POV-RAY depiction of the diagonal stacking interactions of **1**. Cl-O (green), H-bonding (purple), and π- stacking (orange) interactions side view.

4.3.1.2: $[(Cl2POMP)_4Cu_8(N(CN)_2)_8](H_2O)_9(CH_3CN)$ **(4.3)**

The structure of **4.3** consists of an octanuclear pinwheel similar to that of **4.1**, Figure 4.6a. A structural representation showing just the immediate donor atoms is illustrated in Figure 4.6b. The tetranuclear $[Cu_4\text{-}(\mu\text{-}O)_4]$ core has Cu-O bond distances ranging from 1.944-2.308 Å and Cu-O-Cu angles of 137.96°. The Cu-O connections are all short-long and strictly orthogonal, as is the case with **4.1**. Selected bond lengths and angles are listed in Table 4.3. Like **4.1**, all the Cu centers are bridged by hydrazone oxygen atoms. The Cu-O lengths are 2.005 Å and 2.309 Å, with a Cu-O-Cu angle of 137.5° indicating that the connections between the peripheral and core Cu centers are all short-long and strictly orthogonal. The peripheral Cu centers have the same N_2O ligand coordination environment as in **4.1**, but the two additional sites are filled by nitrogen atoms from dicyanamide ($N(CN)_2^-$; dca) anions. The Cu-N bond distances to the dicyanamide ions are 1.946 Å and 2.125 Å. Cu-Cu distances within the core and between the core and the peripheral centers are similar, with average lengths of 4.009 Å and 4.022 Å respectively. The hydrogen bonding between the anions and ligands observed in **4.1** is absent in **4.3**, and as a result the ligands are planar, and the Cl-Cl distances are 5.541 Å, which is typical of compounds in this class.

The unit cell of **4.3** is shown in Figure 4.7. It consists of four stacks of pinwheel molecules, slightly staggered to accommodate the dca arms. The channels between the stacks are filled with acetonitrile molecules, which have been removed from the image for clarity. The stacking appears to result from short contacts (3.372 Å) between the central dca N (N9) and chlorine atoms (Cl1) on adjacent pinwheels (Figure 4.7b). There

are four such contacts between each pair of pinwheels, leading to the stacked arrangement. There are no direct bonding contacts between molecules but the Cl-N contacts are considered significant. Interactions between N and Cl atoms are well known and in the absence of H-bonds generally lie in the range of 3.0-3.6 Å [106-108]. The interactions in **4.3** are then moderate to strong and it is reasonable to assume that they are responsible for the long range ordering in this compound.

Table 4.3: Selected bond distances (Å) and angles (°) for **4.3**.

Cu2-N6	1.936(2)	Cu2-Cu2	4.009
Cu2-O2	1.9955(18)	Cu1-Cu2	4.022
Cu2-N7	2.016(2)		
Cu2-N4	2.020(2)	Cl1-Cl1	5.541
Cu2-O2	2.2985(18)		
Cu2-O1	2.3088(19)	Cl1-N9	3.373
Cu1-N2	1.937(3)		
Cu1-N8	1.947(3)		
Cu1-O1	2.005(2)	Cu2-O2-Cu2	137.95(10)
Cu1-N1	2.021(2)	Cu1-O1-Cu2	137.49(10)
Cu1-N11	2.123(3)		

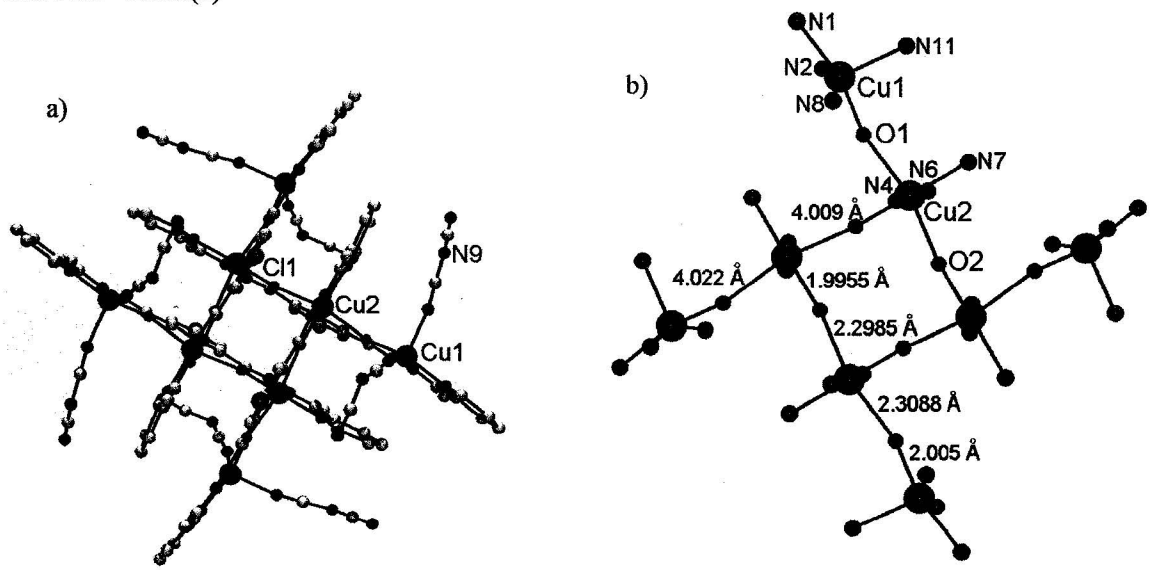

Figure 4.6: POV-RAY depiction of **4.3**. a) Main cation; Cu = magenta, N = blue, O = red, Cl = green, C = grey. b) Simplified structure showing coordinated atoms.

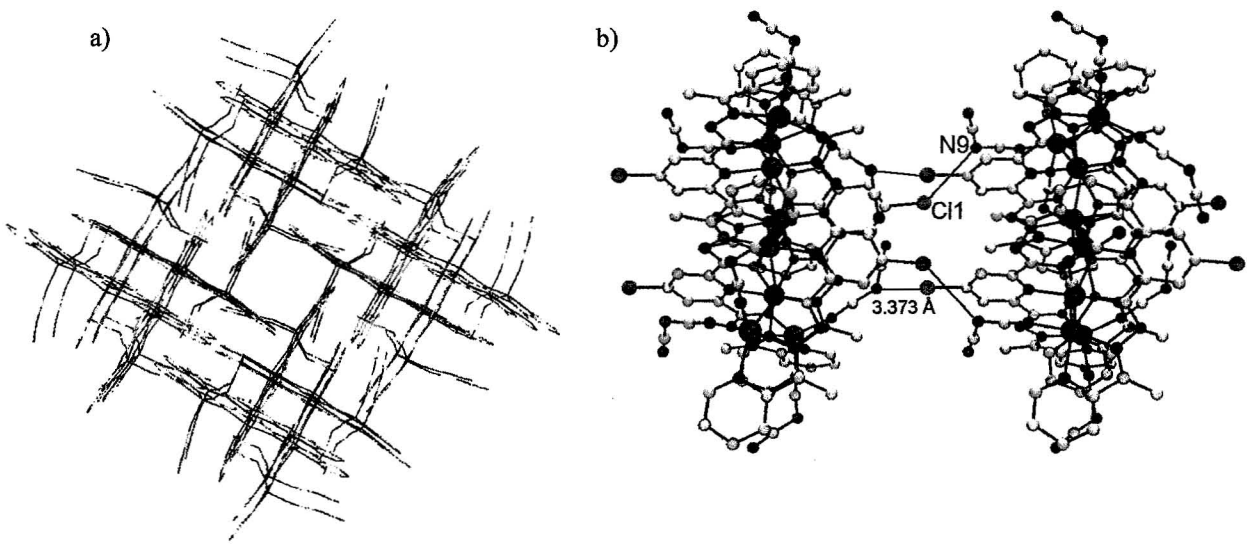

Figure 4.7: a) POV-RAY rod diagram of the unit cell of **4.3**. b) Cl-N interaction between stacked pinwheels.

4.3.1.3: $[(SEt2POMP)_4Cu_8(H_2O)_8](PF_6)_8(CH_3OH)_6(CH_3CN)_{1.5}$ (**4.5**)

The main cation of **4.5** is illustrated in Figure 4.8a. An abbreviated structure highlighting the donor atoms and bridging atoms is shown in Figure 4.8b. **4.5** has the $[Cu_4\text{-}(\mu\text{-}O)_4]$ core, typical of the pinwheel systems as a whole. Cu-O bond lengths fall in the range 2.102-2.327 Å, with Cu-O-Cu angles in the range 139.88-140.53°. The Cu-O connections within the core are again short-long and strictly orthogonal. Relevant bond distances and angles are listed in Table 4.4.

The peripheral bridge connection to the outer copper centers is a diazine group as

opposed to the hydrazone oxygen atoms found in **4.1** and **4.3**. The Cu-$N_{diazine}$ bond distances lie between 1.920 and 2.490 Å, the latter of which is extremely long. This leads to Cu-Cu distances of 4.072 Å and 4.104 Å within the core.

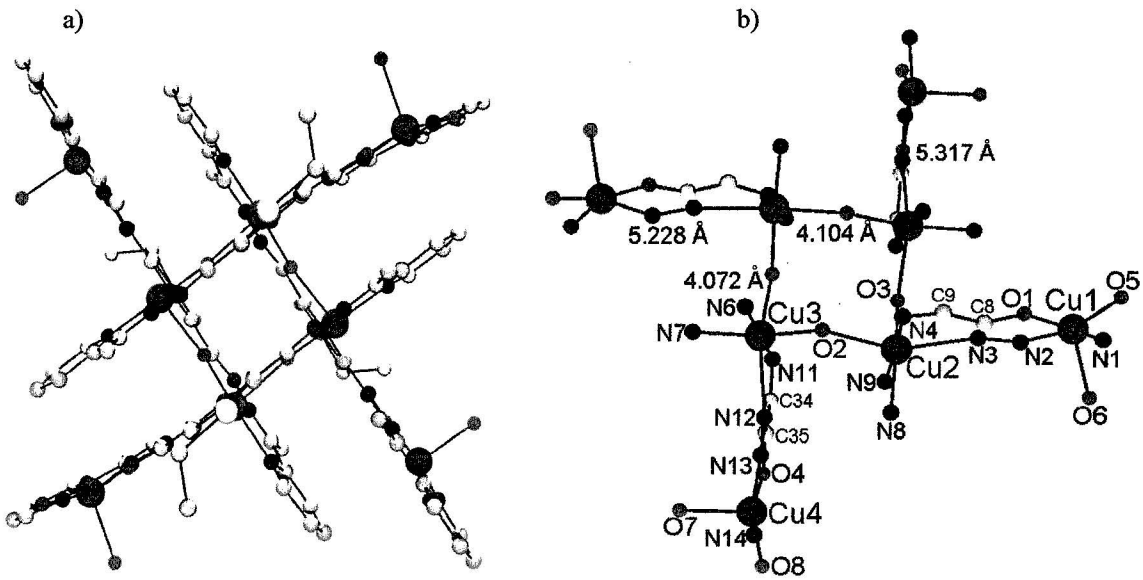

Figure 4.8: a) POV-RAY depiction of **4.5** (H atoms removed); Cu = magenta, N = blue, O = red, C = grey, S = yellow. b) Non-coordinating (non-bridging) atoms removed.

The Cu-N-N-Cu torsion angles are 173.0° and 161.3°, but the connections are short-long, and thus orbitally orthogonal, so any significant antiferromagnetic exchange across the diazine bridge would not be expected. There is a secondary four bond non-orthogonal ligand bridge (OCCN) linking the core and peripheral Cu centers via a non-bridging hydrazone oxygen atom of the ligand, which is bonded to the peripheral copper centers. This bridge is quite long, but the connections between the Cu centers are short-

short (equatorial-equatorial) and it is thus possible for a weak, long range antiferromagnetic effect to be observed via this bridge.

Table 4.4: Selected bond distances (Å) and angles (°) for **4.5**.

Cu1-N2	1.920(6)	Cu2-O3-Cu3	140.5(2)
Cu1-O5	1.930(8)	Cu3-O2-Cu2	139.9(2)
Cu1-O1	1.961(5)		
Cu1-N1	2.004(7)	Cu2-N3-N2-Cu1	161.3
Cu1-O6	2.154(11)	Cu3-N12-N13-Cu4	173.0
Cu2-N9	1.934(5)		
Cu2-N4	2.011(5)	Cu3_2-Cu2	4.104
Cu2-O3	2.032(4)	Cu2-Cu3	4.072
Cu2-N8	2.036(6)	Cu2-Cu1	5.288
Cu2-O2	2.322(4)	Cu3-Cu4_2	5.317
Cu2-N3	2.477(6)		
Cu3-N6	1.943(5)	S1-S1_1	5.181
Cu3-N11	1.999(5)	S2-S2_2	5.580
Cu3-O2	2.011(4)		
Cu3-N7	2.029(6)	S1_2-S2	3.839
Cu3-O3	2.327(4)	S1-S2	3.776
Cu3-N12	2.490(6)		
Cu4-O8	1.923(7)		
Cu4-N13	1.927(6)		
Cu4-O4	1.966(5)		
Cu4-N14	2.008(7)		
Cu4-O7	2.220(9)		

An extended structure of **4.5** (Figure 4.9) also shows that there is long range ordering between pinwheel subunits, but this time through S-S interactions (Figure 4.10). The distances between the stacks are too long (> 6 Å) for there to be any significant interaction between them, but within each stack the pinwheels are held in close proximity by S-S interactions. Each pinwheel has four SEt moieties, two on each face of the molecule. They are situated in a diagonal arrangement above and below the square core of the molecule (Figure 4.8). S-S distances within a pinwheel are 5.181 Å and 5.580 Å. Between each pair of pinwheels, the sulphur atoms form a planar, nearly square

arrangement with S-S distances of 3.839 Å and 3.776 Å (Figure 4.10). These distances are greater than the sum of the van der Waals radii for two sulphur atoms (3.6 Å). Significant S-S contacts reported in the literature [79-83] range from 3.0 Å to >4 Å, so the distances in compound **4.5** are not unreasonable for a weak intermolecular interaction.

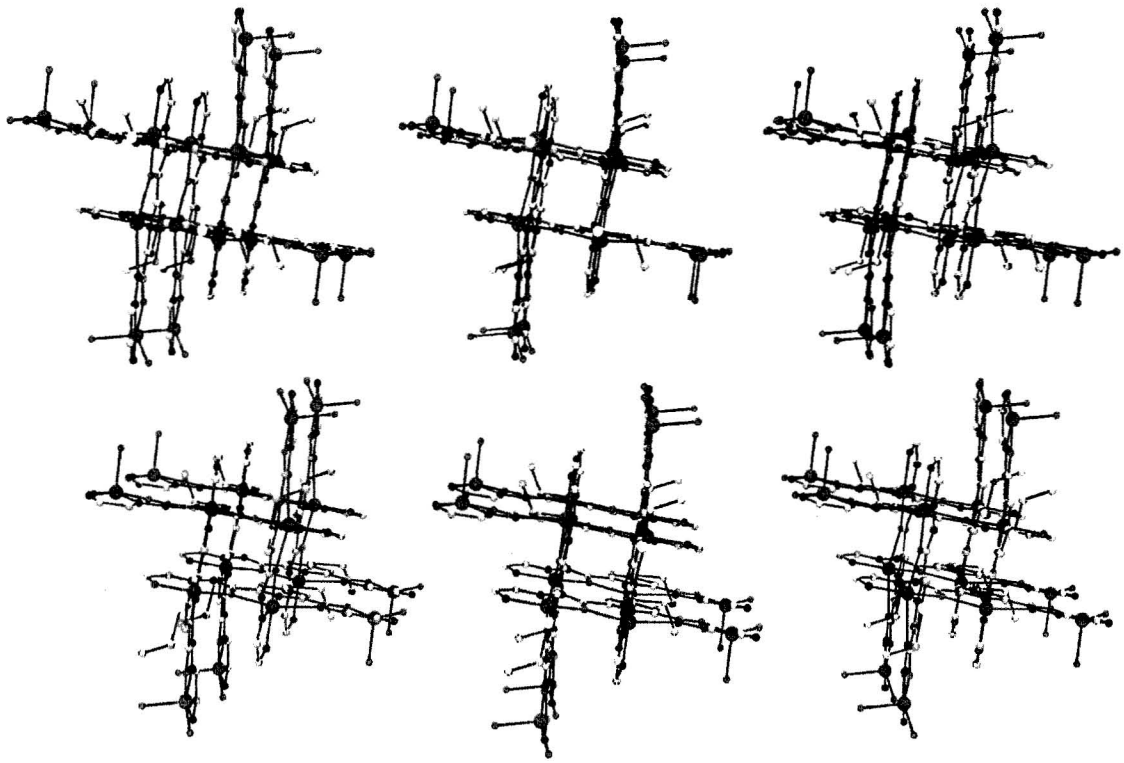

Figure 4.9: POV-RAY depiction of the unit cell of **4.5**. Peripheral groups, counter anions and solvent removed.

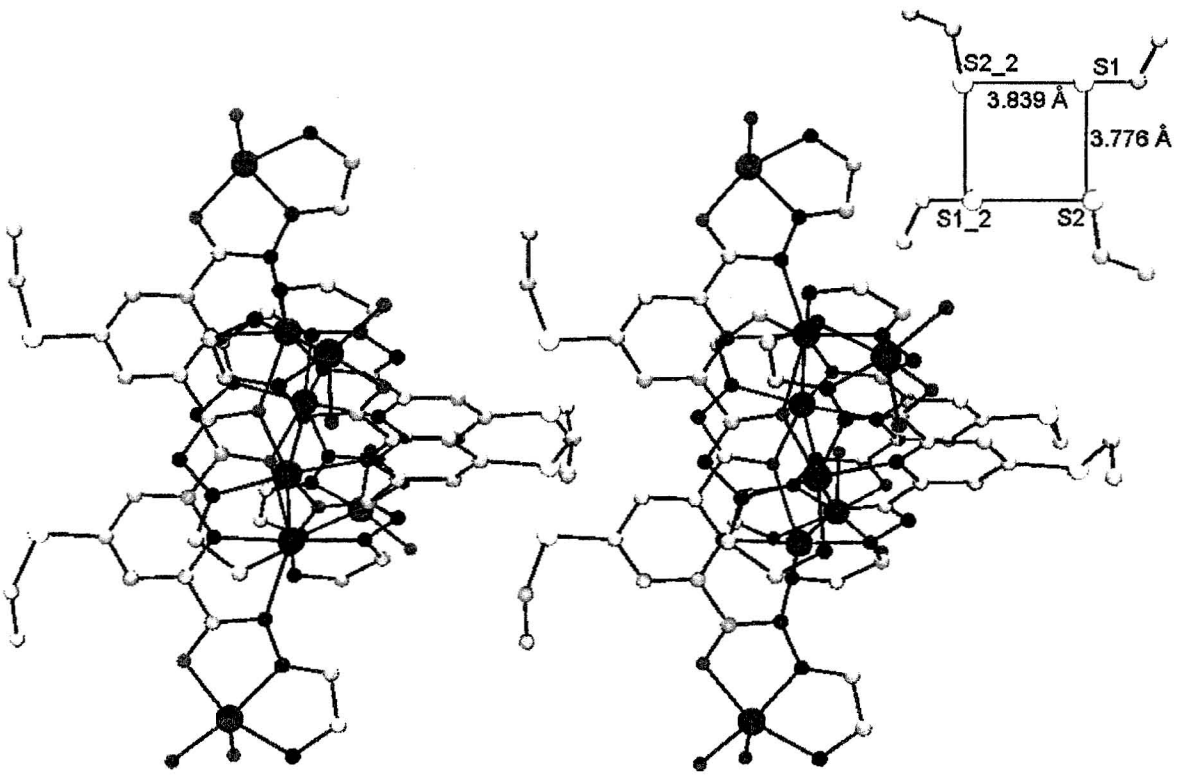

Figure 4.10: POV-Ray depiction of **4.5**, showing extended interaction via S groups.

4.3.2: Magnetic Properties:

Figure 4.11 shows a magnetic exchange model for the diazine bridged pinwheel compounds (e.g. **4.5**). The same model would also apply to compound **4.1** and **4.3**, with all μ-O connections. With the exception of the long indirect bridges in compounds **4.3**, all the bridges between Cu centers in the pinwheel compounds have short-long connections and are thus strictly orthogonal, and so one would expect to observe ferromagnetic rather than antiferromagnetic exchange. The exchange Hamiltonian for a typical pinwheel is given in Equation 1. Two J values are included, corresponding to exchange coupling

within the tetranuclear core and to the coupling between the core and the peripheral copper atoms. For compounds with similar μ-O bridges between the core and the periphery, e.g. **4.1** and **4.3**, it is reasonable to simplify the situation by assuming J = J1 = J2.

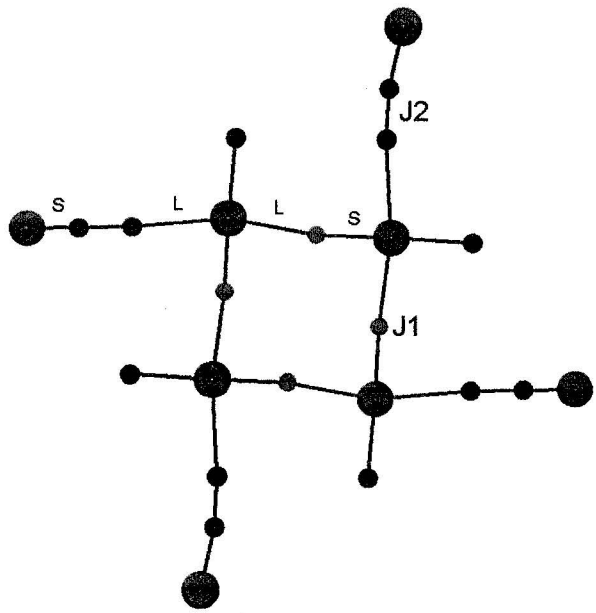

Figure 4.11: Magnetic model for pinwheel compounds.

Dealing with such a complex exchange situation from first principles, and deriving the appropriate exchange expression for two different J values, is very time consuming, and not a trivial exercise. The total spin states (S') and their energies (E(S')) can be calculated using vector addition principles [47] and substituted directly into the van Vleck equation (Equation 2) within the framework of the convenient software package MAGMUN 4.1 [49]. Corrections for intermolecular effects (θ, Weiss-like

correction), for the fraction of paramagnetic impurity (α), and for the temperature independent paramagnetism (TIP) are applied (Equation 3).

$$H_{ex} = -J_1(S_1S_2 + S_2S_3 + S_3S_4 + S_4S_1) - J_2(S_1S_5 + S_2S_6 + S_3S_7 + S_4S_8) \quad [1]$$

$$\chi_{M'} = \left[\frac{N\beta^2 g^2}{3k(T-\theta)}\right]\left[\frac{\sum S'(S'+1)(2S'+1)e^{-E(S')/kT}}{\sum(2S'+1)e^{-E(S')/kT}}\right] \quad [2]$$

$$\chi_M = \chi_{M'}(1-\alpha) + \frac{4S(S+1)N\beta^2 g^2 \alpha}{3kT} + TIP \quad [3]$$

The MAGMUN software nominally allows the input of any exchange energy term for any bridging connection, but is limited in the sense that non-linear regression fits cannot be used where two or more J values are direct variables. In cases where the two bridge types are dissimilar, e.g. in **4.5**, it is possible to evaluate J2 as a fraction of J1 using the non-linear regression routines built into the MAGMUN4.1 software. For example if input values are expressed as J1 = -1, J2 = -0.2, then J1/J2 = 5, and non-linear regression will return a fitted J which will be a factor by which both J1 and J2 are then multiplied.

The magnetic moment vs. temperature profile for **4.1** is depicted in Figure 4.12. The moment at room temperature is 5.5 μ_B, which is well above the spin only value for eight S=1/2 centers (4.9 μ_B). The moment rises to a value of 6.9 μ_B at 2 K consistent with ferromagnetic exchange within the cluster. This is in agreement with the orthogonal Cu-O-Cu bridges observed in the structure. The data were fitted to equations 1-3, with equation 1 simplified by assuming J1 = J2 = J. The best fit of the data returned

g = 2.177, J = 4.90 cm^{-1}, TIP = 400*10^{-6} $cm^3 \cdot mol^{-1}$, α = 0, θ = -1 K, 10^2R = 1.27, $R = [\Sigma(\chi_{obs}-\chi_{calc})^2/ \Sigma \chi_{obs}^{\ 2}]^{1/2}$ (solid line in Figure 4.12). These values are consistent with those of published pinwheel compounds [28, 54, 63].

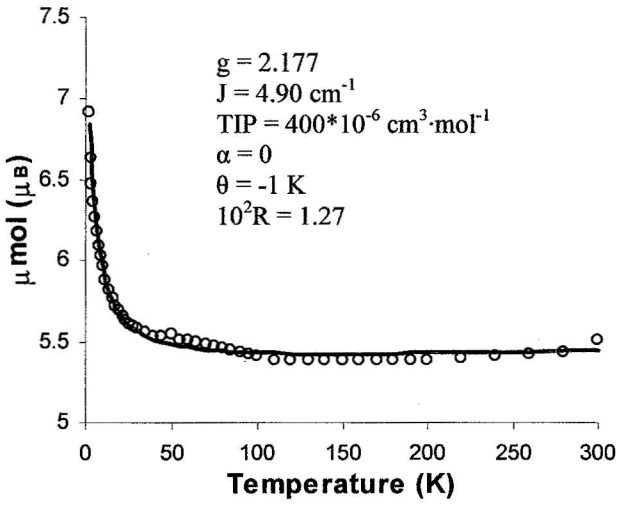

Figure 4.12: Variable temperature magnetic moment profile for **4.1**. Solid line represents calculated fit.

The structure of **4.2** is unknown but it is reasonable to assume it is similar to **4.1** since the ligand is the same. The magnetic profile of **4.2** is similar to that of **4.1**, with a magnetic moment of 5.6 μ_B at room temperature, which decreases slightly to 5.29 μ_B before rising sharply to 8.31 μ_B at 2 K, typical of compounds in this class. The temperature dependent magnetic data for **4.2** were fit to equations 1-3 assuming J1 = J2 = J. The best fit gave values of g = 2.13, J = 4.57 cm^{-1}, TIP = 450*10^{-6} $cm^3 \cdot mol^{-1}$, α = 0, θ = 0.1 K, 10^2R = 2.37. These values are consistent with those of other pinwheel compounds [28, 54, 63]. The magnetic data for compound **4.3** are shown in Figure 4.13

as a plot of moment (per mole) as a function of temperature. The room temperature moment is 5.81 μ_B and rises to 8.62 μ_B at 2 K, much higher overall than observed for the parent compound $[(Cl2POMP)_4Cu_8(NO_3)_8](H_2O)_{15}$ (**4.1**) [54], and in comparison with other similar systems. In addition there is a weak but significant maximum present in the profile, centered at 80 K, which is absent in other systems which do not have significant intermolecular connections, suggesting that the difference is due solely to an intermolecular effect caused by the proximity in which the dca ions hold the pinwheel subunits together.

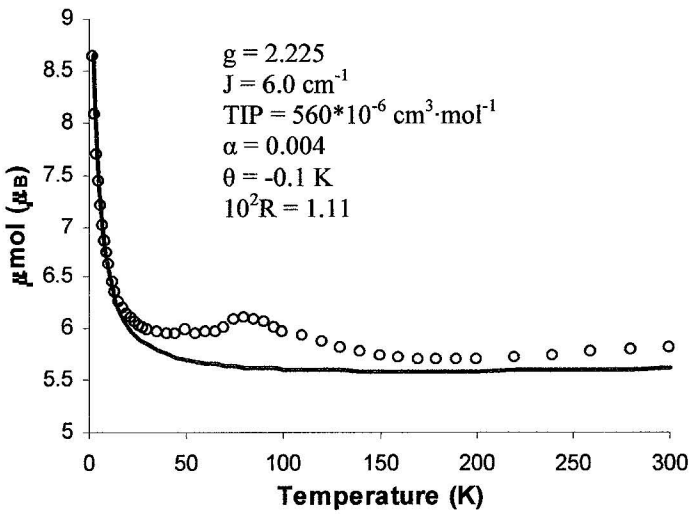

Figure 4.13: Magnetic moment vs. temperature profile for **4.3**. Solid line represents fitted parameters, calculated using unit weighting of data.

Long range magnetic effects via intermolecular Cl based contacts can be quite significant. Christou et al [98-100] have reported a dimer arrangement of Mn_4 single

molecule magnets, which displayed antiferromagnetic interactions and quantum tunnelling effects via relatively long Cl···H-C bonding and Cl-Cl contacts. The distances between the subunits were 3.71 Å through the H-bonds and 3.86 Å through the Cl-Cl contacts. These distances are much larger than the Cl···N separations in **4.3**, and so it is not unreasonable to suggest a cooperative magnetic effect associated with these interactions.

The magnetization vs. field data for **4.3**, measured at 2 K (Figure 4.14), show a steep increase in M to a value of 8.9 Nβ at 5.0 T. The solid line in Figure 4.14 is calculated for g = 2.225, S = 4 (at 2 K) using the appropriate Brillouin function. This is consistent with a ground state of S = 4, and so confirms the ferromagnetic nature of the intramolecular exchange, but does not offer any concrete indication of a putative extended magnetic interaction. Variable field magnetic data (50-200 Oe) were obtained in the range 40-140 K, and show an increase in magnetic moment as a function of increasing field with a maximum at 80 K, suggesting that any possible long range effect may be ferromagnetic in nature. Further studies will be required to establish this more firmly.

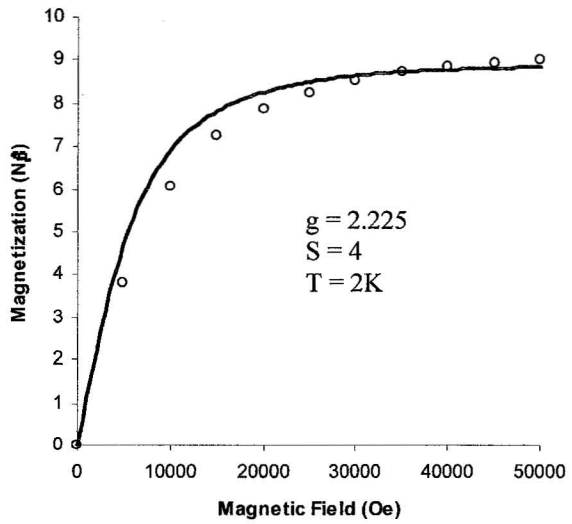

Figure 4.14: Magnetization vs. field for **4.3**.

On the assumption that the intramolecular and long range exchange terms can be treated separately an attempt was made using equations 1-3 to fit the data for **4.3** (J = J1 = J2), with unit weighting of the data. A fit gave g = 2.225(2), J = 6.0 cm^{-1}, TIP = 560 * 10^{-6} $cm^3 \cdot mol^{-1}$, θ = -0.1 K, α = 0.004, (10^2R = 1.11). The solid line in Figure 4.13 was calculated with these parameters. This result is entirely consistent with that obtained for the parent complex **4.1**. The possible formation of a small amount of a decomposition product from the reaction of **4.3** with dicyanamide, which could be responsible for the anomalous magnetic properties, should perhaps be considered. One likely candidate, $Cu(dca)_2$, can however be excluded, since it is a weak antiferromagnet [103].

The structure of **4.4** has not been determined, thus the type of bridging between the Cu centers is unknown. However it is clear from analytical and magnetic data that it consists of a pinwheel structure, and certainly the core would be similar to that in **4.1**. In the simplest case it is reasonable to assume that J = J1 = J2, and so the data have been

fitted to equations 1-3 in MAGMUN 4.0 using one J value. The magnetic profile of **4.4** is similar to that of the other pinwheel compounds, with a magnetic moment of 5.4 μ_B at room temperature, rising to 7.4 μ_B at 2 K. An excellent fit of the data gave g = 2.12, J = 4.83 cm^{-1}, α = 0.002, θ = -0.4 K, TIP = 495 * 10^{-6} $cm^3 \cdot mol^{-1}$ and 10^2R = 0.97, confirming at least the pinwheel nature of the compound.

The magnetic profile of **4.5** is generally similar to the profiles of other pinwheel compounds (Figure 4.15). The magnetic moment at room temperature is 5.1 μ_B, dropping slightly to 5.0 μ_B at 40 K, and then rising sharply to 7.0 μ_B at 2 K. The profile is overall slightly lower than usual for compounds in this class, and in particular, the minimum at 40 K is lower than typical for pinwheel systems. The data were initially fitted to equations 1-3 using a one J model. The best fit of the data gave g = 2.02, J = 2.84 cm^{-1}, α = 0, θ = 0 K, TIP = 550 x 10^{-6} $cm^3 \cdot mol^{-1}$, 10^2R = 2.6. Both the value of g and of J are lower than typical for pinwheels, suggesting that there may be an antiferromagnetic component in the coupling.

Attempts were made to fit the compound to a two J model with an antiferromagnetic contribution representing coupling through the long, non-orthogonal bridge through the ligand backbone, but were unsuccessful. The pinwheel molecules are stacked in what are effectively chains with significant S-S interactions within the chains. These intermolecular associations could be responsible for an additional long range antiferromagnetic effect, resulting in a lower than normal magnetic moment.

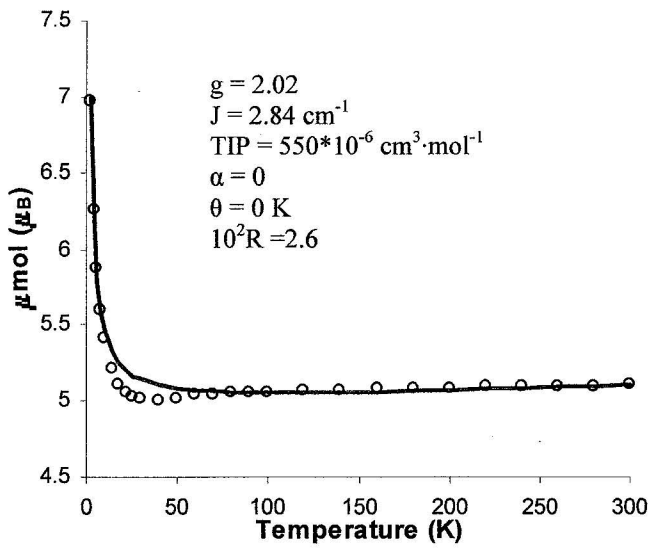

Figure 4.15: Magnetic Moment vs. temperature profile for **4.5**. Solid line represents fitted data calculated using a 1 J model.

The structure of **4.6** is not known, but it is likely that it is similar to that of **4.5**, which has both orthogonal μ-diazine and μ-O bridges. The magnetic moment is 5.4 μ_B at room temperature, dropping very slightly down to ~100 K, and then rising to 8.0 μ_B at 2 K (Figure 4.15). The data were initially fitted using the single J model (equation 1, J = J1 = J2). A good fit to eqns. 1-3 gave g = 2.095(9), J = 5.0(2) cm^{-1}, α = 0.001, θ = -0.05 K, TIP = 572 * 10^{-6} $cm^3 \cdot mol^{-1}$, 10^2R = 1.63. The solid line in Figure 4.16 was calculated with these parameters. To test the validity of this approach to fitting a pinwheel with two different types of bridges, the data were also fitted to models where J2 = 0.75*J1, J2 = 0.5*J1, J2 = 0.25*J1, J2 = 0, and J2 =-0.25*J1 (small antiferromagnetic value to simulate effect of non-orthogonal long bridge in **4.5**). The models with an antiferromagnetic component or no coupling between the peripheral and central Cu(II) centers would not fit

the profile satisfactorily. This indicates that ferromagnetic coupling occurs in between peripheral and central Cu(II) centers in **6**. For the models with two ferromagnetic J values, the goodness of fit increased with increasing J2. (10^2R = 1.87, 1.84, 1.78 for J2 = 0.25*J1, 0.5*J1, and 0.75*J1, respectively) It is difficult to interpret this information without knowing the structure of **4.6**. Similar J1 and J2 values could indicate that the bridging is similar, as is the case for **4.1** and **4.3**. However, since **4.5** and **4.6** were prepared from the same ligand, it seems more likely that the bridging is similar to **4.5,** and that a two J model would be more appropriate. If this is the case, it would indicate that the calculations are simply not sensitive enough to interpret the subtleties of weak ferromagnetic interactions. Under those circumstances one would conclude that a simple one J fit is a good approximation for any pinwheel system.

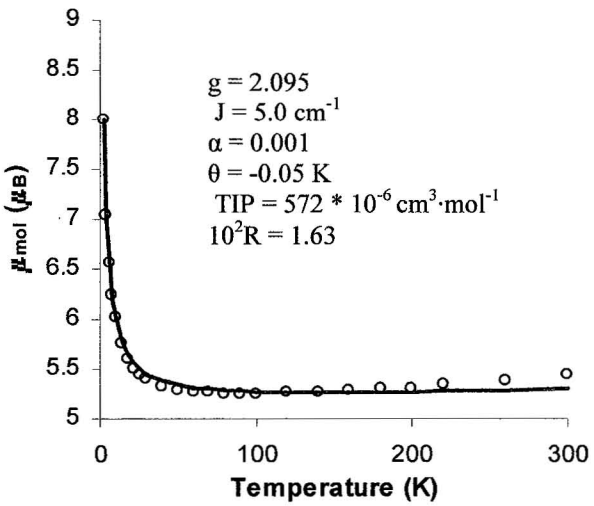

Figure 4.16: Magnetic moment vs. temperature profile for **4.6**.

4.4: Summary:

Octanuclear Cu(II) pinwheels form with a variety of ligands. The pinwheel is composed of two sets of two parallel ligands, arranged perpendicular to each other, bound to the eight Cu(II) centers. The ligands can adopt two different binding modes, which leads to two different bridging scenarios. In binding mode (a), the Cu(II) centers are all bridged by hydrazone oxygen atoms, and Cu-Cu distances within the tetranuclear core, and between the core and peripheral Cu(II) centers are similar. In this case, one can assume a magnetic model with one ferromagnetic J value. In binding mode (b), the core Cu(II) centers are bridged by hydrazone oxygen atoms while the peripheral Cu(II) centers are bridged to the core by diazine groups. The distance between core Cu(II) cations is then much shorter than the distance between core and peripheral Cu(II) centers. In this case, a model with two ferromagnetic exchange intergrals would be more appropriate. In practice, it is possible to fit the pinwheels with two bridge types to a variety of models. This indicates that it is difficult to distinguish the contributions of such small ferromagnetic exchange integrals, and that a one J model is a sensible approximation for pinwheel systems in general.

The pinwheel clusters are heteroleptic, and as such it is possible to exchange weakly bonded counter anions or solvent molecules for more strongly binding ones. Potentially bridging anions have been used in the hope of creating direct links between the molecules, however this has only been successful in one case [63]. In the compound $[(2POMP)_4Cu_8Br_6](CuBr_4)(H_2O)_{11}$, pinwheel molecules were directly linked through a bromide ion, which bridged peripheral Cu centers. However, the bridging connections

were orthogonal, and the linking did not result in any change in the magnetic properties of the compound as a whole. Ligand functional groups and coordinated counter anions cause extensive intermolecular interactions which have resulted in the organization of the molecules into stacks in the crystal lattice in several cases. The organization appears to affect the magnetic properties leading to a ferromagnetic effect in **4.3**, manifesting as a higher than usual overall profile and a maximum in the profile at 80 K. In **4.5**, the stacking appears to result in an antiferromagnetic effect overall, and a decrease in moment throughout the temperature range in the magnetic moment vs. temperature profile. These results are promising, as they demonstrate that linking ferromagnetic subunits through intermolecular interactions can affect the bulk magnetic properties, and that different interactions lead to different magnetic effects. This paves the way towards synthesis of bulk magnetic materials constructed from ferromagnetic subunits, and also provides a way of fine-tuning the magnetic properties of the material.

Chapter 5: $Cu(II)_9$, $Ni(II)_9$, and $Co(II)_9$ [3x3] grids and grid fragments

5.1: Preamble:

Square, [nxn] grid complexes of transition metals have attracted a great deal of attention for their interesting properties, and aesthetic appeal, as well as being a fascinating example of efficient self-assembly. A family of [2x2] M_4 grids has been synthesized, using the ditopic ligand POAP and related ligands (Figure 5.1a) (M = Cu(II), Ni(II), Zn(II),Co(II)) [22, 23, 25]. [2x2] M_4 grids have also been prepared from ditopic terpyridine based ligands (Figure 5.1b) and Cu(I), Co(II), and Zn(II) salts [17-18, 53, 110].

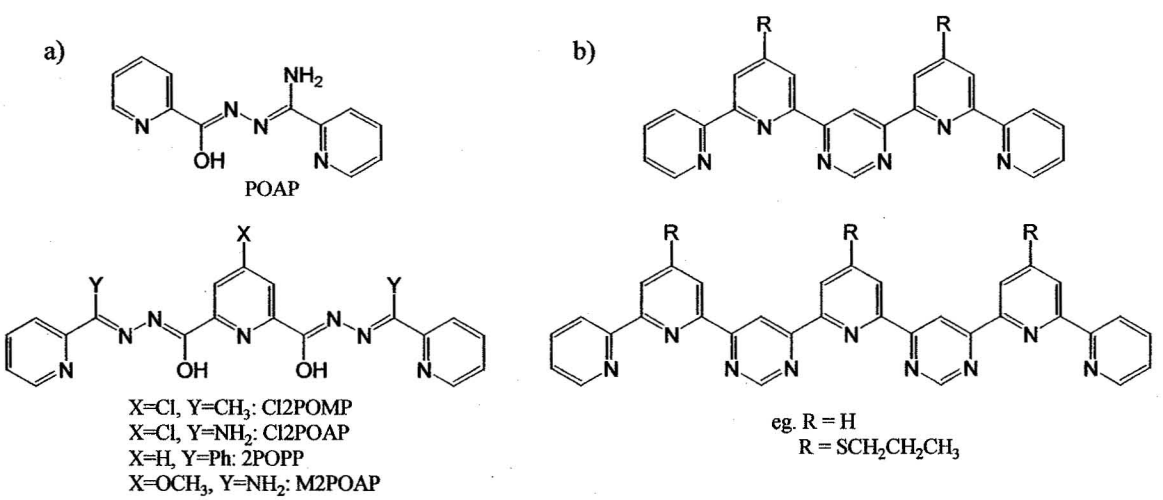

Figure 5.1: a) di and tritopic 2POAP type ligands. b) di and tritopic terpyridine ligands.

$Mn(II)_9$ [3x3] grids have received a great deal of recent attention due to their facile, reproducible and reversible four electron oxidation, leading to a significant change in their spectroscopic and magnetic properties [32, 66-67, 111]. This reversible change in

properties makes them suitable candidates for molecular devices such as bistable switches, qubit analogues or quantum dot cellular automata (QCA) [39-43, 67-69]. Less attention has been given to [3x3] grids of metal cations other than Mn(II), although several of these have been prepared. Structures of $Cu(II)_9$ and $Zn(II)_9$ grids with 2POAP and related ligands [29, 54, 64, 94] have been published along with magnetic data for analogous Ni(II) and Co(II) systems, while non-magnetic $Ag(I)_9$, $Zn(II)_9$, and $Hg(II)_9$ grids have been reported with terpyridine based ligands [16, 20]. In addition to the [3x3] grids, a [4x4] $Pb(II)_{16}$ grid has been reported based on a tetratopic terpyridine-type ligand [21].

No structures of $Ni(II)_9$ or $Co(II)_9$ [3x3] grid compounds of 2POAP or related ligands have been obtained so far. Characterization of the complexes by other means is complicated by the formation of grid fragments in both cases and by aerial oxidation of the complexes in the case of cobalt(II). [3x3] M_9 grids are structurally similar to the [2x2] $M(II)_4$ grids, with hydrazone oxygen bridges, and similar bond distances and M-O-M bridging angles. Therefore the magnetic properties of the [3x3] M_9 grids may be expected to be similar to those of their [2x2] counterparts. $Ni(II)_4$ and $Co(II)_4$ [2x2] grids are both weak antiferromagnets, similar to the previously reported [3x3] M_9 grids with these metal ions. Furthermore, in the case of the [2x2] grids, $Mn(II)_4$ have the smallest M-O-M angles and the weakest antiferromagnetic coupling, followed by the $Co(II)_4$ grids with slightly larger M-O-M angles, and slightly stronger antiferromagnetic coupling, and finally by the $Ni(II)_4$ grids, with even larger M-O-M angles and even stronger antiferromagnetic coupling. It is reasonable to assume that this trend will extend to the

[3x3] grid complexes. Thus in the absence of fitted magnetic data for the $Co(II)_9$ [3x3] grids, we would expect the J values to be intermediate between the -4 to -5 cm^{-1} range typical of $Mn(II)_9$ grids, and the -6 to -8 cm^{-1} range reported for $Ni(II)_4$ and $Ni(II)_9$ grids [22-23, 29, 32].

It is worthwhile considering why the $Mn(II)_9$ grids form with apparent ease compared with grids of other first row transition metal cations. One factor might be the relative "plasticity" of Mn(II). With a d^5 electron configuration and no ligand field stabilization energy (LFSE), Mn(II) may be able to adapt to the relatively rigid coordination environment provided by the ligand pockets in the grid backbone more easily than the other metals. Fe(III) is much smaller than the M(II) cations due to its charge, so it is no surprise that Fe(III) grids are rare, since the pockets are larger than ideal for such a small cation. Indeed, $Fe(III)_5$ complexes, where the side sites of the grid are vacant, seem to form preferentially [64].

Another important factor may be the pH during synthesis. In most of the $Mn(II)_9$ grids reported so far, with picolinic dihydrazone based ligands, all the ligand molecules are doubly deprotonated, while in the case of the $Cu(II)_9$ grids it is normal for some or all of the ligand molecules to be singly deprotonated. For the $Ni(II)_9$ and $Co(II)_9$ grids, (*vide ante*) the number of anions required by the elemental analysis indicates that some of the ligands tend to be singly deprotonated or even neutral. The neutral or singly deprotonated ligand would have significant double bond character in the hydrazone C-O bond, and this may discourage coordination to metals with weaker Lewis acid character, and make grid formation more difficult. In the cases of Co(II) and Fe(II), the metals are

also susceptible to aerial oxidation, which would firstly lower the chances of obtaining a grid with a single oxidation state of the metal, and would make the compound more difficult to characterize in the absence of a structural solution. Should aerial oxidation to Co(III) or Fe(III) occur before the formation of the grid, the smaller size of the M(III) cation would also discourage full grid formation. It is additionally possible that oxidation of the complexed cation could cause the grid molecule to decompose, or the ligand to undergo hydrolysis leading to a rearrangement of the compound. This chapter will discuss some $Cu(II)_9$, $Ni(II)_9$ and $Co(II)_9$ grids, as well as a $Ni(II)_6$ grid fragment with the intention of comparing the properties of these grids and a partial Ni(II) grid to the $Mn(II)_9$ analogues and [2x2] M_4 grids.

5.2: Experimental:

5.2.1: Complex synthesis:

5.2.1.1: $[(SEt2POAP)_6Cu_9](CF_3SO_3)_{12}(H_2O)_{4.5}(CH_3OH)_2$ **(5.1)**

$Cu(CF_3SO_3)_2$ (1.53 g, 4.2 mmol) was dissolved in methanol (25 mL). SEt2POAP (0.51 g, 1.1 mmol) was added, and rapidly dissolved, forming a clear green solution, which was refluxed overnight then filtered and left to stand in air. Brown crystals (200 mg, 21 %), not suitable for x-ray diffraction, were collected after several weeks. Elemental Analysis: Found (%): C; 31.84, H; 2.50, N; 14.33. Calc. (%) for $[(C_{21}H_{20}N_9O_2S)_6Cu_9](CF_3SO_3)_{12}(H_2O)_{4.5}(CH_3OH)_2$: C; 31.87, H; 2.62, N; 14.34.

5.2.1.2: $[(SEt2POAPz)_6Cu_9](CF_3SO_3)_9(CH_3OH)_{3.5}(H_2O_{)6.5}$ **(5.2)**

$Cu(CF_3SO_3)_2$ (0.24 g, 6.6 mmol) was dissolved in methanol (10 mL). SEt2POAPz (0.10 g, 0.22 mmol) was added along with acetonitrile (10 mL). The ligand

rapidly dissolved forming a clear green-brown solution which was heated for 15 mins, filtered and left to cool. The solvent was evaporated to dryness, forming a clear glass, which was redissolved in methanol (10 mL). Red-brown crystals (60 mg, 33 %), not suitable for x-ray crystallography, formed over several weeks. Elemental analysis: Found (%): C; 30.87, H; 2.60, N; 18.76. Calc (%) for $[(C_{19}H_{17}N_{11}O_2S)_3(C_{19}H_{18}N_{11}O_2S)_3 Cu_9](CF_3SO_3)_9(CH_3OH)_{3.5}(H_2O)_{6.5}$: C; 30.84, H; 2.70, N; 18.76.

5.2.1.3: $[(SEt2POAP)_5Ni_6](CF_3SO_3)_7(H_2O)_{14}$ **(5.3)**

$Ni(CF_3SO_3)_2$ (aq) (30 mL (0.08 gmL^{-1}), 6.7 mmol) was diluted with methanol (20 mL), and SEt2POAP (1.0 g, 2.2 mmol) was added. The ligand dissolved, forming a clear green brown solution which was heated for ~ 8 hours, then filtered and left to stand. Green-brown crystals, (350 mg, 20 %), suitable for x-ray crystallography, formed over several days. Vis-nir (acetonitrile): $\lambda = 970$ nm, $\varepsilon = 288$ $Lmol^{-1}cm^{-1}$. Elemental analysis: Found (%): C; 33.96, H; 2.85, N; 15.95. Calc. (%) for $[(C_{21}H_{21}N_9O_2S)_2(C_{21}H_{20}N_9O_2S)(C_{21}H_{19}N_9O_2S)_2Ni_6](CF_3SO_3)_7(H_2O)_{14}$: C; 33.97, H; 3.26, N; 15.92.

5.2.1.4: $[(Cl2POPP)_6Ni_9](ClO_4)_{11}(H_2O)_{11}$ **(5.4)**

Cl2POPP (0.1 g, 0.2 mmol) was added to a solution of $Ni(ClO_4)_2{\cdot}(H_2O)_6$ (0.24g, 0.7 mmol) in 30 mL of acetonitrile. The resulting clear green solution was heated, and 10 mL of absolute ethanol was added. The resulting brown solution was heated for 10 mins then filtered and allowed to cool. Brown crystals (60 mg, 35 %), not suitable for x-ray diffraction, formed over several days. Vis-nir (acetonitrile): $\lambda_1 = 1180$ nm, $\lambda_2 = 844$ nm. Elemental Analysis: Found (%): C; 43.20, H; 2.88, N; 11.53. Calc. (%), for

$[(C_{31}H_{20}N_7O_2Cl)_5(C_{31}H_{19}N_7O_2Cl)Ni_9](ClO_4)_{11}(H_2O)_{11}$: C; 43.28, H; 2.89, N;11.40.

5.2.1.5: $[(SEt2POAP)_6Ni_9](H_2O)_{60}(CH_3OH)_3$ (**5.5**)

SEt2POAP (0.10 g, 0.22 mmol) was suspended in acetonitrile/methanol (20 mL, 3:1). Aqueous sodium hydroxide solution (4 mL, 0.1 $molL^{-1}$) was added, resulting in a bright orange mixture. $Ni(NO_3)_2 \cdot 6H_2O$ (0.26 g, 0.89 mmol) was dissolved in methanol (10 mL) and added to the ligand mixture. The solid dissolved, forming a clear, deep brown solution which was heated for 20 mins, then filtered. A brown powder (100 mg) formed after several days. Vis-nir (acetonitrile/methanol, 2:1): $\lambda = 958$ nm, $\varepsilon = 605$ $Lmol^{-1}cm^{-1}$. Elemental analysis: Found (%): C; 34.61, H; 2.75, N; 16.92. Calc. (%) for $[(C_{21}H_{19}N_9O_2S)_6Ni_9](H_2O)_{60}(CH_3OH)_3$: C; 34.63, H; 5.54, N; 16.90. While the C/N ratio for this compound is approximately correct, the large number of solvent molecules required to match the analysis is unlikely to be accurate. The absence of nitrate can be attributed to the removal of three protons from each ligand molecule. The sample has been resubmitted for analysis.

5.2.1.6: $[(SEt2POAP)_6Co_9](Br)_{12}(H_2O)_7$ (**5.6**)

$CoBr_2$ (0.32 g, 1.5 mmol) was dissolved in methanol (20 mL). SEt2POAP (0.1g, 0.2 mmol) was added, and rapidly dissolved forming a clear brown solution which was heated 30 minutes, then filtered and allowed to cool. Brown crystals and powder (90 mg, 62 %) formed over 2 days. Vis-nir (acetonitrile/methanol, 2:1): $\lambda = 580$ nm, $\varepsilon = 1080$ $Lmol^{-1}cm^{-1}$, (Nujol mull): $\lambda_1 = 994$ nm, $\lambda_2 = 572$ nm. Elemental Analysis: Found (%): C; 34.29, H; 3.11, N; 17.47. Calc (%), for $[(C_{21}H_{20}N_9O_2S)_6Co_9]Br_{12}(H_2O)_7$: C; 34.47, H; 3.07, N; 17.23.

5.2.2: Crystallography:

The diffraction intensities of a green-brown prismatic crystal of **5.3** (0.205 x 0.283 x 0.094 mm) were collected using graphite monochromatized Mo-Kα radiation on a Rigaku AFC8-Saturn 70 CCD diffractometer at -120 °C to a maximum 2θ value of 62.1°. Data were collected and processed using CrystalClear [112]. The data were corrected for Lorentz and polarization effects. The structure was solved by direct methods [72-73]. Non-H atoms were refined anisotropically except for one disordered triflate anion, which was refined isotropically. H atoms were introduced in calculated positions with thermal parameters set at twenty percent greater than those of their bonded partners. They were refined using the riding model. The structure contains twenty and 1/2 partial and two full occupancy water molecules as lattice solvent. These were modelled isotropically and their H atoms were omitted from the model. The model also contains a full occupancy methanol molecule, which was refined anisotropically with H atoms introduced in calculated positions, except for the hydroxyl proton which could not be located in the difference map. There are a total of forty six H atoms omitted from the model. Neutral atom scattering factors [74], and anomalous dispersion terms [75-76] were taken from the usual sources. All calculations were performed using the teXsan [77] crystallographic software package of the Molecular Structure Corporation except for refinement, which was performed using SHELXL-97 [72a]. Crystal data for **5.3** can be found in Table 5.1.

Table 5.1: Summary of crystallographic data for **5.3**.

Empirical Formula	$C_{113}H_{149}F_{21}N_{45}Ni_6O_{54.5}S_{12}$
M/gmol^{-1}	4145.58
Crystal System	Triclinic
Space Group	P-1 (#2)
a/Å	18.6174(14)
b/Å	19.2391(15)
c/Å	26.272(2)
α/°	79.147(7)
β/°	74.629(6)
γ/°	77.008(7)
V/ Å^3	8758.0(12)
ρ_{calcd} /gcm^{-3}	1.572
T/°C	-120(1)
R1	0.1182
wR2	0.3135

5.3: Results and discussion:

5.3.1: Description of crystal structure:

$[(SEt2POAP)_5Ni_6](CF_3SO_3)_7(H_2O)_{14}$ (**5.3**)

The main cationic fragment in **5.3** is depicted in Figure 5.2 a,c, and important bond distances and angles are located in Table 5.2. The structure contains six Ni(II) cations, coordinated in a homoleptic arrangement to five SEt2POAP ligands. The Ni(II) cations are arranged in two rows, in the terminal pockets of three parallel ligands, one singly deprotonated and the other two neutral, which have adopted a bent conformation (Figure 5.2b). The central ligand pockets do not coordinate metal cations, but are filled with H-bonded water and methanol molecules (Figure 5.2c). The remaining two ligands

are doubly deprotonated, adopt a linear conformation, and lie perpendicular to the first three. One lies on each face of the molecule, and each coordinates one of the rows of three Ni(II) cations.

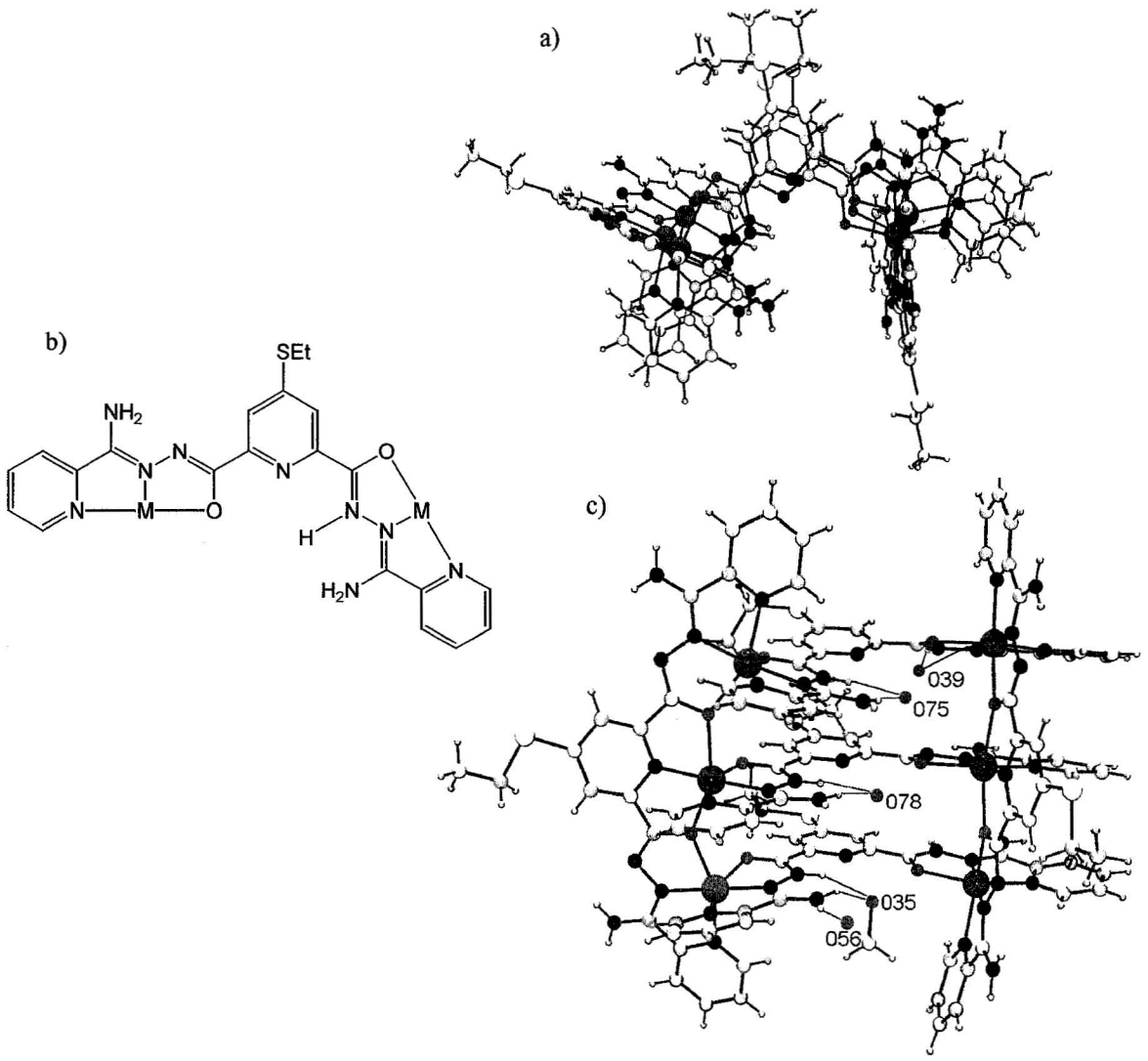

Figure 5.2: a) POV-RAY depiction of **5.3**, with counter anions and lattice solvent removed for clarity. Ni = magenta, S = yellow, C = grey, N = blue, O = red, H = aquamarine. b) Ligand in bent conformation (singly protonated). c) top view of **5.3**, with H-bonded O atoms in pockets.

The overall arrangement of the Ni(II) cations is similar to a grid with the central row of Ni(II) missing. However, the molecule is curved due to the bent conformation of three ligands. The Ni(II) coordination environments are similar to those found in a typical grid. The four corner Ni(II) cations have a *cis*-NiN_4O_2 coordination environment, and the central Ni(II) has a *mer*-NiN_3O_3 coordination environment. Ni-N bond distances fall between 1.942 and 2.135 Å, while Ni-O bond distances range from 2.107 to 2.216 Å. Adjacent Ni(II) ions within a row are bridged by the hydrazone O atoms of the ligand. Ni-O-Ni angles range from 137.79 to 140.6°.

It is instructive to consider the C-O bond lengths to the hydrazone oxygen atoms. The linear, doubly deprotonated ligands have hydrazone C-O distances ranging from 1.302 to 1.320 Å. These distances are typical of C-O single bonds. The hydrazone oxygen atoms in the neutral ligands have C-O bond distances of 1.238-1.258 Å. This is indicative of significant double bond character, and of ketonic character of the oxygen atoms. For the singly deprotonated ligand the C-O bond distances are 1.260 Å for the protonated hydrazone group and 1.291 Å for the deprotonated hydrazone group. The ligand molecules which possess double bonded hydrazone oxygen atoms have vacant central pockets, while those with single bonded hydrazone oxygen atoms are completely coordinated.

The unit cell of **5.3** is depicted in Figure 5.3 showing a layered arrangement of Ni_6 cations. Within each layer, the molecules are arranged in sheets with π- π interactions and H-bonding between adjacent molecules (Figure 5.4a, b). Two molecules are held in close proximity by a displaced π-stacking interaction between two terminal pyridine

rings. The closest contact distance is 3.523 Å. Each of these molecules has H-bonding contacts with other clusters through an amine nitrogen atom and a terminal pyridine proton. The N···H distance is 2.945 Å with an N···H-C angle of 127.61°, which is reasonable for a weak contact to a CH proton. There is an additional H-bonding contact between pairs of molecules at the opposite corner of the molecule (Figure 5.5). The contact is between a hydrazone oxygen atom and an amine proton, and has an O···H distance of 2.566 Å and an O···H-N angle of 153.62°. There are two of these contacts between each pair of molecules.

Table 5.2: Selected bond distances (Å) and angles (°) for **5.3**.

Ni1-N3	1.966(5)	Ni4-N12	1.946(5)
Ni1-N25	1.993(5)	Ni4-N39	1.985(5)
Ni1-N27	2.061(5)	Ni4-N37	2.066(5)
Ni1-O1	2.114(4)	Ni4-N10	2.106(5)
Ni1-N1	2.119(5)	Ni4-O9	2.107(4)
Ni1-O6	2.203(5)	Ni4-O3	2.110(4)
Ni2-N5	1.978(5)	Ni5-N30	1.954(5)
Ni2-N34	2.001(4)	Ni5-N14	1.981(5)
Ni2-O2	2.119(4)	Ni5-O3	2.166(4)
Ni2-O1	2.130(4)	Ni5-O7	2.169(4)
Ni2-N36	2.135(5)	Ni5-O4	2.170(4)
Ni2-O8	2.144(5)	Ni5-N28	2.132(5)
Ni3-N7	1.942(5)	Ni6-N16	1.949(5)
Ni3-N43	1.985(5)	Ni6-N21	2.000(5)
Ni3-N45	2.061(5)	Ni6-N19	2.081(6)
Ni3-N9	2.090(5)	Ni6-O5	2.110(4)
Ni3-O2	2.108(4)	Ni6-N18	2.122(5)
Ni3-O10	2.216(4)	Ni6-O4	2.149(4)
Ni1-O1-Ni2	138.6(2)	π- π interactions:	
Ni3-O2-Ni2	137.79(19)	C45···C45'	3.523
Ni4-O3-Ni5	138.7(2)	C45···C44'	3.751
Ni6-O4-Ni5	140.6(2)		
H-bonding interactions:		S-N interactions:	
N11···H88-C	2.945, 127.61	S5···N38	3.638
O6···H1-N	2.566, 153.62		

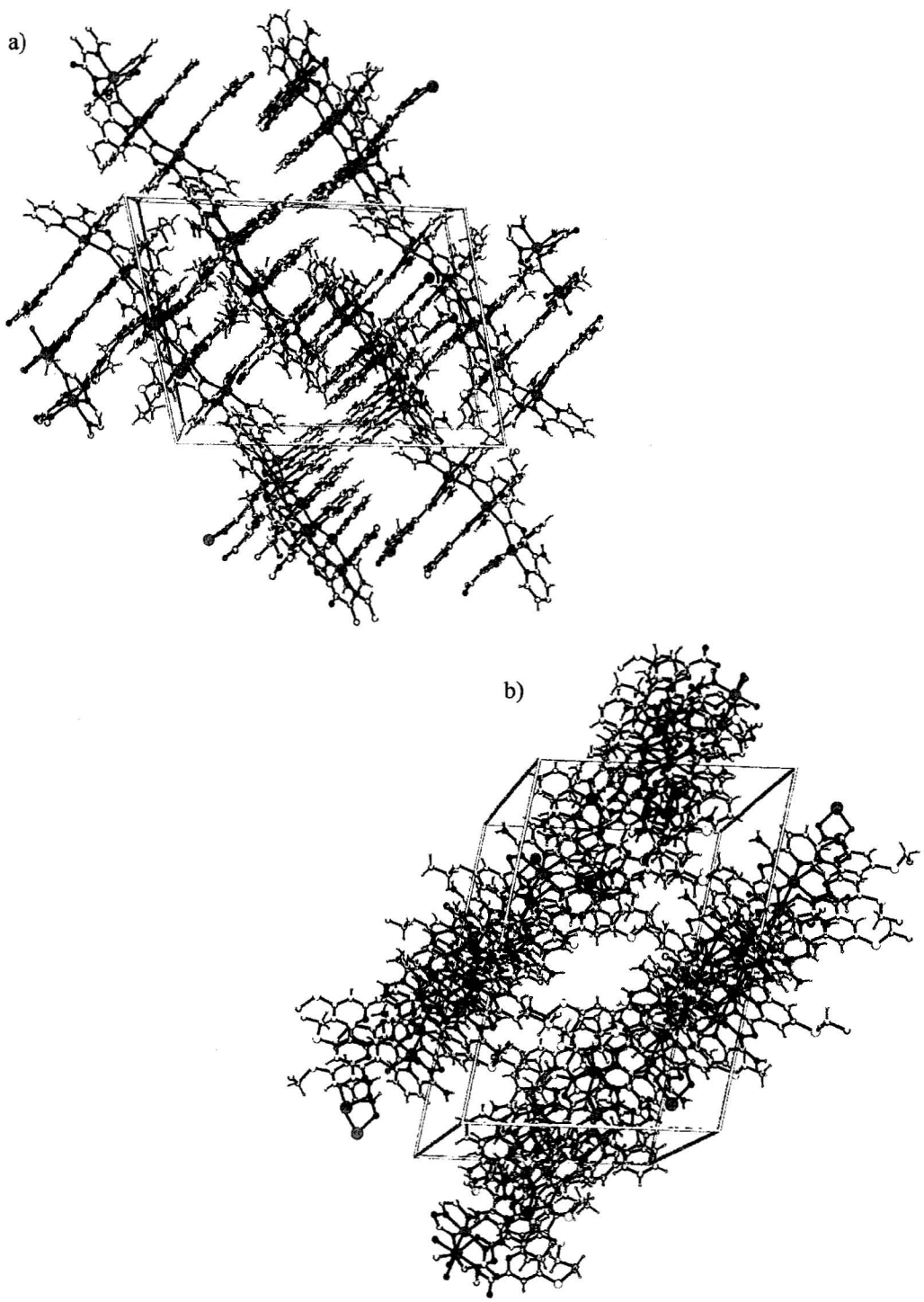

Figure 5.3: POV-RAY depiction of the unit cell of **5.3** a) along y–axis b) along x–axis.

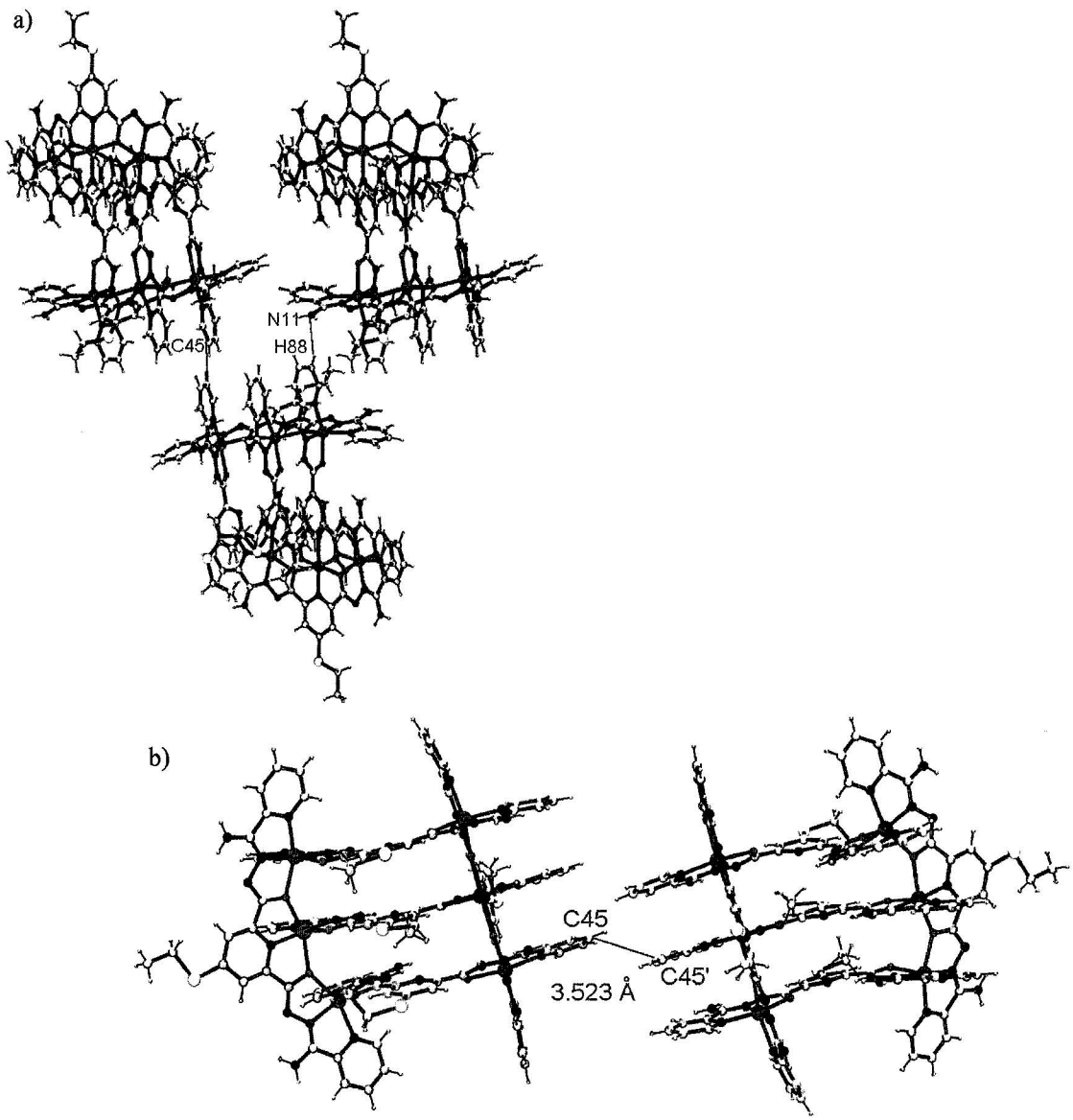

Figure 5.4: a) Intra-layer interactions in **5.3**. b) Top view of π-stacking interaction.

The layers are held loosely together via contacts involving the SEt group. The most significant of these is between the SEt group of one molecule and the amine N atom in the molecule below (above) it (Figure 5.5). The S···N distance is 3.638 Å. There are

two of these contacts between each pair of molecules. This distance is somewhat larger than the sum of the van der Waals radii for S and N (3.35 Å) [84], but in the absence of stronger intermolecular interactions this interaction could dominate the packing of the layers [32]. There are additionally some longer contacts between aromatic carbon atoms and S atoms of molecules in the next layer, but these are quite long with respect to the sum of the van der Waals radii of carbon and sulphur and are more likely a result of the close packing of the layers in the crystal rather than a significant interaction.

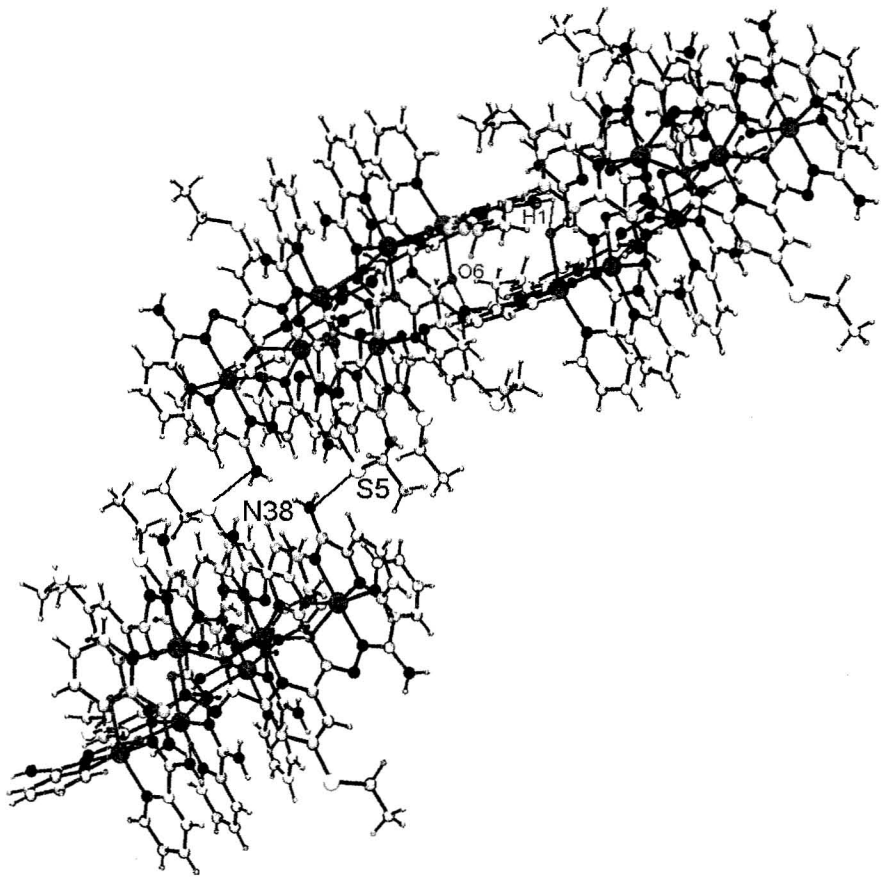

Figure 5.5: Inter-layer interactions in **5.3**, highlighted in purple. Intra-layer H-bonding highlighted in green.

5.3.2: Visible-NIR Spectroscopy:

In the absence of structural data, visible-nir spectroscopy can provide information about the coordination environments of the metal centers. For **5.3**, a weak absorption was observed at a wavelength of 970 nm. This corresponds well to the first transition in octahedral Ni(II) (ν_1; $^3T_{2g} \leftarrow {}^3A_{2g}$), which generally ranges from 775 nm for ligands with a weak field to 1470 nm, for ligands with a strong field [114]. The Ni(II) sites in **5.3** have a mixed oxygen-nitrogen coordination environment, and would be expected to be in the middle of the range. The extinction coefficient, with a value of 288 $Lmol^{-1}cm^{-1}$, is relatively large for a d-d band, but represents six Ni(II) centers and is typical of d-d transitions in this class of compounds [66]. For the putative $Ni(II)_9$ grids, **5.4** and **5.5**, the ν_1 transitions were observed at 1180 nm and 958 nm (ε = 605 $Lmol^{-1}cm^{-1}$) respectively, and for **5.4**, the second transition was observed at 844 nm (ν_2; $^3T_{1g} \leftarrow {}^3A_{2g}$). In the case of **5.6**, the $Co(II)_9$ grid, the lowest energy transition (ν_1; $^4T_{2g} \leftarrow {}^4T_{1g}$), was observed at 994 nm, which is well within the range of accepted values for octahedral Co(II) (1100nm-1750 nm) [114]. The second transition was also observed, at 572 nm, as a shoulder on the charge transfer band (ν_2; $^4A_{2g} \leftarrow {}^4T_{1g}$). The extinction coefficient for this transition in solution, at 1080 $Lmol^{-1}cm^{-1}$, is very high, but this is not unexpected as it occurs as a shoulder on a charge transfer band from which it can steal intensity. The octahedral geometries of the M(II) centers in **5.4-5.6** supports the assignment of the grid structure to these compounds.

5.3.3: Magnetic Properties:

While no structures of [3x3] grid molecules are presented in this chapter, it is reasonable to assume based on published structures of Mn(II), Cu(II) and Zn(II), that the compounds consist of nine M(II) cations arranged in a square [3x3] grid where the M(II) centers are bridged by hydrazone oxygen atoms (Figure 5.6). The isotropic spin only exchange Hamiltonian for any of these systems is:

$$H_{ex} = -J1(\Sigma_{i=1-7}\, S_i \cdot S_{i+1} + S_8 \cdot S_1) - J2(S_2 + S_4 + S_6 + S_8) \cdot S_9 \qquad [1]$$

where J1 represents the coupling between metal cations around the outer eight membered ring and J2 represents the coupling between the side cations and the central metal, and $S_{1\text{-}9}$ represent the spin quantum number of the appropriate metal cation. Dipole-dipole, second order ligand field and Zeeman terms are ignored.

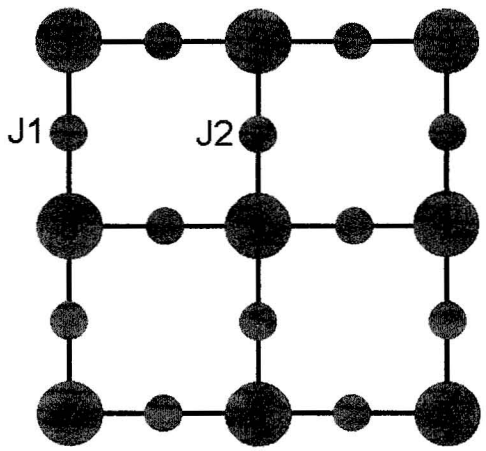

Figure 5.6: Magnetic model for M_9 grid.

The systems discussed in this chapter are simpler than the $Mn(II)_9$ grids in that they possess less unpaired electrons; nine for Cu(II) grids, eighteen for Ni(II) grids, and twenty seven for Co(II) grids. While these systems are large, the spin vector coupling matrices required are small enough that the exchange problem can be solved on a PC, and it is not necessary to simplify the problem using the Fisher model, as is the case for Mn(II) (See Chapter 3 for a full discussion of this method). The program OW01 is used to calculate the total spin state combinations and their energies [47] using normal vector addition principles. The output from this program is read into MAGMUN 4.1 [49], which substitutes the spin states and energies into the van Vleck equation (Equation 2). Corrections are made for intermolecular effects (θ, Weiss-like correction), for the fraction of paramagnetic, Curie-like impurity (α), for the temperature independent paramagnetism (TIP) (Equation 3), and for the zero field splitting (D) in the cases of Ni(II) and Co(II) (Equations 4, 5 respectively). The zero field splitting correction is implemented by replacing χ_{mol} for the lowest energy state with the χ_z term [87] for the axially distorted octahedral system with zero field splitting, as χ_z is more significant than χ_x and χ_y in axially distorted systems.

$$\chi_{M'} = \left[\frac{N\beta^2 g^2}{3k(T-\theta)}\right]\left[\frac{\sum S'(S'+1)(2S'+1)e^{-E(S')/kT}}{\sum(2S'+1)e^{-E(S')/kT}}\right] \qquad [2]$$

$$\chi_M = \chi_{M'}(1-\alpha) + \frac{4S(S+1)N\beta^2 g^2 \alpha}{3kT} + TIP \qquad [3]$$

$$\chi_{z/Ni} = \left[\frac{2Ng_z^2\beta^2}{kT}\right]\left[\frac{e^{-D/kT}}{1+2e^{-D/kT}}\right] \qquad [4]$$

$$\chi_{z/Co} = \left[\frac{Ng_z^2\beta^2}{4kT}\right]\left[\frac{1+9e^{-2D/kT}}{1+e^{-2D/kT}}\right] \qquad [5]$$

5.3.3.1: $Cu(II)_9$ grids:

Cu(II) grids are unusual because all reported compounds have dominant ferromagnetic properties instead of the antiferromagnetic properties demonstrated by all grids of the other paramagnetic transition metal cations. The known $Cu(II)_9$ grids are similar in structure to the $Mn(II)_9$ grids, with a $[Cu_9(\mu\text{-}O)_{12}]$ core, where the Cu(II) centers are bridged by hydrazone oxygen atoms [54, 94]. In the case of the $Cu(II)_9$ [3x3] grids, the exchange situation is complicated by the different magnetic ground states of the Cu(II) centers in the outer ring and the central Cu(II) sites. To better understand the situation it is helpful to consider the structure of a known $Cu(II)_9$ grid. Figure 5.7 illustrates the core structure of a $Cu(II)_9$ grid with the ligand M2POAP (see Figure 5.1a) [54]. All of the Cu(II) ions have distorted octahedral geometries, however the Cu(II) centers on the outer ring are axially elongated, giving them a $d_{x^2-y^2}$ ground state, while the central Cu(II) is axially compressed, resulting in a nominally d_{z^2} ground state. The resulting bridging is all long-long (axial-axial), or long-short (axial-equatorial) and therefore magnetically orthogonal, and so one would not expect to observe any antiferromagnetic exchange. While this is true of the Cu(II) centers around the ring, surprisingly, antiferromagnetic exchange is observed between the side and center sites, with an average of two Cu(II) centers being spin coupled. This results in the S = 7/2

ground state observed in all reported $Cu(II)_9$ grids [54, 64, 94, 111]. It is not difficult to rationalize the existence of antiferromagnetic coupling in this system because the d_{z^2} orbital has components on all three axes. Therefore antiferromagnetic coupling is possible between the side and central Cu(II) sites.

Since both ferromagnetic and antiferromagnetic exchange are observed in $Cu(II)_9$ grids, a two J model must be used to analyze the magnetic data. While MAGMUN 4.1 nominally allows non linear regression to be performed only on systems with one J value, it is possible to model the $Cu(II)_9$ system by evaluating J2 as a function of J1 (e.g. J2 = -10*J1). The fitted J value returned by MAGMUN 4.1 would then be a factor by which both J1 and J2 are multiplied.

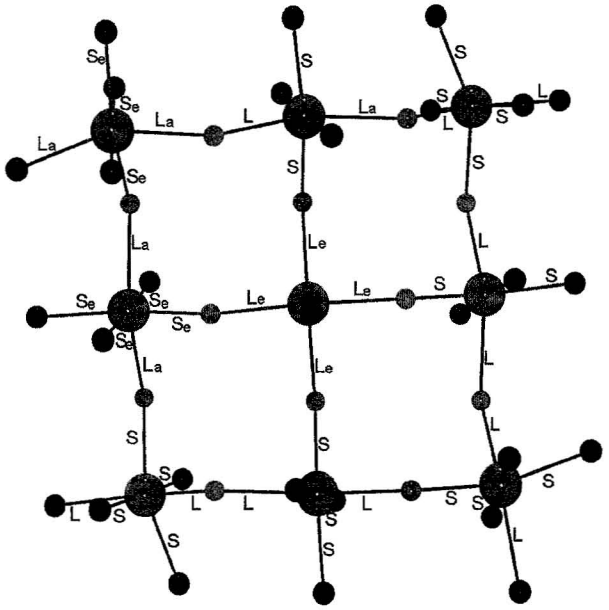

Figure 5.7: Core of a [3x3] $Cu(II)_9$ grid showing long (L) and short (S) bonds. Axial (a) and equatorial (e) bonds are indicated for one corner, one side and the central Cu(II) site.

The magnetic moment vs. temperature profile for the putative $Cu(II)_9$ grid **5.1** is shown in Figure 5.8. The magnetic moment is ~6.0 μ_B at room temperature dropping rapidly to a minimum of ~5.4 μ_B at 30K before rising to ~7.2 μ_B, at 2 K. This shape is typical of the $Cu(II)_9$ grids as a whole, and agrees with the assessment based on the orientation of the orbitals. The antiferromagnetic contribution represented by J2 manifests itself as the drop in moment between 300K and 30 K. At lower temperatures the ferromagnetic interaction (J1) becomes dominant, as evidenced by the rise in magnetic moment between 30 K and 2 K.

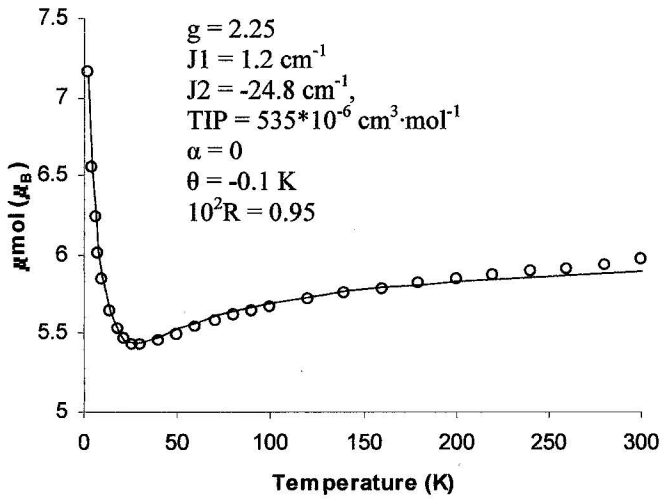

Figure 5.8: Magnetic moment vs. temperature profile for **5.1**.

The magnetic data for **5.1** were fitted using MAGMUN 4.1 (J2 = -20*J1), with the best fit of the data giving g = 2.25, J1 = 1.2 cm^{-1}, J2 = -24.8 cm^{-1}, TIP = 535*10^{-6} $cm^3 \cdot mol^{-1}$, α = 0.0, θ = -0.1 K, 10^2R = 0.95 ($10^2R = [\Sigma(\chi_{obs}-\chi_{calc})^2/ \Sigma \chi_{obs}^2]^{1/2}$) (solid line in Figure 5.8). These parameters are consistent with the reported $Cu(II)_9$ grids

[54, 94, 111]. The small negative θ value could indicate very weak intermolecular antiferromagnetic coupling. The magnetic profile of **5.2** is similar to that of **5.1**, with a μ_{mol} of 6.5 μ_B at 2 K, dropping to a minimum of 5.5 μ_B at 18 K, then rising slightly to 6.1 μ_B at ambient temperature. The best fit of the data (J2 = -30*J1) gave g = 2.29, J1 = 0.46 cm^{-1}, J2 = -14.8 cm^{-1}, TIP = 650*10^{-6} $cm^3 \cdot mol^{-1}$, α = 0.003, θ = 0 K, 10^2R = 1.46. These values, particularly the J2 value, are significantly smaller than those obtained for **5.1**, which could be due to the difference in the ligand structures. **5.2** was prepared using a ligand with terminal pyrazine rings instead of pyridine rings as in **5.1**. Pyrazine rings are much better π-acceptors than pyridine rings and this could affect the magnetic properties of the complex [115].

5.3.3.2: $[(SEt2POAP)_5Ni_6](CF_3SO_3)_7(H_2O)_{14}$ (**5.3**)

5.3 has six Ni(II) centers arranged in two parallel rows of three metal centers (Figure 5.9). The rows are too far apart (> 9Å) for there to be any significant magnetic communication between them, but within a row, the Ni(II) centers are bridged by single hydrazone oxygen atoms, with large Ni-O-Ni angles. Therefore we would expect to see antiferromagnetic coupling between Ni(II) centers within a row. The exchange Hamiltonian for this system is

$$H_{ex} = -J(S_1S_2 + S_2S_3 + S_4S_5 + S_5S_6) \qquad [7]$$

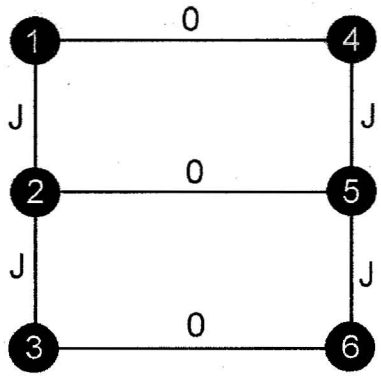

Figure 5.9: Magnetic model for **5.3**.

The magnetic profile for **5.3** is shown in Figure 5.10. The magnetic moment is 7.9 μ_B at room temperature, decreasing sharply to 3.3 μ_B at 2 K, characteristic of intramolecular antiferromagnetic coupling. The value at ambient temperature is somewhat higher than the spin only magnetic moment for six isolated Ni(II) centers (6.9 μ_B) which is not unusual for Ni(II) since the "g" value tends to be significantly greater than 2.0. The magnetic data were fitted to equations 7 and 2-4 using MAGMUN 4.1. The best fit of the data gave g = 2.28, J = -9.23 cm^{-1}, TIP = 480*10^{-6} $cm^3 \cdot mol^{-1}$, α = 0.002, θ = -1.6 K, D = 1.9 cm^{-1}, 10^2R = 1.36 (solid line in Figure 5.10). The low value of μ_{mol} at 2 K, as well as the significant negative θ value, suggest that there may be an additional antiferromagnetic interaction, perhaps a long range interaction between the Ni(II) cations at the ends of rows, or a small interaction between the rows.

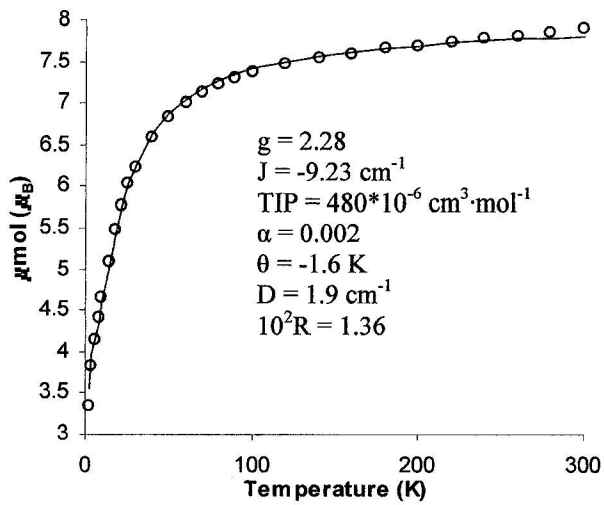

Figure 5.10: Magnetic moment vs. temperature profile for **5.3**.

5.3.3.3: $Ni(II)_9$ grids:

While no structures of $Ni(II)_9$ grids have been obtained so far, mass spectral and magnetic evidence, and elemental analyses indicate that they do form [54]. The formation of grid fragments such as **5.3** lends strong support to the formation of the [3x3] grids. The structure of a fully formed $Ni(II)_9$ grid would be expected to resemble that of a $Mn(II)_9$ grid, with a $[Ni_9(\mu\text{-}O)_{12}]$ core, where the Ni(II) centers are bridged by hydrazone oxygen atoms. The octahedral Ni(II) centers cannot be orbitally orthogonal to each other as they have unpaired electrons in both the $d_{x^2-y^2}$ and the d_{z^2} orbitals. Thus we would expect to see antiferromagnetic coupling both around the outer ring of eight Ni(II) cations and between the cations occupying the side sites and the central site. In order to simplify the data fitting, J2 was assumed to be equal to J1, which is consistent with the

situation in the manganese [3x3] grids, where J2 in mixed oxidation state grids has been found to be similar in magnitude to J1 in $Mn(II)_9$ grids [43, 66].

The magnetic moment vs. temperature profile for **5.4** is illustrated in Figure 5.11. The magnetic moment falls from 9.5 μ_B at 300K to 3.2 μ_B at 2 K. The moment at 2 K is typical for one octahedral Ni(II) center, and indicates antiferromagnetic coupling within the grid with the cancellation of spins leaving one uncoupled Ni(II) center, presumably at the center site. This parallels the situation observed for the $Mn(II)_9$ grids. The data were fitted to equations 1-4 using MAGMUN 4.1, assuming S = 1. An excellent fit of the data gives g = 2.23, J = -7.8 cm^{-1}, α = 0.002, θ = 0 K, TIP = 480*10^{-6} $cm^3 \cdot mol^{-1}$, D = 0.4 cm^{-1}, 10^2R = 1.52. The solid line in Figure 5.11 was calculated using these parameters. These results are consistent with both the Ni_4 [2x2] grids and other Ni_9 [3x3] grids reported previously [23, 29].

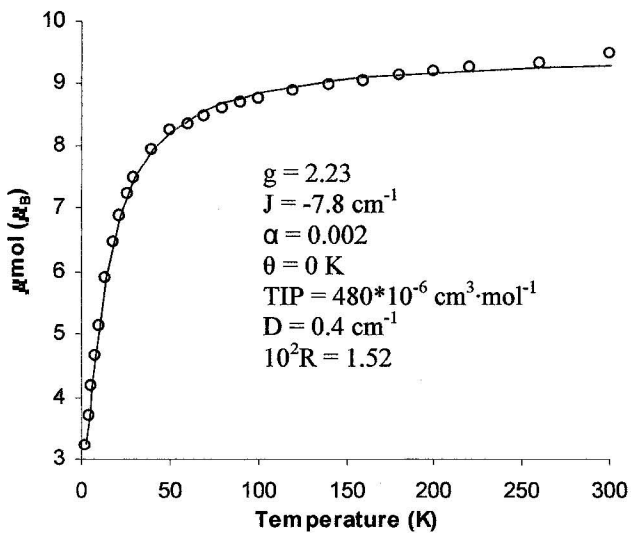

Figure 5.11: Magnetic moment vs. temperature profile for **5.4**.

For comparison purposes, the data for **5.4** were also fitted using the chain model (*vide infra*) which has been used to fit the $Mn(II)_9$ grids. A good fit of the data gave g = 2.17, J = -7.3 cm^{-1}, (Note that J represents the coupling around the outer ring of eight Ni(II) centers, J2 is set to zero, as the central Ni(II) is assumed to be isolated in the Fisher model. See Chapter 3 for a full discussion of the chain model.), $\alpha = 0.001$, $\theta = -2.5$ K, TIP = $480*10^{-6}$ $cm^3 \cdot mol^{-1}$, $10^2R = 1.94$. In general these parameters, notably the magnitude of J, are similar to those obtained from the full grid fit. Since the chain model assumes no coupling between the outer ring of eight Ni(II) centers and the central metal, the contribution of J2 generally manifests itself in the form of the large negative θ value. The model does not correct for zero field splitting. It should be noted that the chain model works better for large values of S, as the approximation of S as a classical vector is more accurate for large S values [87]. However the close correspondence between the methods suggests the chain model is adequate to approximate the magnetic properties of the [3x3] $Mn(II)_9$ grid systems.

The magnetic moment of **5.5** is 10.0 μ_B at room temperature, and decreases sharply to 3.7 μ_B at 2 K, indicative of dominant antiferromangnetic coupling. The magnetic moment at 2 K is close to the spin only value for one Ni(II) cation, which corresponds well with the situation in the $Mn(II)_9$ and other $Ni(II)_9$ grids. A preliminary fit of the data to the full grid model was performed. The best fit of the data gave parameters g = 2.34, J = -8.6 cm^{-1}, $\alpha = 0.002$, $\theta = 1$ K, TIP = $1900*10^{-6}$ $cm^3 \cdot mol^{-1}$, D = 3.8 cm^{-1}, $10^2R = 3.9$. These values are reasonable for Ni(II) [22, 23].

5.3.3.4: $Co(II)_9$ grids:

No structures have been obtained so far for any $Co(II)_9$ grid. However elemental analyses and magnetic evidence indicate that the compounds do form [29]. Structures have been obtained for partial Co grids comprised of five ligand molecules and six or seven cobalt cations but with a mixture of Co(II) and Co(III) sites [65]. A $Co(II)_9$ grid would be expected to have the same $[Co_9(\mu\text{-}O)_{12}]$ core as observed in the $Mn(II)_9$ and $Cu(II)_9$ grids, and to display antiferromagnetic coupling between Co(II) cations in the outer ring and between side Co(II) centers and the central Co(II) cation.

Any attempt to explain the magnetic properties of Co(II) is complicated by several factors, including contributions to the magnetic properties by spin orbit coupling and by zero field splitting. It is therefore instructive to begin the analysis by attempting a Curie-Weiss fit of the susceptibility data, in order to gauge the effect of spin orbit coupling.

A plot of $1/\chi_{mol}$ vs. temperature for **5.6** is shown in Figure 5.12. The value at room temperature is 14.5 cm^3mol^{-1}, dropping linearly to a value of 2.15 cm^3mol^{-1} at 14 K, then curving sharply down below 14 K. A simulation of the data to the Curie-Weiss law gives C = 24 $cm^3mol^{-1}K^{-1}$ (2.66 $cm^3mol^{-1}K$ per Co(II)) and θ = -45 K. The high value of C (a typical value of C for an S = 3/2 center is 1.88 $cm^3mol^{-1}K$ assuming g = 2) indicates significant orbital contributions to the magnetic susceptibility. The drop in $1/\chi_{mol}$ at low temperature, coupled with the large negative θ value, are indicative of antiferromagnetic coupling in the compound as well.

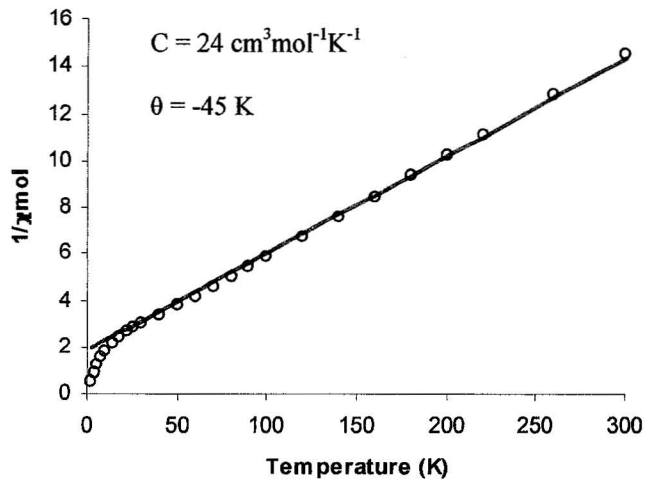

Figure 5.12: Plot of $1/\chi_{mol}$ vs. temperature for **5.6**, simulated parameters represented by solid red line.

The magnetic moment vs. temperature profile for **5.6** is depicted in Figure 5.12. The magnetic moment is 12.7 μ_B at room temperature, falling to 5.7 μ_B at 2 K. These values are consistent with a previously reported $Co(II)_9$ grid [29]. The values are larger than the spin only values for the system (11.6 μ_B for nine S = 3/2 centers, 3.87 μ_B for one S = 3/2 center), which can be attributed to the large "g" value generally associated with Co(II), as well as to the orbital contribution indicated by the Curie-Weiss simulation of the data.

Since the Curie-Weiss simulation indicates the presence of antiferromagnetic coupling, the data were fitted to equations 1-3 and 5 (S = 3/2), using MAGMUN 4.1 in order to approximate exchange parameters for the system. The fit assumes that J1 = J2 = J, and does not account for spin orbit coupling. The best fit of the data gave the parameters g = 2.28, J = -5.44 cm^{-1}, $\alpha = 0$, $\theta = 1.0$ K, TIP = $400*10^{-6}$ $cm^3 \cdot mol^{-1}$, D = 2

cm^{-1}, $10^2R = 2.5$. These parameters are consistent with expectations for Co(II). The positive θ value could reflect the contribution of spin orbit coupling to the system. The data were also fitted to the chain model (*vide supra*) for comparison purposes. The best fit of the data gave g = 2.25, J = -8.4 cm^{-1}, α = 0.002, θ = 1.5 K, TIP = $500*10^{-6}$ $cm^3 \cdot mol^{-1}$, $10^2R = 2.51$. It is interesting to note that these parameters do not agree well with the previous analysis, which suggests that for the $Co(II)_9$ grids, the chain model is not appropriate. Magnetic fitting for the $Co(II)_9$ grid cannot be considered rigorous using either model since it does not include spin-orbit coupling effects.

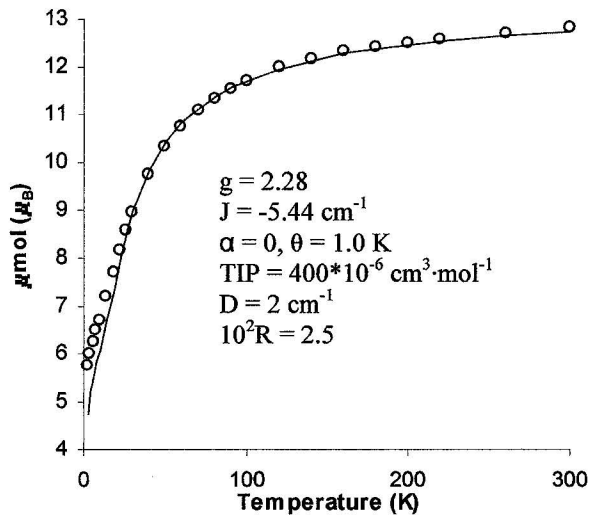

Figure 5.13: Magnetic moment vs. temperature profile for **5.6**.

5.4: Summary:

Relatively few examples of [3x3] grids of metal cations other than Mn(II) have been described. While examples of [3x3] grids of Zn(II) and Cu(II) have been published,

they are much less numerous than the Mn(II) compounds, and examples of [3x3] grids of Co(II), Ni(II) or Fe(III) are rare. Several factors may contribute to the difficulty of obtaining non-Mn(II) grids. Firstly, the arrangement of the ligands in the grid creates coordination pockets for the metals cations which have a fairly rigid geometry. Mn(II), with no ligand field stabilization energy, is relatively plastic and therefore able to distort easily and meet the coordination requirements of the pocket. It is much less favourable for other metals, especially those of much smaller size than Mn(II) (e. g. Fe(III)) to occupy the same sites.

The effects of pH on the system are significant, since the ligands do not lose protons readily at low pH (hydrazone oxygen, diazine nitrogen atoms), which discourages coordination to the metal cations in the grid. For metals like Ni(II) and Co(II) the energy advantage of the thermodynamically favourable grid formation may not be enough to overcome the energy disadvantage of coordinating an oxygen atom which has significant ketonic character. The formation of **5.3** lends support to this hypothesis in that the central pockets of the three parallel, neutral or singly deprotonated ligands are vacant. The C-O bonds to the hydrazone oxygen atoms in **5.3** display significant double bond character, and the vacant central pockets mean that the ketone-like hydrazone oxygen atom is then only coordinated to one Ni(II) cation instead of two as it would be in a grid. Additionally, singly deprotonated or neutral ligands in the bent conformation have a diazine proton which intrudes into the coordination pocket of the ligand which may directly hinder complexation of a metal in this pocket, or which may indirectly hinder it by encouraging H-bonded solvent molecules to occupy the pocket. A Co(II)

analogue of this system has also been obtained [65]. Upon addition of base to the system, the full grid molecule, **5.5**, is obtained using the same ligand as **5.3**. This difference illustrates the profound effect of pH on the self assembly process in the case of the picolinic dihydrazone ligands. It is interesting to note that the bent binding mode of the ligand molecules has only been observed in complexes of metals other than Mn(II). The rotation around the single bond resulting in the bent conformation can only occur while the central pocket is vacant. This suggests that the coordination of the central ligand pocket is crucial and must occur quickly in order to prevent the rotation of the ligand into the bent conformation. If this is the case, then the pH of the system may be a dominant effect in systems with less plastic metal cations than Mn(II).

The $Cu(II)_9$ [3x3] grids, like their [2x2] analogues, display dominant ferromagnetic behaviour due to orbital orthogonality of the Cu(II) cations in the outer ring. The coupling between the central Cu(II) site and the side sites is antiferromagnetic. Magnetic data and fitted parameters for **5.1** and **5.2** are consistent with published examples of $Cu(II)_9$ grids.

Structural studies of Ni(II) compounds have been hindered by the difficulty of obtaining single crystals of these systems, and by solvent loss and poor diffraction when crystals have been obtained. Compound **5.3** is a rare example of a Ni(II) complex with a 2POAP-like ligand where it has been possible to obtain structural results. The compound is not a grid, but rather a hexanuclear partial grid, where one end of three of the ligands has rotated around the single bond to the central pyridine ring resulting in a bent conformation. This conformation prevents coordination of the central ligand pocket and

the formation of a grid. Magnetically, the compound can be modelled as two isolated linear trinuclear subunits, however, a large negative θ value, and a low temperature magnetic moment below the spin only value for two isolated Ni(II) cations suggest a slightly more complicated situation. The value of the coupling constant J, at ~ -9 cm^{-1}, is consistent with both the coupling constants for the [2x2] and [3x3] Ni(II) grids reported in the literature [23, 29], and with the [3x3] Ni_9 grids reported in this work. This is to be expected since the coordination environments of the Ni(II) centers, particularly the bond distances to bridging atoms and bridging angles in **5.3** are similar to those in reported [2x2] Ni_4 grids [22, 25].

No structures for the [3x3] grids of Co(II) or Ni(II) are reported. However, the visible-nir spectral data support the assignment of octahedral geometries to the M(II) centers, and the magnetic data are consistent with grid exchange models and with other grids reported in the literature. The fit obtained for each of the compounds has parameters which are consistent with those for analogous [2x2] and [3x3] grid systems. The value of the exchange integral J is generally found to be within the range -4 to -5 cm^{-1} for $Mn(II)_9$ [3x3] grids. The values obtained were -5.4 cm^{-1} for the Co(II) compound, and and -7.8 and -8.6 cm^{-1} for the two Ni(II) compounds. This supports the earlier prediction, based on the increasing size of the M-O-M bond angles, that of the M(II) cations, Mn(II) will have the weakest antiferromagnetic coupling, with Co(II) having slightly stronger coupling and Ni(II) having the strongest coupling of the three, as is the case for the [2x2] M_4 grids. Therefore, in the absence of structural data, the magnetic properties of the Ni(II) and Co(II) grids are diagnostic for grid structures. Mass

spectral evidence (LCMS, MALDI-TOF) has been used in some cases in the analysis of putative Ni(II) and Co(II) grids [113], and while not generally providing a molecular ion peak, sensible grid fragments (e. g. $L_5M_8^+$, $L_5M_7^+$, $L_5M_6^+$) have been obtained, lending additional support to the assignment of the grid structures.

Chapter 6: Reactions of [3x3] $Mn(II)_9$ grids with transition metal cations:

6.1: Preamble:

Chlorine and sulphur functionalized 2POAP-like ligands were developed in order to synthesize functionalized [3x3] $Mn(II)_9$ grids for surface studies. The structural, magnetic, and electrochemical properties of some of these functionalized grids were discussed in detail in Chapter 3. It was determined that the general physical properties of the functionalized $Mn(II)_9$ grids based on SEt2POAP were very similar to those of the 2POAP based $Mn(II)_9$ grids.

In Chapters 3 and 4 the effects of the functional groups on the extended structures of the $Mn(II)_9$ grid and $Cu(II)_8$ pinwheel complexes were discussed. Addition of the Cl and S-based functional groups to the ligand backbone created a series of intermolecular interactions, including H-bonds, Cl···N interactions, S···N interactions and S···S interactions in the crystal packing arrangements of the complexes. These interactions were strong enough to disrupt the π-stacking interactions usually found in 2POAP-based complexes in all of the structures examined, and in the cases of some $Cu(II)_8$ pinwheels, the interactions were strong enough to affect the magnetic properties of the complexes.

The interactions observed between the functional groups and gold surfaces [55, 66, 70-71] as well as the intermolecular interactions between the functional groups in the crystal suggest the possibility of using these functional groups as external coordination sites for additional metal cations. Reactions between the functionalized [3x3] $Mn(II)_9$ grid molecules and large, soft metals like silver and gold could improve our understanding of the interactions between the grid molecules and e.g. Au(111) surfaces,

while reactions with magnetically active transition metal cations via these sites could lead to compounds with interesting extended magnetic properties.

The reactions of **3.1**, $[(SEt2POAP)_6Mn_9](CF_3SO_3)_9(H_2O)_{15}(CH_3CN)_4$, with Cu(II), Fe(III), Ag(I) and Au(III) will be discussed. For comparison purposes, a reaction of Cu(II) with a [3x3] $Mn(II)_9$ grid prepared using 2POAP will also be discussed.

6.2: Experimental:

6.2.1: Complex Synthesis:

6.2.1.1: $[(SEt2POAP)_6Mn_9](CF_3SO_3)_7(H_2O)_{30}(CH_3CN)$ (**6.1**)

$[(SEt2POAP)_6Mn_9](CF_3SO_3)_9(H_2O)_{15}(CH_3CN)_4$ (**3.1**) (100 mg, 0.02 mmol) was dissolved in warm methanol/acetonitrile (20 mL, 2:1). $Cu(CF_3SO_3)_2$ (160 mg, 0.44 mmol) was added, and the resulting solution was warmed. The solution gradually turned brown. Brown crystals (70 mg, 72 %), suitable for X-ray diffraction, formed over several days. Vis-nir: $\lambda_1 = 776$ nm, $\varepsilon_1 = 235$ $Lmol^{-1}cm^{-1}$, $\lambda_2 = 1130$ nm, $\varepsilon_2 = 190$ $Lmol^{-1}cm^{-1}$. Elemental analysis: Found (%): C; 33.14, H; 2.75, N; 15.88. Calc. (%) for $[(C_{21}H_{19}N_9O_2S)_6Mn_9](CF_3SO_3)_7(H_2O)_{30}(CH_3CN)$: C; 33.16, H; 3.65, N; 15.77.

6.2.1.2: $[(SEt2POAP)_6Mn_9](ClO_4)_4(CF_3SO_3)_4(H_2O)_{24}(CH_3OH)_2$ (**6.2**)

$[(SEt2POAP)_6Mn_9](CF_3SO_3)_9(H_2O)_{15}(CH_3CN)_4$ (**3.1**) (50 mg, 0.01 mmol) was dissolved in methanol (10 mL). $Fe(ClO_4)_3 \cdot H_2O$ (0.13 g, 0.35mmol) was dissolved in methanol (10 mL), and added to the reaction solution. An orange precipitate formed immediately and redissolved upon addition of acetonitrile (3 mL). The resulting dark orange-brown solution was heated for 45 minutes, filtered and cooled. Dark crystals (20 mg, 42 %) formed over several days. Selected IR data (cm^{-1}, Nujol): 1099 (νClO_4^-).

Vis-nir: λ_1 = 649 nm, ε_1 = 1540 $Lmol^{-1}cm^{-1}$, λ_2 = 991 nm, ε_2 = 767 $Lmol^{-1}cm^{-1}$. Elemental analysis: Found (%): C; 33.33, H; 2.78, N; 15.91. Calc. (%) for $[(C_{21}H_{19}N_9O_2S)_6Mn_9](ClO_4)_4(CF_3SO_3)_4(H_2O)_{24}(CH_3OH)_2$: C; 33.35, H; 3.60, N; 15.91. Note: Determination of the number of each type of counter ion is difficult in the absence of a chlorine analysis. The formula quoted for the compound is the best fit of the CHN data, taking into account the number of extra triflate carbons required to arrive at the correct C/N ratio, and the presence of perchlorate indicated by the IR spectrum.

6.2.1.3: $[(2POAP)_6Mn_9](ClO_4)_8(H_2O)_{17.5}(CH_3OH)_3$ (**6.3**)

$[(2POAP)_6Mn_9](ClO_4)_6(H_2O)_{18}$ (150 mg, 0.039 mmol) was dissolved in a 1:1 solution of methanol/acetonitrile (20 mL). $Cu(ClO_4)_2 \cdot 6H_2O$ (250 mg, 0.67 mmol) was added, and the resulting solution gradually turned dark brown. The solution was heated for 2 hours, filtered and cooled. Brown crystals (120 mg, 75 %), not suitable for X-ray diffraction, formed over several days. Selected IR data (cm^{-1}, Nujol): 1068 (νClO_4^-). Vis-nir: λ_1 = 694 nm, ε_1 = 495 $Lmol^{-1}cm^{-1}$, λ_2 = 1010 nm, ε_2 = 504 $Lmol^{-1}cm^{-1}$. Elemental analysis: Found (%): C; 34.22, H; 2.36, N; 18.41. Calc. (%) for $[(C_{19}H_{15}N_9O_2)_6Mn_9](ClO_4)_8(H_2O)_{17.5}(CH_3OH)_3$: C; 34.19, H; 3.36, N; 18.40. See note for **6.2**.

6.2.1.4: $[(SEt2POAP)_6Mn_9](CF_3SO_3)_3Ag_3(CN)_5(OH)(H_2O)_{10}$ (**6.4**)

$[(SEt2POAP)_6Mn_9](CF_3SO_3)_9(H_2O)_{15}(CH_3CN)_4$ (**3.1**) (50 mg, 0.01 mmol) was dissolved in methanol (10 mL). $KAg(CN)_2$ (0.04 g, 0.02 mmol) was dissolved in a solution of water and methanol (2 mL: 3 mL), and added to the grid solution. An orange precipitate formed, and methanol (5 mL) and acetonitrile (15 mL) were added. The mixture was stirred ~ 5 hours, then the remaining solid was filtered off, and the filtrate, a

bright orange solution, was cooled and stored in the dark. Red crystals (40 mg, 92 % based on the X-ray formula mass), suitable for X-ray diffraction, formed after several days. Contamination with $KAg(CN)_2$ resulted in a poor elemental analysis.

6.2.1.5: $[(SEt2POAP)_6Mn_9]Ag_6(CF_3SO_3)_3(NO_3)_9(H_2O)_{17}(CH_3CN)$ (**6.5**)

$[(SEt2POAP)_6Mn_9](CF_3SO_3)_9(H_2O)_{15}(CH_3CN)_4$ (**3.1**) (50 mg, 0.01 mmol) was dissolved in methanol (15 mL). $Ag(NO_3)$ (90 mg, 0.5 mmol) was dissolved in methanol and water (5 mL: 2 mL), and added to the grid solution. The resulting solution was heated for 1 hour, and acetonitrile (2 mL) was added. The resulting clear red solution was cooled and stored in the dark. Red crystals (40 mg, 76 %), suitable for X-ray diffraction, formed over several days. Elemental analysis: Found (%): C; 29.91, H; 2.58, N; 17.11. Calc. (%) for $[(C_{21}H_{19}N_9O_2S)_6Mn_9]Ag_6(CF_3SO_3)_3(NO_3)_9(H_2O)_{17}(CH_3CN)$: C; 29.92, H; 2.90, N; 17.06.

6.2.1.6: $[(SEt2POAP)_6Mn_9(AuCl_3)_4](AuCl_4)_4(H_2O)_{20}(CH_3OH)_{1.5}$ (**6.6**)

$[(SEt2POAP)_6Mn_9](CF_3SO_3)_9(H_2O)_{15}(CH_3CN)_4$ (**3.1**) (100 mg, 0.02 mmol) was dissolved in warm methanol (15 mL). $KAuCl_4$ (100 mg, 0.3 mmol) was dissolved in methanol/water (2.5:1), and added slowly to the grid solution. The resulting solution rapidly turned dark brown, and a brown precipitate formed. Acetonitrile (5 mL) was added, and the precipitate redissolved, forming a clear brown solution, which was heated for 30 mins, filtered, and stored in the dark. A brown microcrystalline product (60 mg, 48 %) formed over one week. Vis-nir: $\lambda = 932$ nm, $\varepsilon = 705$ $Lmol^{-1}cm^{-1}$. Elemental analysis: Found (%): C; 24.43, H; 1.91, N; 12.00, Cl; 15.90. Calc. (%) for $[(C_{21}H_{19}N_9O_2S)_6Mn_9]Au_8Cl_{28}(H_2O)_{20}(CH_3OH)_{1.5}$: C; 24.54, H; 2.58, N; 12.12, Cl;

15.91. Structural data for this compound has been collected, and the structure is currently being refined.

6.2.2: Crystallography:

The diffraction intensities of a purple crystal fragment of **6.1** (0.54 x 0.34 x 0.03 mm) were collected on a Bruker P4/CCD system with graphite monochromated Mo-Kα radiation at -80°C to a maximum 2θ value of 53°. The data were corrected for Lorentz and polarization effects. The structure was solved by direct methods [72-73]. Some non-H atoms were refined anisotropically while the rest were refined isotropically. Hydrogen atoms were included in calculated positions with isotropic thermal parameters set twenty percent greater than those of their bonding partners at the time of their inclusion, but were not refined. There are fifteen hydrogen atoms missing from the lattice water and methanol molecules. One half occupancy triflate anion was modeled with disordered sulphur and oxygen atoms and was fixed for the final round of isotropic refinement to achieve convergence. Neutral atom scattering factors [74], and anomalous dispersion terms [75-76] were taken from the usual sources. All calculations were performed using the teXsan crystallographic software package [77] of Molecular Structure Corporation except for refinement, which was performed using SHELXL-97 [72a].

The diffraction intensities of a red crystal chip of **6.5** (0.35 x 0.26 x 0.06 mm) were collected on a Rigaku Saturn CCD area detector with graphite monochromated Mo-Kα radiation at -120°C to a maximum 2θ value of 61.4°. The data were treated similarly to **6.1**. Hydrogen atoms were introduced in calculated positions with isotropic thermal parameters set twenty percent greater than those of their bonding partners. They were

refined on the riding model. The model contains two full occupancy triflate anions which were refined isotropically, and nine full-occupancy nitrate anions, six refined anisotropically and three refined isotropically; two show some disorder. A charge of -0.75 is missing from the model for charge balance, and the formula has been adjusted to reflect this, assuming that it is 0.75 nitrate anions that should be present, by subtracting this from the lattice solvent molecules. Ag(1) (0.35 occupancy) and Ag(2) (0.15 occupancy) make up one half-occupancy Ag atom, disordered over two sites. C(11), C(12) (both at 0.3 occupancy), C(13) and (C14) (both at 0.7 occupancy) make up one full-occupancy ethyl group, also disordered over two sites. The corresponding five hydrogens have been omitted from the model, but are accounted for in the formula. Ag(5) is at ¼-occupancy. Ag(8) (0.75 occupancy) and Ag(9) (0.25 occupancy) make up a full-occupancy Ag atom, disordered over two sites. The model contains a total of fourteen oxygen atoms (from twenty one partial-occupancy oxygen atoms) as lattice solvent water molecules which were refined isotropically. The corresponding twenty eight hydrogen atoms were not included in the model. In total, there are thirty three hydrogen atoms missing from the symmetry expanded model.

6.4 was treated similarly to **6.5**. Refinement of the structure is not complete, and it is therefore being included as a preliminary structure. Crystal data for **6.1**, **6.4** and **6.5** are abbreviated in Table 6.1.

Table 6.1: Summary of Crystallographic data for **6.1**, **6.4**, **6.5**.

Compound	**6.1**	**6.4**	**6.5**
Empirical Formula	$C_{135}H_{138}O_{39}N_{54}F_{18}S_{12}Mn_9$	$C_{132.75}H_{134}Ag_3F_9Mn_9N_{60}O_{31}S_9$	$C_{128}Ag_{5.75}F_6Mn_9N_{63.75}O_{61.25}S_8H_{142}$
M/gmol^{-1}	4362.05	4343.47	5038.57
Crystal System	triclinic	triclinic	triclinic
Space Group	P-1 (#2)	P-1 (#2)	P-1 (#2)
a/Å	19.171(2)	18.202(7)	18.134(2)
b/Å	20.758(2)	19.477(8)	19.806(7)
c/Å	24.905(2)	30.509(11)	28.352(14)
α/°	81.207(2)	101.807(3)	83.15(7)
β/°	75.954(2)	92.944(6)	79.66(5)
γ/°	83.767(2)	92.944(6)	66.28(6)
V/ Å^3	9475(1)	9650(6)	9158.4(57)
ρ_{calcd}/gcm^{-3}	1.529	1.495	1.827
T/°C	-80(1)	-120(1)	-120(1)
R1	0.093	0.206	0.1139
wR2	0.331	(R_w)0.547	0.3185

6.3: Results and Discussion:

6.3.1: Description of Crystal Structures:

6.3.1.1: $[(SEt2POAP)_6Mn_9](CF_3SO_3)_7(H_2O)_{30}(CH_3CN)$ (**6.1**)

The structure of the main cation of **6.1** is shown in Figure 6.1, and important bond distances and angles are listed in Table 6.2. The structure appears to be a typical [3x3] Mn(II)$_9$ grid, with six ligands homoleptically bound to the [$Mn_9(\mu\text{-}O_{12})$] core. Mn-N bond distances range from 2.017-2.347 Å, Mn-O bond distances fall between 2.146 and 2.321 Å, and Mn-O-Mn angles range from 127.37-135.5°. Mn-Mn distances range from 3.906-4.174 Å. These values are generally typical of Mn(II)$_9$ grids, however, the range

of Mn-N distances and Mn-O-Mn angles is larger than usual, with some Mn-N distances shorter than is typical for $Mn(II)_9$ grids, while some of the Mn-O-Mn angles are larger than the usual values. This is typical in cases where Mn(III) is present [32, 55, 66].

Figure 6.2 depicts the core of the grid, with averaged Mn-L distances for **6.1** compared with averaged Mn-L distances for compound **3.2**. For all four corner sites, and two of the side sites, the averaged bond distances are shorter in **6.1** than in **3.2**, suggesting that oxidation of Mn(II) to Mn(III) has taken place at these sites. Bond valence sum (BVS) calculations [127-130] were performed on **6.1**, and it was found that the four corner sites and one side site had significant Mn(III) character, while the remaining sites were chiefly Mn(II). One side site and the center site were found not to have any Mn(III) character. Since none of the sites could be definitively characterized as being solely occupied by Mn(III), it is reasonable to assume that different sites have been oxidized in individual molecules, and the X-ray structure reveals an averaged situation.

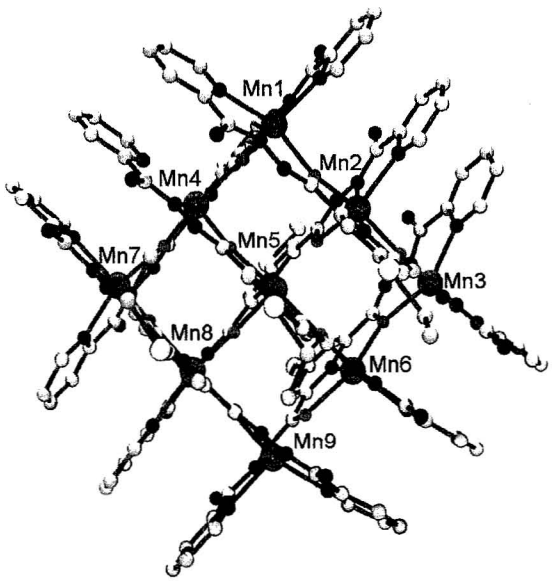

Figure 6.1: POV-RAY image of **6.1**. Mn=magenta, N=blue, O=red, S=yellow, C=grey.

Table 6.2: Selected bond distances (Å) and angles (°) for **6.1**.

Mn1-N3	2.017(5)	Mn6-N16	2.038(5)
Mn1-N30	2.033(5)	Mn6-N50	2.053(6)
Mn1-O1	2.146(4)	Mn6-O12	2.091(5)
Mn1-N1	2.188(6)	Mn6-O11	2.098(5)
Mn1-O7	2.226(4)	Mn6-O11	2.098(5)
Mn1-N28	2.283(5)	Mn6-N18	2.258(5)
Mn2-N39	2.153(5)	Mn7-N34	1.988(6)
Mn2-O9	2.171(4)	Mn7-N21	1.996(6)
Mn2-N5	2.193(5)	Mn7-O8	2.163(4)
Mn2-O1	2.211(4)	Mn7-N36	2.185(6)
Mn2-O2	2.224(5)	Mn7-N19	2.234(6)
Mn2-N37	2.347(5)	Mn7-O5	2.291(5)
Mn3-N7	1.994(8)	Mn8-N43	2.122(5)
Mn3-N48	2.030(8)	Mn8-N23	2.142(5)
Mn3-O2	2.176(5)	Mn8-O10	2.142(4)
Mn3-N46	2.213(6)	Mn8-O6	2.217(5)
Mn3-N9	2.216(6)	Mn8-O5	2.218(4)
Mn3-O11	2.220(5)	Mn8-N45	2.279(6)
Mn4-N12	2.144(5)	Mn9-N25	1.992(7)
Mn4-N32	2.164(5)	Mn9-N52	2.041(8)
Mn4-O3	2.165(4)	Mn9-N27	2.162(7)
Mn4-O8	2.191(4)	Mn9-O6	2.163(4)
Mn4-O7	2.221(4)	Mn9-N54	2.252(6)
Mn4-N10	2.299(6)	Mn9-O12	2.321(5)
Mn5-N41	2.168(5)	Mn-Mn:	3.906-4.174
Mn5-N14	2.183(5)		
Mn5-O3	2.192(4)	S4···N29'	3.695
Mn5-O9	2.197(4)		
Mn5-O10	2.206(4)	S4···C67 3.590	
Mn5-O4	2.245(4)	S4···H73-C67	3.180, 108.16
Mn1-O1-Mn2	129.3(2)	S6···N53 3.865	
Mn3-O2-Mn2	132.0(2)		
Mn4-O3-Mn5	127.37(19)	π- π	3.702
Mn6-O4-Mn5	130.85(19)		
Mn8-O5-Mn7	135.5(2)		
Mn9-O6-Mn8	133.1(2)		
Mn4-O7-Mn1	131.7(2)		
Mn7-O8-Mn4	132.2(2)		
Mn2-O9-Mn5	128.77(19)		
Mn8-O10-Mn5	128.66(19)		
Mn6-O11-Mn3	133.6(3)		
Mn6-O12-Mn9	134.4(3)		

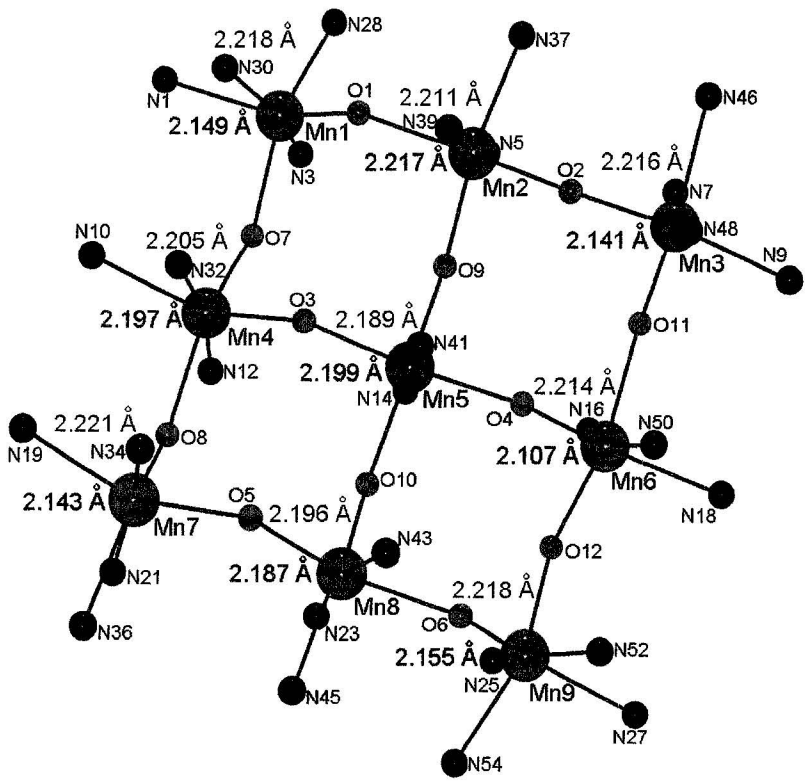

Figure 6.2: Comparison of the average Mn-L bond lengths of **3.1** (pink) to **6.1** (brown).

The unit cell of **6.1** is depicted in Figure 6.3. The compound is layered, with π-interactions between the terminal pyridine rings of the ligands holding the grid molecules in rows (Figure 6.4a). The interactions are displaced, and the shortest contact distance within a row is ~ 3.7 Å. There are no interactions between rows. The layers are loosely held together via S···N and S···H interactions (Figure 6.4b). There is a relatively short contact (3.695 Å) between a sulphur atom on one grid, and an amine nitrogen atom of the adjacent molecule. There is a second contact between the same S atom and a carbon atom for the terminal pyridine ring of the adjacent molecule. The S4···C67 distance is

3.590 Å. The distance between S4 and the aromatic proton is 3.180 Å, with an S4···H73-C67 angle of 108°. This is long for a hydrogen bonding contact, but H-bonds involving C-H have been reported with X···C distances in excess of 4 Å [1], and for hydrogen bonds involving sulphur, S-C distances of longer than 3.4 Å are common [116]. There are similar contacts on the other end of the molecule, involving S6 and N53, with an S···N distance of 3.865 Å.

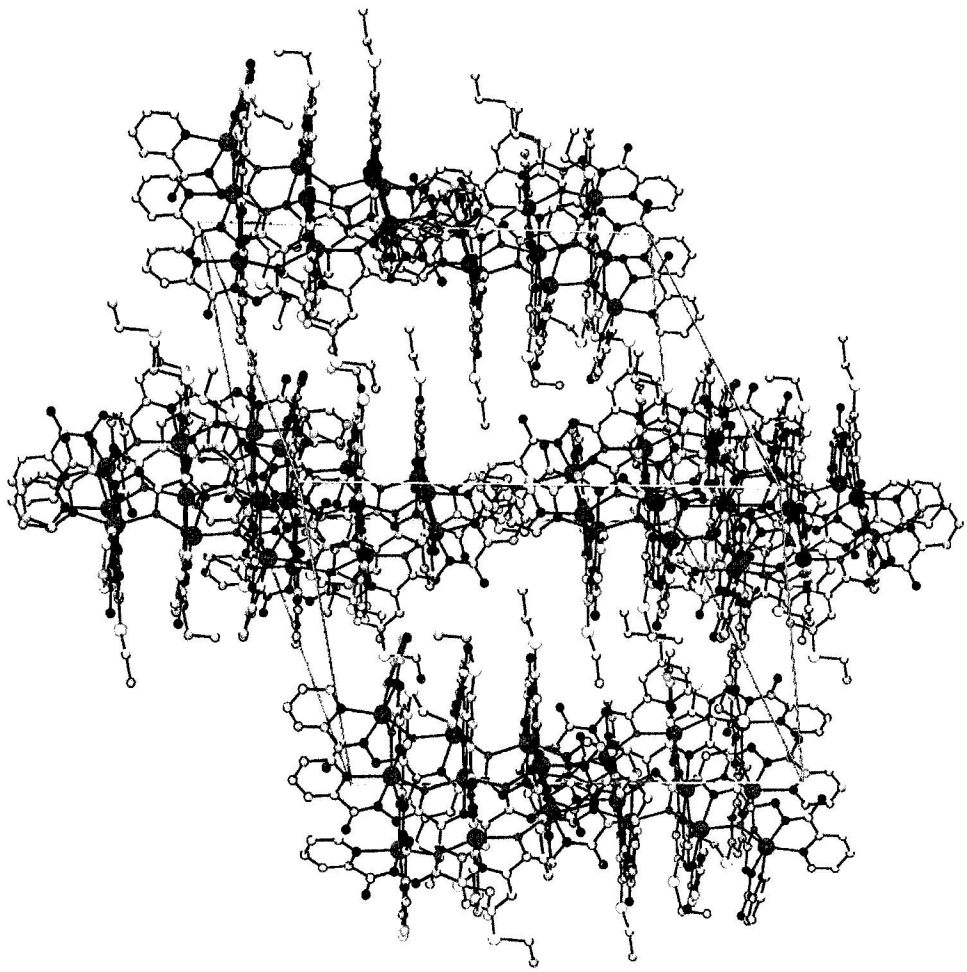

Figure 6.3: Unit cell of **6.1**.

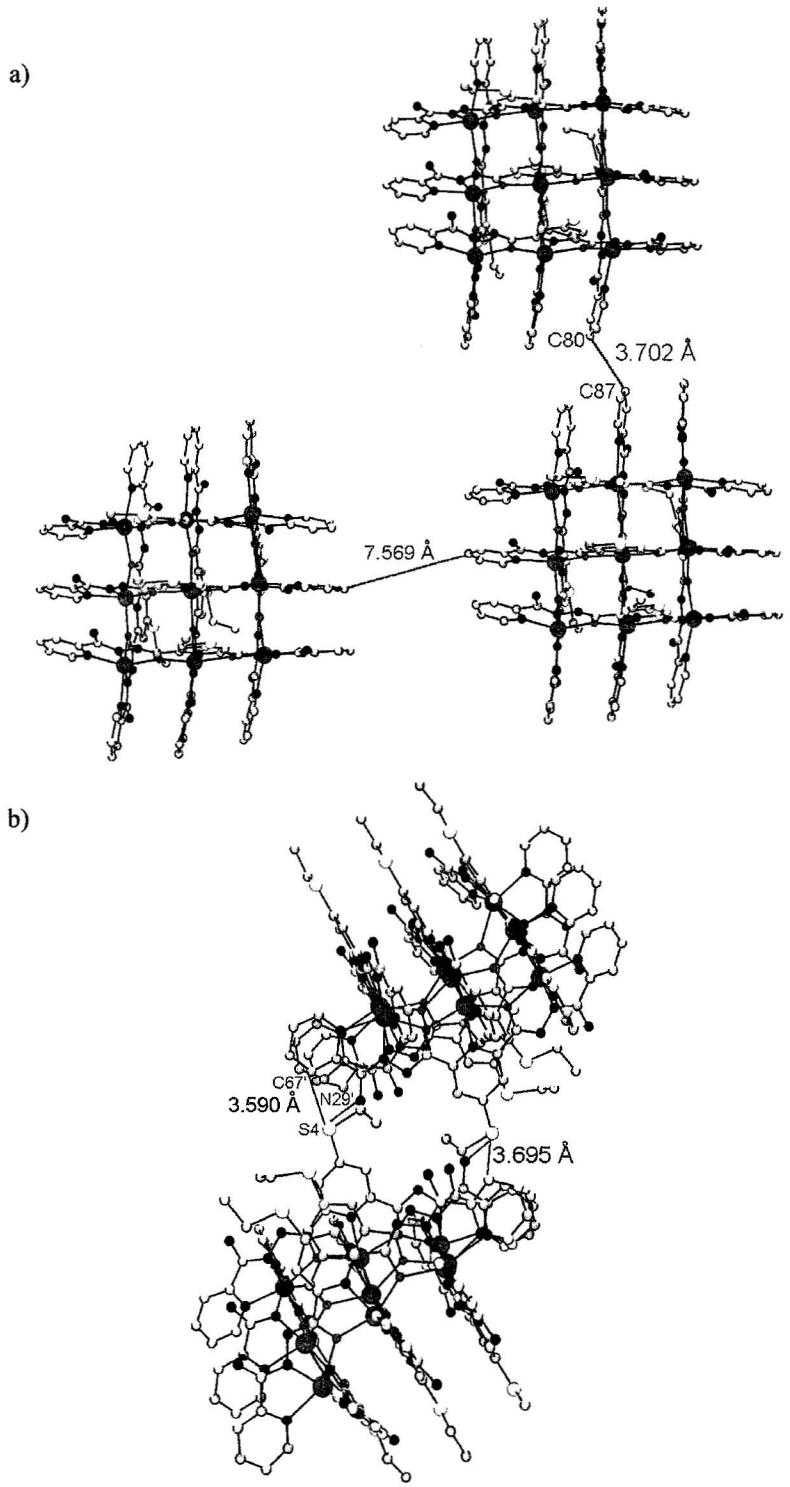

Figure 6.4: a) Edge to edge π-interactions in **6.1**. Long inter-row distance (purple) indicates no interactions between rows. b) S···N interactions in **6.1**.

6.3.1.2: $[(SEt2POAP)_6Mn_9](CF_3SO_3)_3Ag_3(CN)_5(OH)(H_2O)_{10}$ (**6.4**)

The structure of **6.4** is shown in Figure 6.5, and important grid bond distances and angles are listed in Table 6.3. As the structure is preliminary, an in depth discussion is not appropriate. However, for comparison purposes, Mn-N bond distances range from 2.111 to 2.339 Å, Mn-O bond distances range between 2.117 and 2.226 Å, and Mn-O-Mn angles range from 126.6 to 128.2°. Mn-Mn distances range from 3.866 to 3.924 Å. The core of **6.4** is shown in Figure 6.6.

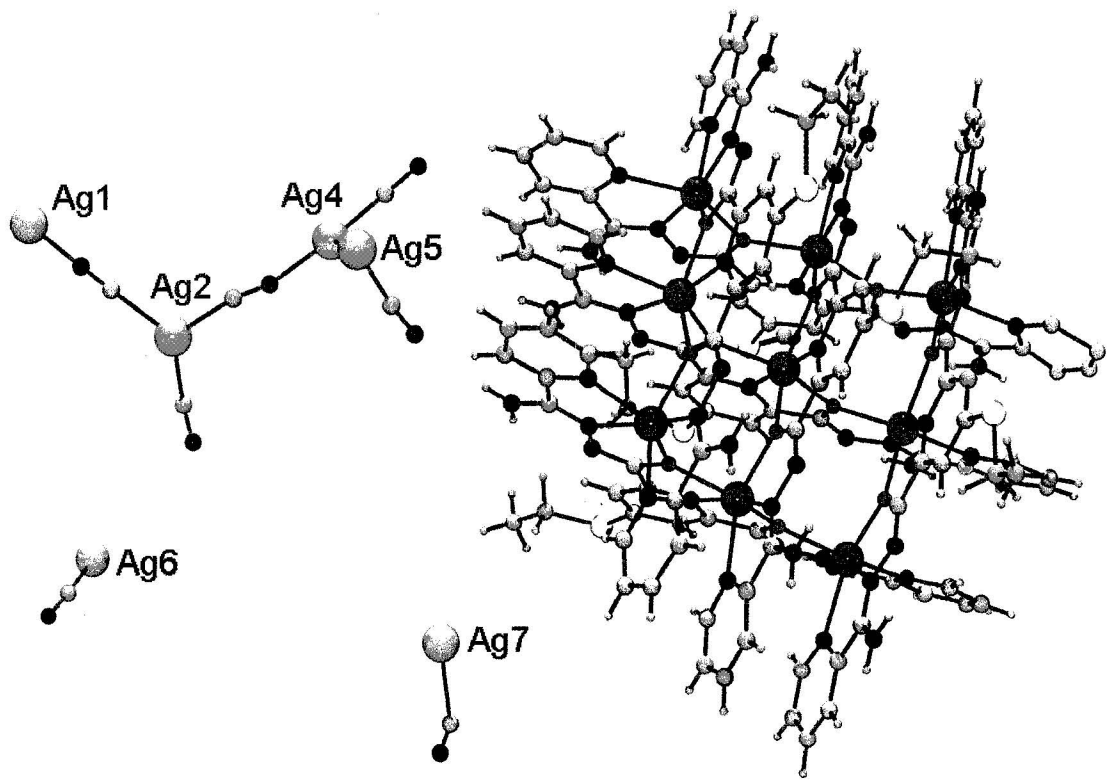

Figure 6.5: POV-RAY depiction of the asymmetric unit of **6.4**. Mn = magenta, N = blue, O = red, S = yellow, H = aquamarine, C = Grey, Ag = blue-grey. Ag6 and Ag7 are free $Ag(CN)_2^-$ anions in the expanded structure.

Table 6.3: Selected bond distances (Å) and angles (°) for **6.4**.

Mn1-N34	2.111(11)	Mn7-N21	2.121(8)
Mn1-O1	2.117(10)	Mn7-O7	2.126(6)
Mn1-N3	2.127(13)	Mn7-N30	2.122(8)
Mn1-O8	2.160(7)	Mn7-O5	2.176(6)
Mn1-N36	2.299(10)	Mn7-N19	2.308(9)
Mn1-N1	2.296(12)	Mn7-N28	2.321(8)
Mn2-N43	2.112(9)	Mn8-N39	2.121(7)
Mn2-N5	2.137(9)	Mn8-O9	2.136(6)
Mn2-O10	2.151(6)	Mn8-N23	2.168(8)
Mn2-O2	2.180(7)	Mn8-O5	2.180(6)
Mn2-O1	2.211(8)	Mn8-O6	2.222(6)
Mn2-N45	2.319(10)	Mn8-N37	2.323(7)
Mn3-N52	2.132(9)	Mn9-N48	2.122(7)
Mn3-012	2.136(9)	Mn9-O6	2.136(6)
Mn3-N7	2.144(8)	Mn9-N25	2.148(7)
Mn3-O2	2.170(7)	Mn9-O11	2.155(5)
Mn3-N9	2.309(9)	Mn9-N46	2.264(8)
Mn3-N54	2.339(8)	Mn9-N27	2.340(8)
Mn4-N12	2.131(9)	Mn1-O1-Mn2	127.9(4)
Mn4-N32	2.142(9)	Mn2-O2-Mn3	128.0(3)
Mn4-O3	2.159(7)	Mn4-O3-Mn5	126.8(3)
Mn4-O8	2.226(7)	Mn6-O4-Mn5	126.9(3)
Mn4-O7	2.223(6)	Mn7-O5-Mn8	127.4(3)
Mn4-N10	2.338(11)	Mn9-O6-Mn8	127.4(3)
		Mn7-O7-Mn4	127.0(3)
Mn5-N41	2.164(7)	Mn1-O8-Mn4	127.0(4)
Mn5-O9	2.171(6)	Mn8-O9-Mn5	128.2(3)
Mn5-O3	2.174(6)	Mn2-O10-Mn5	127.7(3)
Mn5-O10	2.190(6)	Mn9-O11-Mn6	126.6(2)
Mn5-N14	2.184(7)	Mn3-O12-Mn6	128.1(3)
Mn5-O4	2.190(6)		
		Mn-Mn:	3.866-3.9924
Mn6-O4	2.132(6)		
Mn6-N16	2.143(7)	Ag···S:	3.199, 3.757
Mn6-N50	2.155(7)		
Mn6-O11	2.196(6)	CN···C_{ar}	3.456, 3.538, 3.353
Mn6-O12	2.219(6)	CN···C_{me}	3.886
Mn6-N18	2.333(7)	CN···NH_2	3.301, 3.580

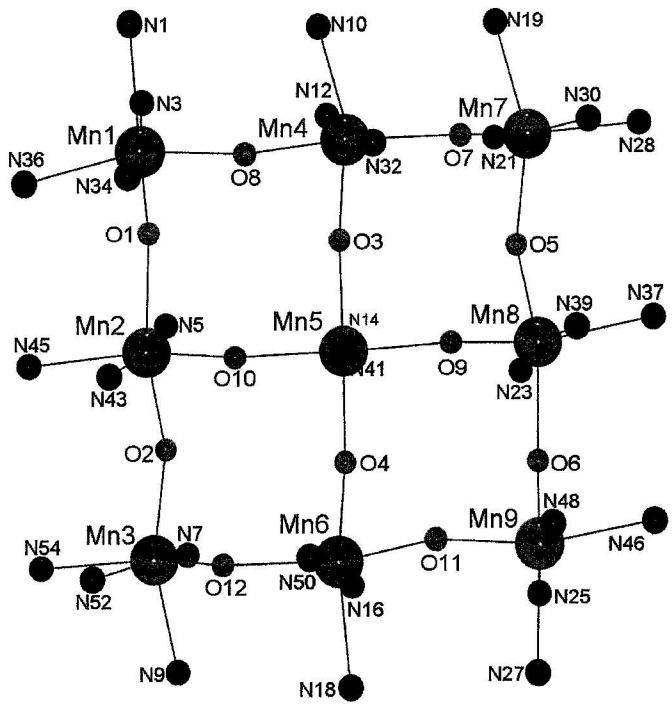

Figure 6.6: POV-RAY depiction of the core of **6.4.**

There are three triflate anions present in the structure. The remaining positive charge from the $Mn(II)_9$ grid is balanced by a polymeric $Ag(CN)_x$ chain and two partial occupancy $Ag(CN)_2$ anions. The polymeric $Ag(CN)_x$ chain is pictured in Figure 6.7. It consists of a repeating unit of six $Ag(CN)_x$ groups. Three of these are directly bonded to each other in a linear arrangement (Ag4-Ag5-Ag4), with an Ag-Ag bond distance of 3.019 Å, and an Ag-Ag-Ag angle of 180.0°. Ag-Ag distances in previously reported $Ag(CN)_x$ chain structures range from 2.7 to 3.2 Å, so a distance of 3.019 Å indicates an interaction of moderate strength [117-119]. Ag5 has a distorted square planar geometry, while the Ag4 sites at the ends of the linear fragment have distorted T-shaped geometry. The linear fragment is bridged by a CN group to a distorted trigonal planar Ag center

(Ag2) at either end. The Ag-N distance to the bridging cyanide anion is 2.088 Å. Ag2 is in turn bridged to a linear Ag cation (Ag1), with an Ag-N bridging distance of 2.062 Å. Ag-N distances vary widely in literature reports, from 2.085- 2.979 Å [118,121-124]. The distances in the present compound are extremely short, indicating a strong interaction. Ag1 is bridged to a second Ag2 cation, which is bridged to the next linear three Ag fragment to repeat the chain. Bond distances and angles specific to the $Ag(CN)_x$ chain are listed in Table 6.4.

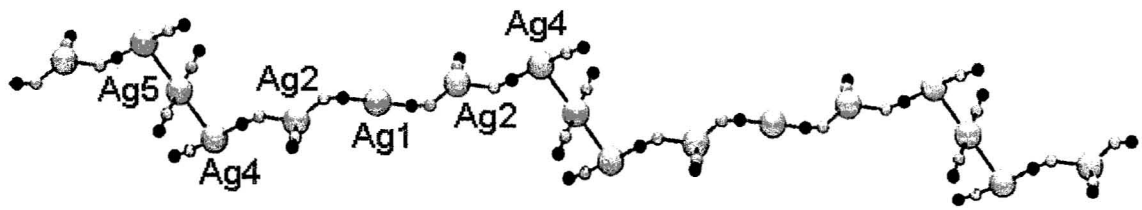

Figure 6.7: Polymeric $Ag(CN)_x$ chain.

Table 6.4: Selected bond distances (Å) and angles (°) for the $Ag(CN)_x$ chain.

Ag1-N55	2.062(14)	Ag4-Ag5-Ag4	179.998(1)
Ag1-N55	2.062(14)		
Ag2-C128	2.076(12)		
Ag2-C127	2.175(11)		
Ag2-C129	2.280(11)		
Ag4-C130	1.96(3)		
Ag4-N57	2.088(12)		
Ag4-O13	2.165(9)		
Ag4-Ag5	3.0195(17)		
Ag5-C131	1.985(18)		
Ag5-C131	1.985(18)		
Ag5-Ag4	3.0196(17)		
Ag5-Ag3	3.032(4)		
Ag6-C132	1.993(18)		
Ag6-C132	1.993(18)		
Ag7-C133	2.32(4)		

There are no direct bonding interactions between the $Ag(CN)_x$ chain and the $Mn(II)_9$ grid. However, there are some close contacts between the two (Figure 6.8). There are two S···Ag contacts, one between Ag2 and S5, with an Ag···S distance of 3.199 Å, which is well within the sum of the van der Waals radii for Ag and S (3.52 Å) [116], and a second between Ag1 and S6, with an Ag···S distance of 3.757 Å. There are also a number of contacts which appear to be H-bonding in nature. At the current level of refinement, it is not appropriate to discuss the positions of the hydrogen atoms. However, the distances between the cyanide nitrogen atoms of the chain and the grid should be reliable. There are two probable hydrogen bonds between cyanide N atoms and amine groups of the grid. The N-N distances are 3.301 and 3.580 Å. These are within the range of reasonable N-X distances for amine H-bonding [1]. There are two probable H-bonds between cyanide N atoms and aromatic protons. The N-C distances are 3.538 and 3.456 Å. Again, these values are reasonable for weak H-bonds. Finally, there is one possible H-bond from a cyanide N atom to the methyl group of a thioether. The N-C distance is 3.886 Å, which is within the reported range for weak H-bonds involving alkane protons [1]. The unit cell of **6.4** is pictured in Figure 6.9. The $Ag(CN)_x$ chains run along the outside of the unit cell, but do not penetrate it. The grid molecules fit into the bends in the chains.

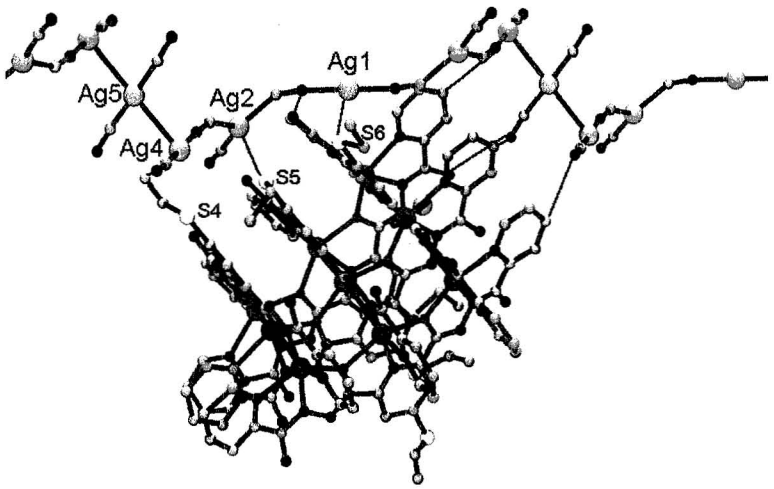

Figure 6.8: Interactions between the $Mn(II)_9$ grid and the $Ag(CN)_x$ chain. Ag-S interactions are highlighted in green, H-bonding interactions in purple.

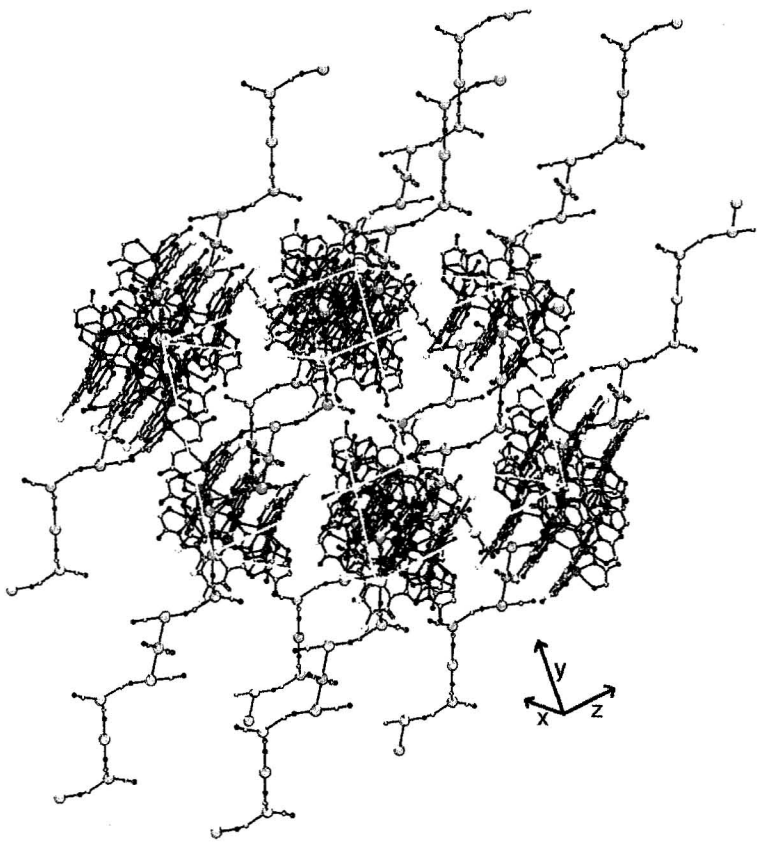

Figure 6.9: Unit cell of **6.4**.

6.3.1.3: $[(SEt2POAP)_6Mn_9]Ag_6(CF_3SO_3)_3(NO_3)_9(H_2O)_{17}(CH_3CN)$ (**6.5**)

The asymmetric unit of **6.5** is pictured in Figure 6.10, and important bond distances and angles are listed in Table 6.5. The core structure consists of a typical [3x3] $Mn(II)_9$ grid. Mn-N distances range from 2.118-2.404 Å, Mn-O distances are between 2.140 and 2.257 Å, and Mn-O-Mn angles range from 124.0-130.0°. Some of these Mn-N distances are longer than is generally observed in [3x3] $Mn(II)_9$ grids, while some of the Mn-O-Mn angles are smaller. This may indicate a slight distortion of the grid core. Mn-Mn distances are typical, ranging from 3.855 to 4.023 Å. The diagonal Mn-Mn distances of the $[Mn_9(\mu\text{-}O_{12})]$ core are 10.895 and 10.681 Å, which are slightly further apart than typical of $Mn(II)_9$ grids and may again indicate a slight distortion of the core of the molecule. The core of the grid is pictured in Figure 6.11.

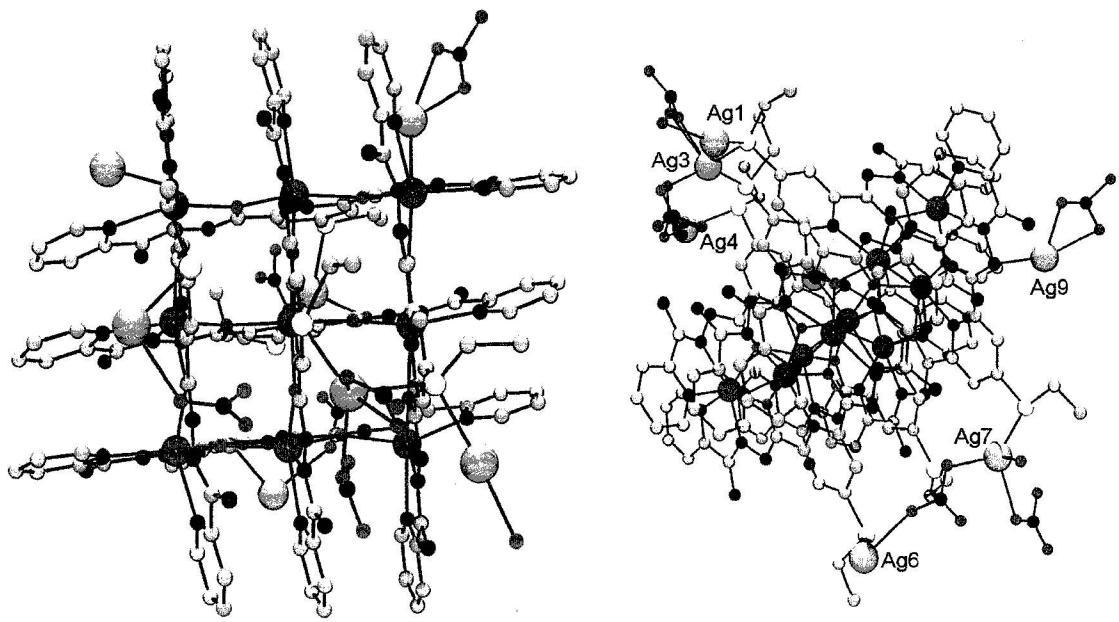

Figure 6.10: Asymmetric unit of **6.5**. Mn = magenta, N = blue, O = red, S = yellow, Ag = grey-blue, C = grey.

Table 6.5: Selected bond distances (Å) and angles (°) for **6.5**.

Mn1-N3	2.144(8)	Mn7-N34	2.138(9)	Ag1-O21	2.39(2)
Mn1-N30	2.157(8)	Mn7-N21	2.149(9)	Ag1-O53	2.56(4)
Mn1-O1	2.172(7)	Mn7-O8	2.175(7)	Ag1-S1	2.586(6)
Mn1-O7	2.226(7)	Mn7-O5	2.226(7)		
Mn1-N28	2.273(10)	Mn7-N19	2.288(9)	Ag3-O19	2.374(13)
Mn1-N1	2.404(10)	Mn7-N36	2.375(10)	Ag3-S2	2.480(4)
				Ag3-O33	2.48(4)*
Mn2-O9	2.148(7)	Mn8-O10	2.140(7)	Ag3-O36	2.53(4)*
Mn2-N39	2.165(9)	Mn8-N43	2.146(9)	Ag3-S1	2.751(5)
Mn2-N5	2.180(8)	Mn8-O6	2.182(8)		
Mn2-O2	2.214(8)	Mn8-N23	2.189(8)	Ag4-N22	2.269(8)
Mn2-O1	2.257(7)	Mn8-O5	2.225(7)	Ag4-O39	2.390(9)
Mn2-N37	2.304(10)	Mn8-N45	2.314(10)	Ag4-S3	2.497(3)
				Ag4-O39	2.533(9)
Mn3-N7	2.132(11)	Mn9-N25	2.133(10)		
Mn3-O11	2.175(8)	Mn9-N52	2.148(9)	Ag5-O56	2.02(8)
Mn3-N48	2.181(12)	Mn9-O6	2.168(7)	Ag5-N24	2.502(11)
Mn3-O2	2.217(7)	Mn9-O12	2.209(8)		
Mn3-N9	2.287(11)	Mn9-N27	2.306(10)	Ag6-N31	2.266(9)
Mn3-N46	2.302(12)	Mn9-N54	2.312(10)	Ag6-O43	2.419(9)
				Ag6-S4	2.483(3)
Mn4-N12	2.132(8)	Mn1-O1-Mn2	130.0(3)	Ag6-O43	2.573(8)
Mn4-O3	2.174(7)	Mn2-O2-Mn3	130.4(4)		
Mn4-N32	2.192(7)	Mn4-O3-Mn5	128.9(3)	Ag7-O50	2.343(16)
Mn4-O8	2.223(7)	Mn6-O4-Mn5	129.6(3)	Ag7-O22	2.439(11)
Mn4-O7	2.245(7)	Mn8-O5-Mn7	124.0(3)	Ag7-S6	2.477(5)
Mn4-N10	2.363(9)	Mn9-O6-Mn8	126.9(3)	Ag7-S5	2.526(3)
		Mn1-O7-Mn4	125.6(3)		
Mn5-O9	2.183(7)	Mn7-O8-Mn4	129.6(3)	Ag9-O30	2.201(19)
Mn5-N14	2.192(8)	Mn2-O9-Mn5	125.8(3)	Ag9-O23	2.274(14)
Mn5-O10	2.193(7)	Mn8-O10-Mn5	127.7(3)	Ag9-O29	2.35(6)*
Mn5-O4	2.198(7)	Mn3-O11-Mn6	127.3(4)	Ag9-N49	2.413(14)
Mn5-O3	2.202(7)	Mn6-O12-Mn9	128.8(3)	Ag9-O28	2.57(3)*
Mn5-N41	2.208(8)				
		Mn-Mn: 3.855-4.023		Mn-Mn (intergrid): shortest	
Mn6-N16	2.118(11)				
Mn6-O4	2.155(7)	edges:	7.734, 7.855	bridged:	12.252
Mn6-N50	2.183(9)		7.985, 7.888		
Mn6-O12	2.190(8)			non-bridged:	8.458
Mn6-O11	2.253(8)	diagonals:	10.895, 10.681		
Mn6-N18	2.321(11)				
Ag1-Ag3	4.468	Ag4-Ag4'	3.889	Ag7-Ag9	7.912
Ag1-Ag3'	5.903	Ag4-O-Ag4'	104.35	Ag7-Ag9'	4.844
Ag1-Ag1'	5.577			Ag7-Ag7'	8.312
Ag3-Ag3'	8.862	Ag6-Ag6'	3.998	Ag9-Ag9'	10.143
		Ag6-O-Ag6'	106.39		

* O atoms are disordered over two sites

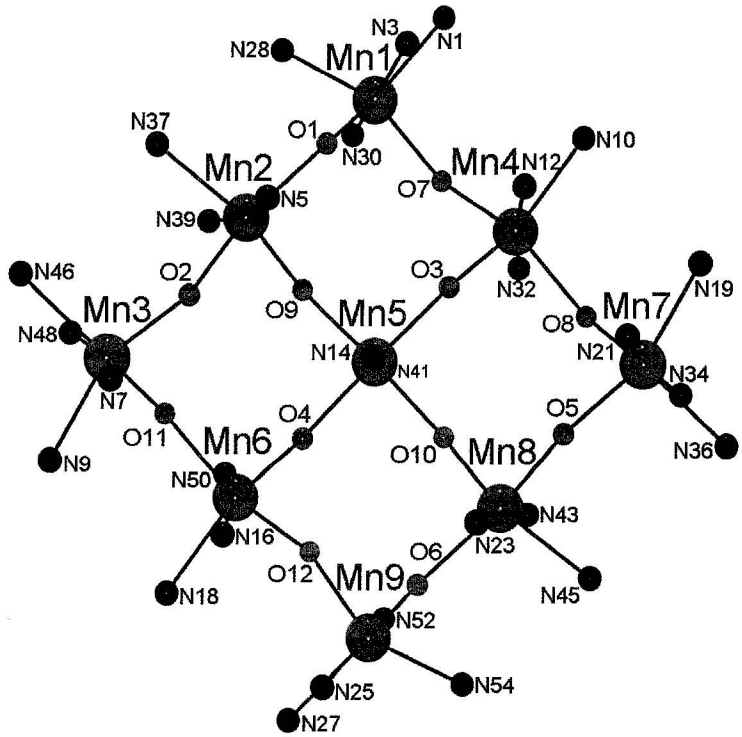

Figure 6.11: Core of **6.5**, showing only coordinating atoms.

The structure of **6.5**, unlike that of **6.4**, has direct bonding connections between Ag(I) cations and the grid molecule. There are an average of six Ag(I) sites per grid, though in the structure some of the cations are disordered over two sites making it appear as though there are more Ag(I) cations in the compound. Some of these have been removed from the structural representations for clarity. Ag(I) interactions occur with the sulphur atoms of the ligand thioether groups, as well as with diazine nitrogen atoms. All of the Ag(I) cations have bonds to sulphur, except Ag5 and Ag9, which are bound to a diazine nitrogen atom and to oxygen atoms, from lattice water in the case of Ag5, and nitrate anions in the case of Ag9. Ag3 and Ag7 bridge two sulphur atoms, while all other Ag(I) cations only bind one S-group. Ag-S bond distances range from 2.477 to 2.751 Å,

which is within the normal range for Ag-S bonds (2.47 to 2.97 Å) in the literature [116, 119, 125]. Ag-N bond distances range from 2.266-2.502 Å, which is well within the normal range for Ag-N bonds (*vide supra*). Ag-O distances in **6.5** range from 2.02-2.503 Å, with all but one falling in the range 2.343-2.503 Å. Ag-O distances reported in the literature generally range between 2.371 and 2.594 Å [116, 125-126].

Closer examination of the structure reveals that the grid molecules are not discrete, but are in fact bridged to each other by silver cations, forming a three dimensional network (Figure 6.12). Steric considerations due to the formation of the network may be responsible for the shorter than average Ag-O bonds observed in **6.5**. Each grid molecule is bridged to four others, one on each corner of the grid, with two of the bridges on each face of the grid molecule.

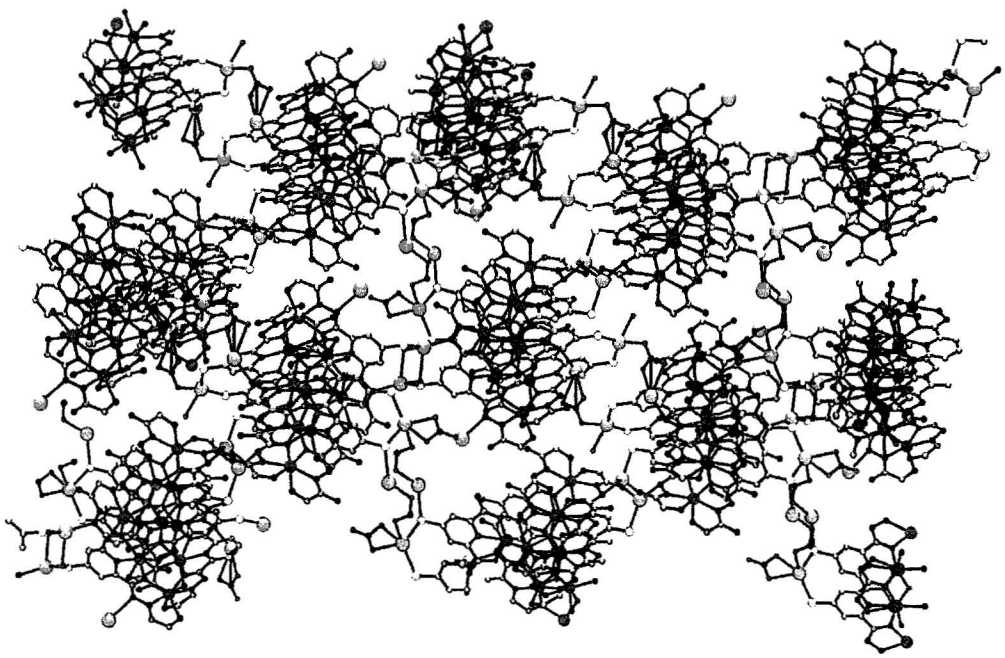

Figure 6.12: Three dimensional network of bridged grid molecules in **6.5**. Mn = magenta, N = blue, O = red, S = yellow, Ag = grey-blue, C = grey.

The first inter-grid bridge is very long, and involves four Ag(I) cations; Ag1 and Ag3 from each of the bridged grids. The inter-grid connection is pictured in Figure 6.13. The pathway of the interactions starts at S1 of the first grid molecule, which is bound to Ag1. Ag1 is coordinated by one oxygen atom of a nitrate anion. A second oxygen atom of the nitrate binds to Ag3', which is coordinated to S1'and S2' of the adjacent grid molecule. The same connection is repeated from Ag1' of the second grid molecule to Ag3 of the first, resulting in a ring of four Ag(I) cations bridging the two grid molecules. The distance between Ag1 and Ag3' is 5.903 Å, which results in a Mn-Mn separation of ~18 Å in the bridged grid molecules.

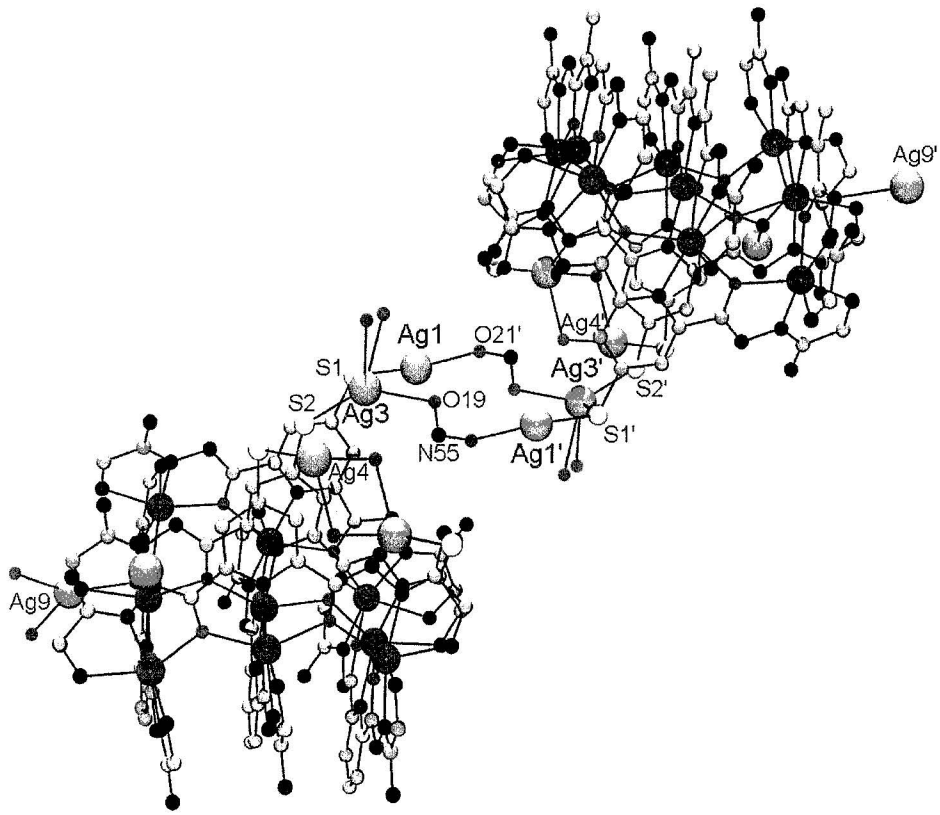

Figure 6.13: Bridging pathway via Ag1 and Ag3. Non-coordinating atoms removed for clarity.

The second inter-grid bridge involves two Ag(I) cations, Ag4 of each of the two bridged grids. This bridge is located on the same face of the grid molecule as is the Ag1-Ag3' bridge. The Ag4 bridge is short, running from S3 of the first grid molecule to Ag4, which is coordinated to a diazine nitrogen atom of the second grid. The reverse pathway occurs from the second grid molecule to the first. There is a second connection between grids involving the Ag4 sites as Ag4 is bridged to Ag4' by two single oxygen atom bridges (nitrate). The Ag···Ag distance is 3.889 Å, with an Ag-O-Ag angle of 104.35°. These values are similar to those reported for other nitrate-oxygen bridged Ag(I) cations [126]. These short inter-grid bridges lead to a Mn-Mn separation of 12.252 Å between Mn(II) sites in bridged grid molecules. The Ag4 bridging connections are pictured in Figure 6.14.

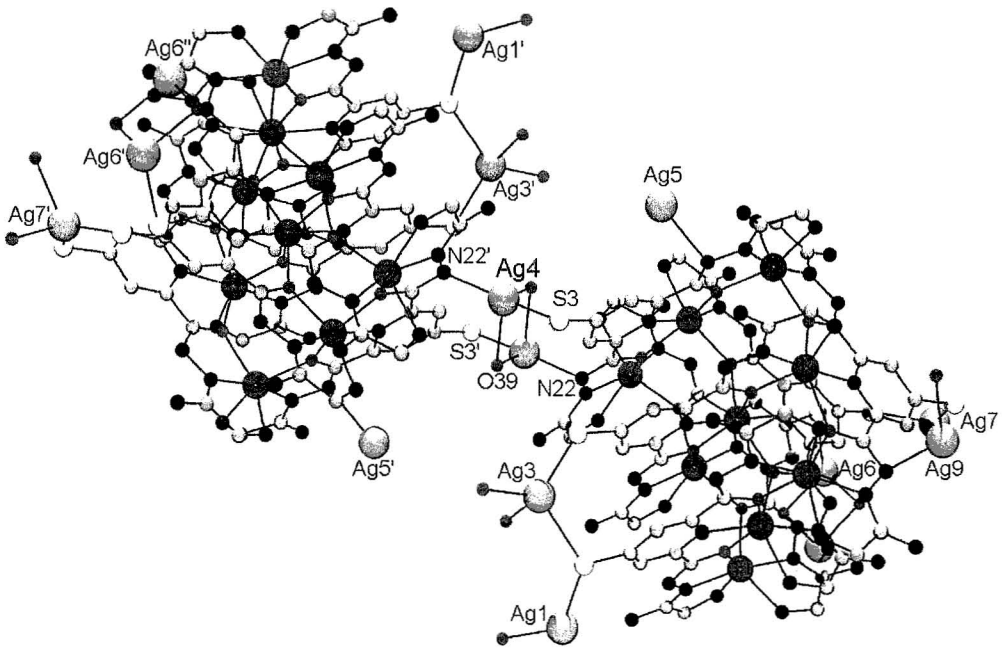

Figure 6.14: Bridging pathway via Ag4. Atoms not involved in the bridging have been removed for clarity.

The third inter-grid bridging connection occurs between the Ag6 cations of the two connected grids. The connection is largely similar to the Ag4 connection on the opposite face of the grid molecules, with the short path running from S4 of the first grid, to Ag6 and then to diazine N31' of the adjacent grid molecule. The nitrate bridged Ag6···Ag6' connection is slightly longer than the Ag4···Ag4' connection, with an Ag···Ag distance of 3.998 Å and an Ag-O-Ag angle of 106.39°. The Mn(II)-Mn(II) distances between grids are also slightly longer, at 12.346 Å.

The final bridging connection between grids involves four Ag(I) cations; Ag7 and Ag9 of the two bridged grid molecules (Figure 6.15). The pathway begins at diazine N29, which is bound to Ag9. Ag9 is further coordinated by a bidentate nitrate anion. The third nitrate oxygen bridges Ag9 to Ag7' of the second grid molecule, which coordinates S5' and S6'. The connection runs symmetrically from Ag9' to Ag7. The Ag7···Ag9 distance for this bridge is 4.844 Å, leading to a Mn(II) Mn(II) separation of 12.942 Å in bridged grid molecules.

It is interesting to note that the Ag1-Ag3 bridging pathway is the only one of the four not to involve diazine N atoms. This results in a Mn(II)-Mn(II) separation approximately 6 Å longer than those created by the other pathways. Of additional interest, Mn(II)-Mn(II) distances in adjacent, but non-bridged, grid molecules in the lattice are as short as 8.458 Å.

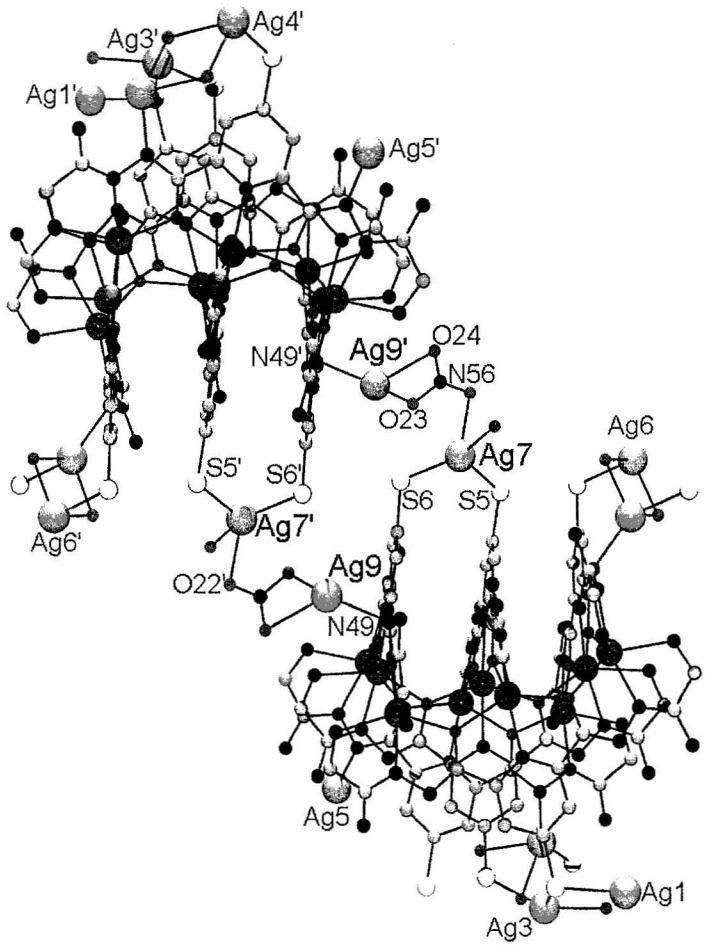

Figure 6.15: Bridging pathway via Ag7 and Ag9. Atoms not involved in bridging have been removed for clarity.

6.3.2: Vis-nir spectroscopy:

The characteristic red orange colour observed for the [3x3] $Mn(II)_9$ grids of 2POAP-type ligands is due to an intense ligand localized $\pi \rightarrow \pi^*$ transition. In the complex $[(2POAP)_6Mn_9](ClO_4)_6(H_2O)_{18}$, for example, the $\pi \rightarrow \pi^*$ transition occurs at a wavelength of 372 nm [32]. There is no significant absorption in the spectrum above 700

nm. As the [3x3] $Mn(II)_9$ grids become oxidized, two new absorptions appear in the visible-nir region of the spectra. The first occurs at a wavelength of approximately 700 nm (14,300 cm^{-1}) and it has been assigned as an intervalence charge transfer band between Mn(II) and Mn(III) centers. The intensity of this band increases with the number of Mn(III) centers in the compound to a maximum of four, and then decreases with further oxidation [66]. This supports the assignment of this band as an intervalence charge transfer; the oxidation of four Mn(II) centers to Mn(III) yields four Mn(II)→ Mn(III) pairs, while further oxidation removes Mn(II), decreasing the intensity of the band. The second new band to appear in the visible-nir region of the spectra of oxidized grids occurs at a wavelength of approximately 1000 nm (10,000 cm^{-1}). This band is assigned as a (μ-O)→Mn(III) ligand to metal charge transfer band. The intensity of this band increases with an increasing number of Mn(III) cations, up to the maximum of eight Mn(III) centers that has been achieved so far. The intensities of both charge transfer bands generally range from 400-800 $Lmol^{-1}cm^{-1}$ for reported $[Mn(II)_5Mn(III)_4]$ and $[Mn(II)_6Mn(III)_3]$ [3x3] grid systems [32, 66].

The visible-nir spectrum for **6.1** is shown in Figure 6.16. Two absorptions appear in the visible-nir region of the spectrum; the first at a wavelength of 776 nm, with an extinction coefficient of 235 $Lmol^{-1}cm^{-1}$, and the second at a wavelength of 1130 nm with an extinction coefficient of 190 $Lmol^{-1}cm^{-1}$. These bands are similar to those observed in oxidized grids of 2POAP-like ligands. The absorptions are shifted to lower energy than for the 2POAP grids, a difference which is likely caused by the differences in the ligand functional groups. The absorptions are less intense than the reported values for three and

four electron oxidized grids, which suggests a lesser degree of oxidation. These results are consistent with the short bond distances in the structure and with the BVS calculations which suggested oxidation of some Mn(II) centers to Mn(III).

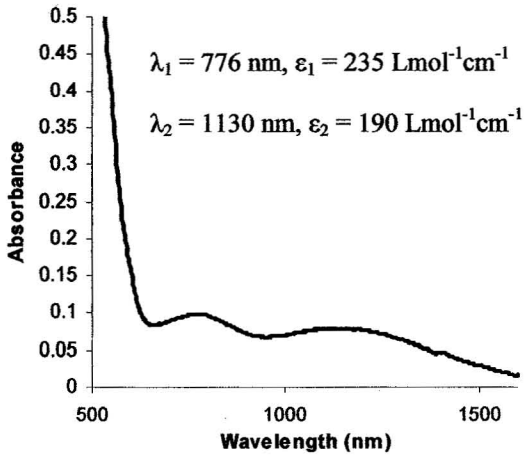

Figure 6.16: Visible-nir spectrum for **6.1**.

The visible-nir spectrum of **6.2** has two absorptions occurring at wavelengths of 649 nm and 991 nm, with intensities of 1540 Lmol^{-1}cm^{-1} and 767 Lmol^{-1}cm^{-1}, respectively. While these bands are similar to those that occur in other Mn(II)/Mn(III) grids, the bands have shifted to shorter wavelength with respect to both **6.1** and the 2POAP systems. Additionally, the intensities of these bands are unusually large. While the elemental analysis (*vide supra*) and the magnetic data (*vide ante*) suggest a $Mn(II)_7Mn(III)_2$ grid system, other possibilities, including Fe(II) substitution into the grid, are being explored to explain the differences in the visible-nir spectrum.

The visible-nir spectrum of **6.3** is similar to that of **6.2**, with two absorptions occurring at wavelengths of 694 nm and 1010 nm,, with intensities of 495 Lmol^{-1}cm^{-1} and 504 Lmol^{-1}cm^{-1}, respectively. The ligand for **6.3** is 2POAP, and the wavelengths at

which the absorptions occur are very close to those in the reported Mn(II)/Mn(III) 2POAP based grids. Additionally, the intensities fall within the range of reported values for the oxidized grid systems. This is consistent with both the elemental analysis (*vide supra*) and with the magnetic data (*vide ante*) for **6.3**.

The visible-nir spectrum for **6.6** is pictured in Figure 6.17. Only one discrete absorption band is observed, at a wavelength of 932 nm with an intensity of 705 $Lmol^{-1}cm^{-1}$, and a distinct shoulder is observed near 690 nm. The band is at higher energy than is typical for Mn(II)/Mn(III) grid systems, however, the intensity is consistent with a three or four electron oxidized grid. Additionally, there is no decrease of intensity after the maximum is reached, suggesting overlap with another band.

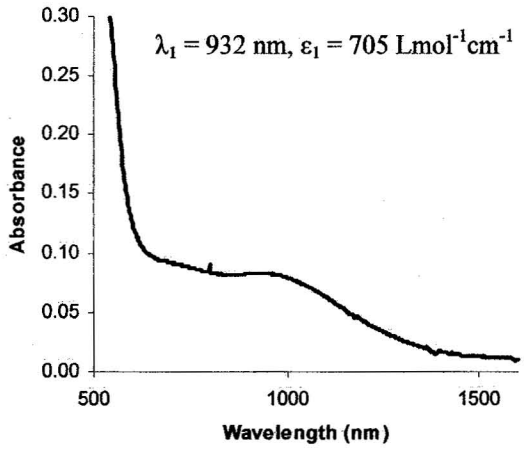

Figure 6.17: Visible-nir spectrum for **6.6**.

6.3.3: Magnetic Properties:

Compounds **6.1-6.6** all possess the (Mn_9-μO_{12}) core typical of [3x3] grids based on 2POAP-type ligands. The magnetic model for a $Mn(II)_9$ grid was discussed in detail in

Chapter 3. Compounds **6.1-6.3** and **6.6** are partially oxidized grids, and the magnetic exchange situation is more complicated. Previously reported $[Mn(II)_xMn(III)_{9-x}]$ grids all display antiferromagnetic coupling, with magnetic moment vs. temperature curves similar in shape to those of the $Mn(II)_9$ grids [32, 55, 66]. The susceptibility vs. temperature profile of the grid compounds does change as the compounds become oxidized. In the $Mn(II)_9$ grids, there is a slight shoulder on the susceptibility vs. temperature plot at low temperature. As the level of oxidation increases, the shoulder first becomes more pronounced, and shifts to higher temperature, finally becoming a well defined maximum for $Mn(II)_6Mn(III)_3$ at 40 K and for $Mn(II)_5Mn(III)_4$ grids at 55K [66]. This maximum is an indication of intramolecular antiferromagnetic coupling. The Mn(III) sites occur in the outer ring of eight Mn cations and have S = 4/2 spin states, compared with the S = 5/2 spin state associated with Mn(II). Antiferromagnetic coupling therefore results in one unpaired electron being left on any Mn(II) sites which are spin coupled to a neighbouring Mn(III) cation. These extra electrons on the outer ring can then couple with the central Mn(II) cation, leading to the maximum in the susceptibility vs. temperature profile, and resulting in a ground state of less than 5/2 for the compound. Figure 6.18 illustrates the possible combinations of Mn(II) and Mn(III) cations, and the resulting ground states for the Mn_9 grid.

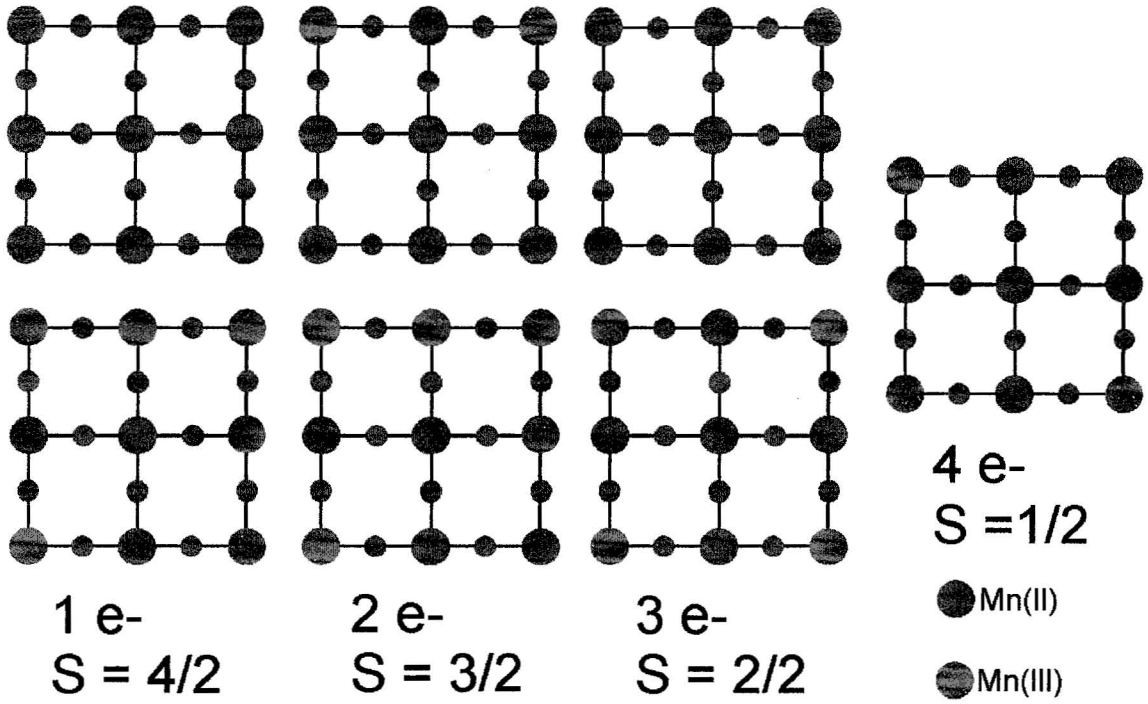

Figure 6.1.8: Spin ground states for grids of varying oxidation states.

The magnetic moment vs. temperature profile for **6.1** is pictured in Figure 6.19. The magnetic moment at room temperature is 16.7 μ_B, dropping to a value of 4.5 μ_B at 2 K, indicative of antiferromagnetic coupling. The profile is generally similar to that of a $Mn(II)_9$ grid, however the magnetic moment at low temperature is significantly lower than the spin only value for an S = 5/2 system (5.9 μ_B). At 4.5 μ_B, the value at 2 K is closer to that of an S = 4/2 ground state (4.9 μ_B). This would mean that an average of one electron has been removed from each grid molecule, which is consistent with the elemental analysis, and in agreement with the structure and bond valence summation calculations.

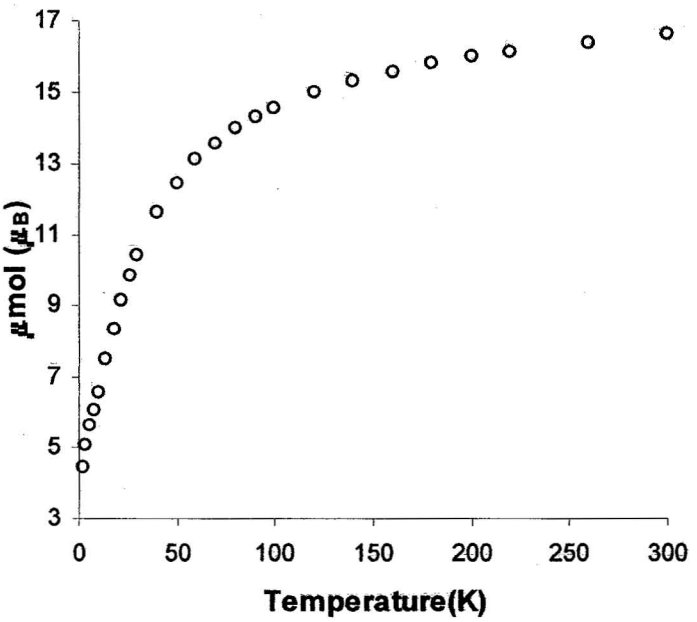

Figure 6.19: Magnetic moment vs. temperature for **6.1**.

The magnetic moment of **6.2** is 15.6 μ_B at room temperature, falling to 3.7 μ_B at 2K. The low temperature value is close to the spin only value for a system with an S = 3/2 ground state. The magnetization vs. field profile for **6.2** is shown in Figure 6.20. The solid line represents a system where g = 2.0, S = 3/2 and T = 2K. The agreement with the experimental data is reasonable, which suggests that the ground state assignment based on the magnetic moment vs. temperature data is correct and that two electrons on average have been removed from the grid. This assessment is consistent with the elemental analysis, and with the appearance of intervalence charge transfer bands in the visible-nir spectrum of **6.2**. Closer examination of the magnetization vs. field data reveals a change in slope of the magnetization curve above 3 T. This change has been attributed to a field

dependent population of the next ascending spin state [67]. The change in slope makes fitting the magnetization vs. field data difficult, thus simulations are used to confirm the magnetic ground state of the compound.

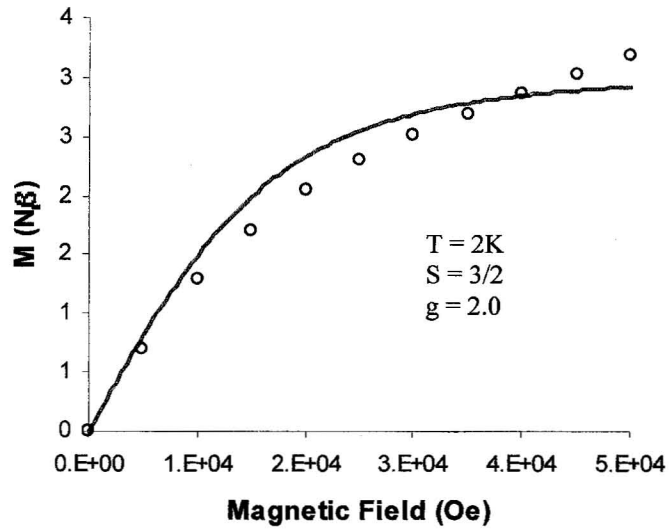

Figure 6.20: Magnetization vs. field data for **6.2**. The solid line represents the simulated data for the given parameters.

The magnetic moment of **6.3** is 16.3 μ_B at room temperature, falling to a value of 3.7 μ_B at 2 K. This is very similar to the profile of **6.2**, which is reasonable, as both compounds result from the reaction of a $Mn(II)_9$ grid with Fe(III). The low temperature value is very close to the spin only value for a system with a ground state of S = 3/2, and the magnetization vs. field data (Figure 6.21) agree with this assessment. The solid line in Figure 6.21 was calculated using S = 3/2, g = 2, T = 2K. As in the case of **6.2**, the change in the slope of the magnetization vs. field profile makes fitting the magnetization

vs. field data difficult, and a simulation was used to confirm the S = 3/2 ground state. The S = 3/2 ground state indicates removal of two electrons from the system, which is consistent with the elemental analysis, and in good agreement with the visible-nir spectrum of **6.3**.

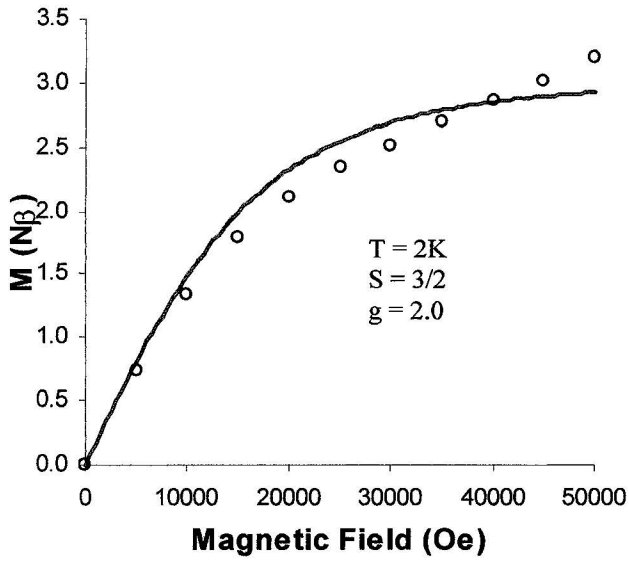

Figure 6.21: Magnetization vs. field data for **6.3**. The solid line represents the simulated data for the given parameters.

The magnetic moment vs. temperature profile for **6.4** is pictured in Figure 6.22. The magnetic moment is 16.9 μ_B at room temperature, dropping to a value of 5.9 μ_B at 2 K. These values are typical for a $Mn(II)_9$ grid. The data were fit using the Fisher model [85-87] (see Chapter 3 for a full description) and the molar mass from the X-ray formula of **6.4**. The best fit of the data gave the parameters g = 2.018, J1 = -5.0 cm^{-1}, J2 = 0 cm^{-1}, θ = -3.5 K, α = 0.001, $10^2R = 2.9$ ($10^2R = [\Sigma(\chi_{obs}-\chi_{calc})^2/ \Sigma \chi_{obs}^{\ 2}]^{1/2}$). The solid line in

Figure 6.22 was calculated using these parameters. This fit should be treated as preliminary until a sample of **6.4** clean enough for elemental analysis can be prepared and the measurements are repeated. However, the calculated parameters are consistent with [3x3] $Mn(II)_9$ grid compounds. It should be noted that the Fisher model neglects any coupling between the outer ring of eight Mn(II) cations and the center site (J2 is set as 0 cm^{-1}). The contribution of J2 to the fit manifests itself as a negative θ value. Typical values of θ for the $Mn(II)_9$ grids range from -1 K to -4.5 K [32, 55] (See also Chapter 3).

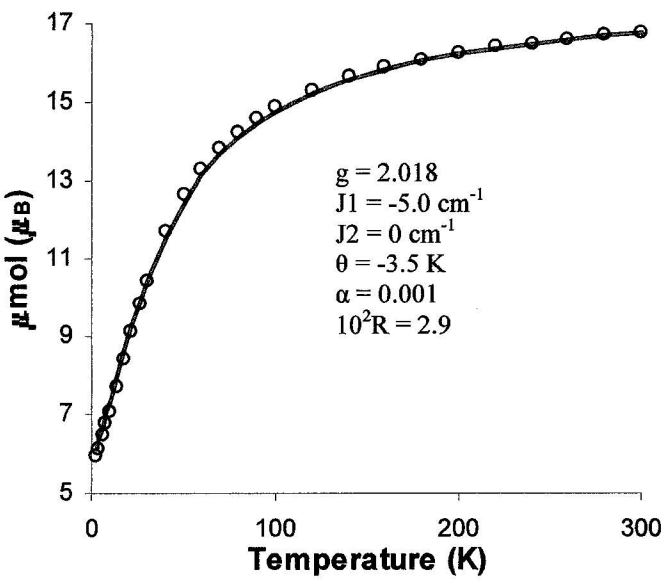

Figure 6.22: Magnetic moment vs. temperature for **6.4**.

The magnetic moment of **6.5** is 16.8 μ_B at room temperature, dropping to a value of 5.5 μ_B at 2 K. These values are typical of a $Mn(II)_9$ grid, despite the direct bonding connections between grid molecules. This result is not unexpected, as the inter-grid Mn(II)-Mn(II) separations are very large (~ 8.5 Å for non-bonded grids, and 12 Å for

bonded grids). Because magnetic interactions decrease with distance, one would expect any inter-grid interaction in **6.5** to be very small compared to the intra-grid coupling. The magnetic data for **6.5** were fitted to the Fisher model. The best fit of the data gave parameters g = 2.03, J1 = -4.6 cm^{-1}, J2 = 0 cm^{-1}, θ = -7.5 K, α = 0.001, 10^2R = 3.9. The J and g values for **6.5** are similar to $Mn(II)_9$ grids as a whole, however the θ value is much larger than usual. This could indicate that there are intermolecular effects present in the compound in addition to the exchange between the central Mn(II) cation and the outer $Mn(II)_8$ ring.

The magnetic moment vs. temperature profile for **6.6** is pictured in Figure 6.23. The magnetic moment is 15.1 μ_B at room temperature, dropping to a value of 2.3 μ_B at 2 K. The low temperature value is in between the spin only magnetic moments for an S = 1 system (2.83 μ_B) and and S = ½ system (1.73 μ_B). The molar susceptibility vs. temperature profile for **6.6** is pictured in Figure 6.24. There is a pronounced maximum in the profile, centered at 50 K, which is typical of the $[Mn(II)_5Mn(III)_4]$ grids. It seems likely that in the bulk sample some of the grids have undergone a three electron oxidation, while the remaining molecules have lost four electrons. The magnetic profile represents the averaged situation. Reasonable elemental composition values can be calculated for either the $[Mn(II)_5Mn(III)_4]$ grid or the $[Mn(II)_6Mn(III)_3]$ grid, and the difference in molar mass is not significant enough to have an effect on the magnetic data for the compound.

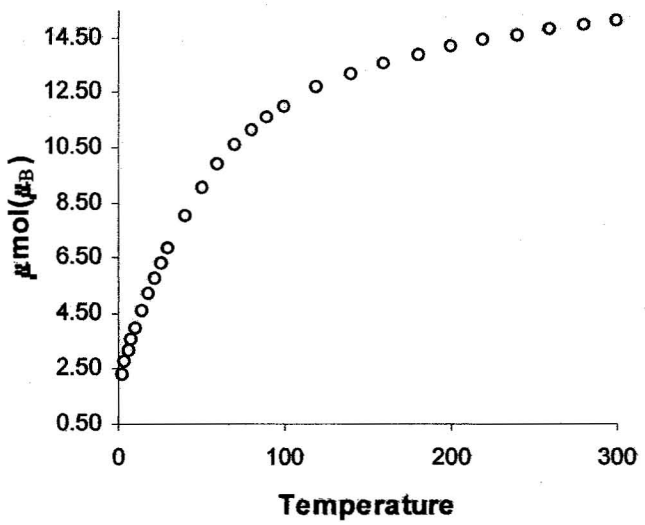

Figure 6.23: Magnetic moment vs. temperature for **6.6**.

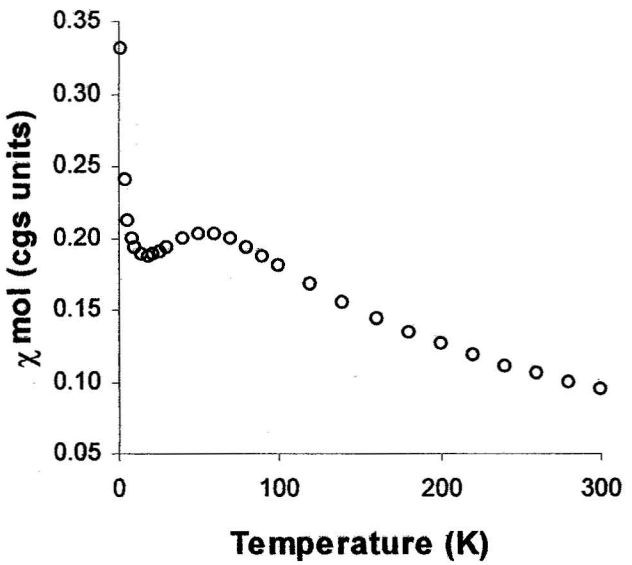

Figure 6.24: Susceptibility vs. temperature for **6.6**.

6.4: Summary:

[3x3] $Mn(II)_9$ grids were found to react with other transition metal salts in two ways; on the one hand by becoming oxidized, and on the other by coordination of additional metal cations to the outside of the grid molecule. Cu(II), Fe(III), and Au(III) were all found to oxidize $Mn(II)_9$ grids. Au(III) removed three to four electrons from the grid molecules, Fe(III) removed two electrons, and Cu(II) removed one electron in the case of **6.1** and two electrons in the case of **6.3**. The standard reduction potential of $AuCl_4^-$ to $AuCl_2^-$ is 0.926 V (vs. NHE) [131]. As the grids generally undergo the first four electron oxidation at a potential of approximately 0.5 V vs. the NHE, $AuCl_4^-$ has enough oxidizing potential to remove these first four electrons. The standard reduction potential of Fe(III) to Fe(II) is somewhat lower, at a potential of 0.77 V (vs. NHE) [131]. This potential should be high enough to remove the first four electrons from a $Mn(II)_9$ grid, yet only two electrons are removed from **6.2**. Perhaps a longer reaction time, or a more careful control of the stoichiometry of the reaction would permit a four electron oxidation to occur. The Cu(II) mediated oxidation of the grid is more problematic. The standard reduction potential of Cu(II) to Cu(I) is 0.159 V (vs. NHE), which is much lower than the potential at which grid oxidation occurs. However the reactions were performed in acetonitrile, which, due it its ability to stabilize Cu(I), clearly enhances the oxidation power of Cu(II), sufficient for the removal of one or two electrons from the grid.

It is interesting to note that Fe(III) and Cu(II) were found to oxidize both the S-functionalized SEt2POAP-based grid molecules, and the unfunctionalized 2POAP based

grids. This suggests that the oxidation is mediated by a group common to both ligands. The NH_2 groups are the obvious candidates. In order to test this hypothesis, $Mn(II)_9$ grids with the Schiff-base ligands 2POPP and Cl2POMP (compounds **3.3** and **3.4**) were reacted with Cu(II). In both cases, the grid molecule was destroyed, and a $Cu(II)_8$ pinwheel was isolated as the only product [132]. These results, coupled with the electrochemical studies on compounds **3.3** and **3.4** support the hypothesis that the oxidation mechanism for the grid molecules is outer sphere, involving the amidrazone NH_2 groups.

When the compound **3.1** was reacted with $AgNO_3$, the result was a three dimensional network comprised of grid molecules bridged to each other by Ag(I) cations. The Ag(I) was largely bound to the sulphur atoms of the thioether functional groups, which is not unexpected based on HSAB theory [89]. Three of the four different bridging connections involved Ag(I) cations which had coordinated to diazine N atoms, and one Ag(I) cation was determined to bind only to diazine nitrogen. This result, while surprising, suggests the possibility of coordinating additional metal sites to grids not possessing sulphur-based functional groups. A magnetically active cation coordinated to one of these sites would be bridged to a Mn(II) center via a diazine bridge, and spin communication would then be possible, which might lead to interesting magnetic properties. A reasonable strategy might be to start with a complex with one labile ligand that could be replaced by the diazine N atom. Compounds with lower coordination numbers would be more likely to react as there would be less steric interference with the central pyridine ring and NH_2 group of the grid ligand.

The standard reduction potential of Ag(I) to Ag is 0.8 V (vs. NHE), which should be sufficient to oxidize at least some of the Mn(II) centers. There was no indication of direct oxidation of the $Mn(II)_9$ grid in either **6.4** or **6.5**. However, in one case, magnetic measurements indicated that the product of a reaction of **3.1** with $Ag(ClO_4)$ had undergone a two electron oxidation after it had been exposed to daylight for several days [133]. This result suggests that it may be possible to prepare $Mn(II)_9$ grid complexes with externally coordinated Ag(I) which could undergo photochemical oxidation.

As Ag(I) has been observed to coordinate to the thioether S atoms of **3.1**, it is reasonable to expect that Au(I) might do the same. Au(I) is produced in the redox process that occurs between $AuCl_4^-$ and **3.1**. The elemental analysis of **6.6**, and, indirectly, the magnetic properties of the compound, suggest the presence of gold in the structure. Structural studies are required to determine whether the Au(I) is bound to the grid molecule, or occurs as $AuCl_2^-$ anions in the lattice. From the structure of **6.5**, several different silver-grid binding modes have been observed; Ag(I) cations were found to coordinate one or two of the thioether S atoms, or a diazine N atom, or a combination of thioether S atoms and diazine N atoms. A structure of **6.6** would be useful to understand more directly the interactions between the S-functionalized $Mn(II)_9$ grids and Au(111) surfaces.

Chapter 7: Limitations of rational design: Serendipitous formation of unusual compounds via *in situ* ligand solvolysis

7.1: Preamble:

2POAP-like ligands are prepared using condensation reactions between hydrazones and the appropriate imino-ester, aldehyde or ketone, in which water or an alcohol are eliminated. Consequently, the reverse solvolysis reaction can occur in the presence of water or alcohol. Hydrazone linkages in particular are vulnerable. Hydrolytic decomposition of the ligand has been observed during some ligand preparations, where generally after the initial formation of the desired ligand a hydrolysis reaction occurs at one or both of the two hydrazone linkages (Scheme 7.1a), resulting in either a return to the starting hydrazone, or to the corresponding ester or carboxylic acid and a new hydrazone resulting from addition of the hydrazide moiety to the end piece. In the latter case the new hydrazone can react with the end piece forming, for example, the known ligand PAHAP (Scheme 7.1b), which due to its frequent formation in hydrolysis reactions, appears to be a thermodynamic sink [109,138]. Ligand solvolysis has also been observed after reaction with a transition metal, where presumably polarizing effects due to metal ion coordination assist in the hydrolysis of the ligand [109, 139]. In this situation the outcome of the reaction can generally only be determined using X-ray crystallography.

Schiff-base ligands involving aldehydes or ketones seem to be more vulnerable to solvolysis than their amidrazone based counterparts. Amidrazones are weaker electrophiles than Schiff-bases and are therefore more stable to solvolysis. As one might

expect, decomposition occurs more frequently when heated polar solvents are used. The chances of decomposition are also increased when strong nucleophiles, such as the acetate counter anion in **7.2,** are used in reactions with transition metal salts. The coordination of the transition metal itself may also contribute to the solvolysis reaction by enhancing the electrophilic qualities of the ligand.

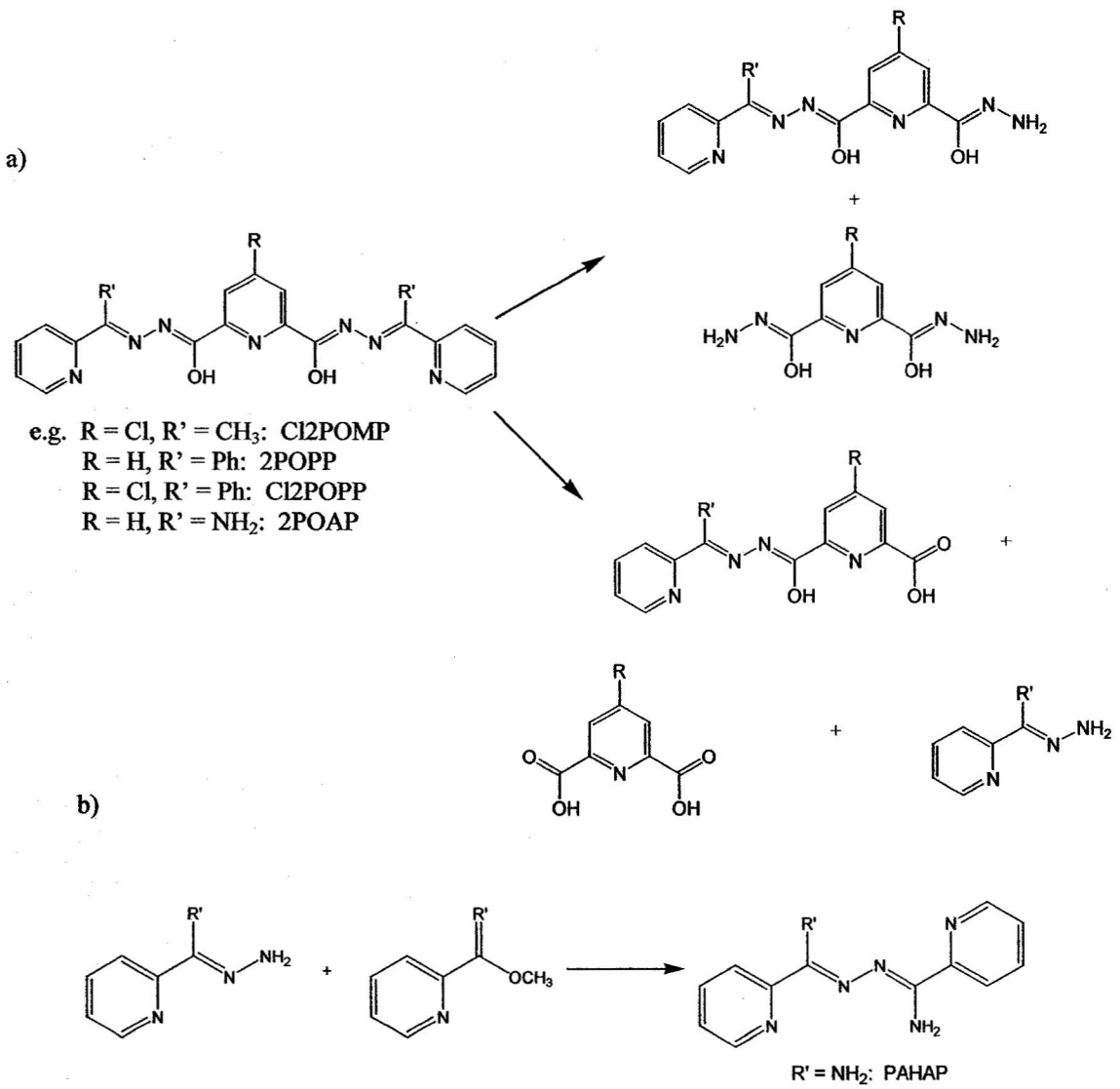

Scheme 7.1: a) Solvolysis of ligand during synthesis. b) Formation of PAHAP from solvolysis product.

Cl2POMP and 2POPP (Scheme 7.1a) both form Cu_8 pinwheel clusters [54, 63] and [3x3] Mn_9 grids [32,55] similar to those of the amidrazone-based ligands. However, Cl2POPP has proved more challenging, both to synthesize and to complex with transition metal cations. The ligand synthesis must be performed in a 3:1 mixture of chloroform and methanol over a period of three days, as opposed to an overnight reflux in methanol, which suffices for the other Schiff-base ligands. Failure to use chloroform results in a mixture of the hydrazone starting material, the half ligand, and the carboxylic acid resulting from the solvolysis of the starting hydrazone. While grid and pinwheel complexes with Cl2POPP do occur, it has not been possible to obtain structural solutions for these compounds. However, an usual mononuclear nickel complex has been obtained, as well as two novel decomposition products, one a 2D network with Cu(II), the other a dodecanuclear mixed valent cobalt compound. *In situ* decomposition products of Cl2POPP are illustrated in Scheme 7.2.

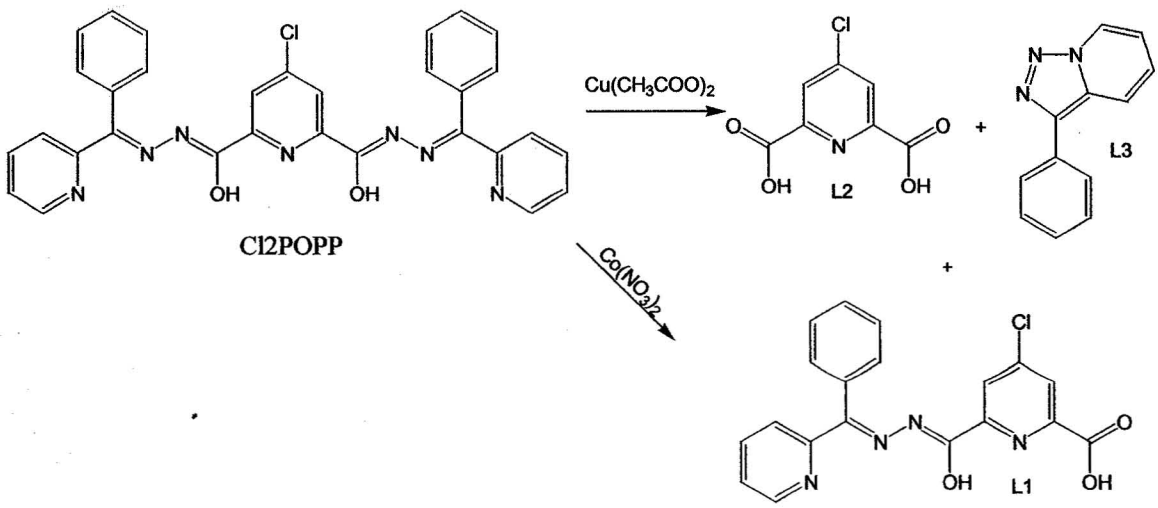

Scheme 7.2: Solvolysis of Cl2POPP with Cu(II) and Co(II).

7.2: Experimental:

7.2.1: Complex synthesis:

7.2.1.1: [Ni(Cl2POPP)] (**7.1**)

$NiCO_3$ (0.18 g, 1.5 mmol) was suspended in 1:1 acetonitrile/ethanol (20 mL). Cl2POPP (0.10 g, 018 mmol) was added and the mixture was heated. Water (5 mL) was added and heating continued for 15 min. with the formation of a red solution. The solution was filtered to remove excess nickel carbonate, and allowed to stand at room temperature. Red crystals suitable for structural analysis formed after two days (Yield 60 mg, 55%).

7.2.1.2: $[Cu_2(L1)(L2)](H_2O)_2(CH_3OH)(L3)$ (**7.2**)

Cl2POPP (0.10 g, 0.18 mmol) was added to a solution of $[Cu(CH_3COO)_2(H_2O)]_2$ (0.18 g, 0.23 mmol) in methanol (20 mL), forming a clear brown solution. Red brown crystals of **7.2**, suitable for a structural determination, were obtained in low yield (35 mg, 38 %) after the solution was allowed to evaporate to a small volume. Elemental Analysis: Found (%): C, 44.47; H, 2.67; N, 11.08. Calc. (%), for $[(C_{19}H_{11}N_4O_3Cl)(C_7H_2NO_4Cl)Cu_2](C_{12}H_9N_3)(H_2O)_7$: C, 44.53; H, 3.52; N, 10.94.

7.2.1.3 $[(Cl2POPP)_3(L1)_6Co(III)_6Co(II)_6(H_2O)_6(NO_3)_6][Co(H_2O)_6](NO_3)_{12}(CH_3CN)_3(H_2O)_{10}$ (**7.3**)

Cl2POPP (0.10 g 0.18 mmol) was added to a solution of $Co(NO_3)_2(H_2O)_6$ (0.17 g, 0.59 mmol)in acetonitrile/methanol, and the mixture stirred in air. A red solution formed, which deposited dark red crystals (30 mg, 23 %), suitable for structural analysis, on standing for several days. Found (%): C, 40.26; H, 2.69; N, 14.57. Calc. (%), for

$[(C_{31}H_{21}N_7O_2Cl)_3(C_{19}H_{11}N_4O_3Cl)_6Co_{12}(NO_3)_6(H_2O)_6][Co(H_2O)_6](NO_3)_{11}$ $(CH_3CN)_4(H_2O)_{14}$: C, 40.34; H, 3.04; N, 14.45.

7.2.2: Crystallography:

A red prismatic crystal of **7.1** with dimensions of 0.15 x 0.08 x 0.40 mm was mounted on a glass fiber. Diffraction data were collected on a Rigaku AFC6S diffractometer with graphite monochromated Mo-Kα radiation at 26°C to a maximum 2θ value of 55.1°. The data were corrected for Lorentz and polarization effects. The structure was solved by direct methods [72-73]. The non-H atoms were refined anisotropically. Hydrogen atoms were placed in calculated positions with thermal parameters set twenty percent greater than those of their bonding partners at time of their inclusion but were not refined. Neutral atom scattering factors [74], and anomalous dispersion terms [75-76] were taken from the usual sources. All calculations were performed using the teXsan [77] crystallographic software package of the Molecular Structure Corporation except for refinement, which was performed using SHELXL-97 [72a].

The diffraction intensities of a red-brown plate crystal of **7.2** (0.79 x 0.19 x 0.06 mm) were collected using graphite monochromatized Mo-Kα radiation on a Bruker P4/CCD diffractometer at -80 °C to a maximum 2θ value of 52.8°. The data were treated similarly to **7.1**.

A dark orange crystalline fragment of **7.3** (0.50 x 0.40 x 0.30 mm) was treated similarly to **7.2**. The data were treated similarly to **7.1** and **7.2**. There are a total of twelve "water" hydrogen atoms omitted from the model. A disordered phenyl group was

modeled using a rigid group for the 25% occupancy component. The 75% component was refined isotropically. Crystal data for **7.1**, **7.2**, and **7.3** are summarized in Table 7.1.

Table 7.1: Summary of Crystallographic data for **7.1**, **7.2**, **7.3**.

Compound	**7.1**	**7.2**	**7.3**
Empirical Formula	$C_{31}H_{20}N_7O_2NiCl$	$C_{39}H_{30}N_8O_{10}Cl_2Cu_2$	$C_{213}H_{171}N_{62}O_{84}Cl_9Co_{13}$
M/gmol^{-1}	616.70	968.71	6028.27
Crystal System	monoclinic	monoclinic	hexagonal
Space Group	Cc (#9)	C2/c (#15)	$P6_3/m$ (#176)
a/Å	14.405(3)	29.927(3)	24.2682(6)
b/Å	17.663(5)	29.927(3)	
c/Å	10.689(4)	30.906(3)	29.470(2) Å
β/°	103.73(3)	109.832(2)	
V/ Å^3	2642(1)	7720(1)	15030.9(8)
ρ_{calcd}/gcm^{-3}	1.550	1.667	1.332
T/°C	+26(1)	-80(1)	-80(1)
R1	R = 0.043	0.044	0.094
wR2	R_W = 0.040	0.111	0.335

7.3: Results and Discussion:

7.3.1: Description of crystal structures:

7.3.1.1: [Ni(Cl2POPP)] (7.1)

The crystal structure of **7.1** is illustrated in Figure 7.1, and relevant bond lengths and angles are found in Table 7.2. The structure is very simple, consisting of a single ligand molecule bound to a single distorted square planar Ni(II) (NiN_4) cation. The ligand has been doubly deprotonated resulting in a charge balance with the Ni(II) cation, and no

counter anions were found in the structure. The Ni-N distances lie in the range 1.822-1.930 Å, and *cis*-N-Ni-N angles range from 81.81-102.15°. The distortion of the square planar environment likely results from the unusual ligand binding mode. The ligand adopts a sterically crowded, *cis*-like conformation as it wraps around the Ni(II) cation. The Ni(II) center is bound to the central pyridine N atom, one terminal pyridine N atom and two diazine N atoms. The free terminal pyridine ring lies above the bound one, presumably held by a slipped π-π interaction. The N-N distance between the rings is 3.101 Å, characteristic of a strong π-stacking interaction, and the distances between the corresponding neighbouring C atoms are 3.836 and 3.896 Å. The distance between the N atom of the free pyridine ring and the Ni(II) cation is 3.440 Å, too far to be considered a weak bond or van der Waals interaction.

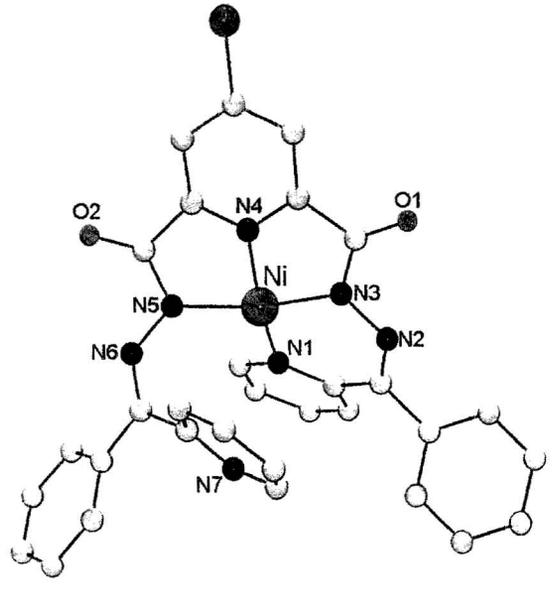

Figure 7.1: POV-RAY representation of **7.1**. Ni = magenta, N = blue, O = red, Cl = green, C = grey.

Table 7.2: Selected bond distances (Å) and angles (°) for **7.1**.

Ni1-N1	1.906(5)	π-π, intermolecular:	
Ni1-N3	1.843(5)	ph-py: C3-C24	3.293
Ni1-N4	1.822(5)	py-ph: C9-C31	2.531
Ni1-N5	1.930(5)		
		Cl-N:	
N1-Ni1-N3	94.0(2)	Cl1-N2	3.267
N1-Ni1-N4	159.4(2)	Cl1-N3	3.551
N1-Ni1-N5	102.1(2)	Cl1-N6	3.787
N3 -Ni1-N4	83.7(3)	Cl1-N5	4.242
N3-Ni1-N5	163.7(2)		
N4- Ni1-N5	81.8(3)	H-bonds:	
		Cl1···H17-C28	2.901, 150.52
π-π, intramolecular:		Cl1···H19-C30	2.916, 140.30
N1-N7	3.101	O1···H2-C2	2.499, 145.08
C5-C31	3.896	N6···H19-C30	2.694, 134.53
C1-C276	3.836	O2···H20-C31	2.620, 126.61
		O2···H10-C15	2.679, 122.09

The unit cell of **7.1** is pictured in Figure 7.2. It consists of chains of molecules in a head-to-head, toe-to-toe alternating arrangement. The chains form layers with close contacts at the head to head portion of the chain. The toe-to-toe interactions consist of slipped π- π interactions between terminal pyridine and terminal phenyl rings. There are two groups of interactions between each set of toe-to-toe molecules (Figure 7.3); one between the bound terminal pyridine ring of the first molecule and a phenyl ring of the second, with a closest contact distance of 3.293 Å, and another between the free terminal pyridine molecule of the second molecule and a phenyl ring of the first, with a closest contact distance of 3.531 Å.

The head-to-head interactions (Figure 7.4) are slightly more complex as there are two types of contact present. The most significant appears to be Cl-N interactions between the Cl atom of one molecule and an uncoordinated diazine N atom of the other. The Cl-N distance is 3.267 Å. The Cl-N distance to the coordinated N atom of the

diazine is 3.551 Å, which is close enough to be considered a weak interaction. The Cl atom of the second molecule also has close contacts with the diazine N atoms of the first, with Cl-N distances of 3.787 and 4.242 Å between the Cl atom and the uncoordinated and coordinated diazine N atoms respectively. There is also a Cl···H hydrogen bond at each end of the head-to-head interaction, with a Cl···H distance of 2.901 Å and a Cl-H-C angle of 150.52°. It should be noted that while the central pyridine rings of the head-to-head molecules appear to line up, the distance between them is greater than 5 Å, which is too great to be considered a π- π interaction.

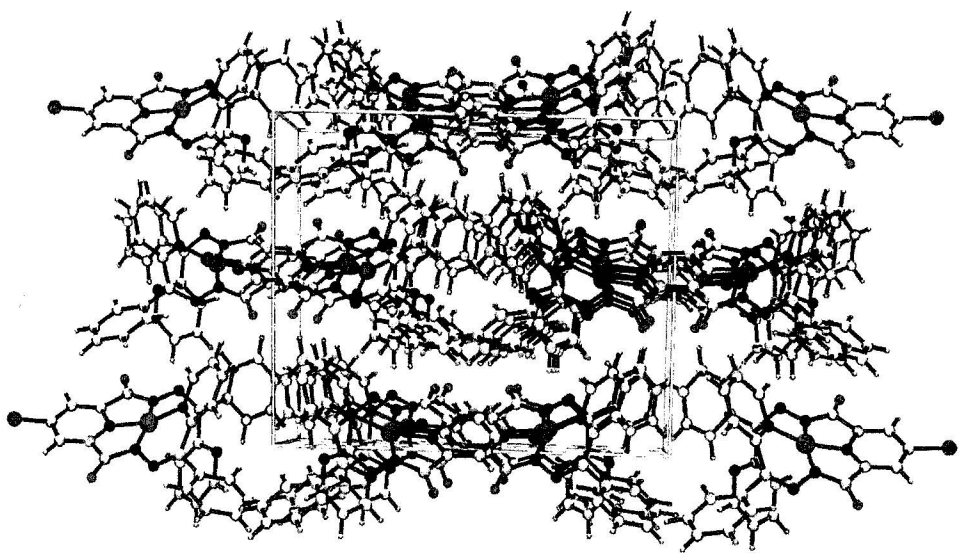

Figure 7.2: POV-RAY depiction of the unit cell of **7.1**. Head-to head interactions refer to those at the chlorinated pyridine ring.

The layers of molecules are arranged so that the head-to-head interaction in one layer lies above the toe-to-toe interaction in the next. There are several interactions between them. There is a weak π- π interaction between the central pyridine ring of one molecule and a terminal phenyl ring in an adjacent layer. The closest contact distance in this case is 3.550 Å. There are also H-bonding contacts between layers. The most significant is an O···H-C contact between the O atom and the H of a terminal phenyl ring, with an O···H distance of 2.499 Å and an O···H-C angle of 145.08°. This is followed by an N···H-C contact between an uncoordinated diazine N atom and a terminal pyridine H atom, with an N···H distance of 2.694 Å and N···H-C angle of 134.53°. There are two weaker O···H bonds to terminal pyridine H atoms with distances of 2.620 and 2.679 Å, and O···H-C angles of 126.61 and 122.09° respectively. These values all fall within the accepted range for weak X···H-C hydrogen bonds [1, 105].

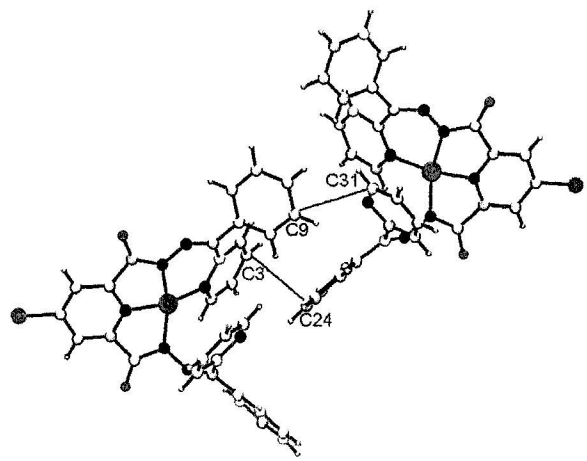

Figure 7.3: Intra-layer toe-to-toe interactions between molecules of **7.1**. Shortest π- π distances are highlighted in green.

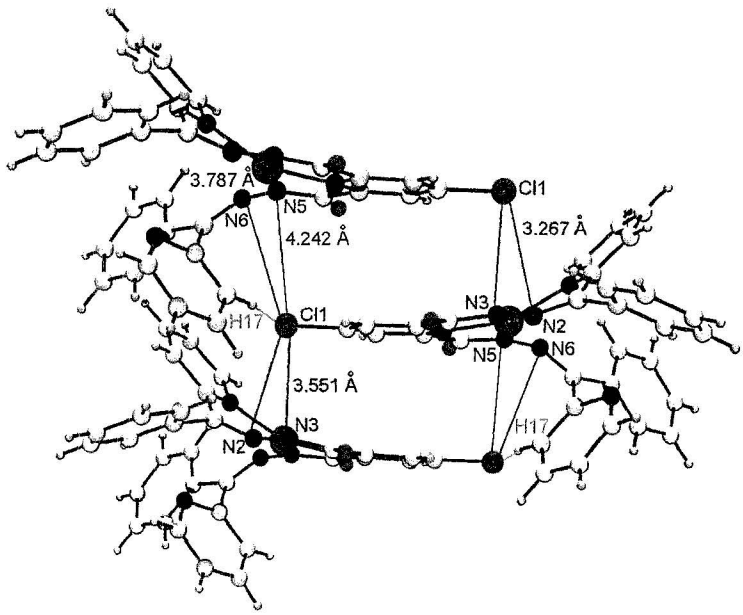

Figure 7.4: Intra-layer head-to-head interactions between molecules of **7.1**. Cl-N interactions are highlighted in green and purple, H-bonding in orange.

7.3.1.2: $[Cu_2(L1)(L2)](H_2O)_2(CH_3OH)(L3)$ (**7.2**)

The asymmetric unit of **7.2** is shown in Figure 7.5, and relevant bond distances and angles are listed in Table 7.3. The first surprise offered by this structure is that the ligand Cl2POPP is entirely absent. Instead, there are three new ligands, all resulting from the solvolysis of Cl2POPP (Scheme 7.2). L1 is 4-chloro-2,6-pyridinedicarboxylic acid, resulting from the solvolysis of the ligand at both hydrazide groups. L2 is the acid resulting from the solvolysis of the ligand at only one hydrazide site, and L3 is 3-phenyltriazolo[1,5-a]pyridine. The asymmetric unit contains two Cu(II) centers, which appear to be distorted square planar (Cu1 = CuN_3O) and distorted square pyramidal

(Cu2 = CuN_2O_3). Cu-N bond lengths range from 1.903 to 2.368 Å, while Cu-O bond lengths lie between 1.971 and 2.033Å. The Cu(II) centers are bridged by the diazine group of L2. The torsional angle across the diazine bridge is quite large (Cu-N-N-Cu = 178°) but the distance between the Cu(II) centers is also quite long (4.977 Å) and the connections are short-long (equatorial-axial) and thus orbitally orthogonal, so antiferromagnetic exchange between the Cu(II) cations would not be expected by this pathway. There is additionally a three atom bridge connecting the Cu(II) centers, via N3 and O1. This pathway is non-orthogonal, and antiferromagnetic exchange is therefore possible via this route. The path length of this secondary bridge is longer, so we would not expect it to have a dominant effect.

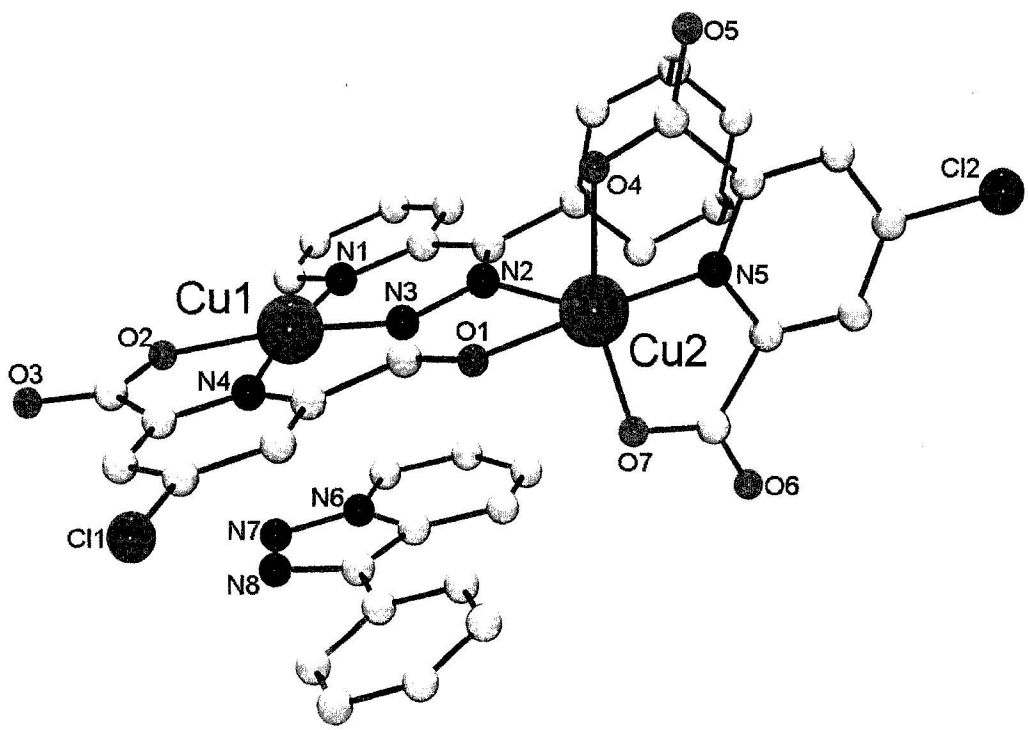

Figure 7.5: POV-RAY depiction of the asymmetric unit of **7.2**. Cu = magenta, O = red, N = blue, Cl = green, C = grey.

Table 7.3: Selected bond distances (Å) and angles (°) for **7.2.**

Cu1-N4	1.903(3)	Cu1-Cu2	4.977	
Cu1-N1	1.922(3)	Cu2-N2-N3-Cu1	-178.02(16)	
Cu1-N3	1.926(3)			
Cu1-O2	2.005(2)	Cu2-Cu2	6.143	(dimer, chain)
Cu1-O3	2.632	Cu1-Cu1	5.041	(2D lattice)
Cu2-N5	1.903(2)	π-π interactions: L3		
Cu2-O1	1.971(2)	asymmetric unit:	3.195-3.693	
Cu2-O7	2.031(2)	extended structure:	3.327-3.720	
Cu2-O4	2.033(2)			
Cu2-N2	2.368(3)	H-bonds: L3		
Cu2-O6	2.375(2)	asymmetric unit:	O7···H17-C30	2.590, 140.88
			O7···H18-C34	2.430, 152.31
		extended structure:	O4···H16-C29	2.408, 129.97

The most unusual aspect of the asymmetric unit is the 3-phenyltriazolo[1,5-a] pyridine molecule, which is not directly bonded to either Cu(II) center, and is therefore held in place only by intermolecular interactions. Upon closer examination, it is evident that the triazolo-unit sits directly above the aromatic rings of L2. The pyridine rings line up, with close contacts at distances of ~3.3-3.4 Å, the phenyl ring lies above the Cl-pyridine ring of L2, with close contacts in the realm of 3.3-3.6 Å, and finally, the triazole ring sits above the Cu(II) chelate ring with atom-atom distances of 3.4-3.8 Å. There are even closer contacts to the conjugated C=O group attached to the ring, with distances of 3.1-3.2 Å, and additionally, two H bonds between a carboxylate oxygen, and protons on both the phenyl and pyridine rings of the triazolo fragment exist, with O···H distances of 2.430 and 2.590 Å and O···H-C angles of 152.31and 140.88° respectively. While π-π interactions and H-bonds are common with 2POAP type ligands [32, 55, 63], the presence of an uncoordinated organic molecule is unusual in coordination compounds.

The extended structure of **7.2** offers further surprises (Figure 7.6). Cu2 is found to have an axially elongated octahedral environment, with a long bond to the carboxylate O6 atom of L1 (Cu-O = 2.374 Å). Cu2 is bridged to its symmetry related counterpart through the carboxylate group forming a tetranuclear dimer. The Cu2-Cu2 distance is quite long, at 6.143 Å, and the Cu-O connections through the carboxylate bridge are axial-equatorial, and orbitally orthogonal, so we do not expect to see antiferromagnetic coupling through this bridging connection. The tetranuclear subunits are cross-linked, through this same Cu2-O6 interaction to form a zig-zag chain (Figure 7.7).

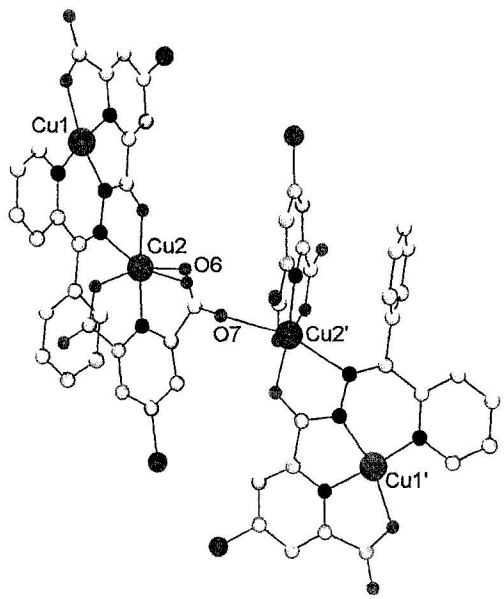

Figure 7.6: Dimer formed via Cu2-O6-O7-Cu2'.

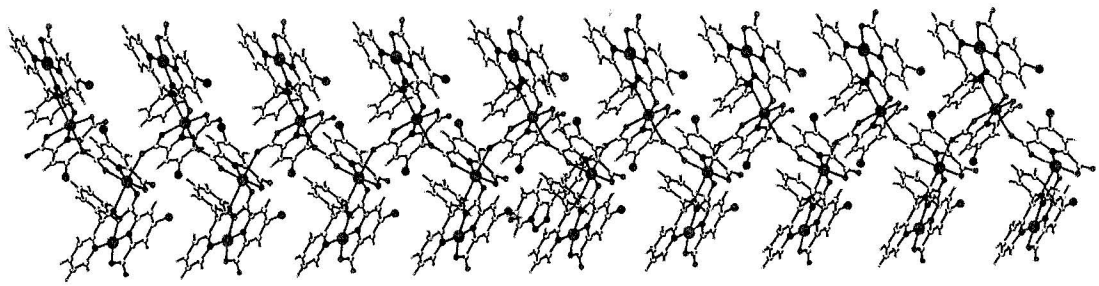

Figure 7.7: Chain formed by cross-linking at Cu2-O6.

Closer study of Cu1 reveals that it has in fact a distorted square pyramidal coordination environment, with an extremely long bond to a carboxylate oxygen atom of L2 (Cu1-O3 = 2.632 Å). Cu1 is bridged to a symmetry related counterpart via two of these carboxylate links, with a Cu1-Cu1 distance of 5.041 Å. The bridging connections are again long-short (axial-equatorial) and strictly orthogonal. This interaction cross-links the chains into a 2D lattice (Figure 7.8).

A closer look at the bridging connection (Figure 7.9) reveals that each of the Cu1 coordination environments is surrounded by two 3-phenyltriazolo[1,5-a]pyridine molecules. One of these comes from its own asymmetric unit, and the other from the Cu1-Cu1 bridging group adjacent to it in the lattice. The π-π distances for the second triazolo unit are comparable to those within the asymmetric unit, with closest contacts of 3.1-3.4 Å. There is also a hydrogen bond between a carboxylate oxygen and a pyridine hydrogen atom, with an O···H distance of 2.408 Å and an O···H-C angle of 129.97°. Each of the cavities within the lattice contains two 3-phenyltriazolo[1,5-a]pyridine molecules, which, because of the cross-linking in the structure, are sandwiched between aromatic

groups, not simply lying above one system as one presumes from the asymmetric unit. Thus the 3-phenyltriazolo[1,5-a]pyridine molecule is behaving as a guest in the cavities of the host lattice. Organic and inorganic-organic host-guest behaviour is not uncommon in the literature. Neutral functionalized aromatic guests have been reported in pores of clathrates [140], organic anionic guests have been reported inside spheroid polyoxovanadates [141], and cationic guest polymerizations inside inorganic zeolites have been intensively studied as a route to polymer hybrid materials [142].

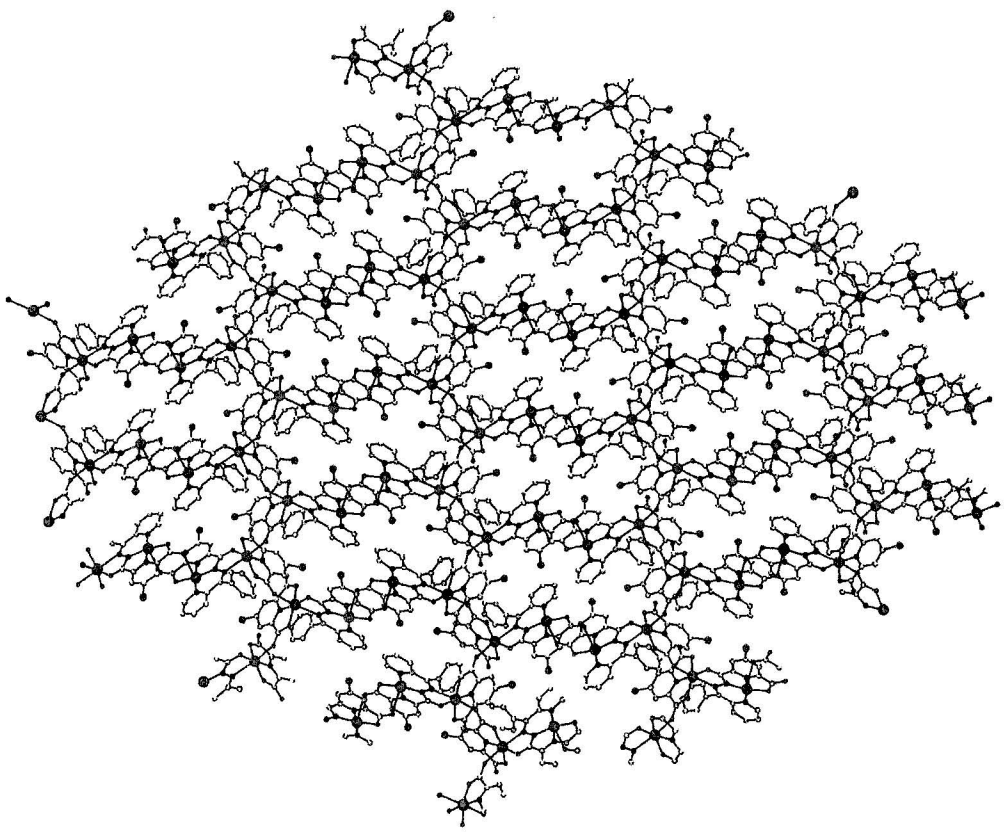

Figure 7.8: Extended structure of **7.2**, 3-phenyltriazolo[1,5-a]pyridine molecules removed for clarity.

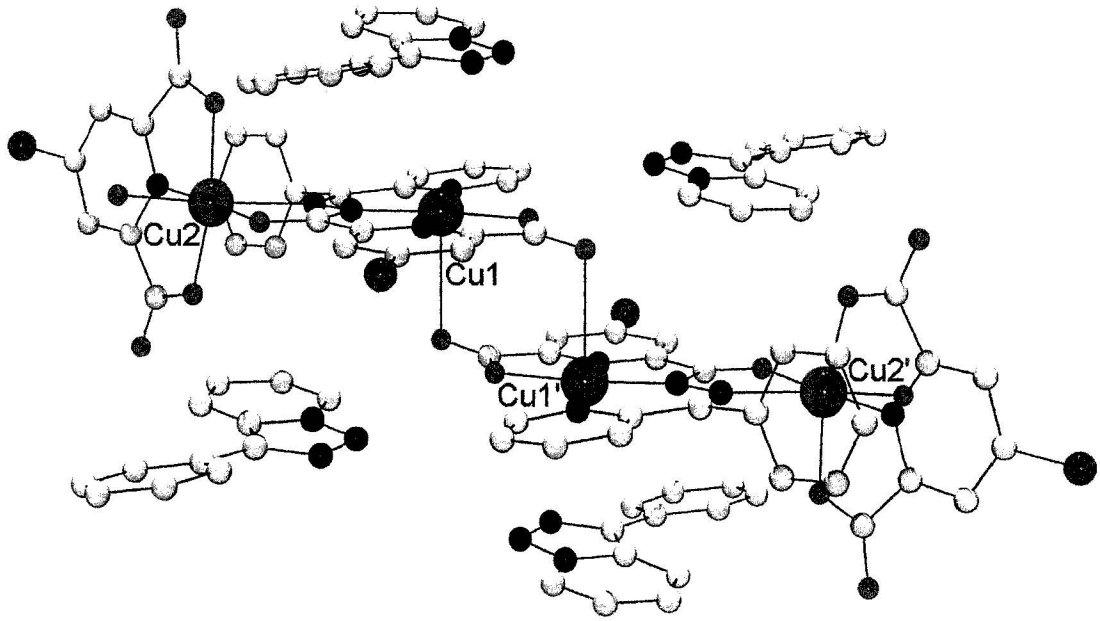

Figure 7.9: Cross-linking of chains into a 2D lattice through Cu1, showing 3-phenyltriazolo[1,5-a]pyridine guests.

7.3.1.3: $[(Cl2POPP)_3(L1)_6Co(III)_6Co(II)_6(H_2O)_6(NO_3)_6][Co(H_2O)_6](NO_3)_{12}(CH_3CN)_3(H_2O)_{10}$ (**7.3**)

The structure of **7.3** is pictured in Figure 7.10, and relevant bond lengths and angles are listed in Table 7.4. The main cation is an unusual dodecanuclear cluster with threefold symmetry, consisting of two almost planar layers of three L2 ligands (Cl2POPP molecules which have been hydrolysed at the 2 position of the central pyridine ring). Each L2 ligand bonds to two Co centers, which are bridged by a hydrazone oxygen atom, with a Co1-Co2 distance of 3.991 Å and a Co-O-Co angle of 138.92°. Carboxylate groups bridge each pair of inner (Co2) centers in a *syn-anti* conformation, forming a ring (Figure 7.11). The distance between Co2 centers is 5.180 Å. The layers are joined by

three Cl2POPP ligands, which bond to the outer (Co1) cations at both terminal pockets. The central pocket is empty (Figure 7.12). The overall molecule is shaped like a triangular prism.

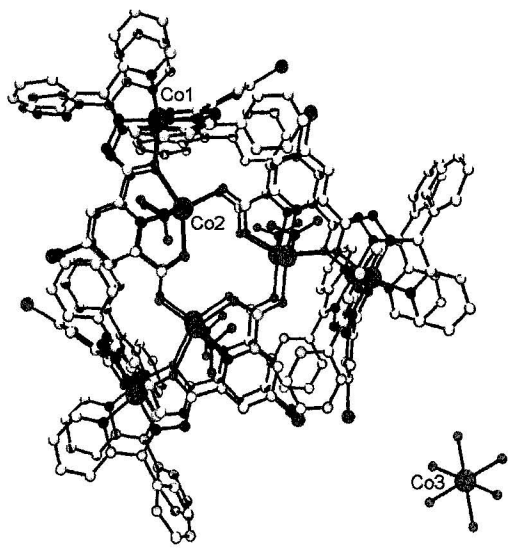

Figure 7.10: POV-RAY depiction of **7.3**. Co = magenta, O = red, N = blue, Cl = green C = grey. H-atoms removed for clarity.

Co1 has an octahedral environment, with a CoN_4O_2 coordination sphere. Co-N distances range from 1.845-1.925 Å and Co-O bond lengths fall between 1.905 and 1.939 Å. These distances are all quite short, and suggest that the outer Co cations are Co(III). Co2 also has an octahedral geometry, but with a $CoNO_5$ coordination environment, where axial positions are filled by nitrate oxygen atoms. The Co-N bond distance is 2.062 Å, while Co-O bond distances range from 2.022 to 2.321 Å. These distances are

significantly longer than those of Co1, which suggests that the inner Co centers are Co(II) cations. The central cavity of the molecule contains a disordered nitrate anion and an acetonitrile molecule as well as three coordinating oxygen atoms (presumably from water molecules). There is one additional isolated Co cation (Co3) in the lattice, which is octahedrally coordinated to six water molecules. Due to the symmetry of the compound, all Co-O bond distances for Co3 are 2.118 Å, suggesting that it is Co(II). BVS calculations were performed for the three types of Co, and were found to be consistent with the above oxidation state assignments [127-128]. There is no evidence of any interaction between the hexaaquocobalt(II) and the main cation.

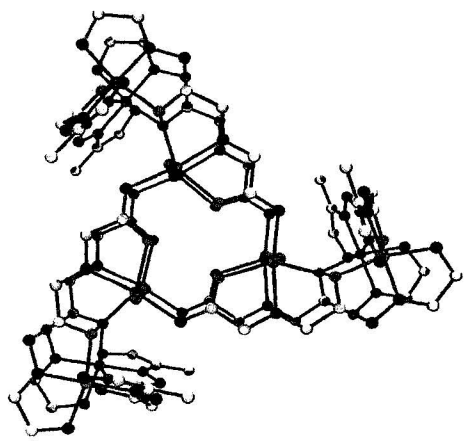

Figure 7.11: Abbreviated top view of **7.3**.

Due to the disorder in the phenyl rings of the L2 ligands, a full discussion of the long range interactions in **7.3** is not appropriate. However, it is evident that the unit cell is layered (Figure 7.13). Within a layer, there appear to be π- π interactions between adjacent phenyl rings at each corner of the triangular prism, with distances of 3.5-3.8 Å (Figure 7.14). Thus each molecule is surrounded by six others, three above and three

below, at the corners of the triangular prism. Between layers there are displaced π-π interactions between terminal pyridine rings of Cl2POPP with distances of 3.555 Å.

Table 7.4: Selected bond distances (Å) and angles (°) for **7.3**.

Co1-N6	1.845(5)	Co1-Co2	3.991
Co1-O4	1.905(4)	Co1-O1-Co2	138.9(2)
Co1-N2	1.865(6)		
Co1-N1	1.916(6)	Co2-Co2	5.180
Co1-N5	1.925(6)		
Co1-O1	1.939(4)		
Co2-O3	2.023(5)	π- π interactions: intra-layer	
Co2-O14	2.053(6)	ph-ph:	ca. 3.5-3.8*
Co2-N4	2.062(5)		
Co2-O5	2.085(5)	π- π interactions: inter-layer	
Co2-O2	2.114(5)	py-py: C26-C27	3.555
Co2-O1	2.321(4)	py-ph:	ca. 3.5*
Co3-O15	2.117(8)		
Co3-O15	2.117(8)		
Co3-O15	2.118(8)		
Co3-O15	2.118(8)		
Co3-O15	2.118(8)		
Co3-O15	2.118(8)		

*Due to disorder in the phenyl rings, these distances are approximate, and based on the 75% occupancy C atom.

There are additionally some pyridine (L2) to phenyl (Cl2POPP) interactions with distances as low as 3.5 Å. Finally, there are several short O-C distances (ca. 2.9 Å) between nitrate oxygen atoms and phenyl carbons which are likely hydrogen bonds, but cannot be properly quantified due to the disorder in the phenyl rings.

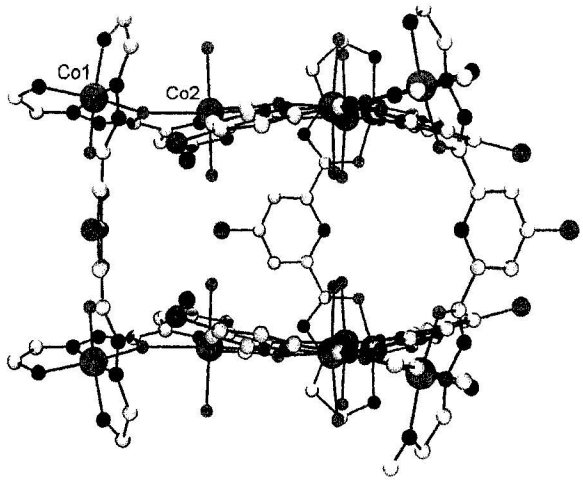

Figure 7.12: Side view of **7.3**, showing layers. Terminal aromatic rings removed for clarity.

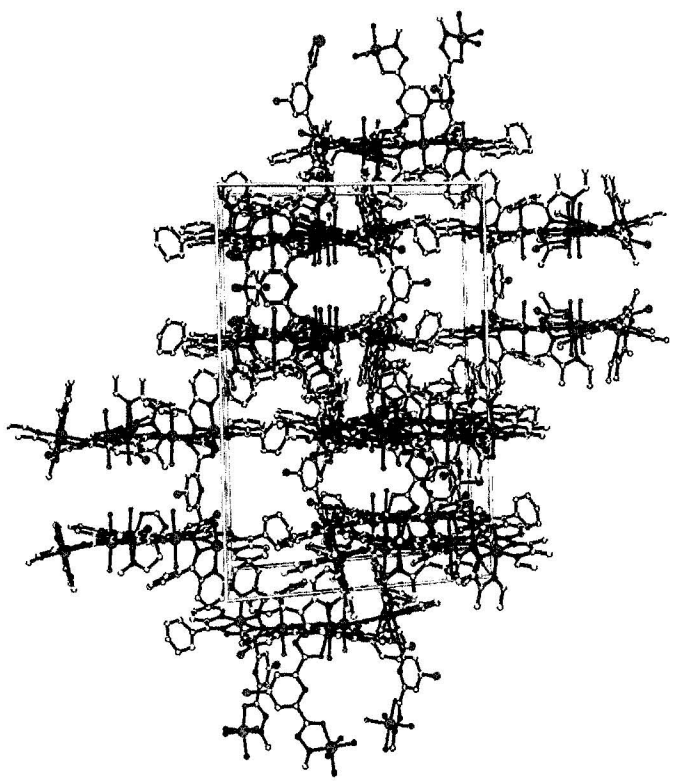

Figure 7.13: Unit cell of **7.3** from the side, showing layering.

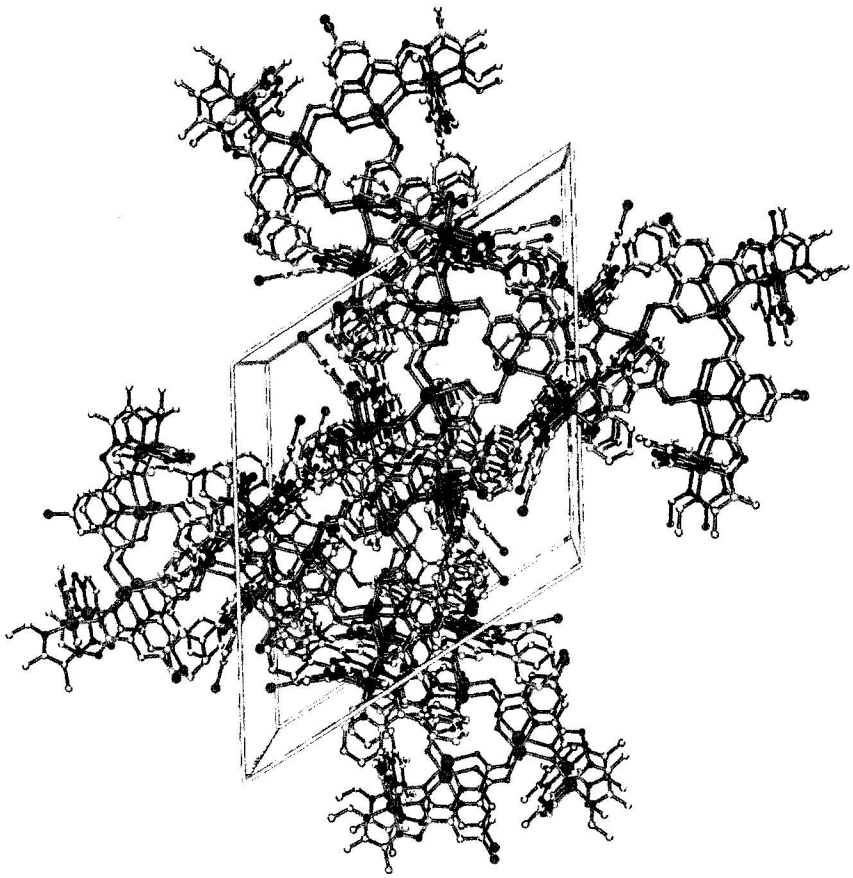

Figure 7.14: Unit cell of **7.3** from the top, showing threefold symmetry.

7.3.2: Magnetic properties:

Compound **7.1** is mononuclear, consisting of one square planar Ni(II) cation and one ligand molecule. It is diamagnetic as is expected for square planar Ni(II).

The variable temperature magnetic properties of **7.2** show an essentially constant magnetic moment (2.9 - 3.2 μ_B) in the range 2-300 K. There is no significant interaction between the Cu(II) centers. This is consistent with the structure as the short Cu(II)-Cu(II) connections are strictly orthogonal, and the non-orthogonal connections are longer and would not be expected to provide a significant antiferromagnetic pathway.

Compound **7.3** is a mixed oxidation state compound where the outer Co cations in each hexanuclear layer are Co(III), while the inner cations are Co(II). The complex cation in the lattice is hexaquacobalt(II). Co(III) is diamagnetic, and thus we would not expect any contribution to the magnetic moment from the outer Co(III) cations. The inner Co(II) cations are quite far apart (ca. 5 Å), and the bridging arrangement via the carboxylate groups is *syn-anti,* which would lead to weak coupling because the orbital overlap is not very effective due to the unfavourable orientation of the contributions of the oxygen 2p orbitals [143-146]. The magnetic moment of **7.3** at room temperature is 11.2 μ_B, dropping to 8.8 μ_B at 2 K. The spin only magnetic moment for seven uncoupled Co(II) centers is 10.2 μ_B , somewhat lower than the experimental value. This is reasonable for Co(II), which normally has a "g" value that is significantly greater than 2.0. The significant drop in magnetic moment at low temperature suggests antiferromagnetic behaviour, but zero field splitting associated with high spin Co(II) cannot be ignored. Since Co(III) is diamagnetic, a model (Figure 7.15) was developed for this system which included two rings of three Co(II) cations and an additional isolated Co(II). The exchange Hamiltonian for the two rings is:

$$H_{ex} = -J[S_1S_2 + S_2S_3 + S_3S_1 + S_4S_5 + S_5S_6 + S_6S_4] + S_7 \qquad [1]$$

Coupling between all centers in the ring is assumed to be equal, and there is no coupling between the rings, or with the isolated Co(II) cation.

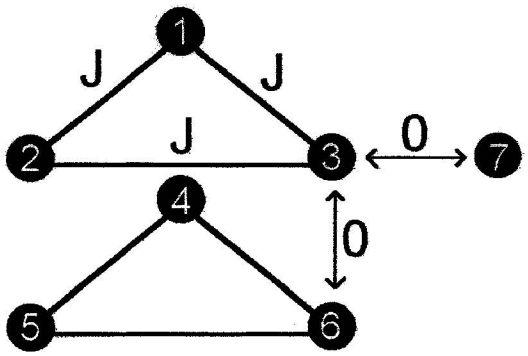

Figure 7.15: Magnetic model for **7.3**.

The magnetic profile of **7.3** is depicted in Figure 7.16. MAGMUN 4.1 [49] was used to fit the magnetic data for **7.3** to the van Vleck equation (Equation 2), corrected for intermolecular effects (θ, a Weiss-like temperature correction), for the fraction of paramagnetic impurity (α), and temperature independent paramagnetism (TIP) (Equation 3), and for zero field splitting (D) (Equation 4). Note that MAGMUN 4.1 implements the zero field splitting correction by replacing χ_{mol} for the lowest energy state with the χ_z term [87] for an axially distorted octahedral system. This model does not account for a contribution due to spin-orbit coupling, which is significant for Co(II), and thus parameters obtained by this method are approximate.

$$\chi_{M'} = \left[\frac{N\beta^2 g^2}{3k(T-\theta)}\right]\left[\frac{\sum S'(S'+1)(2S'+1)e^{-E(S')/kT}}{\sum(2S'+1)e^{-E(S')/kT}}\right] \qquad [2]$$

$$\chi_M = \chi_{M'}(1-\alpha) + \frac{S(S+1)N\beta^2 g^2 \alpha}{3kT} + TIP \qquad [3]$$

$$\chi_{z/Co} = \left[\frac{Ng_z^2\beta^2}{4kT}\right]\left[\frac{1+9e^{-2D/kT}}{1+e^{-2D/kT}}\right] \qquad [4]$$

The best fit of the data (solid line in Figure 7.16) gave g = 2.22, J = -1.4 cm^{-1}, TIP = 300 x $10^{-6}cm^3 \cdot mol^{-1}$, $\alpha = 0$, $\theta = 0.5$ K, D = 4 cm^{-1}, $10^2R = 2.5$ ($10^2R = [\Sigma(\chi_{obs}-\chi_{calc})^2/\Sigma\chi_{obs}^2]^{1/2}$). As suggested from the structure, there is very weak antiferromagnetic coupling between the Co(II) centers within each hexanuclear layer. The other parameters are consistent with Co(II).

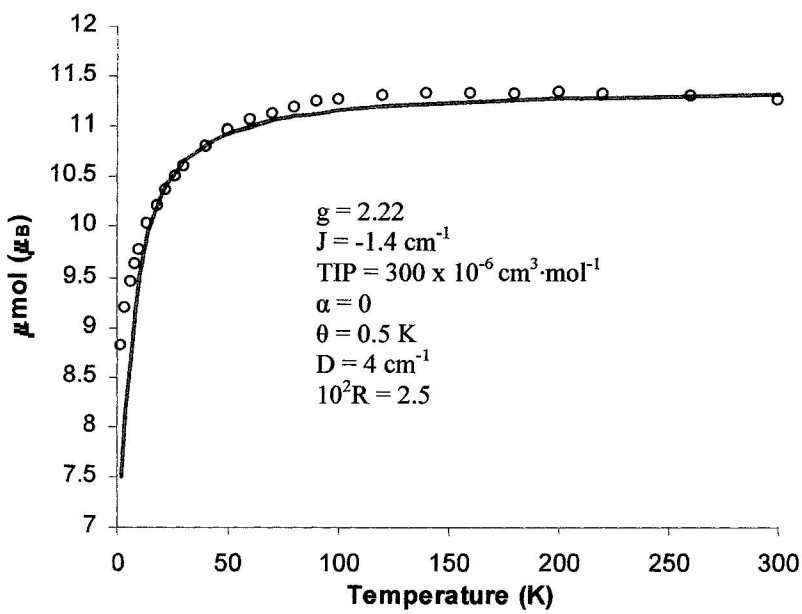

Figure 7.16: Magnetic moment vs. temperature profile for **7.3**.

7.4: Ligand solvolysis:

CHN and mass spectral data, along with the crystal structure of **7.1** prove that the ligand Cl2POPP does form initially (Chapter 2), and decomposes after reaction with transition metal cations. In the case of **7.2**, the ligand decomposes into three products, 4-chloro-2,6-pyridine dicarboxylic acid, the mono carboxylate ligand, and 3-phenyltriazolo[1,5-a]pyridine. The first two of these are easily explained by solvolysis of the hydrazone linkages at the carboxylic acid sites as opposed to the Schiff-base hydrazone sites. This presumably happens after initial coordination of Cu(II) by the ligand. Since the reaction was performed in a heated polar solvent, with acetate, a strong electrophile, as a counter anion, it is likely that the original product was a linear trinuclear compound [91, 134]. The formation of 3-phenyltriazolo[1,5-a]pyridine, while unexpected, is understandable when one considers the methods by which it and its dipyridyl ketone analogue, 3-(2-pyridyl)-triazolo[1,5-a]pyridine, are synthesized. 3-phenyltriazolo[1,5-a]pyridine can be prepared by oxidative cyclization of the hydrazone of 2-benzoyl pyridine with silver oxide[137], while 3-(2-pyridyl)-triazolo[1,5-a]pyridine can be synthesized either by reaction of dipyridyl ketone and hydrazine in air [135], by reaction of dipyridyl ketone hydrazone with nickel(II) peroxide in benzene [136], or most tellingly, by the reaction of dipyridyl ketone hydrazone with copper(II) nitrate in air [135]. As L1 and L2 have formed simultaneously with L3, it seems reasonable to assume that after complexation of Cl2POPP with Cu(II), ligand solvolysis occurred first at the carboxylic acid sites, resulting in phenyl pyridyl ketone hydrazone, either free or

complexed to Cu(II). This was followed by an oxidative cyclization of the hydrazone, presumably catalyzed by Cu(II), resulting in L3.

In the case of **7.3**, there are two organic molecules present in the structure; the ligand Cl2POPP and its half solvolysed derivative L2. While no structures of Co(II) or Ni(II) [3x3] grids have been obtained, magnetic and other evidence suggest that grid structures do form with 2POAP and related ligands. Structures of partial grids comprised of five ligand molecules and six (Ni), seven (Co), or eight (Ni) transition metal cations have been obtained [65]. Therefore, it seems reasonable to assume that the initial product of the reaction of Co(II) with Cl2POPP is a grid, or a partial grid. Co(II) is susceptible to aerial oxidation, and oxidation of a bound Co(II) to Co(III) could lead to the solvolysis of the ligand because of the high polarizing power of Co(III). This would reasonably lead to the decomposition of the initial grid, and subsequent rearrangement of the fragments into **7.3**. The presence of Co(III) in **7.3** supports this hypothesis.

7.5: Summary:

2POAP and its derivatives are formed by condensation reactions of the 2,6-pyridinedihydrazone and an iminoester, aldehyde, or ketone. For this reason they are susceptible to solvolysis by the reverse reaction in the presence of water or an alcohol. Schiff base ligands in particular undergo solvolysis reactions, both during the synthesis of the ligand and during reaction of the ligand with transition metal cations. Cl2POPP, unlike the unfunctionalized 2POPP, must be synthesized in a non-polar solvent mixture to prevent *in situ* solvolysis. While CHN, mass spectral and structural evidence prove that the ligand forms, it is very susceptible to solvolysis in reaction with transition metal

cations. With Cu(II), the ligand decomposes into three organic molecules; the half solvolysed ligand, the fully hydrolysed 4-chloro-2,6-pyridinedicarboxylic acid, and 3-phenyltriazolo[1,5-a]pyridine, which self assemble with Cu(II) to form an infinite 2D lattice, with the former two organic molecules acting as ligands to the Cu(II) centers and the latter acting as a guest in the cavities of the lattice. With Co(II), a dodecanuclear cluster results, with Cl2POPP and the half hydrolysed ligand coordinating six Co(II) and six Co(III) centers. While we can rationalize the formation of these products after the fact, it is impossible to predict their formation beforehand, and the complexes could not be identified without X-ray crystallographic data. Thus the serendipitous formation of these compounds through ligand solvolysis, while interesting, is a significant obstacle to rational design. Use of dry, non-polar solvents where possible, and of inert atmospheres in the case of easily oxidized salts such as Co(II) and Fe(II) should minimize the risk of ligand hydrolysis, making the task of constructing specific clusters more easily accomplished.

Chapter 8: General Conclusions:

A series of new, functionalized 2POAP-like ligands was synthesized, characterized, and used to prepare a variety of [3x3] $M(II)_9$ grids and grid fragments, $Cu(II)_8$ pinwheels, and interesting ligand hydrolysis products. Chlorine and ethyl- and methylthio groups were introduced to the central pyridine rings of six ligands to observe the effects of the functional group on the structure and properties of complexes, and to provide a platform from which to attach complexes to gold and graphite surfaces. Terminal groups were also varied, from iminoesters based on pyridine and pyrazine, which form amidrazone linkages, to 2-acetylpyridine and 2-benzoylpyridine, which form Schiff base linkages.

Introduction of the electron rich chlorine and sulphur sites to the ligand backbone created a series of intermolecular interactions in the crystal packing arrangements of the resultant complexes. These included hydrogen bonding, Cl···N interactions, S···N interactions, S···S interactions, and in the cases of compounds **6.4** and **6.5**, S···Ag interactions. These new interactions completely replaced the π-π interactions that generally dominate the extended structures of complexes of 2POAP-like ligands in all but one case. In compound **4.3**, strong Cl···N interactions resulted in stacking of the $Cu(II)_8$ pinwheel molecules, and a long range ferromagnetic interaction in the bulk sample. In compound **4.5**, S···S interactions also lead to stacking of the $Cu(II)_8$ pinwheels, but in this case a long range antiferromagnetic effect was observed. In compound **6.5**, an unusually large, negative, θ correction was observed, which indicates possible intermolecular

antiferromagnetic coupling, presumably via the direct Ag(I) mediated bridging connections between grid molecules.

Functional groups were found to have a profound effect on the electrochemical properties of the [3x3] $Mn(II)_9$ grid complexes. Changing the functional group on the 4-position of the central pyridine ring results in slight changes in potential for the redox events, while the overall electrochemical properties remain essentially the same. Changing the end-groups of the 2POAP-like ligands has a more dramatic effect; exchanging a terminal pyridine ring for a pyrazine ring results in a 200mV shift to higher potential for all five redox waves, while replacing the amidrazone-based linkage for a Schiff-base linkage results in the complete disruption of the normal suite of redox processes observed in the [3x3] $Mn(II)_9$ grids. This suggests the involvement of the amidrazone NH_2 group in the redox processes. This hypothesis is supported by the reactions of SEt2POAP and 2POAP based $Mn(II)_9$ grids with other transition metal cations, which result in partially oxidized [3x3] $Mn(II)_xMn(III)_{9-x}$ grids. When [3x3] $Mn(II)_9$ grid complexes with Schiff-base linkages are reacted with Cu(II) salts, the grid is destroyed, and only $Cu(II)_8$ pinwheels are isolated.

The pH of the reaction was found to have a profound effect on the outcome of the reaction, especially for reactions with transition metal cations other than Mn(II). In cases where the ligand was found to be singly deprotonated or neutral, there was a high instance of adoption of the bent conformation in the ligand molecules. This conformation prevents the formation of the [3x3] $M(II)_9$ grid compounds. When Ni(II) was reacted with SEt2POAP in the presence of NaOH, a [3x3] $Ni(II)_9$ grid complex was the result. A

similar reaction conducted in the absence of base resulted in a $Ni(II)_6$ grid fragment, where one singly deprotonated and two neutral and ligand molecules adopted the bent conformation, preventing coordination of the central ligand pockets by Ni(II) cations.

Reaction of a [3x3] $Mn(II)_9$ SEt2POAP grid with $AgNO_3$ resulted in an extended network of grid molecules, which were directly connected by either two or four Ag(I) bridges. Ag(I) was found to bind to the grid molecule in several ways; by a single sulphur atom, between two sulphur atoms, or to diazine nitrogen atoms. The interactions between the Ag(I) cations and the grid may help to identify the types of interactions which occur between a sulphur functionalized grid and an Au(111) surface. The binding of Ag(I) to the diazine nitrogen atoms of the grid suggests the possibility of binding additional transition metal cations to the outside of the grid molecules in such a way as to be bridged to the internal Mn(II) cations of the grid, which could lead to larger clusters with interesting magnetic properties.

Cl2POPP was found to be difficult to synthesize due to hydrolytic instability. This same instability was found to lead to solvolysis processes when the ligand was reacted with transition metal cations. The result was a pair of interesting polynuclear complexes based on the fragments produced by the solvolysis of the ligand. An extended network based around a $Cu(II)_2$ subunit was prepared which served as a host to a neutral aromatic fragment also produced by the ligand solvolysis. An interesting mixed valent Co_{13} cluster was formed from a combination of Cl2POPP ligands and half-ligands generated by ligand solvolysis. This complex displayed weak antiferromagnetic coupling between Co(II) cations.

Appendix 1: Vector coupling approach to magnetic modelling:

A1.1: Binuclear compounds:

For a binuclear compound, the exchange Hamiltonian is given by:

$$H_{ex} = -2J_{12}\, S_1 \cdot S_2 \qquad [1]$$

If S', the total spin quantum number combinations are:

$$S' = S_1 + S_2 \qquad [2]$$

then

$$S' \cdot S' = (S_1 + S_2)^2 = S_1^2 + S_2^2 + 2S_1S_2 = 2S(S+1) + 2S_1S_2 \qquad [3]$$

and the Hamiltonian can be rewritten:

$$H_{ex} = -J_{12}[S'(S'+1)-2S(S+1)] \qquad [4]$$

The energy is then

$$E(S') = -J_{12}[S'(S'+1)-2S(S+1)] \qquad [5]$$

although the second term is often neglected in the literature in the calculation of the energy levels. For this simple case, calculating the allowed spin states and energies is a trivial exercise. The allowed spin states can be obtained using the addition rule for two vectors:

$$S' = (S_1 + S_2), (S_1 + S_2 - 1),.....(S_1-S_2) \qquad [6]$$

If cobalt(II) is used as an example, $S_1 = S_2 = 3/2$, and the states and energies are listed in Table A1.1.

Table A1.1: Spin states and energies for a binuclear cobalt (II) compound.

Electrons	S'	S' + 1	2S'+1	E(S')=J[S'(S'+1)]
↑ ↑ ↑ ↑ ↑ ↑	3	4	7	12J
↑ ↑ ↑ ↑ ↑ ↓	2	3	5	6J
↑ ↑ ↑ ↓ ↑ ↓	1	2	3	2J
↑ ↓ ↑ ↓ ↑ ↓	0	1	1	0

The generalized form of the van Vleck equation is:

$$\chi_M = \frac{N\beta^2 g^2}{3kT} \frac{\sum S'(S'+1)\Omega(S')(2S'+1)e^{-E(S')/kT}}{\sum (2S'+1)\Omega(S')e^{-E(S')/kT}} \qquad [7]$$

Note that Ω(S') represents the degeneracies of the energy levels. This term was ignored in the earlier discussion as MAGMUN4.1 calculates all the energy levels separately. For a relatively simple system such as the described Co(II) binuclear compound, spin states and energies can be substituted directly into the van Vleck equation (the degeneracy term is equal to one for a binuclear system):

$$\chi_M = \frac{Ng^2\beta^2}{3kT} \frac{(3)(4)(7)e^{\left(\frac{-12J}{kT}\right)} + (2)(3)(5)e^{\left(\frac{-6J}{kT}\right)} + (1)(2)(3)e^{\left(\frac{-2J}{kT}\right)}}{7e^{\left(\frac{-12J}{kT}\right)} + 5e^{\left(\frac{-6J}{kT}\right)} + 3e^{\left(\frac{-2J}{kT}\right)} + 1} + TIP \qquad [8]$$

if x = exp(J/kT), the expression is multiplied through by x^{12}, and $Ng^2\beta^2/3k = K$, the expression becomes:

$$\chi_M = \frac{6K}{T} \frac{14 + 5x^6 + x^{10}}{7 + 5x^6 + 3x^{10} + x^{12}} + TIP \qquad [9]$$

A1.2: Trinuclear Compounds:

A compound with three magnetic centers could be organized in several ways; an equilateral triangle having one J value, an isosceles triangle, or linear compound, having two different J values, or a scalene triangle, having three J values. This last case will not be dealt with here, as scalene triangles are not often observed experimentally. The isosceles triangle and the linear compound may be treated in the same manner. A diagram for the trinuclear case is pictured in Figure A1.1.

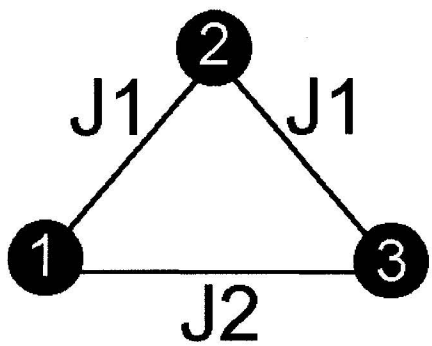

Figure A1.1: Magnetic model for trinuclear compounds.

The above illustration represents the general trinuclear case. J2 could represent either the short side of an isosceles triangle, or the interaction between the two ends of a linear compound. If J2=J1, then the diagram represents an equilateral triangle.

The exchange Hamiltonian for the general trinuclear case is:

$$H_{ex} = -2J1[S_1S_2 + S_2S_3] + -2J2[S_1S_3] \qquad [10]$$

S* is defined $S^* = S_1 + S_3$, and $S' = S_1 + S_2 + S_3$ ($= S^* + S_2$). As in the binuclear case, the rules of vector addition are used to define the allowed states of S* as $(S_1 + S_3)$, $(S_1 + S_3 - 1)$,...$(S_1 - S_3)$ and S' as (S* + S2), (S* + S2 -1),...(S* - S2). Then using S*S*:

$$S^*S^* = 2S(S+1) + 2S_1S_3 \qquad [11]$$

And

$$S_1S_3 = \tfrac{1}{2}S^*(S^*+1) - 2S(S+1) \qquad [12]$$

Next,

$$S'S' = 3S(S+1) + 2S_1S_2 + 2S_2S_3 + 2S_1S_3 \qquad [13]$$

Rearranging for $S_1S_2 + S_2S_3$ and substituting into 10:

$$H_{ex} = -J1[S'(S'+1) + S^*(S^*+1) - S(S+1)] - J2[S^*(S^*+1) - 2S(S+1)] \qquad [14]$$

And

$$E(S,S') = -J1[S'(S'+1) + S^*(S^*+1) - S(S+1)] - J2[S^*(S^*+1) - 2S(S+1)] \qquad [15]$$

For J1 = J2 the equations simplify to:

$$H_{ex} = -J1[S'(S'+1) - 3S(S+1)] \qquad [16]$$

And

$$E(S,S') = -J1[S'(S'+1) - 3S(S+1)] \qquad [17]$$

The spin states and energies for an equilateral triangle with S1 = S2 = S3 = 3/2 are collected in Table A1.2 to illustrate the degeneracy terms. The 3S(S+1) term has been omitted from the energies.

Table A1.2: Spin states, energies, and degeneracies for a trinuclear compound with S = 3/2.

$S_1 + S_3$	$S^* + S_2$	S'	Ω(S')	E(S*,S')
3	9/2,7/2,5/2,3/2	9/2	1	99/4 J1
2	7/2,5/2,3/2,1/2	7/2	2	63/4 J1
1	5/2,3/2,1/2	5/2	3	35/4 J1
0	3/2	3/2	4	15/4 J1
		½	2	3/4 J1

The spin states, energies and degeneracies could be substituted into the van Vleck equation to obtain an exact solution at this stage. It is more convenient to use a simple computer program to calculate the spin states and energies and input them into the van Vleck equation in an iterative process. An example of the core of one such program, equitri.bas, is included in Figure A.2. The full program runs in the TurboBasic platform, and is capable of fitting variable temperature magnetic data, and generating plots of magnetic susceptibility, magnetic moment and χT vs. temperature.

Calc. of mu (eff)

```
Evaluate:
Espin=0: muo# = 0: muu# = 0
J1=J1/1.4388
Sa = S1 + S3
For SK = Sa to abs(S1-S3) step -1
      hi=SK+S2: lo = SK-S2
if lo<0 then lo=-lo
if hi<lo then swap hi,lo
For ST = hi to lo step -1
a = ST*(ST+1)
```

```
                    d= 1+(2*ST)
                        Sp=S*(S+1)
                    term1= J1*(a-3*Sp)
Espin = term1
Espin = Espin/T
top# = (a*d)*(e^Espin)
bot# = d*(e^Espin)
muo# = muo# +top#
muu# = muu# +bot#
Next ST
next SK
chi = muo#/muu#
chi=chi*const*g*g/(3*(T-th))
chi=chi*(1-ro)+TIP+ro*const*g*g*S*(S+1)/(3*T)
J1=J1*1.4388
Return
```

Figure A1.2: Section of TurboBasic program used for magnetic modeling equilateral triangle-like systems.

A1.3: Tetranuclear Compounds:

A general tetranuclear exchange model is illustrated in Figure A1.3.

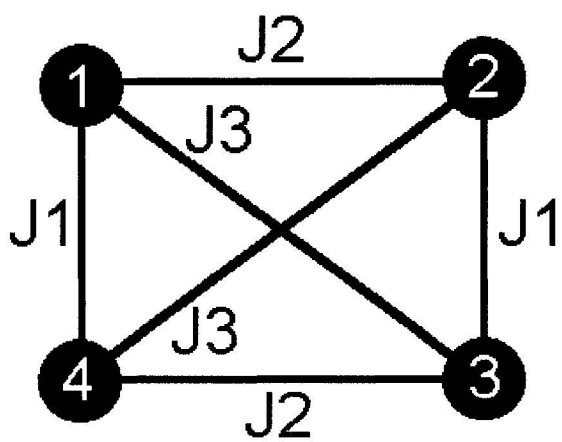

Figure A1.3: General tetranuclear exchange model.

For this model, the exchange Hamiltonian is:

$$H_{ex} = -2J1[S_1S_4 + S_2S_3] -2J2[S_1S_2 + S_3S_4] -2J3[S_1S_3 + S_2S_4] \quad [18]$$

The following are defined:

$$S^* = S_1 + S_3 \quad [19]$$

$$S^+ = S_2 + S_4 \quad [20]$$

$$S^{**} = S_1 + S_2 \quad [21]$$

$$S^{++} = S_3 + S_4 \quad [22]$$

$$S' = S^* + S^+ \quad [23]$$

Then 19-23 can be rearranged to give

$$S_1 \cdot S_3 = \tfrac{1}{2} (S^* \cdot S^*) - S(S + 1) \quad [24]$$

$$S_2 \cdot S_4 = \tfrac{1}{2} (S^+ \cdot S^+) - S(S + 1) \quad [25]$$

$$S_1 \cdot S_2 = \tfrac{1}{2} (S^{**} \cdot S^{**}) - S(S + 1) \quad [26]$$

$$S_3 \cdot S_4 = \tfrac{1}{2} (S^{++} \cdot S^{++}) - S(S + 1) \quad [27]$$

Next, $S' = S_1 + S_2 + S_3 + S_4$, and $S' \cdot S'$ is:

$$S' \cdot S' = S_1S_1 + S_2S_2 + S_3S_3 + S_4S_4 + S_1S_2 + S_1S_3 + S_1S_4 + S_2S_3 + S_2S_4 + S_3S_4 \quad [28]$$

which is simplified and rearranged:

$$S_1S_4 + S_2S_3 = \tfrac{1}{2} (S' \cdot S') - S_1S_2 - S_1S_3 - S_2S_4 - S_3S_4 - 2S(S + 1) \quad [29]$$

then substituting 24, 25, 26, and 27 into 29, we obtain

$$S_1S_4 + S_2S_3 = \tfrac{1}{2}(S' \cdot S') - \tfrac{1}{2}(S^{**} \cdot S^{**}) - \tfrac{1}{2}(S^* \cdot S^*) - \tfrac{1}{2}(S^+ \cdot S^+) - \tfrac{1}{2}(S^{++} \cdot S^{++}) \quad [30]$$

finally, 29, 24, 25, 26 and 27 are substituted into 18 to obtain the new exchange Hamiltonian:

$$H_{ex} = -J1[S'(S'+1) - S^{**}(S^{**}+1) - S^{++}(S^{++}+1) - S^{+}(S^{+}+1) - S^{*}(S^{*}+1)] - J2[S^{++}(S^{++}+1) + S^{++}(S^{++}+1)] - J3[S^{*}(S^{*}+1) + S^{+}(S^{+}+1) - 4S(S+1)] \quad [31]$$

The general tetranuclear Hamiltonian can be simplified to represent specific cases. If J3 = 0, then the model represents a rectangular system with no cross coupling. The exchange Hamiltonian for this system is:

$$H_{ex} = -J1[S'(S'+1) - S^{**}(S^{**}+1) - S^{++}(S^{++}+1) - S^{+}(S^{+}+1) - S^{*}(S^{*}+1)] - J2[S^{**}(S^{**}+1) + S^{++}(S^{++}+1)] \quad [32]$$

For a square with cross coupling, J1 = J2 and the exchange Hamiltonian becomes:

$$H_{ex} = -J1[S'(S'+1) - S^{*}(S^{*}+1) - S^{+}(S^{+}+1)] - J3[S^{*}(S^{*}+1) + S^{+}(S^{+}+1) - 4S(S+1)] \quad [33]$$

For a square without cross coupling, the exchange Hamiltonian becomes:

$$H_{ex} = -J1[S'(S'+1) - S^{*}(S^{*}+1) - S^{+}(S^{+}+1)] \quad [34]$$

Finally, if J1 = J2 = J3, the model can represent a tetrahedron:

$$H_{ex} = -J1[S'(S'+1) - 4S(S+1)] \quad [35]$$

Again, simple computer programs can be written to model magnetic data using these expressions.

A1.4: Summary:

The chief disadvantage to using vector coupling methods for magnetic modeling is that it takes time to write the exchange equations, and for systems with larger numbers of spins, or very little symmetry, the calculations quickly become unmanageable. The iterative approach, used in the sample TurboBasic program also takes more time to model

the data than does MAGMUN4.1. The advantage to this approach is that it is possible to perform non-linear regressions on several different exchange integrals (J) independently of one another, instead of as multiples of the same general J factor as is necessary in MAGMUN4.1.

Appendix 2: Magnetic models, OW01.ini files, and spk files:

A2.1: $Cu(II)_8$ pinwheels:

The exchange Hamiltonian for a pinwheel compound is:

$$H_{ex} = -J1[S_1S_2 + S_2S_3 + S_3S_4 + S_4S_1] - J2[S_1S_5 + S_2S_6 + S_3S_7 + S_4S_8]$$

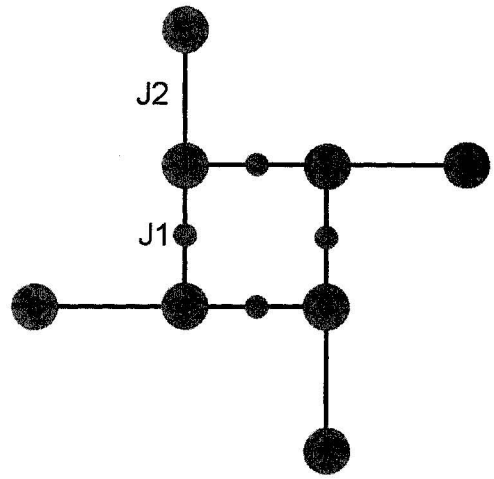

Figure A2.1: $Cu(II)_8$ pinwheel model.

If J1 = J2 = J, then the input file OW01.ini is:

Spins: 1 1 1 1 1 1 1 1
Couplings: 12 23 34 41 15 26 37 48
Strengths: -1 -1 -1 -1 -1 -1 -1 -1
Output: Cu(II)8pinwheel

And the *.spk file generated by OW01.exe is:

MDA 01.00 SPK 00
#PROGRAM:
Program OW0L, (c) Oliver Waldmann, Version 11.5.01
#HAMILTONIAN:
Heisenberg Hamiltonian
#SYSTEM:
Spins = 1/2 1/2 1/2 1/2 1/2 1/2 1/2 1/2
Couplings = 1-2 2-3 3-4 4-1 1-5 2-6 3-7 4-8
#PARAMETER:
Strengths = -1 -1 -1 -1 -1 -1 -1 -1
Emin = -3.46716625452677
#COMMENT:
sorted spektrum with classification
#DATA: (Column one is the relative energy, and column 2 is 2S'+1)

0	0	0
0.4352118386	2	0
0.8496005729	2	1
0.8496005729	2	2
1.121004724	4	0
1.220186651	0	1
1.612528575	2	3
1.647414962	0	2
1.760059473	0	3

1.760059473	0	4
1.835647006	2	4
1.835647006	2	5
1.941479134	4	1
1.953381756	2	6
2.015560292	2	7
2.323043449	4	2
2.323043449	4	3
2.381016361	2	8
2.381016361	2	9
2.467166255	2	10
2.467166255	0	5
2.612528575	4	4
2.664366643	4	5
2.708931467	0	6
2.825544582	2	11
2.825544582	2	12
2.849132266	6	0
2.870197971	2	13
2.912208122	0	7
3.03015023	4	6
3.03015023	4	7
3.064134538	2	14
3.174273036	0	9
3.174273036	0	8
3.269965866	4	8
3.299689836	2	15
3.299689836	2	16
3.311787285	2	17
3.467166255	0	10
3.467166255	4	9
3.467166255	2	18
3.467166255	0	11
3.725818277	4	10
3.760059473	6	1
3.760059473	6	2
3.789232983	2	19
3.789232983	2	20
3.870197971	4	11
3.904182279	4	12
3.904182279	4	13
3.918772217	2	21
4.151371466	2	22
4.151371466	2	23

4.168284139	2	24
4.26910399	0	12
4.321803934	2	25
4.467166255	6	3
4.467166255	4	14
4.512318589	0	13
4.605227229	2	26
4.605227229	2	27
4.61128906	4	15
4.61128906	4	16
4.734201353	4	17
4.813327785	4	18
4.918772217	4	19
5.085200243	6	4
5.174273036	6	5
5.174273036	6	6
5.467166255	8	0

If J2 = -10 J1, J2 is 10 times larger than J1 and has the opposite sign, and because the inner core of the pinwheel molecules is ferromagnetic, in this case J2 is antiferromagnetic.

The input file is:

Spins: 1 1 1 1 1 1 1 1
Couplings: 12 23 34 41 15 26 37 48
Strengths: -1 -1 -1 -1 10 10 10 10
Output: Cu(II)8pinwheela

The *.spk file is similar in format, but the spin states and energies are different.

A2.2: Ni(II)$_9$ grid molecule:

The exchange Hamiltonian for the system is:

$$H_{ex} = -J1[S_1S_2 + S_2S_3 + S_3S_4 + S_4S_5 + S_5S_6 + S_6S_7 + S_7S_8 + S_8S_1] - J2[S_2S_9 + S_4S_9 + S_6S_9 + S_8S_9]$$

If J1 = J2 = J, then the input file OW01.ini is:

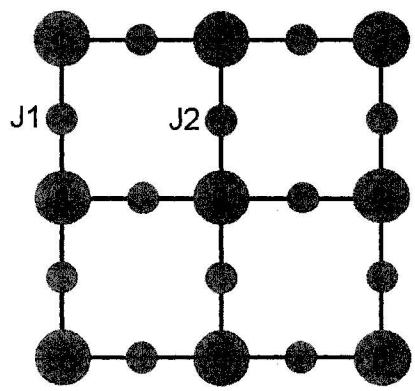

Figure A2.2: M_9 model.

Spins: 2 2 2 2 2 2 2 2 2
Couplings: 12 23 34 45 56 67 78 81 29 49 69 89
Strengths: -1 -1 -1 -1 -1 -1 -1 -1 -1 -1 -1 -1
Output: Ni9

And the *.spk file is:

MDA 01.00 SPK 00
#PROGRAM:
Program OW0L, (c) Oliver Waldmann, Version 11.5.01
#HAMILTONIAN:
Heisenberg Hamiltonian
#SYSTEM:
Spins = 2/2 2/2 2/2 2/2 2/2 2/2 2/2 2/2 2/2
Couplings = 1-2 2-3 3-4 4-5 5-6 6-7 7-8 8-1 2-9 4-9 6-9 8-9
#PARAMETER:
Strengths = -1 -1 -1 -1 -1 -1 -1 -1 -0.1 -0.1 -0.1 -0.1
Emin = -11.5028844665091
#COMMENT:
sorted spektrum with classification
#DATA:
0 2 0...

The list of states and energies for this system is over 60 pages long. The complexity of the calculation grows very quickly with the number of spin states.

A2.3: $Ni(II)_6$ grid fragment:

The exchange Hamiltonian for the system is:

$H_{ex} = -J[S_1S_2 + S_2S_3 + S_4S_5 + S_5S_6]$

and the OW01.ini file is:

Spins: 2 2 2 2 2 2
Couplings: 12 23 45 56
Strengths: -1 -1 -1 -1
Output: Ni6

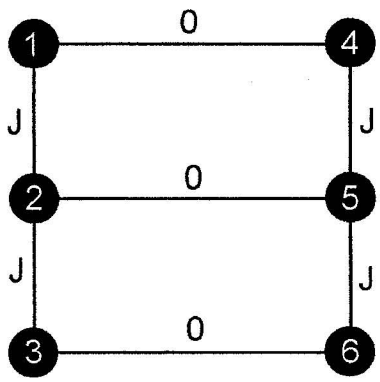

Figure A2.3: $Ni(II)_6$ model.

A2.4: $Co(II)_{13}$ cluster:

The exchange Hamiltonian for the system is:

$$H_{ex} = -J[S_1S_2 + S_2S_3 + S_3S_1 + S_4S_5 + S_5S_6 + S_6S_4] + S_7$$

Spins: 3 3 3 3 3 3 3
Couplings: 12 23 31 45 56 64
Strengths: -1 -1 -1 -1 -1 -1
Output: Co13

Note: the diamagnetic Co(III) cations are excluded from the magnetic model.

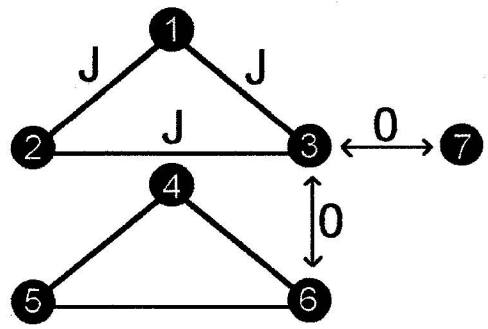

Figure A2.4: Co_{13} model.

A2.5: Summary:

The examples outlined in this Appendix represent the majority of the structures included in this report. The $Cu(II)_9$ and $Co(II)_9$ grids were not included in this appendix as they are largely similar to the other examples. Calculation times for the majority of the *.spk files are a matter of seconds. The Ni structures and the Co_{13} structure take several minutes to calculate. The $Co(II)_9$ grid is the largest calculation, with twenty seven unpaired electrons. This calculation had to be performed on a PC with 4 GB of RAM, and the calculation took approximately two hours.

Appendix 3: Expanded structural data:

A3.1: $[(SEt2POAP)_6Mn_9](SCN)_6(H_2O)_{13}(CH_3OH)_2$ (**3.2**)

A. Crystal Data

Empirical Formula:	$C_{140.50}H_{156}O_{24}N_{60}S_{12}Mn_9$
Formula Weight:	3948.33
Crystal Color, Habit:	red-orange, block
Crystal Dimensions:	0.48 X 0.22 X 0.19 mm
Crystal System:	monoclinic
Lattice Type:	Primitive
Lattice Parameters:	a = 28.447(3) Å b = 21.338(2) Å c = 33.290(4) Å β = 111.525(2)° V = 18798(3) $Å^3$
Space Group:	$P2_1/c$ (#14)
Z value:	4
Dcalc:	1.395 g/cm^3
F_{000}:	8112.00
μ(MoKα):	7.92 cm^{-1}

B. Intensity Measurements

Diffractometer:	Bruker P4/CCD
Radiation:	MoKα (λ = 0.71073 Å) graphite monochromated
Temperature:	-80 + 1°C
Scan Rate:	30 sec, 0.3 deg frames
2θmax :	52.9°
No. of Reflections Measured:	Total: 141230 Unique: 38393 (Rint = 0.082)
Corrections:	Lorentz-polarization SADABS correction (trans factors 0.8649 – 0.7039)

C. Structure Solution and Refinement

Structure Solution:	Direct Methods (SHELX97)
Refinement:	Full-matrix least-squares on F2
Function Minimized:	$\Sigma w (Fo^2 - Fc^2)^2$

Least Squares Weights:	$w = 1/ [\sigma^2(Fo^2) + (0.2000 \cdot P)^2 + 0.0000 \cdot P]$ where $P = (Max(Fo^2,0) + 2Fc^2)/3$
Anomalous Dispersion:	All non-hydrogen atoms
No. Observations:	38393
No. Variables:	2113
Reflection/Parameter Ratio:	18.17
Residuals: R1; wR2:	0.104 ; 0.369
Goodness of Fit Indicator:	1.14
Max Shift/Error in Final Cycle:	0.01
Maximum peak in Final Diff. Map:	2.83 $e^-/Å^3$
Minimum peak in Final Diff. Map:	-1.26 $e^-/Å^3$

A3.2: $[(Cl2POMP)_6Mn_9](ClO_4)_6(H_2O)_{15}$ **(3.3)**:

A. Crystal Data

Empirical Formula:	$C_{126}H_{96}Cl_6Mn_9N_{42}O_{12}$
Formula Weight:	3097.61
Crystal Color, Habit:	orange, block
Crystal Dimensions:	0.35 X 0.20 X 0.12 mm
Crystal System:	monoclinic
Lattice Type:	Primitive
Lattice Parameters:	a = 18.086(2) Å b = 28.177(3)) Å c = 34.491(4)) Å β = 94.693(2) ° V = 17518(4) $Å^3$
Space Group:	P2(1)/c
Z value:	4
Dcalc:	1.175 g/cm^3
F_{000}:	6276
μ(MoKα):	7.76 cm^{-1}

B. Intensity Measurements

Diffractometer:	Bruker Proteum M
Radiation:	MoKα (λ = 0.71073 Å) graphite monochromated
Temperature:	120 +/- 2K
2θmax :	50°
No. of Reflections Measured:	Total: 92140 Unique: 30766 (Rint =0.1138)

Corrections:	Lorentz-polarization SADABS correction (trans factors1– 0.100719)

C. Structure Solution and Refinement

Structure Solution:	Direct Methods (SHELX97)
Refinement:	Full-matrix least-squares on F2
Function Minimized:	$\Sigma w (Fo^2 - Fc^2)^2$
Least Squares Weights:	$w = 1/ [\sigma^2(Fo^2) + (0.0692 \cdot P)^2 + 0.0000 \cdot P]$ where $P = (Max(Fo^2,0) + 2Fc^2)/3$
Anomalous Dispersion:	All non-hydrogen atoms
No. Observations:	30766
No. Variables:	1768
Reflection/Parameter Ratio:	17.40
Residuals: R1; wR2:	0.0718; 0.2072
Goodness of Fit Indicator:	1.002

A3.3: $[(2POPP)_6Mn_9](NO_3)_6(H_2O)_{12}$ **(3.4)**

A. Crystal Data

Empirical Formula	$C_{186}H_{138}N_{46}O_{30}Mn_9$
Formula Weight	3991.87
Crystal Color, Habit	red-brown, prism
Crystal Dimensions	0.76 X 0.30 X 0.29 mm
Crystal System	tetragonal
Lattice Type	Primitive
Lattice Parameters	a = 20.279(1) Å c = 54.873(6) Å V = 22566(2) $Å^3$
Space Group	$P4_12_12$ (#92)
Z value	4
D_{calc}	1.175 g/cm^3
F_{000}	8164.00
μ(MoKα)	5.54 cm^{-1}

B. Intensity Measurements

Diffractometer	Bruker P4/CCD
Radiation	MoKα (λ = 0.71073 Å) graphite monochromated
Temperature	-80 ± 1°C
Scan Rate	30s, 0.3 deg frames
$2\theta_{max}$	52.9°
No. of Reflections Measured	Total: 125625 Unique: 23102 (R_{int} = 0.115)
Corrections	Lorentz-polarization SADABS correction (trans factors 0.8557 – 0.6780)

C. Structure Solution and Refinement

Structure Solution	Direct Methods (SHELX97)
Refinement	Full-matrix least-squares on F^2
Function Minimized	$\Sigma w (Fo^2 - Fc^2)^2$
Least Squares Weights	$w = 1/ [\sigma^2(Fo^2) + (0.2000 \cdot P)^2 + 0.0000 \cdot P]$ where $P = (Max(Fo^2,0) + 2Fc^2)/3$
Anomalous Dispersion	All non-hydrogen atoms
No. Observations (I>2.00σ(I))	15252
No. Variables	1175
Reflection/Parameter Ratio	12.98
Residuals: R1; wR2	0.111 ; 0.323
Goodness of Fit Indicator	1.12
Max Shift/Error in Final Cycle	0.00
Maximum peak in Final Diff. Map	1.16 $e^-/Å^3$
Minimum peak in Final Diff. Map	-0.84 $e^-/Å^3$

A3.4: $[(Cl2POMP)_4Cu_8(NO_3)_8](H_2O)_{15}$ **(4.1)**

A. Crystal Data

Empirical Formula	$C_{84}H_{88}N_{36}O_{44}Cl_4Cu_8$
Formula Weight	2956.01

Crystal Color, Habit	green, prism
Crystal Dimensions	0.29 X 0.09 X 0.08 mm
Crystal System	tetragonal
Lattice Type	I-centered
Lattice Parameters	a = 21.2562(8) Å c = 12.7583(9) Å V = 5764.5(4) $Å^3$
Space Group	I-4 (#82)
Z value	2
D_{calc}	1.703 g/cm^3
F_{000}	2992.00
μ(MoKα)	16.41 cm^{-1}

B. Intensity Measurements

Detector	Bruker/P4 CCD
Radiation	MoKα (λ = 0.71073 Å) graphite monochromated
Temperature	-80 $\pm$ 1°C
Scan Rate	30 sec, 0.3 deg Frames
$2\theta_{max}$	52.8°
No. of Reflections Measured	Total: 17468 Unique: 5873 (R_{int} = 0.064)
Corrections	Lorentz-polarization SADABS correction Trans. Factors 0.8799 and 0.6475

C. Structure Solution and Refinement

Structure Solution	Direct Methods (SHELX97)
Refinement	Full-matrix least-squares on F^2
Function Minimized	Σ w (Fo^2 - Fc^2)^2
Least Squares Weights	$w = 1/ [\sigma^2(Fo^2) + (0.0948 \cdot P)^2 + 0.0000 \cdot P]$ where $P = (Max(Fo^2,0) + 2Fc^2)/3$
Anomalous Dispersion	All non-hydrogen atoms
No. Observations (I>2.00σ(I))	4743
No. Variables	398
Reflection/Parameter Ratio	11.92
Residuals: R1; wR2	0.055 ; 0.148
Goodness of Fit Indicator	1.01

Max Shift/Error in Final Cycle	0.00
Maximum peak in Final Diff. Map	1.34 $e^-/Å^3$
Minimum peak in Final Diff. Map	-0.35 $e^-/Å^3$

A3.5: $[(Cl2POMP)_4Cu_8(N(CN)_2)_8](H_2O)_9(CH_3CN)_2$ **(4.3)**

A. Crystal Data

Empirical Formula	$C_{104}H_{70}N_{54}O_8Cl_4Cu_8$
Formula Weight	2854.23
Crystal Color, Habit	green, prism
Crystal Dimensions	0.80 X 0.20 X 0.15 mm
Crystal System	tetragonal
Lattice Type	I-centered
Lattice Parameters	a = 20.8401(5) Å c = 13.1228(6) Å V = 5699.4(3) $Å^3$
Space Group	I-4 (#82)
Z value	2
D_{calc}	1.663 g/cm^3
F_{000}	2872.00
μ(MoKα)	16.39 cm^{-1}

B. Intensity Measurements

Diffractometer	Bruker P4/CCD
Radiation	MoKα (λ = 0.71073 Å) graphite monochromated
Temperature	-80 $\pm$ 1°C
Scan Rate	30s, 0.3 deg frames
$2\theta_{max}$	52.8°
No. of Reflections Measured	Total: 16218 Unique: 5823 (R_{int} = 0.024)
Corrections	Lorentz-polarization SADABS correction Trans factors 0.7911 – 0.3539

C. Structure Solution and Refinement

Structure Solution	Direct Methods (SHELX97)
Refinement	Full-matrix least-squares on F^2
Function Minimized	$\Sigma w (Fo^2 - Fc^2)^2$
Least Squares Weights	$w = 1/ [\sigma^2(Fo^2) + (0.0528 \cdot P)^2 + 0.0284 \cdot P]$ where $P = (Max(Fo^2,0) + 2Fc^2)/3$
Anomalous Dispersion	All non-hydrogen atoms
No. Observations (I>2.00σ(I))	5823
No. Variables	395
Reflection/Parameter Ratio	14.74
Residuals: R1; wR2	0.029 ; 0.079
Goodness of Fit Indicator	1.06
Max Shift/Error in Final Cycle	0.00
Maximum peak in Final Diff. Map	0.86 $e^-/Å^3$
Minimum peak in Final Diff. Map	-0.36 $e^-/Å^3$

A3.6: $[(SEt2POMP)_4Cu_8(H_2O)_8](PF_6)_8(CH_3OH)_6(CH_3CN)_{1.5}$ **(4.5)**

A. Crystal Data

Empirical Formula	$C_{92.50}H_{106}O_{18.50}F_{48}S_4N_{28}Cu_8P_8$
Formula Weight	3702.35
Crystal Color, Habit	green, prism
Crystal Dimensions	0.52 X 0.34 X 0.18 mm
Crystal System	monoclinic
Lattice Type	C-centered
Lattice Parameters	a = 36.251(5) Å b = 13.134(2) Å c = 35.387(5) Å β = 95.168(3) ° V = 16779(4) $Å^3$
Space Group	C2/c (#15)
Z value	4
D_{calc}	1.465 g/cm^3
F_{000}	7412.00
μ(MoKα)	12.30 cm^{-1}

B. Intensity Measurements

Diffractometer	Bruker P4/CCD
Radiation	MoKα (λ = 0.71073 Å) graphite monochromated
Temperature	-80 ± 1°C
Scan Rate	30 sec, 0.3 deg frames
$2\theta_{max}$	53.0°
No. of Reflections Measured	Total: 64302 Unique: 17250 (R_{int} = 0.070)
Corrections	Lorentz-polarization SADABS correction (trans factors 0.8089 – 0.5672)

C. Structure Solution and Refinement

Structure Solution	Patterson Methods (DIRDIF92 ORIENT)
Refinement	Full-matrix least-squares on F^2
Function Minimized	$\Sigma\, w (Fo^2 - Fc^2)^2$
Least Squares Weights	$w = 1/ [\, \sigma^2(Fo^2) + (0.1785 \cdot P)^2 + 87.5245 \cdot P\,]$ where $P = (Max(Fo^2,0) + 2Fc^2)/3$
Anomalous Dispersion	All non-hydrogen atoms
No. Observations	17250
No. Variables	952
Reflection/Parameter Ratio	18.12
Residuals: R1; wR2	0.096 ; 0.306
Goodness of Fit Indicator	1.07
Max Shift/Error in Final Cycle	0.00
Maximum peak in Final Diff. Map	1.87 $e^-/Å^3$
Minimum peak in Final Diff. Map	-1.44 $e^-/Å^3$

A3.7: $[(SEt2POAP)_5Ni_6](CF_3SO_3)_7(H_2O)_{14}$ (**5.3**)

A. Crystal Data

Empirical Formula	$C_{113}H_{149}F_{21}N_{45}Ni_6O_{54.50}S_{12}$
Formula Weight	4145.58
Crystal Color, Habit	green-brown, prism

Crystal Dimensions	0.285 X 0.203 X 0.094 mm
Crystal System	triclinic
Lattice Type	Primitive
Detector Position	39.95 mm
Pixel Size	0.137 mm
Lattice Parameters	a = 18.6174(14) Å
	b = 19.2391(15) Å
	c = 26.272(2) Å
	α = 79.147(7) °
	β = 74.629(6) °
	γ = 77.008(7) °
	V = 8758.0(12) Å^3
Space Group	P-1 (#2)
Z value	2
D_{calc}	1.572 g/cm^3
F_{000}	4254
μ(MoKα)	8.89 cm^{-1}

B. Intensity Measurements

Detector	Rigaku Saturn
Goniometer	Rigaku AFC8
Radiation	MoKα (λ = 0.71070 Å) graphite monochromated
Detector Aperture	70 mm x 70 mm
Data Images	780 exposures
ω oscillation Range (χ=0.0, ϕ=0.0)	-15.0 - 15.0°
Exposure Rate	80.0 sec./ °
Detector Swing Angle	15.14°
ω oscillation Range (χ=45.0, ϕ=0.0)	-75.0 - 105.0°
Exposure Rate	80.0 sec./ °
Detector Swing Angle	15.14°
ω oscillation Range (χ=45.0, ϕ=180.0)	-75.0 - 105.0°
Exposure Rate	80.0 sec./ °
Detector Swing Angle	15.14°
Detector Position	39.95 mm
Pixel Size	0.137 mm
$2\theta_{max}$	62.1°

No. of Reflections Measured	Total: 99114 Unique: 47243 (R_{int} = 0.052)
Corrections	Lorentz-polarization Absorption (trans. factors: 0.7657 - 0.9291) Secondary Extinction (coefficient: 0.00064(14))

C. Structure Solution and Refinement

Structure Solution	Direct Methods (SHELX97)
Refinement	Full-matrix least-squares on F^2
Function Minimized	$\Sigma\, w\,(Fo^2 - Fc^2)^2$
Least Squares Weights	$w = 1/[\,\sigma^2(Fo^2) + (0.1183 \cdot P)^2 + 23.8345 \cdot P\,]$ where $P = (Max(Fo^2,0) + 2Fc^2)/3$
$2\theta_{max}$ cutoff	62.1°
Anomalous Dispersion	All non-hydrogen atoms
No. Observations (All reflections)	47243
No. Variables	2212
Reflection/Parameter Ratio	21.36
Residuals: R1 (I>2.00σ(I))	0.1182
Residuals: R (All reflections)	0.1477
Residuals: wR2 (All reflections)	0.3135
Goodness of Fit Indicator	1.155
Max Shift/Error in Final Cycle	0.001
Maximum peak in Final Diff. Map	1.77 $e^-/Å^3$
Minimum peak in Final Diff. Map	-1.15 $e^-/Å^3$

A3.8: $[(SEt2POAP)_6Mn_9](CF_3SO_3)_7(H_2O)_{30}(CH_3CN)$ **(6.1)**

A. Crystal Data

Empirical Formula	$C_{135}H_{138}O_{39}N_{54}F_{18}S_{12}Mn_9$
Formula Weight	4362.05
Crystal Color, Habit	purple, fragment
Crystal Dimensions	0.54 X 0.34 X 0.03 mm
Crystal System	triclinic
Lattice Type	Primitive

Lattice Parameters	a = 19.171(2) Å b = 20.758(2) Å c = 24.905(2) Å α = 81.207(2) ° β = 75.954(2) ° γ = 83.767(2) ° V = 9475(1) Å^3
Space Group	P-1 (#2)
Z value	2
D_{calc}	1.529 g/cm^3
F_{000}	4434.00
μ(MoKα)	8.11 cm^{-1}

B. Intensity Measurements

Diffractometer	Bruker P4/CCD
Radiation	MoKα (λ = 0.71073 Å) graphite monochromated
Temperature	-80 ± 1°C
Scan Rate	30s, 0.3 deg frames
$2\theta_{max}$	53.0°
No. of Reflections Measured	Total: 73525 Unique: 38653 (R_{int} = 0.035)
Corrections	Lorentz-polarization Gaussian integration (face indexed) Trans factors (0.81775 – 0.58587)

C. Structure Solution and Refinement

Structure Solution	Direct Methods (SHELX97)
Refinement	Full-matrix least-squares on F^2
Function Minimized	Σ w (Fo^2 - Fc^2)^2
Least Squares Weights	w = 1/ [σ^2(Fo^2) + (0.2000 · P)^2 + 0.0000 · P] where P = (Max(Fo^2,0) + 2Fc^2)/3
Anomalous Dispersion	All non-hydrogen atoms
No. Observations	38653
No. Variables	2441
Reflection/Parameter Ratio	15.83
Residuals: R1; wR2	0.093 ; 0.331

Goodness of Fit Indicator	1.21
Max Shift/Error in Final Cycle	0.00
Maximum peak in Final Diff. Map	2.42 $e^-/Å^3$
Minimum peak in Final Diff. Map	-1.00 $e^-/Å^3$

A3.9: $[(SEt2POAP)_6Mn_9](CF_3SO_3)_3Ag_3(CN)_5(OH)(H_2O)_{10}$ **(6.4)**

A. Crystal Data

Empirical Formula	$C_{132.75}H_{134}Ag_3F_9Mn_9N_{60}O_{31}S_9$
Formula Weight	4343.47
Crystal Color, Habit	red, chunk
Crystal Dimensions	0.45 X 0.39 X 0.13 mm
Crystal System	triclinic
Lattice Type	Primitive
Detector Position	44.42 mm
Pixel Size	0.137 mm
Lattice Parameters	a = 18.202(7) Å b = 19.477(8) Å c = 30.509(11) Å α = 101.807(3) ° β = 92.944(6) ° γ = 112.897(4) ° V = 9650(6) $Å^3$
Space Group	P-1 (#2)
Z value	2
D_{calc}	1.495 g/cm^3
F_{000}	4379.00
μ(MoKα)	10.457 cm^{-1}

B. Intensity Measurements

Detector	Rigaku Saturn
Goniometer	Rigaku AFC8
Radiation	MoKα (λ = 0.71070 Å) graphite monochromated
Detector Aperture	70 mm x 70 mm
Data Images	2160 exposures
ω oscillation Range (χ=0.0, ϕ=0.0)	-70.0 - 110.0°
Exposure Rate	40.0 sec./ °

Detector Swing Angle	20.42°
ω oscillation Range (χ=0.0, ϕ=180.0)	-70.0 - 110.0°
Exposure Rate	40.0 sec./ °
Detector Swing Angle	20.42°
ω oscillation Range (χ=45.0, ϕ=0.0)	-70.0 - 110.0°
Exposure Rate	40.0 sec./ °
Detector Swing Angle	20.42°
ω oscillation Range (χ=45.0, ϕ=180.0)	-70.0 - 110.0°
Exposure Rate	40.0 sec./ °
Detector Swing Angle	20.42°
ω oscillation Range (χ=45.0, ϕ=90.0)	-70.0 - 110.0°°
Exposure Rate	40.0 sec./ °
Detector Swing Angle	20.42°
ω oscillation Range (χ=0.0, ϕ=90.0)	-70.0 - 110.0°
Exposure Rate	40.0 sec./ °
Detector Swing Angle	20.42°
Detector Position	44.42 mm
Pixel Size	0.137 mm
$2\theta_{max}$	63.6°
No. of Reflections Measured	Total: 265390 Unique: 58343 (R_{int} = 0.057)
Corrections	Lorentz-polarization (trans. factors: 0.5122 - 0.7321)

C. Structure Solution and Refinement (in progress)

Structure Solution	Direct Methods (SHELX97)
Refinement	Full-matrix least-squares on F^2
Function Minimized	$\Sigma\, w (Fo^2 - Fc^2)^2$
Least Squares Weights	$w = 1/ [\, \sigma^2(Fo^2) + (0.2000 \cdot P)^2 + 0.0000 \cdot P\,]$ where $P = (Max(Fo^2,0) + 2Fc^2)/3$
Anomalous Dispersion	All non-hydrogen atoms
No. Observations	58343
No. Variables	2102
Reflection/Parameter Ratio	27.8
Residuals: R1; wR2	0.206; 0.547

Goodness of Fit Indicator	1.953
Max Shift/Error in Final Cycle	0.45

A3.10: $[(SEt2POAP)_6Mn_9]Ag_6(CF_3SO_3)_3(NO_3)_9(H_2O)_{17}(CH_3CN)$ (**6.5**)

A. Crystal Data

Empirical Formula	$C_{128}Ag_{5.75}F_6Mn_9N_{63.75}O_{61.25}S_8H_{142}$
Formula Weight	5038.57
Crystal Color, Habit	red, chip
Crystal Dimensions	0.35 X 0.26 X 0.06 mm
Crystal System	triclinic
Lattice Type	Primitive
Detector Position	39.92 mm
Pixel Size	0.137 mm
Lattice Parameters	a = 18.134(2) Å b = 19.806(7) Å c = 28.352(14) Å α = 83.15(7) ° β = 79.66(5) ° γ = 66.28(6) ° V = 9158.4(57) $Å^3$
Space Group	P-1 (#2)
Z value	2
D_{calc}	1.827 g/cm^3
F_{000}	5047
μ(MoKα)	13.94 cm^{-1}

B. Intensity Measurements

Detector	Rigaku Saturn
Goniometer	Rigaku AFC8
Radiation	MoKα (λ = 0.71070 Å) graphite monochromated
Detector Aperture	70 mm x 70 mm
Data Images	780 exposures
ω oscillation Range (χ=0.0, ϕ=0.0)	-65.0 - -35.0°
Exposure Rate	50.0 sec./ °
Detector Swing Angle	15.17°
ω oscillation Range (χ=45.0, ϕ=0.0)	-75.0 - 105.0°

Exposure Rate	50.0 sec./ $^{\circ}$
Detector Swing Angle	15.17°
ω oscillation Range (χ=45.0, ϕ=180.0)	-75.0 - 105.0°
Exposure Rate	50.0 sec./ $^{\circ}$
Detector Swing Angle	15.17°
Detector Position	39.92 mm
Pixel Size	0.137 mm
$2\theta_{max}$	61.4°
No. of Reflections Measured	Total: 77549 Unique: 31883 (R_{int} = 0.053)
Corrections	Lorentz-polarization Absorption (trans. factors: 0.5939 - 0.9254) Secondary Extinction (coefficient: 0.00207(18))

C. Structure Solution and Refinement

Structure Solution	Direct Methods (SHELX97)
Refinement	Full-matrix least-squares on F^2
Function Minimized	Σ w $(Fo^2 - Fc^2)^2$
Least Squares Weights	$w = 1/ [\sigma^2(Fo^2) + (0.1471 \cdot P)^2 + 97.0473 \cdot P]$ where $P = (Max(Fo^2,0) + 2Fc^2)/3$
$2\theta_{max}$ cutoff	50.0°
Anomalous Dispersion	All non-hydrogen atoms
No. Observations (All reflections)	31883
No. Variables	2401
Reflection/Parameter Ratio	13.28
Residuals: R1 (I>2.00σ(I))	0.1139
Residuals: R (All reflections)	0.1266
Residuals: wR2 (All reflections)	0.3185
Goodness of Fit Indicator	1.067
Max Shift/Error in Final Cycle	0.001
Maximum peak in Final Diff. Map	1.82 $e^-/Å^3$
Minimum peak in Final Diff. Map	-1.38 $e^-/Å^3$

A3.11: [Ni(Cl2POPP)] **(7.1)**

A. Crystal Data

Empirical Formula	$C_{31}H_{20}N_7O_2NiCl$
Formula Weight	616.70
Crystal Color, Habit	red, prism
Crystal Dimensions	0.15 X 0.08 X 0.40 mm
Crystal System	monoclinic
Lattice Type	C-centered
No. of Reflections Used for Unit Cell Determination (2θ range)	20 (8.6 - 13.1°)
Omega Scan Peak Width at Half-height	0.22°
Lattice Parameters	a = 14.405(3) Å b = 17.663(5) Å c = 10.689(4) Å β = 103.73(3) ° V = 2642(1) Å^3
Space Group	Cc (#9)
Z value	4
D_{calc}	1.550 g/cm^3
F_{000}	1264.00
μ(MoKα)	8.81 cm^{-1}

B. Intensity Measurements

Diffractometer	Rigaku AFC6S
Radiation	MoKα (λ = 0.71069 Å)graphite monochromated
Take-off Angle	6.0°
Detector Aperture	6.0 mm horizontal 3.0 mm vertical
Crystal to Detector Distance	400 mm
Voltage, Current	50kV, 27.5mA
Temperature	26.0°C
Scan Type	ω-2θ
Scan Rate	4.0°/min (in ω) (up to 4 scans)
Scan Width	(1.52 + 0.35 tan θ)°
$2\theta_{max}$	55.1°

No. of Reflections Measured	Total: 3276 Unique: 3154 (R_{int} = 0.032)
Corrections	Lorentz-polarization Absorption (trans. factors: 0.9190 - 1.0000) Secondary Extinction (coefficient: 3.97700e-009)

C. Structure Solution and Refinement

Structure Solution	Direct Methods (SIR92)
Refinement	Full-matrix least-squares on F
Function Minimized	Σ w (|Fo| - |Fc|)^2
Least Squares Weights	$1/\sigma^2(Fo) = 4Fo^2/\sigma^2(Fo^2)$
p-factor	0.0200
Anomalous Dispersion	All non-hydrogen atoms
No. Observations (I>2.00σ(I))	2206
No. Variables	378
Reflection/Parameter Ratio	5.84
Residuals: R; Rw	0.043 ; 0.040
Goodness of Fit Indicator	1.29
Max Shift/Error in Final Cycle	0.00
Maximum peak in Final Diff. Map	0.38 $e^-/Å^3$
Minimum peak in Final Diff. Map	-0.28 $e^-/Å^3$

A3.12: $[Cu_2(L1)(L2)](H_2O)_2(CH_3OH)(L3)$ (**7.2**)

A. Crystal Data

Empirical Formula	$C_{39}H_{30}N_8O_{10}Cl_2Cu_2$
Formula Weight	968.71
Crystal Color, Habit	red-brown, plate
Crystal Dimensions	0.79 X 0.19 X 0.06 mm
Crystal System	monoclinic
Lattice Type	C-centered
Lattice Parameters	a = 29.927(3) Å b = 8.8728(8) Å c = 30.906(3) Å β = 109.832(2)° V = 7720(1) Å^3
Space Group	C2/c (#15)

Z value	8
D_{calc}	1.667 g/cm^3
F_{000}	3936.00
μ(MoKα)	13.12 cm^{-1}

B. Intensity Measurements

Diffractometer	Bruker P4/CCD
Radiation	MoKα (λ = 0.71073 Å) graphite monochromated
Temperature	-80 $\pm$ 1°C
Scan Rate	30s, 0.3 deg frames
$2\theta_{max}$	52.8°
No. of Reflections Measured	Total: 23564 Unique: 7878 (R_{int} = 0.039)
Corrections	Lorentz-polarization SADABS correction (trans factors 0.9254 – 0.4237)

C. Structure Solution and Refinement

Structure Solution	Direct Methods (SHELX97)
Refinement	Full-matrix least-squares on F^2
Function Minimized	Σ w (Fo^2 - Fc^2)^2
Least Squares Weights	w = 1/ [$\sigma^2(Fo^2)$ + (0.0515 · P)^2 + 16.0206 · P] where P = (Max(Fo^2,0) + 2Fc^2)/3
Anomalous Dispersion	All non-hydrogen atoms
No. Observations (I>2.00σ(I))	6088
No. Variables	550
Reflection/Parameter Ratio	11.07
Residuals: R1; wR2	0.044 ; 0.111
Goodness of Fit Indicator	1.02
Max Shift/Error in Final Cycle	0.00
Maximum peak in Final Diff. Map	0.71 e$^-$/Å^3
Minimum peak in Final Diff. Map	-0.58 e$^-$/Å^3

A3.13: $[(Cl2POPP)_3(L1)_6Co(III)_6Co(II)_6(H_2O)_6(NO_3)_6][Co(H_2O)_6](NO_3)_{12}(CH_3CN)_3(H_2O)_{10}$ (**7.3**)

A. Crystal Data

Empirical Formula	$C_{213}H_{171}N_{62}O_{84}Cl_9Co_{13}$
Formula Weight	6028.27
Crystal Color, Habit	dark orange, fragment
Crystal Dimensions	0.50 X 0.40 X 0.30 mm
Crystal System	hexagonal
Lattice Type	Primitive
Lattice Parameters	a = 24.2682(6) Å c = 29.470(2) Å V = 15030.9(8) $Å^3$
Space Group	$P6_3/m$ (#176)
Z value	2
D_{calc}	1.332 g/cm^3
F_{000}	6118.00
μ(MoKα)	8.61 cm^{-1}

B. Intensity Measurements

Diffractometer	Bruker P4/CCD
Radiation	MoKα (λ = 0.71073 Å) graphite monochromated
Temperature	-80 $\pm$ 1°C
Scan Rate	30s, 0.3 deg. frames
$2\theta_{max}$	52.8°
No. of Reflections Measured	Total: 96973 Unique: 10478 (R_{int} = 0.070)
Corrections	Lorentz-polarization SADABS correction (trans factors: 0.7822 – 0.6727)

C. Structure Solution and Refinement

Structure Solution	Patterson Methods (DIRDIF92 ORIENT)
Refinement	Full-matrix least-squares on F^2
Function Minimized	Σ w (Fo^2 - Fc^2)^2

Least Squares Weights	$w = 1/ [\sigma^2(Fo^2) + (0.1803 \cdot P)^2 + 65.6329 \cdot P]$ where $P = (Max(Fo^2,0) + 2Fc^2)/3$
Anomalous Dispersion	All non-hydrogen atoms
No. Observations (I>2.00σ(I))	10478
No. Variables	570
Reflection/Parameter Ratio	18.38
Residuals: R1; wR2	0.094 ; 0.335
Goodness of Fit Indicator	1.11
Max Shift/Error in Final Cycle	0.00
Maximum peak in Final Diff. Map	1.63 $e^-/Å^3$
Minimum peak in Final Diff. Map	-0.91 $e^-/Å^3$

References:

[1] J. W. Steed, J. L. Atwood, Supramolecular Chemistry,© 2000, John Wiley & Sons, Ltd. New York.

[2] S. Leninger, B. Olenyuk, P. J. Stang, *Chem. Rev.*, **2000**, *100*, 853.

[3] R. E. P. Winpenny, *J. Chem. Soc. Dalton Trans.*, **2002**, 1.

[4] J. C. Goodwin, R. Sessoli, D. Gatteschi, W. Wernsdorfer, A. K. Powell, S. L. Heath., *J. Chem. Soc., Dalton Trans.*, **2000**, 1835.

[5] T. S. M. Abedin, L. K. Thompson, D. O. Miller, E. Krupicka, *Chem. Commun.*, **2003**, 708.

[6] A. J. Tasiopoulos, A. Vinslava, W. Wernsdorfer, K. A. Abboud and G. Christou, *Angew. Chem. Int. Ed.*, **2004**, *43*, 2117.

[7] C. J. Pedersen, *J. Am. Chem. Soc.*, **1967**, *89*, 7017.

[8] R. W. Saalfrank, I. Bernt, E. Uller, F. Hampel, *Angew. Chem. Int. Ed.*, **1997**, *36*, 2482.

[9] F. K. Larsen, E. J. L. McInnes, H. El Mkami, J. Overgaard, S. Piligkos, G. Rajaraman, E. Rentschler, A. A. Smith, G. M. Smith, V. Boote, M. Jennings, G. A. Timco, R. E. P. Winpenny, *Angew. Chem. Int. Ed.*, **2003**, *42*, 101.

[10] J. van Slageren, R. Sessoli, D. Gatteschi, A. A. Smith, M. Helliwell, R. E. P. Winpenny, A. Cornia, A.-L. Barra, A. G. M. Jansen, G. A. Timco, E. Rentschler, *Chem. Eur. J.*, **2002**, *8*, 277.

[11] J. Overgaard, B. B. Iversen, S. P. Palii, G. A. Timco, N. V. Gerbeleu, F. K. Larsen, *Chem. Eur. J.*, **2002**, *8*, 2775.

[12] G. A. Timco, A. S. Batsanov, F. K. Larsen, C. A. Muryn, J. Overgaard, S. J. Teat, R. E. P. Winpenny, *Chem. Commun.*, **2005**, 3649.

[13] R. H. Laye, F. K. Larsen, J. Overgaard, C. A. Muryn, E. J. L. McInnes, E. Rentschler, V. Sanchez, S. J. Teat, H. U. Güdel, O. Waldmann, G. A. Timco, R. E. P. Winpenny, *Chem. Commun.*, **2005**, 1125.

[14] F. Troiani, A. Ghirri, M. Affronte, S. Carretta, P. Santini, G. Amoretti, S. Piligkos, G. Timco, R.E. P. Winpenny, *Phys. Rev. Lett.*, **2005**, *94*, 207208.

[15] R. E. P. Winpenny, personal communication.

[16] P. N. W. Baxter, J.-M. Lehn, J. Fischer, M.-T. Youinou, *Angew. Chem. Int. Ed.*, **1994**, *33*, 2284.

[17] J. Rojo, F. Romero-Salguero, J.-M. Lehn, G. Baum, D. Fenske, *Eur. J. Inorg. Chem.*, **1999**, 1421.

[18] M. Reuben, E. Breuning, J.-P. Gisselbrecht, J.-M. Lehn, *Angew. Chem. Int. Ed.*, **2000**, *39*, 4139.

[19] A. Petitjean, N. Kyritsakas, J.-M. Lehn, *Chem. Commun.*, **2004**, 1168.

[20] E. Breuning, G. S. Hanan, F. J. Romero-Salguero, A. M. Garcia, P. N. W. Baxter, J.-M. Lehn, E. Wegelius, K. Rissanen, H. Nierengarten, A. van Dorsselaer, *Chem. Eur. J.*, **2002**, *8*, 3458.

[21] A. M. Garcia, F. J. Romero-Salguero, D. M. Bassani, J.-M. Lehn, G. Baum, D. Fenske, *Chem. Eur. J.*, **1999**, *5*, 1803.

[22] L. K. Thompson, C. J. Matthews, L. Zhao, Z. Xu, D. O. Miller, C. Wilson, M. A. Leech, J. A. K. Howard, S. L. Heath, A. G. Whittaker, R. E. P. Winpenny, *J. Solid State Chem.*, **2001**, *159*, 308.

[23] C. J. Matthews, K. Avery, Z. Xu, L. K. Thompson, L. Zhao, D. O. Miller, K. Biradha, K. Poirier, M. J. Zaworotko, C. Wilson, A. E. Goeta, J. A. K. Howard, *Inorg. Chem.*, **1999**, *38*, 5266.

[24] Z. Xu, L. K. Thompson, D. O. Miller, *J. Chem. Soc. Dalton Trans.*, **2002**, 2462.

[25] C. J. Matthews, L. K. Thompson, S. R. Parsons, Z. Xu, D. O. Miller, S. L. Heath, *Inorg. Chem.*, **2001**, *40*, 4448.

[26] L. N. Dawe, T. S. M. Abedin, T. L. Kelly, L. K. Thompson, D. O. Miller, l. Zhao, C. Wilson, M. A. Leech, J. A. K. Howard, *J. Mater. Chem.*, **2006**, *16*, 2645.

[27] L. Zhao, C. J. Matthews, L. K. Thompson, S. L. Heath, *Chem. Commun.*, **2000**, 265.

[28] Z. Xu, L. K. Thompson, D. O. Miller, *Chem. Commun.*, **2001**, 1170.

[29] L. Zhao, Z. Xu, L. K. Thompson, D. O. Miller, *Polyhedron*, **2001**, *20*, 1359.

[30] S. K. Dey, L. K. Thompson, unpublished results.

[31] S. M. T. Abedin, L. K. Thompson, unpublished results.

[32] V. A. Milway, S. M. T. Abedin, V. Niel, T. L. Kelly, L. N. Dawe, S. K. Dey, D. W. Thompson, D. O. Miller, M. S. Alam. P. Müller, L. K. Thompson, *J. Chem. Soc. Dalton Trans.*, **2006**, 2835.

[33] C. C. Mann, *Technology Review*, May-June **2000**, 44.

[34] D. A. Thompson, J. S. Best, *The future of magnetic storage technology*, ©2000 IBM

[35] S. J. Tans, A. R. M. Verschuren, C. Dekker, *Nature*, **1998**, *393*, 49.

[36] A. Bachtold, P. Hadley, T. Nakanishi, C. Dekker, *Science*, **2002**, *294*, 1317.

[37] A. R. Pease, J. O. Jeppesen, J. F. Stoddart, Y. Luo, C. P. Collier, J. R. Heath, *Acc. Chem. Res.*, **2001**, *34*, 433.

[38] C. P. Collier, J. O. Jeppesen, Y. Luo, J. Perkins, E. W. Wong, J. R. Heath, J. F. Stoddart, *J. Am. Chem. Soc.*, **2001**, *123*, 126321.

[39] C. S. Lent, B. Isaksen, M. Lieberman, *J. Am. Chem. Soc.*, **2003**, *125*, 1056.

[40] M. Reuben, J. Rojo, F. J. Romero-Salguero, L. H. Uppadine, J.-M. Lehn, *Angew. Chem. Int. Ed.*, **2004**, *43*, 3644.

[41] F. Meier, J. Levy, D. Loss, *Phys. Rev. Lett.*, **2003**, *90*, 047901.

[42] F. Meier, J. Levy, D. Loss, *Phys. Rev. B.*, **2003**, *68*,134417.

[43] O. Waldmann, H. U. Güdel, T. L. Kelly, L. K. Thompson, *Inorg. Chem.*, **2006**, *45*, 3285.

[44] F. E. Mabbs, D. J. Machin, Magnetism and Transition Metal Complexes, © 1973 Chapman and Hall Ltd., London.

[45] A. Earnshaw, Introduction to Magnetochemistry, © 1968, Academic Press, New York.

[46] Martin, R. L., in New Pathways in Inorganic Chemistry, Eds. E. A. V. Ebsworth,A. G. Maddock, A. G. Sharpe, © 1968, Cambridge Univ. Press.

[47] Kambe, K., *J. Phys. Soc., Japan*, **1950**, *5*, 48.

[48] R. W. Jotham, S. F. A. Kettle, *Inorg. Chim. Acta*, **4**, *1970*, 145.

[49] MAGMUN4.1 is available free of charge from http://www.ucs.mun.ca/~lthomp/index.html. It has been developed by Dr. Zhiqiang Xu (Memorial University), in conjunction with Dr. O. Waldmann (University of Bern, Switzerland). We do not distribute the source codes. The programs may only be utilized for scientific purposes, and economic utilization is not allowed. If the routine is used to obtain scientific results which are published, the origin of the programs should be quoted.

[50] L. K. Thompson, O. Waldmann, Z. Xu, *Coordination Chemistry Reviews*, **2005**, *249*, 2677.

[51] A. Zharkouskaya, Doctoral dissertation, Mehrkernige Übergangsmetallkomplexe als Basis für neue Klassen magnetischer Materialien, Friedrich-Schiller-Universität Jena, Belarus, 2005.

[52] G. S. Hanan, U. S. Schubert, D. Volkmer, E. Riviere, J.-M.Lehn, N. Kyritsakas, J. Fisher, *Can. J. Chem.*, **1997**, *75*, 169.

[53] J. Rojo, J.-M. Lehn, G. Baum, D. Fenske, O. Waldmann, P.Muller, *Eur. J. Inorg. Chem.*, **1999**, 517.

[54] V. A. Milway, V. Niel, S. M. T. Abedin., Z. Xu, L. K. Thompson, H. Grove, D. O. Miller, S. R. Parsons, *Inorg. Chem.*, **2004**, *43*, 1874.

[55] L. Zhao, Z. Xu, H. Grove, V. A. Milway, L. N. Dawe, T. S. M. Abedin, L. K. Thompson, T. L. Kelly, R. G. Harvey,D. O. Miller, L. Weeks, J. G. Shapter, and K. J. Pope, *Inorg. Chem.*, **2004**, *43*, 3812.

[56] E. R. Riegel, F. Zwilgmeyer, *Org. Synth.*, **1943**, Coll. Vol. II, 126.

[57] A. O. Fitton, R. K. Smalley, Practical Heterocyclic Chemistry, © 1968, London Press, London, 74.

[58] J. S. Bradshaw, G. E. Maas, J. D. Lamb, R. M. Izatt, J. J. Christensen, *J. Am. Chem. Soc.*, **1980**,*102*, 467.

[59] D. G. Markees, G. W. Kidder, *J. Am. Chem. Soc.*, **1956**, *78*, 4130.

[60] D. G. Markees, *J. Org. Chem.*, **1963**, *28*, 2530.

[61] F. Drawert, K.-H. Reuther, F. Born, *Chemische Berichte*, **1960**, *93*, 3056.

[62] L. N. Dawe, S. K. Dey, V. A. Milway, L. K. Thompson, unpublished results.

[63] V. A. Milway, S. M. T. Abedin, L. K. Thompson, D. O. Miller., *Inorg. Chim. Acta.*, **2006**, 359,2700.

[64] L. K. Thompson, L. Zhao, Z. Xu, D. O. Miller, W. M. Reiff, *Inorg. Chem.*, **2003**, *42*, 128.

[65] V. A. Milway, L. Zhao, T. L. Kelly, L. K. Thompson, unpublished results, manuscript in preparation.

[66] L. K. Thompson, T. L. Kelly, L. N. Dawe, H. Grove, M. T. Lemaire, J. A. K. Howard, E. C. Spencer, C. J. Matthews, S. T. Onions, S. J. Coles, P. N. Horton, M. B, Hursthouse, M. E. Light, *Inorg. Chem.*, **2004**, *43*, 7605.

[67] O. Waldmann, L. Zhao, L. K. Thompson, *Phys. Rev. Lett.*, **2002**, *88*, 066401.

[68] T. Guidi, S. Carretta, P. Santini, E. Liviotti, N. Magnani, C. Mondelli, O. Waldmann, L. K. Thompson, L. Zhao, C. D. Frost, G. Amoretti, R. Caciuffo, *Phys. Rev. B*, **2004**, *69*, 104432.

[69] O. Waldmann, *Phys. Rev. B*, **2005**, *71*, 094412.

[70] L. Weeks, L. K. Thompson, J. G. Shapter, K. J. Pope, Z. Xu, *J. Microsc.*, **2003**, *212*, 102.

[71] J.G. Shapter, L. Weeks, L. K. Thompson, K. J. Pope, Z. Xu, M. R. Johnston, *Proc. SPIE*, **2004**, *5275*, 59.

[72] (a) G. M. Sheldrick, SHELXL97. Program for Crystal Structure Solution, University of Göttingen, Germany, 1997. (b) A. Altomare, M. Cascarano, C. Giacovazzo, A. Guagliardi, SIR97. *J. Appl. Crystallogr.*, **1993**, *26*, 343.

[73] P.T. Beurskens, G. Admiraal, G. Beurskens, W.P. Bosman, R. de Gelder, R. Israel, J. M. M. Smits, DIRDIF94. The DIRDIF-94 program system, Technical Report of the Crystallography Laboratory, University of Nijmegen, The Netherlands, 1994.

[74] D. T. Cromer, J. T Waber, International Tables for X-ray Crystallography, Vol. IV, The Kynoch Press, Birmingham, England, Table 2.2 A, 1974.

[75] J. A. Ibers, W. C. Hamilton, *Acta. Crystallogr.*, **1964**,*17*, 781.

[76] D. C. Creagh, W.J. McAuley, International Tables for Crystallography, Vol C, (A.J.C. Wilson, ed.), Kluwer Academic Publishers, Boston, USA, Table 4.2.6.8, 1992, 219.

[77] teXsan for Windows version 1.06. Crystal Structure Analysis Package, Molecular Structure Corporation, 1997-9.

[78] P.van der Sluis, A. L. Spek, *Acta Cryst. A*, **1990**, *46*, 194.

[79] T. S., Cameron, M. T. Lemaire, J. Passmore, J. M. Rawson. K. V. Shuvaev, L. K. Thompson, *Inorg. Chem.*, **2005**, *44*, 2576.

[80] S. Brownridge, H. Du, S. A. Fairhurst, R. C. Haddon, H. Oberhammer, S. Parsons, J. Passmore, M. J. Schriver, L. H. Sutcliffe, N. P. C. Westwood, *J. Chem. Soc. Dalton Trans.*, **2000**, 3365.

[81] J. L. Brusso, O. P. Clements, R. C. Haddon, M. E. Itkis, A. A. Leitch, R. T. Oakley, R. W. Reed, J. F. Richardson, *J. Am. Chem. Soc.*, **2004**, *126*, 14692.

[82] J. Huang, M. Kertesz, *J. Phys. Chem. B*, **2005**, *109*,12891.

[83] S. S. Staniland, W. Fujita, Y. Umezono, K. Awaga, P. J. Camp, S. J. Clark, N. Robertson, *Inorg. Chem.*, **2005**, *44*, 546.

[84] A. Bondi, *J. Phys. Chem.*, **1964**, *68*, 441.

[85] M. E. Fisher, *Am. J. Phys.*, **1964**, *32*, 343.

[86] M. J. Baldwin, J. W. Kampf, M. L. Kirk, V. L. Pecoraro, *Inorg. Chem.*, **1995**, *34*, 5252.

[87] O. Kahn, Molecular Magnetism,© 1993, VCH Publishers Inc., New York.

[88] L. N. Dawe, Honours Thesis, Spectroelectrochemical studies of some magnetically active [3x3] manganese (II) grid complexes, Memorial University of Newfoundland, 2002.

[89] R. G. Pearson, *J. Am. Chem. Soc.*, **1963**, *85*, 3533.

[90] D. J. Pond, V. A. Milway, L. K. Thompson, unpublished results.

[91] L. Zhao, L. K. Thompson, Z. Xu, D. O. Miller, D. R. Stirling, *J. Chem. Soc. Dalton Trans.*, **2001**, 1706.

[92] V. A. Milway, L. Zhao, S. M. T. Abedin., L. K. Thompson, Z. Xu, *Polyhedron*, **2003**, *22* 1271.

[93] V. A. Milway, Honours Thesis, Complexes of unsymmetrical ligands: Structural and magnetic properties, Memorial University of Newfoundland, 2002.

[94] L. Zhao, Z. Xu, L. K. Thompson, S. L. Heath, D. O. Miller, M. Ohba, *Angew. Chem. Int. Ed.*, **2000**, *39*, 3114.

[95] R. Sessoli, D. Gatteschi, A. Caneschi, M. A. Novak, *Nature*, **1993**, *365*, 141.

[96] L. Thomas, F. Lionti, R. Ballou, D. Gatteschi, R. Sessoli, B. Barbara, *Nature*, **1996**, *383*, 145.

[97] D. Gatteschi, R. Sessoli, *Angew. Chem. Int. Ed.*, **2003**, *42*, 268.

[98] W. Wernsdorfer, N. Aliaga-Alcalde, D. N. Hendrickson, G. Christou, *Nature*, **2002**, *416*, 406.

[99] S. Hill, R. S. Edwards, N. Aliaga-Alcalde, G. Christou, *Science*, **2003**, *302* 1015.

[100] J. M. North, N. S. Dalal, D. Foguet-Albiol, A. Vinslava, G. Christou, *Phys. Rev. B*, **2004**, *69*, 174419.

[101] S. Ferlay, T. Mallah, R. Ouahès, P. Veillet, M. Verdaguer, *Nature*, **1995**, *378*, 710.

[102] R. Garde, F. Villain, M. Verdaguer, *J. Am. Chem. Soc.*, **2002**, *124*, 10531.

[103] S. R. Batten, P. Jensen, B. Moubaraki, K. S. Murray, R. Robson, *Chem. Commun*, **1998**, 439.

[104] P.T. Beurskens, G. Admiraal, G. Beurskens, W.P. Bosman, S. Garcia-Granda, R.O. Gould, J. M. M. Smits, C. Smykalla, ORIENT. The DIRDIF program system, Technical Report of the Crystallography Laboratory, University of Nijmegen, The Netherlands (1992).

[105] G. R. Desiraju, *Acc. Chem. Res.*, **1996**, *29*, 441.

[106] C. N. Sanrame, C. P. Suhrada, H. Dang, M. A. Garcia-Garibay, *J. Phys. Chem. A.*, **2003**, *107*, 32287.

[107] D. S. Reddy, Y. E. Ovchinnikov, O. V. Shishkin, Y. T. Struchkov, G. R. Desiraju, *J. Am. Chem. Soc.*, **1996**, *118*, 4085.

[108] S. V. Lindeman, J. K. Kochi, *Crystal Growth & Design*, **2004**, *4*, 563.

[109] T. L. Kelly, V. A. Milway, H. Grove, V. Niel, T. S. M. Abedin, L. K. Thompson, L. Zhao, R. G. Harvey, D. O. Miller, M. Leech, A. E. Goeta, J. A. K. Howard, *Polyhedron*, **2005**, *24*, 807.

[110] O. Waldmann, J. Hassmann, P. Müller, G. S. Hanan, U. S. Schubert, J. M. Lehn. *Phys. Rev. Lett.*, **1997**, *78*, 3390.

[111] O. Waldmann, R. Koch, S. Schromm, P. Müller, L. Zhao, L. K. Thompson, *Chemical Physics Letters*, **2000**, *332*, 73.

[112] CrystalClear: Rigaku Corporation, 1999. CrystalClear Software User's Guide, Molecular Structure Corporation, (c) 2000, J.W.Pflugrath (1999) *Acta Cryst. D.*, *55*, 1718.

[113] Z. Xu, V. A. Milway, L. K. Thompson, unpublished results.

[114] A. B. P. Lever, Inorganic Electronic Spectroscopy, Physical Inorganic Chemistry Monograph, M. F. Lappert Ed. © 1968 Elsevier Publishing company, Amsterdam.

[115] P. J. Steel, *Coordination Chemistry Reviews*, **1990**, *106*, 227.

[116] X.-H. Bu, Y.-B. Xie, J.-R. Li, R.-H. Zhang, *Inorg. Chem.*, **2003**, *42*, 7422.

[117] X. Liu, G.-C.Guo, M.-L. Fu, W.-T. Chen, Z.-J. Zhang, J.-S. Huang, *J. Chem. Soc. Dalton Trans.*, **2006**, 884.

[118] C. J. Shorrock, B.-Y. Xue, P. B. Kim, R. J. Batchelor, B. O. Patrick, D. B. Leznoff, *Inorg. Chem.*, **2002**, *41*, 6743.

[119] F. B. Stocker, D. Britton, V. G. Young, Jr., *Inorg. Chem.*, **2000**, *39*, 3479.

[120] I. P. Y. Shek, W.-Y. Wong, T.-C. Lau, *New J. Chem.*, **2000**, *24*, 733.

[121] H.-P. Wu, C. Janiak, G. Rheinwald, H. lang, *J. Chem. Soc. Dalton Trans.*, **1998**, 183.

[122] D. Fortin, M. Drouin, P. D. Harvey, F. G, Herring, D. A. Summers, R. C. Thompson, *Inorg. Chem.*, **1999**, *38*, 1253.

[123] C. Kleina, E. Graf, M. W. Hosseini, A. De Cian, J. Fischer, *Chem. Commun.*, **2000**, 239.

[124] G. A. Bowmaker, Effendy, J. C. Reid, C. E. F. Rickard, B. W. Skelton, A. H. White, *J. Chem. Soc. Dalton Trans.*, **1998**, 2139.

[125] H. A. Buchholz, G. K. Surya Prakash, J. F. S. Vaughan, R. Bau, G. A. Olah, *Inorg. Chem.*, **1996**, *35*, 4076.

[126] R.-Q. Zou, J.-R. Li, Y.-B. Xie, R.-H. Zhang, X.-H. Bu, *Crystal Growth & Design*, **2004**, *4*, 79.

[127] G. J. Palenik, *Inorg. Chem.*, **1997**, *36*, 122.

[128] R. M. Wood, G. J. Palenik, *Inorg. Chem.*, **1998**, *37*, 4149.

[129] H. H. Thorp, *Inorg. Chem.*, **1992**, *31*, 1585.

[130] W. Liu, H. H. Thorp, *Inorg. Chem.*, **1993**, *32*, 4102.

[131] A.J. Bard, R. Parsons, and J. Jordan, Standard Potentials in Aqueous Solutions, © 1985, IUPAC, (Marcel Dekker), New York.

[132] V. A. Milway, L. K. Thompson, unpublished results.

[133] V. A. Milway, L. K. Thompson, unpublished results.

[134] Z. Xu, L.K. Thompson, D.O. Miller, *Polyhedron*, **2002**, *21*, 1715.

[135] L.P. Battaglia, M. Carcelli, F. Ferraro, L. Mavilla, C. Pelizzi, G. Pelizzi, *J. Chem. Soc., Dalton Trans.*, **1994**, 2651.

[136] H. Ogura, S. Mineo, K. Nakagawa, S. Shiba, *Yakugaka Zasshi*, **1981**,*101*, 329.

[137] J.H. Boyer, R. Borgers, L.T. Wolford, *J. Am. Chem. Soc.*, **1957**, *79*, 678.

[138] V. A. Milway, S. M. T. Abedin, L. K. Thompson, unpublished results.

[139] V.A. Milway, L.K. Thompson, D.O. Miller, *Chem. Commun.*, **2004**, 1790.

[140] J. A. Swift, A. M. Reynolds, M. D. Ward, *Chem. Mater.*, **1998**, *10*, 4159.

[141] A. Müller, R. Sessoli, E. Krickemeyer, H. Bögge, J. Meyer, D. Garreschi, L. Pardi, J. Westphal, K. Hovemeier, R. Rohlfing, J. Döring, F. Hellweg, C. Beugholt, M. Schmidtmann, *Inorg. Chem.*, **1997**, *36*, 5239.

[142] S. Spange, A. Gräser, H. Müller, Y. Zimmermann, P. Rehak, C. Jäger, H. Fuess, C. Baehtz, *Chem. Mater.*, **2001**, *13*, 3698.

[143] E. Colacio, J.-M. Dominguez-Vera, J.-P. Costes, R. Kivekäs, J.-P., Laurent, J. Ruiz, M. Sundberg, *Inorg. Chem.*, **1992**, *31*, 774.

[144] V. Tangoulis, G. Psomas, C. Dendrinou-Samara, C. P. Raptopoulou, A. Terzis, D. P. Kessissoglou, *Inorg. Chem.*, **1996**, *35*, 7655.

[145] E. Colacio, J.-M. Dominguez-Vera, M. Ghazi, R. Kivekäs, M. Klinga, J. M. Moreno, *Eur. J. Inorg. Chem.*, **1999**, 441.

[146] E. Colacio, M. Ghazi, R. Kivekäs, J. M. Moreno, *Inorg. Chem.*, **2000**, *39*, 2882.